



**HAL**  
open science

# Development of novel tools based on patient-specific models for guidance and education in orthognathic surgery

Jean-Christophe Lutz

► **To cite this version:**

Jean-Christophe Lutz. Development of novel tools based on patient-specific models for guidance and education in orthognathic surgery. Surgery. Université de Strasbourg, 2017. English. NNT : 2017STRAD017 . tel-01743747

**HAL Id: tel-01743747**

**<https://theses.hal.science/tel-01743747>**

Submitted on 26 Mar 2018

**HAL** is a multi-disciplinary open access archive for the deposit and dissemination of scientific research documents, whether they are published or not. The documents may come from teaching and research institutions in France or abroad, or from public or private research centers.

L'archive ouverte pluridisciplinaire **HAL**, est destinée au dépôt et à la diffusion de documents scientifiques de niveau recherche, publiés ou non, émanant des établissements d'enseignement et de recherche français ou étrangers, des laboratoires publics ou privés.

# THÈSE

présentée et soutenue publiquement le 26 juin 2017 par :

**Jean-Christophe LUTZ**

pour obtenir le grade de

**Docteur en SCIENCES de l'Université de Strasbourg**

Spécialité : Informatique

**DEVELOPMENT OF NOVEL TOOLS  
BASED ON PATIENT-SPECIFIC MODELS  
FOR GUIDANCE AND EDUCATION  
IN ORTHOGNATHIC SURGERY**

**THÈSE DIRIGÉE PAR :**

Yves RÉMOND

Professeur, ICube, Université de Strasbourg

Luc SOLER

Professeur, Directeur de Recherches IRCAD / IHU Strasbourg

**RAPPORTEURS:**

Marie-Christine HO BA THO

Professeur, Laboratoire de Biomécanique et Bioingénierie,  
Université de Technologie de Compiègne

Didier FASS

Professeur, LORIA, Université de Lorraine

**EXAMINATEURS:**

Dominique GOGA

Professeur, Université de Tours

Didier MUTTER

Professeur, Université de Strasbourg

Stéphane NICOLAU

Examineur Brevet, Office Européen des Brevets  
Munich, Allemagne



# Acknowledgements

First, I would like to thank the members of my Jury,

Yves Rémond for his support, inspiration and kindness all along this work.

Luc Soler, for encouraging my passion for this research field and for the everyday support he brought me along with his inspiring personality.

Didier Mutter for making me the honor of being the chairman of my jury and for his strong encouragement.

Marie-Christine Ho Ba Tho for accepting to be part of my jury, for the kind interest with which she considered my work and for the perspectives she offers to my research.

Didier Fass for the interest and passion he showed in the assessment of this work.

Dominique Goga for the leadership and vision he brings to maxillofacial surgery and for his full support to my professional development.

Stéphane Nicolau for his insight, method, friendship and humor. For his tremendous support in the initial steps of this work along with enthusiastic dissertations about French semantics.

To the people who have also strongly supported me along this research,

Jacques Marescaux for his welcoming me in IRCAD, his goodwill and strong support over the years.

Astrid Wilk for encouraging me in a University curriculum and for believing in my research, for the example she set for future generations of maxillofacial surgeons.

Vincent Agnus for his availability, patience, outstanding educational skills and the great help he provided me throughout all the steps of this work.

Alexandre Hostettler for his passion, energy and paramount help in the final steps of this work. For the exhilarating conversations we had and his vast enthusiasm.

Daniel Georges, for his support, insight and help in capitalizing on this work.

To my lab mates Caroline Trompf, Nicolas Maire, Guillaume Munsch, Bénédicte Fahrer, Michaël Kugler for their support that has definitely smoothed my labor.

To the University staff,

Jean Sibilia, Dean of the Medical School, for his support.

Isabelle Lapierre, Nathalie Kostmann, Isabelle Mula for their goodwill.

To the staff in IRCAD and iCube, especially

Pamela Lhote, for her kindness, availability, professionalism and smile that eased the days of hard labor.

Thomas Parent for his friendship, passion, humor and coffees who have lightened up my days.

Olivia Bilger, Marie Obringer, Pascale Musard, the front desk staff (Isa, Audrey, Delphine...), the IT team (Bertrand, Kouami), the audiovisual team (Carlos, David, Melody, Thibaut...) for their kindness and warm welcoming.

To friends and colleagues in IHU and Visible Patient, especially,

Mourad Bouhadjar, Yann Lemblé, Anne-Blandine Mackowski for their kindness and availability.

To friends and colleagues in Prometeus, Gilbert Decker, Juan Hernandez, Maryline Oswald.

To friends and colleagues in the hospital maxillofacial and plastic surgery department, Frédéric Bodin, Simone Zink, Caroline Dissaux, Jean-Francois Garnier, Jacques Nussbaumer.

To my friends and research mates in Master, Fabien Bornert and Fabrice Hubelé, who have greatly helped me along these early years of research.

To Nadia Jessel and her Team, to Florence Fioretti for welcoming me among them.

To friends and colleagues in the Odontology Department, Catherine-Isabelle Gros, and to Anne-Marie Musset and Marie-Cécile Manière for their support.

To my lifelong dear friends, Stephen Lemay, Mathieu Berthel, Yves Schlecht, Mohamed El-Okeily, Melih Duskunkorur, Fadi Khoury, Serge Himy, Mauro Alunno for their faithful and supporting friendship throughout ups and downs in life.

To my dear wife Claire for her unstinting support and love throughout these years of research. I could not have made it without you.

To my beloved children Edgar and Agathe for their love and the energy they brought me.

To my dear father, for nurturing my interest in science and research and teaching me the taste for things achieved properly. For showing me the way, supporting me and guiding me through life.

This work is dedicated to my beloved mother who raised me with paramount love and gave me confidence. She inspired me with selflessness, compassion and a taste for teaching. She must be very proud from above.

# Table of contents

Foreword.....	1
Chapter 1. Introduction .....	3
1.1. Medical Imaging: a great step for practitioners.....	3
1.2. From diagnosis to surgical procedure .....	4
1.3. A computer-assisted navigation system for maxillo-facial surgery .....	5
1.4. Computer-assisted surgery based on bone structures .....	5
1.4.1. Orthognathic surgery.....	7
1.4.2. Neurosurgery, ENT and orthopedics.....	8
1.5. Purpose of our research .....	10
1.6. Structure of our brief.....	11
1.7. Contributions.....	14
References .....	16
Chapter 2. Orthognathic Surgery: Issues and development purposes.....	19
2.1. Principles in orthognathic surgery .....	20
2.2. Issues in orthognathic surgery and existing solutions .....	26
2.2.1. Planning surgery .....	26
2.2.2. Simulating the facial morphological outcome resulting from surgery.....	27
2.2.3. Transferring surgical planning to the operating theatre and role of navigation.....	29
2.3. Drawbacks of existing solutions .....	33
2.3.1. Drawbacks in planning .....	33
2.3.2. Drawbacks in simulation .....	34
2.3.3. Drawbacks in surgical transfer of the planning and of navigation.....	36
2.4. Summary of existing problems and improvements necessary for practical medical use.....	39
2.4.1. Planning software.....	39
2.4.2. Simulation software.....	39
2.4.3. Navigation system.....	39
2.5. Specification goals of our development and scientific choices.....	40
2.5.1. Planning .....	40
2.5.2. Simulation .....	40
2.5.3. Navigation: surgical transfer of the planning .....	40
2.5.3.1. Interactive Augmented Reality: manual registration using visual landmarks.....	42
2.5.3.2. Automated Augmented Reality: automated registration of head movements, and of the maxilla using a tracking system.....	43
2.6. Conclusion.....	45
References .....	46

Chapter 3. Modeling: Segmentation - from DICOM data to the virtual model .....	61
3.1. Definition .....	62
3.2. Structures of interest .....	63
3.3. Issues .....	64
3.3.1. Continuum between the maxilla and the mandible .....	64
3.3.2. Dental metal artifacts .....	64
3.4. Computation .....	70
3.4.1. Tools .....	70
3.4.1.1. Hardware .....	70
3.4.1.2. VR-Med Software (cf. Appendix I) .....	70
3.4.2. Process .....	70
3.4.2.1. Interactive bone segmentation .....	70
3.4.2.2. Automated bone and skin segmentation pipeline .....	75
3.4.2.2.1. Bone and teeth segmentation method .....	76
3.4.2.2.2. Skin and soft tissue layer segmentation method .....	87
3.4.2.2.3. Discussion .....	99
3.4.2.3. Conclusion .....	101
3.5. Segmentation evaluation .....	102
3.5.1. Method .....	102
3.5.2. Results .....	105
3.5.3. Discussion .....	107
References .....	109
Chapter 4. Planning and Simulation .....	115
4.1. Surgical planning: cutting the bone mesh and moving bone segments .....	117
4.1.1. Cutting planes definition .....	117
4.1.2. Software integration .....	119
4.1.3. Translation and rotation axes medical definition .....	120
4.1.3.1. Translation medical definition .....	120
4.1.3.2. Rotation medical definition .....	120
4.1.4. Mathematical conversion of the medical definition of maxillary model displacements .....	122
4.1.4.1. Translation .....	122
4.1.4.2. Rotation .....	123
4.1.4.3. Examples .....	125
4.2. Simulation in orthognathic surgery .....	126
4.2.1. State of the art .....	126
4.2.1.1. Geometrical models .....	127
4.2.1.2. Physical models .....	129
4.2.1.2.1. Discrete methods .....	130
4.2.1.2.2. Continuum-based methods .....	133
4.2.2. Preliminary conclusion .....	138

4.3. Methods available in IRCAD.....	140
4.3.1. Language, Frameworks, Library .....	140
4.3.2. Code organization .....	141
4.4. Description of our software.....	142
4.4.1. Input data .....	142
4.4.2. Simulation .....	145
4.4.2.1. Mechanical approach .....	145
4.4.2.2. Boundary conditions .....	146
4.4.2.3. Software integration.....	147
4.5. Evaluation .....	151
4.5.1. Evaluation protocol.....	151
4.5.2. Computation methods and reference values .....	154
4.5.2.1. Point to point error .....	154
4.5.2.2. Point-to-surface error.....	156
4.5.2.3. Point-to-weighted-surface error .....	157
4.5.2.4. Preliminary conclusion.....	160
4.5.3. Software integration and evaluation display.....	161
4.5.4. Reference values .....	162
4.5.5. Accuracy of simulation software outcome.....	166
4.6 Conclusion .....	171
References .....	173
Chapter 5. Navigation software: development and evaluation .....	179
5.1. Material and method .....	181
5.1.1 Head phantom.....	181
5.1.2 Electromagnetic tracking system .....	181
5.1.3 Experimental set-up .....	184
5.2. Navigation software development .....	185
5.2.1. Prerequisite calibration and registration issue .....	185
5.2.1.1. Calibration of the head in relation to the sensor attached to the forehead .....	187
5.2.1.2. Calibration of the splint in relation to its embedded sensor .....	188
5.2.2. Navigation interface .....	188
5.2.2.1. The three views of the virtual 3D head model and its color-code.....	189
5.2.2.2. Colored crosshair and its color code .....	190
5.2.2.3. Additional features .....	192
5.3. Conclusion regarding navigation software development .....	194
5.4. Evaluation of navigation software .....	195
5.4.1 Description of the experimental procedure .....	196
5.4.2. Qualitative evaluation .....	198
5.4.3. Quantitative evaluation.....	198



5.4.4. Results .....	199
5.4.4.1. Qualitative evaluation .....	199
5.4.4.2. Quantitative evaluation .....	200
5.5. Discussion .....	203
5.5.1. Considering the operator's level of expertise .....	203
5.5.2. Considering the nature of the experimental task.....	204
5.5.3. Advantages of the electromagnetic system .....	204
5.5.3.1. Low bulk .....	204
5.5.3.2. Relevance of system design and accuracy for surgery .....	204
5.5.3.3. Unnecessary invasive head fixation .....	205
5.5.4. Software and user interface .....	205
5.6. Conclusion.....	206
References .....	207
Chapter 6. CONCLUSION .....	211
6.1. Achievements .....	212
6.2. Perspectives .....	217
6.3. General conclusion .....	221
Chapter 6. <i>bis</i> CONCLUSION ( <i>version française du chapitre 6</i> ) .....	223
6.1. <i>bis</i> Réalisations.....	224
6.2. <i>bis</i> Perspectives.....	230
6.3. <i>bis</i> Conclusion générale .....	235
Appendices	
Appendix I: VR-MED® user's manual and image processing operators .....	237
Appendix II: French Patent for colored-crosshair based navigation Interface .....	249
Appendix III: Object Service Registry (OSR) diagram for navigation software .....	267
Figure caption .....	273
Table caption .....	279
Graph caption .....	279

# Foreword

---

*In our everyday practice of orthognathic surgery, we face the limitations of conventional tools such as bidimensionnal radiographs and dental casts and the lack of intraoperative assistance. These limitations occur at every step of the surgical workflow:*

- *Planning: designing the procedure and making the optimal surgical choices*
- *Simulation: validating the planning according to the simulated outcome and delivering appropriate information to the patient*
- *Navigation: providing the surgeon with relevant intraoperative assistance.*

*If computer science has provided convenient tools for planning, yet simulation appears improvable and navigation remains experimental.*

*Our aim was to propose a convenient system dedicated to navigation in orthognathic surgery including a user-friendly interface. In order to achieve this goal, preliminary steps were mandatory:*

- *Elaborating 3D models of the facial structures*
- *Defining a target position for navigation, which is determined through planning.*

*Along this research, it became obvious that simulation of the surgical outcome would complete the toolset we sought developing for orthognathic surgery. We therefore addressed this goal.*

---



# Chapter 1

## Introduction

### 1.1. Medical Imaging: a great step for practitioners

---

*The advent of medical imaging technology during the late 20<sup>th</sup> century brought medical practitioners to a whole new level of understanding. Indeed, little less than one century after Wilhelm Röntgen<sup>1</sup> discovered radiography in 1895 (Cf. Figure 1.1), the development of computed tomography (CT scan) techniques allowed seeing through the human body and therefore visualizing anatomical and pathological structures as never before.*

*At first, only sectional views were available and medical images therefore depicted, on one slice or more, some physical specifications of the structures of interest. Radiography and CT scan provide an image depending on the thickness of the various tissues and on the atomic number of the atoms they consist of. Physical properties of neighboring organs often being different, the medical practitioner is able to detect most of anatomical and pathological structures on the images. The exact three-dimensional location, conformation, and extent of pathological structures can be understood only with difficulty from such series of two-dimensional CT scan sections. To help clarify spatial relations, computer aids have been applied to reformat the scan data into sagittal, coronal, and paraxial planar images.*

*In the early 1980's, researchers developed algorithms in order to display CT scan information in three-dimensional form (Marsh and Vannier 1983b) : 3D models were born.*

---



**Figure 1.1:** From the first medical X-ray by Wilhelm Röntgen of his wife's hand (November 8<sup>th</sup>, 1895) (left) to the futuristic use of Computed Tomography 3D models (right).  
Source: [http://www.orthopedie-maroc.com/wp-content/uploads/2014/01/slide\\_1.jpg](http://www.orthopedie-maroc.com/wp-content/uploads/2014/01/slide_1.jpg)

---

<sup>1</sup> Wilhelm Röntgen, German Physicist, 1845-1923, was appointed as a lecturer at the University of Strasbourg in 1874

## 1.2. From diagnosis to surgical procedure

The quality and accuracy of medical imaging allowed surgeons to refine their diagnosis. The availability of 3D models facilitated the evaluation and follow-up of pathology and their use appeared particularly relevant in neurosurgery, ENT (Ears Nose Throat), orthopaedics (Woolson et al. 1985) and craniomaxillofacial surgery (Marsh and Vannier 1983b; Marsh and Vannier 1983a; Vannier, Marsh, and Warren 1984).

Most importantly, 3D models made **surgical planning** possible in a much more convenient fashion than previously. Indeed, most surgical procedures imply access through a specific path, section along dedicated planes and angles, and accurate positioning of surgical instruments (needles, burs, scalpels) or implants (screws, plates). Thanks to realistic virtual models, the surgeon can spend as much time as he wants, ahead of the procedure, in order to plan every step and easily apprehend three-dimensional anatomical constraints.

Aside from coelioscopic surgery, planning is crucial in neurosurgery, ENT, orthopedics (Zdravkovic and Bilic 1990) and craniomaxillofacial surgery (Vannier, Marsh, and Warren 1984). The clinical needs lead to the wide development of 3D-planning software in these surgical fields. Indeed, surgical planning allows increased accuracy and confidence for the surgeon and decreased operative time. The learning curve can also be improved, turning trainees into experienced surgeons in a short time.

Nevertheless, the use of planning information displayed on a screen is questionable during surgery. Indeed, the surgeon mainly faces the difficulty of matching the preoperative planning he has achieved with his intraoperative sight of the patient. Therefore, the specialist needs to conduct a mental registration, the outcome of which will mainly depend on his ability to use the patient's anatomical landmarks.

When the surgeon performs this abstract mental computation, his accuracy is affected.

In order to prevent such inconveniency, specialists should be able to simultaneously visualize reality and the corresponding image of the planning they have achieved. In order to overcome this difficulty, two distinct problems need to be solved:

- The computation of the patient's 3D position during the procedure
- The development of a visualization system merging the two datasets.

The computation of the 3D position of the patient's structures relies on the determination of the geometrical transformation between the CT scan coordinate system and the coordinate system of the acquisition device used to track the patient in the operating theatre. The hypothesis of such computation, known as registration, are different whether the acquisition device operates real-time (such as ultrasound imaging) or non real-time (case of most CT and MR Imaging devices). In the first

case, the problem is fundamentally rigid<sup>2</sup> and requires real-time tracking of the source of acquisition with respect to the patient. In the second case, the preoperative information acquired non real-time is different from the reality with which we wish to merge it. We thus distinguish two possibilities: either the difference is supposed negligible (case where the patient is immobilized and the pathology static with respect to the patient) and the relation is rigid, or the alterations and potential movements are too important and need to be modeled in order to compensate them through a non rigid registration (case where the patient has significantly moved between the time of acquisition and the time of surgery).

A third possibility can actually be considered if the pathology is static with respect to the patient but significant movements occur both, between the time of acquisition and the time of surgery, and during surgery: rigid registration can be achieved prior to surgery and real-time tracking can be used during surgery.

These are the bases of a real-time **navigation system**.

### 1.3. A computer-assisted navigation system for maxillo-facial surgery

Over the recent years, computer-assisted **navigation** have become widely used in numerous surgical fields such as neurosurgery (Gering et al. 1999; Lawton et al. 1998; Mert et al. 2014), ENT and orthopedics (Peuchot, Tanguy, and Eude 1995)

Cranio-maxillo-facial (CMF) surgery mainly addresses trauma, tumors and deformities of the craniofacial complex. Like orthopaedics, CMF surgery implies bone fixation and the diversity of pathology addressed in CMF is often neighboring the field of neurosurgery and ENT.

The part of cranio-maxillo-facial surgery focusing on the rehabilitation of dentofacial deformities is called orthognathic surgery. Surgical **planning** in CMF surgery relied for a long time on traditional methods based on 2D radiographs and, especially in orthognathic surgery, on dental casts.

If researchers early identified how computer assistance could benefit to cranio-maxillo-facial surgery (Marsh and Vannier 1983a; Marsh and Vannier 1983b), its routine practice remained vacant from such technology. Yet, the complexity of cranio-maxillo-facial anatomy and the difficulty of visualizing the surgical approach in 3 dimensions represent a significant clinical need for computer assistance. Not only could computer technology help **planning** the procedure, it could also solve crucial issues such as predicting the outcome and assisting the surgeon in its achievement.

### 1.4. Computer-assisted surgery based on bone structures

Computer systems registering the real world and the virtual information coming from preoperative imaging have been initially developed for tumor ablation in **neurosurgery** in the mid 1980's (Cf. Figures 1.2 and 1.3) (Gering et al. 1999) (Maurer et al. 1997) (Gumprecht, Widenka, and Lumenta 1999) (Edwards et al. 2000) (Jannin et al. 2002) (Shaikhouni and Elder 2012).

---

<sup>2</sup> Given that the image underwent preprocessing in order to restrict potential spatial distortion induced by the acquisition device.

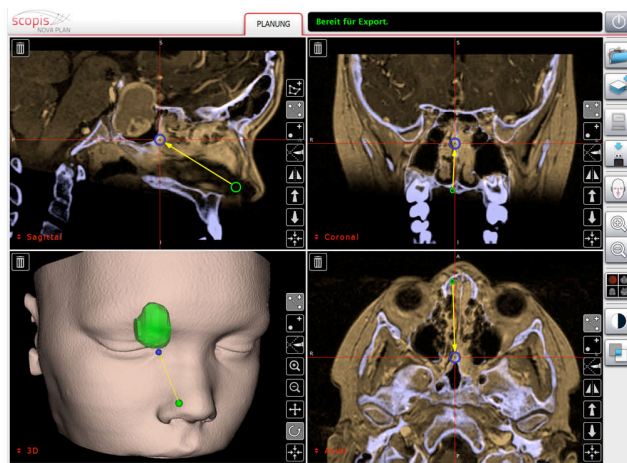


**Figure 1.2:** Scopis® Planning station and surgical navigation system for Neurosurgery.

Source: <http://www.scopis.com/en/products/scopis-planning-station/>

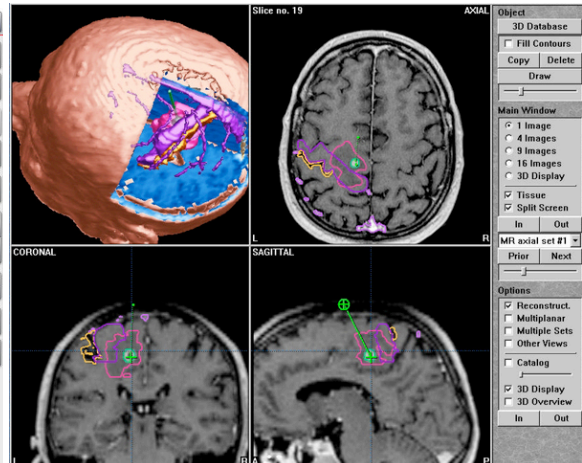


**Figure 1.3:** Four area split-screen displaying a neurosurgical tumor and its vicinity.

Source: [http://www.helios-privatkliniken.de/fileadmin/\\_processed\\_/csm\\_Neurochirurgie\\_Navigation](http://www.helios-privatkliniken.de/fileadmin/_processed_/csm_Neurochirurgie_Navigation)

In **orthopedic surgery**, appropriate placement of implants and prosthesis is improved by the use of navigation systems (Cf. Figure 1.4). Software such as Arcadis® Orbic 3D (Siemens®) and VectorVision® fluoro 3D trauma (Brainlab®) (Cf. Figure 1.5) are of common use and provide an accuracy of 95% (Bredow et al. 2016).



**Figure 1.4:** Navigation in orthopedic surgery. (prosthetic knee replacement)

Source : [mg.medicaexpo.fr/images\\_me](http://mg.medicaexpo.fr/images_me)

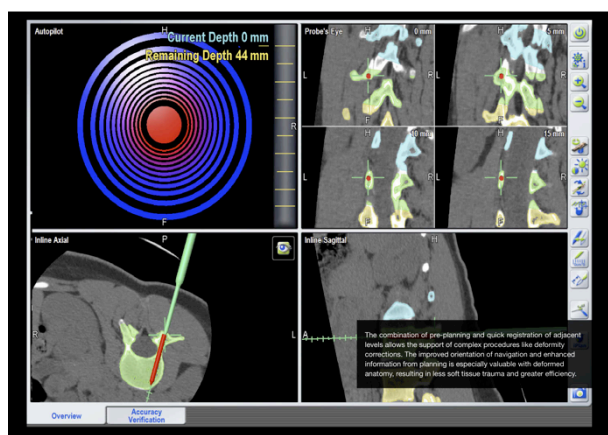


**Figure 1.5:** Brainlab® Spinal navigation system.

Source: <https://www.brainlab.com/en/surgery-products/overview-spinal-trauma-products/spinal-navigation/>

In **oral implantology**, the two main issues are the placement of dental implant with an appropriate angle and drilling depth in order to preserve the nerves and vessels in its vicinity. Numerous software have been developed for planning such as Simplant® (Cf. Figure 1.6), Surgicase®, ProPlan®, Cadimplant® as described and compared in Mischkowski et al. 2006. Intraoperative transfer is achieved thanks to custom-made 3D physical drilling-guides printed according to the planning from CT scan data (Ruppin et al. 2008) (Chen et al. 2016). The Robodent® software offers augmented virtuality navigation based on optical-based tracking (Cf. Figure 1.7) (Meyer et al. 2003) (Schermeier et al. 2002).

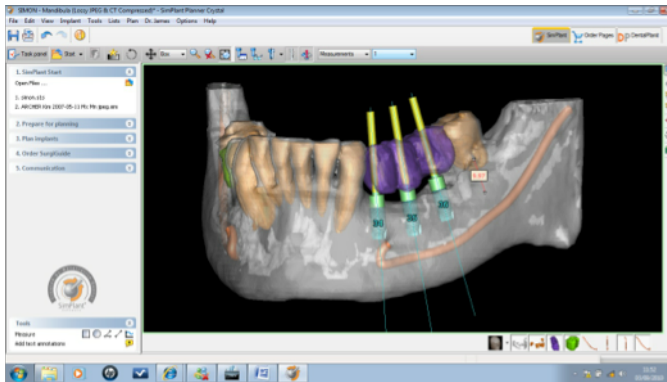


**Figure 1.6:** Simplant® planning software for oral implantology.

Source: [www.simplant.com](http://www.simplant.com)

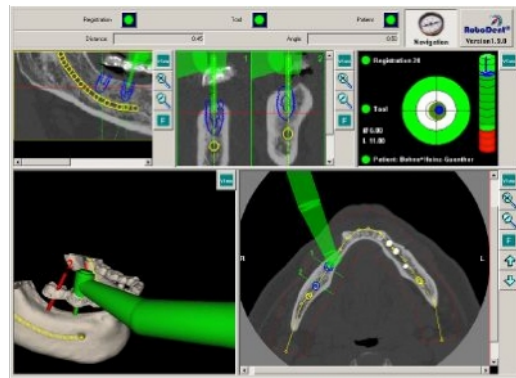


**Figure 1.7:** Robodent® navigation software for oral implantology.

Source: [www.osseotech.com](http://www.osseotech.com)

The purpose of the above is mainly to help the surgeon apprehending the 3D position either of a structure to be removed or the optimal position of an implant to be placed.

The software used in these surgical fields rely on several common features:

- A 4 areas split-screen user interface displaying three 2D sectional views and one 3D model
- The position of the surgical instruments in real-time

In neurosurgery, orthopedics and oral implantology, **simulation** is based on displaying the position of the instruments, since surgery will not actually alter patient's external morphology (unlike in orthognathic surgery).

In orthopedics, bone movements can be tracked under the condition that a fiducial is rigidly attached to the considered bone.

The limits are therefore, in neurosurgery and ENT, the sole visualization of instruments without any visualization of tissue response, and in orthopedics, the required invasive fixation of fiducial markers onto the patient in order to track bone movements.

### 1.4.1. Orthognathic surgery

It consists indeed in cutting whole segments of the upper and the lower jaw in order to achieve facial harmony and appropriate relation between teeth (dental occlusion). This field of Maxillo-facial surgery is dedicated to the treatment of dentofacial deformities. **Surgical planning** is traditionally based on the tracings performed on 2D radiographs from the patient's skull and the manipulation of dental casts. If planning has been substantially improved by 3D software relying on virtual models from CT scans, the **transfer** to the OR remains quite critical. Indeed, intraoperative **navigation**, ensuring the surgeons that the procedure actually matches the planning, would prove rather useful.

In order to facilitate **transfer** to the OR, some attempts have been made to transpose the navigation techniques used in other specialties to orthognathic surgery (Cf. Figure 1.7) (Cevitanes et al. 2010b).



### 1.4.2. Neurosurgery, ENT and orthopedics

The tracking of both, instruments and structures of interest is based on optical systems (Grimson et al. 1998) (J. Hoffmann 2004). Nevertheless, their use implies a few constraints:

- invasive fixation of fiducials (steady fixation of patient's head in ENT and neurosurgery using a head support with screws tapped into the skull (Mayfield clamp))
- bulk of these fiducials
- disruption of line of sight

These constraints actually prevent from a convenient use in orthognathic surgery where preservation of the restricted operative sight is a primary concern (Cevitanes et al. 2010a). Subsequently, optical tracking systems did not emerge in routine surgery.

Therefore, in 2007, practitioners developed an **alternative to optical tracking** where transfer to the operating room is based on a computerized mechanical-based approach: computer assisted designed (CAD) splints (Cf. Figure 1.8) (Cevitanes et al. 2010b) (Swennen et al. 2007) are manufactured according to patient-specific planning and then used during surgery to place the bone segments. If these splints allow positioning of the maxilla and the mandible in relation to one another, they do not provide any information such as the centering, pitch, yaw and roll of the maxilla in relation to the skull. Such information proves to be crucial in common cases of facial asymmetry. As a result, the surgeon needs to achieve an inconvenient 3D mental registration between his planning and the actual patient during surgery.

Additionally, splints allow no intraoperative versatility, as we will detail furthermore.

Here again, this technical solution did not establish a paradigm shift in orthognathic practice.

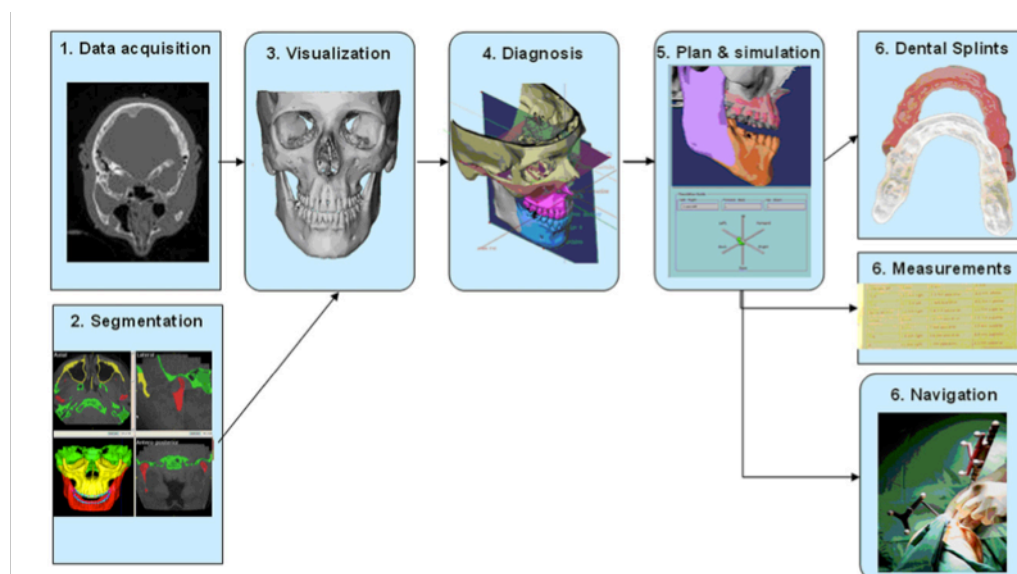


**Figure 1.8:** Computer-assisted workflow in orthognathic surgery from preoperative diagnosis (1-4), planning and simulation (5) to transfer to the operating theatre (6). Here, transfer is achieved through dental splints and/or optical tracking.

Source: Cevitanes L.H.C. et al. 2010. "Three-Dimensional Surgical Simulation." *American Journal of Orthodontics and Dentofacial Orthopedics* 138 (3): 361–71

It then becomes clear that the development of non-invasive and user-friendly intraoperative assistance and navigation software would be of great benefit for the maxillo-facial surgeons and their patients. Indeed, the versatility and display of additional points of view in such a system would allow reducing discrepancy in terms of time and accuracy between experienced surgeons and trainees. It could therefore help standardize maxillary positioning. Along with educational purposes, such a system would be of benefit especially to trainees, as it could provide them with additional information that older surgeons have integrated through experience.

Real-time tracking and ergonomic navigation display are issues addressed by the IRCAD (Institut de Recherche contre le Cancer de l'Appareil Digestif / Research Institute against Digestive Cancer) R&D team even though it is focused on the digestive tract.

The idea of this Thesis arose thanks to the encounter between the author, maxillo-facial surgeon in the Strasbourg University Hospital, the iCube and IRCAD R&D teams. After a Master's degree on Changes in Facial Soft Tissues after Orthognathic Surgery, the author wished to pursue in this topic. After having analyzed the outcome of orthognathic surgery, the author aimed at developing original tools dedicated to all the steps of the orthognathic workflow, from **planning** to **simulation** and **navigation**.

Yves RÉMOND's iCube team is specialized in multi-scale modeling and simulation of heterogeneous materials and living tissues, belonging to the iCube laboratory, which depends on the University of Strasbourg and the CNRS.

Luc SOLER's computer science R&D department in IRCAD focuses in computer assistance in minimally invasive abdominal surgery.

IRCAD has developed image processing software able to automatically reconstruct 3D models of patients internal organs from CT scans (Soler et al. 2001). If the department mainly focused on abdominal organs, the technology was sought to be applied to the maxillo-facial area following specifications established by the author.

From the synergy between these teams came the idea of developing a navigation system dedicated to maxillofacial surgery and especially to orthognathics. This system was designed to merge preoperative and intraoperative data to the real world in order to guide the surgeon, hence consisting of augmented-virtuality. As previously stated, the difficulty in achieving such a system is double. We need to register patient's virtual information at the appropriate position in relation to the real environment since any discrepancy could misguide the surgeon and eventually jeopardize patient's life. Simultaneously, a user interface needs to be designed according to the surgeon's requirements in order to merge all data. Since navigation can only be conceived in relation to the target (planned) position of a virtual model, we decided to address these preliminary steps of modeling and planning. For objectivity, consistency and economical purposes, we chose to develop our own modeling and planning software rather than building on commercially available solutions. In order to complete this computerized toolset for orthognathic surgery, we also addressed simulation of the postoperative result on patient's face.

## 1.5. Purpose of our research

The purpose of our research relies in different steps:

- To develop a dedicated computation procedure for generating **3D models** of patient's facial structures of interest.

To conduct an evaluation of the modelling process.

- To develop virtual **planning** tools which allow cutting and moving segments of the 3D models using geometrical and mathematical criteria according to the surgical procedure.
- To develop a mechanical model of facial soft tissues in order to provide a realistic **simulation** of the facial morphology resulting from skeletal surgical alterations.

To evaluate the accuracy of our simulation software.

- To develop and evaluate a **navigation software** that should meet some prerequisite specifications:

- **Compatible with the inherent constraints of the operative theatre:**
  - Preoperative set-up of the system shall be as quick as possible in order not to increase the overall time the patient spends under general anesthesia
  - Components of the system included into the operative field shall be sterile
  - The system and its components (fiducials) shall result in low bulk since operative sight is crucial in the restricted space of intraoral approaches.

These constraints shall be considered at every step in the development of our system.

- **Providing benefits throughout surgery.** Such benefits can consist in either improved accuracy and/or operative time compared to the usual surgical workflow, or the design of an innovative interface that could impact ergonomics of navigation systems in general.
- **Accounting for patient head movements during surgery.** Indeed, since the system is meant to be non-invasive, steady head fixation is not considered. Therefore, head tracking shall be considered.

## 1.6. Structure of our brief

Our aim is to provide practical tools to intraoperatively help the surgeon (navigation) achieving the surgical goals they have planned (planning). Additionally, we aim at providing simulation of the expected surgical outcome (simulation).

Therefore, in **Chapter 2** we analyze the problem and explain our scientific choices. We detail the purpose, indication, and principles of orthognathic surgery, which is the treatment of numerous dentofacial deformities. We quantify the number of patients affected worldwide and the number of procedures performed per year. Then, we analyze the issues and constraints encountered by the surgeon and identify existing solutions at every step of patient care, from preoperative to intraoperative. Once confronting them to the state of the art, we became aware of limitations and drawbacks in existing software. Subsequently, we were able to list the specification goals of our development according to the requirements of orthognathic surgery. We therefore set our scientific choices regarding modeling, planning, simulation and intraoperative navigation. We describe the type of interface we chose to develop, and explain why we chose electromagnetic tracking technology. We also determine which preliminary development steps are mandatory to achieve our ultimate goal.

**Chapter 3** focuses on **modeling**, and explains how we computed raw DICOM<sup>3</sup> input data from patients CT scans into virtual models. We detail the specifications and mathematical bases of the software we used (Cf. Annex I). We identify the constraints in image processing, such as metal dental artifacts and confront them to our goals. We then explain how segmentation<sup>4</sup> based on a clever approach allows achieving a 3D surface model of skin, bone and teeth that is necessary for the surgeon to analyze and measure the deformity and plan surgical movements. In the last part of the chapter, we conduct an evaluation of our modeling process, comparing an automated pipeline to interactive segmentation. We analyze the results and find that automated segmentation accuracy is relevant.

We are able to obtain a **3D virtual model of the patient**, which allows proceeding to further steps.

---

<sup>3</sup> **DICOM** — Digital Imaging and Communications in Medicine — is *the* international standard for medical images and related information (ISO 12052). It defines the formats for medical images that can be exchanged with the data and quality necessary for clinical use. DICOM is implemented in almost every radiology, cardiology imaging, and radiotherapy device (X-ray, CT, MRI, ultrasound, etc.), and increasingly in devices in other medical domains such as ophthalmology and dentistry. With tens of thousands of imaging devices in use, DICOM is one of the most widely deployed healthcare messaging standards in the world. Since its first publication in 1993, DICOM has revolutionized the practice of radiology, allowing the replacement of X-ray film with a fully digital workflow.

<sup>4</sup> In computer vision, image **segmentation** is the process of partitioning a digital image into multiple segments (sets of pixels, also known as super-pixels). The goal of segmentation is to simplify and/or change the representation of an image into something that is more meaningful and easier to analyze.

**Chapter 4** addresses two crucial topics. In a first part, we focus on **planning**, which consists of the geometrical description of the sections and displacements that the surgeon aims at performing. It is a prerequisite step to further achieve simulation and intraoperative assistance through surgical navigation. Therefore, we first determine which anatomical structures of interest are relevant and which computer processes can be used in order to mimic the surgical procedure. A critical issue relies on analyzing the geometric displacement of bone segments once they are cut. Indeed, bone segments interact with one another in the real environment, whereas virtual models can penetrate into one another, since collisions are usually not considered. Therefore, we have to convert the planned surgical displacements into geometric transformations along and around axes. Then, we aimed at developing a friendly graphical user interface (GUI) dedicated to both, the appropriate definition of cutting planes and the definition of target surgical positions.

In a second part, we address **simulation** through a state of the art of available methods especially the ones appropriate for orthognathic surgical simulation and determine which ones were available to us. We then use the 3D surface model, which reconstruction is described in Chapter 3, to generate a biomechanical model of hard and soft tissues in order to predict the facial postoperative morphological outcome.

We explain how the volume mesh, used to generate the biomechanical model, is generated from the surface mesh. We justify why the “TetGen” library and the “Bullet” physics engine are well suited to our purpose.

We describe the boundary conditions of our system and show how we integrate them to our simulation software.

In the end, we evaluate our simulation software using preoperative and postoperative 3D images of actual patients, and demonstrate that our model allows reasonably accurate prediction of the postoperative facial outcome.

**Chapter 5** is dedicated to the description of the **navigation** system.

First, we explain the system hardware itself, based on EM tracking, and describe all its components as well as the tracked objects. Then, we describe all the necessary calibration steps that need to be performed. We therefore show why an appropriate workflow of data measurement allows a fast and accurate system calibration.

Finally, once an analysis of surgical habits has been conducted, we propose an interface suited for maxillofacial surgeons and show how an original colored 3D crosshair provides efficient help to the surgeon whilst he is setting the maxilla.

This part of our research lead to a patent registration.

Evaluation is always a critical task, particularly in surgery.

Therefore, in the second part of **Chapter 5**, we propose a qualitative and quantitative analysis conducted on a real-size medical plastic head model in realistic operative conditions. The evaluation is based on the action of placing the maxilla from its original location to the target position defined during the planning step. Thus, we propose a set of eight surgical-like positions of the maxilla with increasing difficulty. The results first demonstrated in our qualitative evaluation that our system is rather well accepted by surgeons and would be favorably used in operative theatres.

Results of the quantitative analysis showed that our software definitely allowed a reduction in variability both of time and accuracy among different operators and could therefore help standardize maxillary positioning. It also provided increased accuracy for most operators. It was helpful especially to trainees, as operative time was mainly decreased in their category. Therefore, the educational purpose of such system becomes quite obvious.

Overall, qualitative evaluation reported that surgeons strongly agreed that such a navigation system would prove very helpful in complex deformities and the majority of them stated that it would also be helpful in everyday orthognathic procedures.

Finally, in **Chapter 6**, we provide conclusions and perspectives regarding the theoretical, practical and medical aspects of our research.

## 1.7. Contributions

Our contributions can be summarized in three categories.

- Scientific contributions
  - In order to achieve **planning** we had to convert actual surgical displacements using transformation matrices in order to mimic actual surgical movements on patient's virtual model. We focused on the maxillary surgical step, since it is the most crucial one in the whole procedure. The computed positions were used as target ones on which navigation software evaluation was based. Along this study, we were able to categorize all movements of the maxilla using a standard grid, which, in our understanding had never been achieved previously.
  - As far as **simulation** was concerned, we analyzed and transferred the boundary conditions to the considered surgical context. We proposed a qualitative analysis of soft tissue alterations in the facial areas of interest.
  - We designed a **navigation** system set-up on a mannequin considering spatial and time restrictions that applied in a real operating environment. According to qualitative evaluation conducted on twelve surgeons, this set-up could be directly transferred to the operating theatre. This part of our research was presented during the 4<sup>th</sup> International Conference of Computational & Mathematical Biomedical Engineering - CMBE 2015" on June 2015, 29<sup>th</sup> with the title "Numerical models for medical applications: from constitutive laws of biological tissue to real time numerical tools"(D.George, J.C. Lutz, C. Spingarn, S. Nicolau, Y. Rémond)(George et al. 2015).
  - We conceived an original calibration workflow of the electromagnetic system that allows easy and quick handling of the system.
- Technical contributions
  - We have implemented a semi-automated segmentation pipeline providing swift segmentation of teeth, facial bones and skin from raw CT scan data.
  - We designed and developed a novel user interface for navigation in orthognathic surgery allowing displaying 6 degrees of freedom on one single screen. Part of this interface consisted of a colored 3D-crosshair that provided intuitive information about positions of the maxilla in the surgical field. The GUI was enhanced with views of the 3D model in order to match the real operative set-up. Translation and rotation could therefore be simultaneously visualized on frontal and lateral views.

This research led to registration of a patent entitled “*Equippedement d'aide au positionnement d'un fragment osseux, d'une prothèse ou d'un implant osseux lors d'une intervention chirurgicale*”, on March 27<sup>th</sup> 2015 under the number 15 52596, inventors : LUTZ Jean-Christophe, NICOLAU Stéphane, AGNUS Vincent.<sup>5</sup>

- Experimental contributions
  - We have conducted an evaluation of our segmentation pipeline comparing an interactive process with a semi-automated one and provided a statistical analysis.
  - We have conducted an evaluation of our simulation software on actual patients. To do so, we used a database of preoperative and postoperative CT scans. We compared the outcome simulated from the preoperative on CT scan to the actual postoperative result featured on the postoperative CT scan. This evaluation relied on quantitative measurements that were qualitatively analyzed using color distance-maps.
  - We have conducted an experiment for validation of our navigation software. This evaluation highlighted the needs of maxillofacial surgeons, especially trainees. It also made us understand that standard augmented reality through an external view did not seem to bring a tremendous benefit in terms of navigational assistance.  
This part of our research was presented at the 50<sup>th</sup> National Congress of Maxillo-Facial Surgery in Lyon, France, September 2014. The results were published as “A novel navigation system for maxillary positioning in orthognathic surgery: preclinical evaluation” in Journal of Cranio-Maxillo-Facial Surgery 43 (2015) 1723-1730 by JC LUTZ et al.

---

<sup>5</sup> INPI official bulletin p.27: <https://www.inpi.fr/sites/default/files/bopis/bopi1639.pdf>



## REFERENCES

1. Bredow, Jan, Carolin Meyer, Max Joseph Scheyerer, Florian Siedek, Lars Peter Müller, Peer Eysel, and Gregor Stein. 2016. "Accuracy of 3D Fluoroscopy-Navigated Anterior Transpedicular Screw Insertion in the Cervical Spine: An Experimental Study." *European Spine Journal: Official Publication of the European Spine Society, the European Spinal Deformity Society, and the European Section of the Cervical Spine Research Society*, January. doi:10.1007/s00586-016-4403-x.
2. Cevidanes, Lucia H. C., Scott Tucker, Martin Styner, Hyungmin Kim, Jonas Chapuis, Mauricio Reyes, William Proffit, Timothy Turvey, and Michael Jaskolka. 2010a. "Three-Dimensional Surgical Simulation." *American Journal of Orthodontics and Dentofacial Orthopedics* 138 (3): 361–71. doi:10.1016/j.ajodo.2009.08.026.
3. Chen, Xiaojun, Lu Xu, Yue Yang, and Jan Egger. 2016. "A Semi-Automatic Computer-Aided Method for Surgical Template Design." *Scientific Reports* 6 (February): 20280. doi:10.1038/srep20280.
4. Edwards, P. J., A. P. King, C. R. Maurer, D. A. de Cunha, D. J. Hawkes, D. L. Hill, R. P. Gaston, et al. 2000. "Design and Evaluation of a System for Microscope-Assisted Guided Interventions (MAGI)." *IEEE Transactions on Medical Imaging* 19 (11): 1082–93. doi:10.1109/42.896784.
5. George, Daniel, Jean-Christophe Lutz, Camille Spingarn, Stéphane Nicolau, and Yves Rémond. 2015. "Numerical Models for Medical Applications: From Constitutive Laws of Biological Tissue to Real Time Numerical Tools." *Computational and Mathematical Biomedical Engineering Proceedings*, edited by P.Nithiarasu & E.Budyn, , July, 320–23.
6. Gering, David T., Arya Nabavi, Ron Kikinis, W. Eric L. Grimson, Noby Hata, Peter Everett, Ferenc Jolesz, and William M. Wells. 1999. "An Integrated Visualization System for Surgical Planning and Guidance Using Image Fusion and Interventional Imaging." In *Medical Image Computing and Computer-Assisted Intervention – MICCAI'99*, edited by Chris Taylor and Alain Colchester, 809–19. Lecture Notes in Computer Science 1679. Springer Berlin Heidelberg. [http://link.springer.com/chapter/10.1007/10704282\\_88](http://link.springer.com/chapter/10.1007/10704282_88).
7. Grimson, E., M. Leventon, G. Ettinger, A. Chabrerie, F. Ozlen, S. Nakajima, H. Atsumi, R. Kikinis, and P. Black. 1998. "Clinical Experience with a High Precision Image-Guided Neurosurgery System." In *Medical Image Computing and Computer-Assisted Intervention — MICCAI'98*, edited by William M. Wells, Alan Colchester, and Scott Delp, 63–73. Lecture Notes in Computer Science 1496. Springer Berlin Heidelberg. <http://link.springer.com/chapter/10.1007/BFb0056188>.

8. Gumprecht, H. K., D. C. Widenka, and C. B. Lumenta. 1999. "BrainLab VectorVision Neuronavigation System: Technology and Clinical Experiences in 131 Cases." *Neurosurgery* 44 (1): 97–104; discussion 104–105.
9. J. Hoffmann, D. Troitzsch. 2004. "craniofacial endosseus implant positioning with image-guided surgical navigation", 137–43. doi:10.1142/9789812702678\_0020.
10. Jannin, Pierre, Xavier Morandi, Oliver J. Fleig, Elisabeth Le Rumeur, Pierre Toulouse, Bernard Gibaud, and Jean-Marie Scarabin. 2002. "Integration of Sulcal and Functional Information for Multimodal Neuronavigation." *Journal of Neurosurgery* 96 (4): 713–23. doi:10.3171/jns.2002.96.4.0713.
11. Lawton, Michael T., John G. Golfinos, Thomas R. Geldmacher, and Robert F. Spetzler. 1998. "The State of the Art of Neuronavigation with Frameless Stereotaxy in Intracranial Neurosurgery." *Operative Techniques in Neurosurgery*, General Principles of Cranial Operative Techniques, 1 (1): 27–38. doi:10.1016/S1092-440X(98)80006-6.
12. Marsh, J. L., and M. W. Vannier. 1983a. "The 'Third' Dimension in Craniofacial Surgery." *Plastic and Reconstructive Surgery* 71 (6): 759–67.
13. Marsh, J. L., and M. W. Vannier. 1983b. "Surface Imaging from Computerized Tomographic Scans." *Surgery* 94 (2): 159–65.
14. Maurer, C. R., J. M. Fitzpatrick, M. Y. Wang, R. L. Galloway, R. J. Maciunas, and G. S. Allen. 1997. "Registration of Head Volume Images Using Implantable Fiducial Markers." *IEEE Transactions on Medical Imaging* 16 (4): 447–62. doi:10.1109/42.611354.
15. Mert, Ayguel, Alexander Micko, Markus Donat, Manuela Maringer, Katja Buehler, Garnette R. Sutherland, Engelbert Knosp, and Stefan Wolfsberger. 2014. "An Advanced Navigation Protocol for Endoscopic Transsphenoidal Surgery." *World Neurosurgery* 82 (6 Suppl): S95–105. doi:10.1016/j.wneu.2014.07.032.
16. Meyer, U., H. P. Wiesmann, C. Runte, T. Fillies, N. Meier, T. Lueth, and U. Joos. 2003. "Evaluation of Accuracy of Insertion of Dental Implants and Prosthetic Treatment by Computer-Aided Navigation in Minipigs." *The British Journal of Oral & Maxillofacial Surgery* 41 (2): 102–8.
17. Mischkowski, R. A., M. J. Zinser, J. Neugebauer, A. C. Kübler, and J. E. Zöller. 2006. "Comparison of Static and Dynamic Computer-Assisted Guidance Methods in Implantology." *International Journal of Computerized Dentistry* 9 (1): 23–35.
18. Peuchot, Bernard, Alain Tanguy, and Michel Eude. 1995. "Virtual Reality as an Operative Tool During Scoliosis Surgery." In *Computer Vision, Virtual Reality and Robotics in Medicine*, edited by Nicholas Ayache, 549–54. Lecture Notes in Computer Science 905. Springer Berlin Heidelberg. [http://link.springer.com/chapter/10.1007/978-3-540-49197-2\\_72](http://link.springer.com/chapter/10.1007/978-3-540-49197-2_72).

19. Ruppin, Jörg, Aleksandra Popovic, Mario Strauss, Elmar Spüntrup, Alexander Steiner, and Christian Stoll. 2008. "Evaluation of the Accuracy of Three Different Computer-Aided Surgery Systems in Dental Implantology: Optical Tracking vs. Stereolithographic Splint Systems." *Clinical Oral Implants Research* 19 (7): 709–16. doi:10.1111/j.1600-0501.2007.01430.x.
20. Schermeier, O., T. Lueth, J. Glagau, D. Szymanski, R. Tita, D. Hildebrand, M. Klein, K. Nelson, and J. Bier. 2002. "Automatic Patient Registration in Computer Assisted Maxillofacial Surgery." *Studies in Health Technology and Informatics* 85: 461–67.
21. Shaikhouni, Ammar, and J. Bradley Elder. 2012. "Computers and Neurosurgery." *World Neurosurgery* 78 (5): 392–98. doi:10.1016/j.wneu.2012.08.020.
22. Soler, L., H. Delingette, G. Malandain, J. Montagnat, N. Ayache, C. Koehl, O. Dourthe, et al. 2001. "Fully Automatic Anatomical, Pathological, and Functional Segmentation from CT Scans for Hepatic Surgery." *Computer Aided Surgery: Official Journal of the International Society for Computer Aided Surgery* 6 (3): 131–42. doi:10.1002/igs.1016.
23. Swennen, G. R. J., E. -L. Barth, C. Eulzer, and F. Schutyser. 2007. "The Use of a New 3D Splint and Double CT Scan Procedure to Obtain an Accurate Anatomic Virtual Augmented Model of the Skull." *International Journal of Oral and Maxillofacial Surgery* 36 (2): 146–52. doi:10.1016/j.ijom.2006.09.019.
24. Vannier, M. W., J. L. Marsh, and J. O. Warren. 1984. "Three Dimensional CT Reconstruction Images for Craniofacial Surgical Planning and Evaluation." *Radiology* 150 (1): 179–84. doi:10.1148/radiology.150.1.6689758.
25. Woolson, S. T., L. L. Fellingham, P. Dev, and A. Vassiliadis. 1985. "Three Dimensional Imaging of Bone from Analysis of Computed Tomography Data." *Orthopedics* 8 (10): 1269–73.
26. Zdravkovic, Vilijam, and Ranko Bilic. 1990. "Computer-Assisted Preoperative Planning (CAPP) in Orthopaedic Surgery." *Computer Methods and Programs in Biomedicine* 32 (2): 141–46. doi:10.1016/0169-2607(90)90094-P.

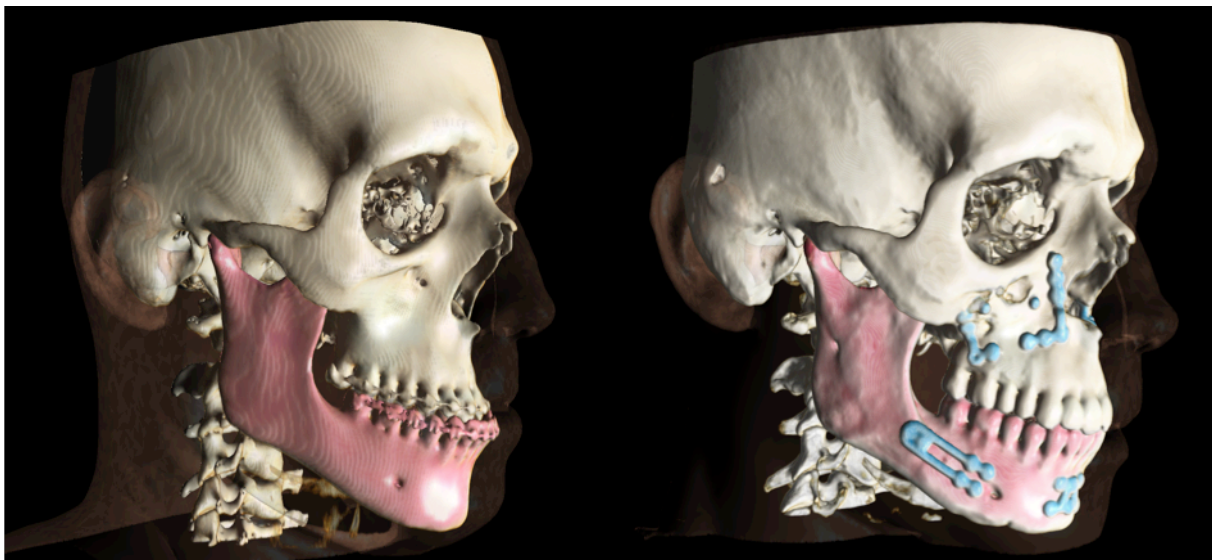
## Chapter 2

### Orthognathic Surgery: Issues and development purposes

---

*In this Chapter, we will address the principles of orthognathic surgery, its issues and explain our scientific choices. We detail the purpose, indication, and principles of orthognathic surgery, which is the treatment of numerous dentofacial deformities. We quantify the number of patients affected worldwide and the number of procedures performed per year. Then, we analyze the issues and constraints encountered by the surgeon and identify existing solutions at every step of patient care, from preoperative to intraoperative. Once confronting them to the state of the art, we became aware of limitations and drawbacks in existing software. Subsequently, we were able to list the specification goals of our development according to the requirements of orthognathic surgery. We therefore set our scientific choices regarding modeling, planning, simulation and intraoperative navigation. We describe the type of interface we chose to develop, and explain why we chose electromagnetic tracking technology. We also determine which preliminary development steps are mandatory to achieve our ultimate goal.*

---



Source: IRCAD® France, courtesy of Pr. Soler

## 2.1. Principles in orthognathic surgery

Maxillofacial surgery is a medical specialty that addresses diseases or impairment affecting both hard and soft tissues of the face as well as the oral cavity. Orthognathic surgery is a subspecialty of maxillofacial surgery. It focuses on dentofacial deformities consisting of discrepancy between facial bones, mainly the maxilla (upper jaw) and the mandible (lower jaw) (Cf. Figure 2.1). Such deformities are possibly unsightly and can cause difficulties in chewing, talking, and can disturb the psychological and social balance (Cf. Figure 2.4). Ultimately, they can lead to the loss of teeth (Cf. Figure 2.2).

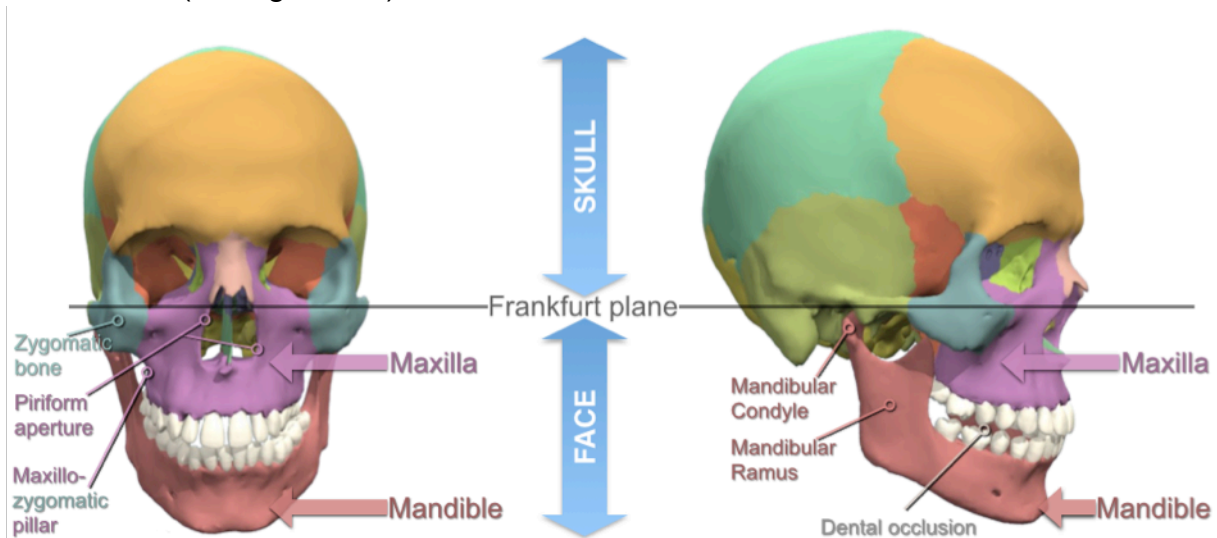


**Figure 2.1:** Basic maxillofacial anatomy for orthognathic surgery.

For further reference, we would like to depict in Figure 2.3, the anatomical definition of reference axes and planes as well as the basic movements along these axes.

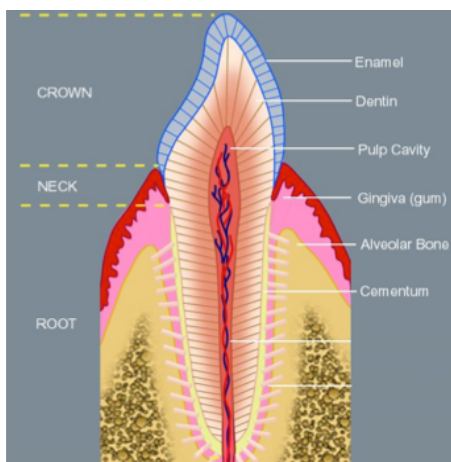


**Figure 2.2:** Sagittal cross-section of a tooth into the alveolar bone illustrating its segments and different mineral layers.

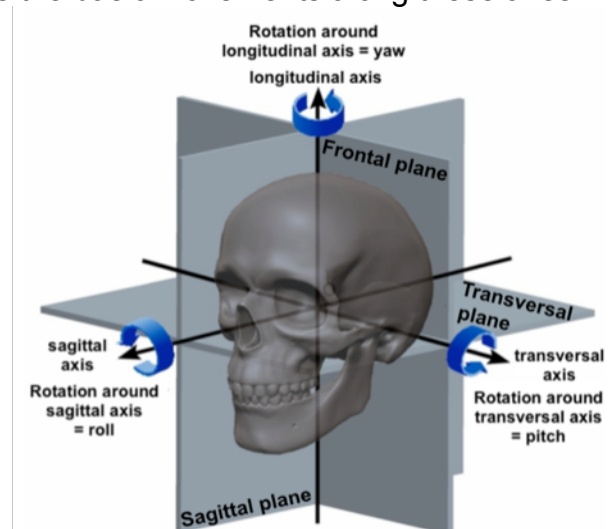


**Figure 2.3:** Anatomical definition of reference axes and planes. Definition of movements along these axes.

Prognathism (class III dentoskeletal deformity) and retrognathism (class II dentoskeletal deformity) are examples of dentofacial deformities. Global facial asymmetry is also rather frequent in the general population (Cf. Figure 2.4).

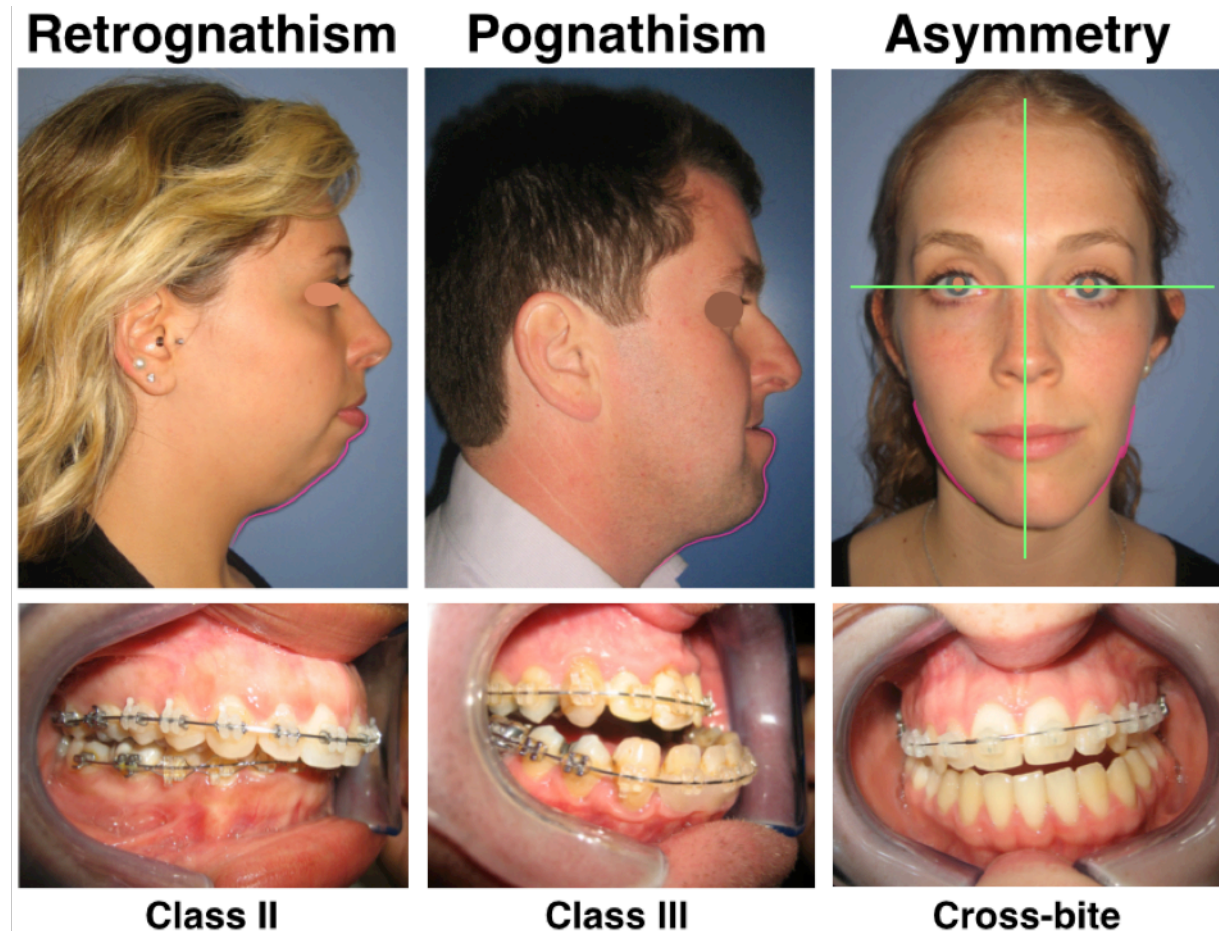


**Figure 2.4: Clinical aspects of retrognathism (left), prognathism (middle) and asymmetry (right).** The location of the deformity is outlined in pink. Vertical midline and horizontal line are featured in green in the asymmetry case.

In the USA, 17 million individuals (aged 12 to 50 years) have dentofacial deformities severe enough to warrant surgical correction (18 % of this population)(James J. Xia et al. 2006). Based on a survey we have conducted in 2012 through international maxillofacial associations, we have estimated that 300 000 orthognathic surgical procedures are performed per year worldwide. In France, 6000 such procedures are performed every year (Cf. Figure 2.5).

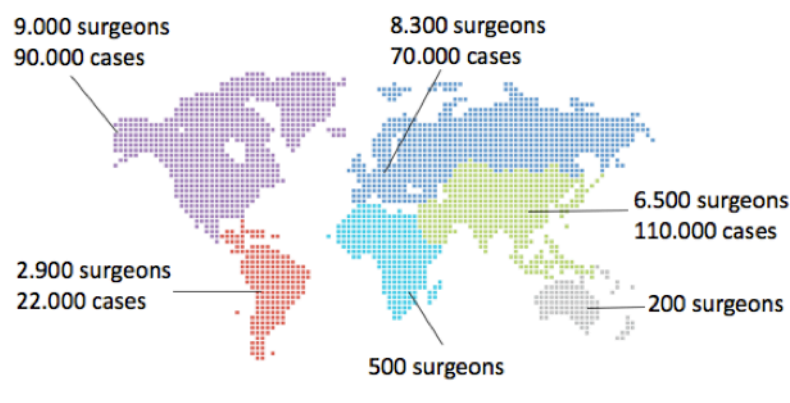


**Figure 2.5: Number of maxillofacial surgeons and orthognathic surgical procedure per year worldwide.**

Orthognathic surgery is usually performed after growth is completed. It is sometimes, wrongly, considered as a failure of an orthopedic treatment. Indeed, dentofacial orthopedics (ortohodontics) are strongly bonded to orthognathic surgery. Often used in combination with surgery after bone growth is completed, dentofacial orthopedics solely can try and correct dentofacial deformities until growth potential is over. Such treatment consists of the appliance of intraoral (Cf. Figure 2.6) or extraoral forces (Cf. Figure 2.7) to stimulate growth centers of the facial skeleton.

At this stage, a great scientific challenge is to achieve 3D modeling of facial bones in order to predict their growth on a multi-scale basis.

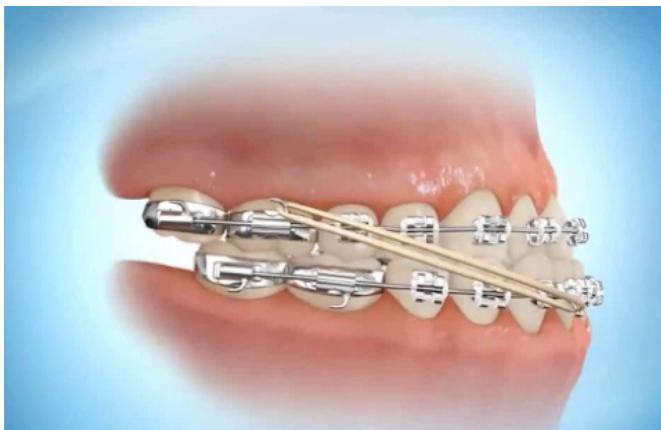


**Figure 2.6:** Intraoral orthodontic appliances used to treat prognathism during growth.

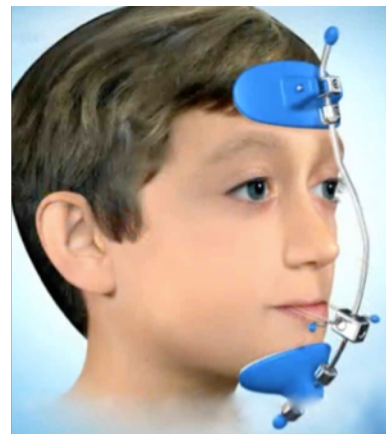


**Figure 2.7:** Extraoral device used to treat prognathism during growth.

In rare cases of severe facial deformities, surgery can be decided **before growth is achieved** and is designated as interceptive surgery. Such procedure uses plates and screws for bone fixation. If left in place, such rigid material is likely to jeopardize further growth making its removal mandatory through a secondary procedure. In order to reduce the number of procedures in a child, resorbable plating systems have been developed for bone fixation instead of titanium miniplates, therefore making plate removal unnecessary. Initially perceived as a great step forward, such material showed some inconveniences. Mainly made of polylactic acid (PLA), these plates are only partially resorbable. This process also causes significant inflammation therefore discomfort for the patient and a higher risk of infection. Additionally, the resorbable plates are not easily bent, making intraoperative use difficult.

If dentofacial deformities are addressed **once growth is achieved**, the correction of bone position through an orthopedic treatment is no longer possible.

Only orthognathic surgery can provide the replacement of the facial bone segments in various directions in order to correct facial bone discrepancy. By means of standard bone cuts (osteotomies), the facial skeleton is corrected therefore achieving adequate tooth position between the upper and the lower jaw (dental occlusion) (Cf. Figures 2.8 and 2.9).

These osteotomies are usually performed horizontally through the maxilla (“Le Fort I” osteotomy) and sagittally through the ascending part (ramus) of the mandible. Either one (maxilla or mandible, namely monomaxillary), or both (maxilla and mandible, namely bimaxillary) facial bones can be cut.

Such procedures are performed under general anesthesia through intraoral approaches (Raphaël, Lebeau, and Morand 2002) (Richter et al. 1998).



**Figure 2.8:** Schematic illustration of a maxillary osteotomy also called « Le Fort I » osteotomy (left) and mandibular osteotomy, also called bilateral sagittal split ramus osteotomy.

Once moved to the desired position, the bone segments are rigidly fixed (osteosynthesis) using titanium miniplates and screws until bone healing is complete. The miniplates can be removed after a 6 to 12 month postoperative period.



**Figure 2.9: Orthognathic osteotomy and fixation.**

Left: Maxillary and mandibular osteotomies. Right: Rigid fixation of bones using titanium miniplates and screws (osteosynthesis).

The two most common movements performed through Le Fort I osteotomy consist of a maxillary advancement and/or an impaction (shortening). A downward position of the maxilla (lengthening) is also commonly achieved.



Subsequently to the repositioning of facial bones, the morphology of the overlying soft tissues (muscles, subcutaneous fat, skin) will change, altering especially the appearance of the lips, chin and nasal regions (Cf. Figures 2.10, 2.11 and 2.12).

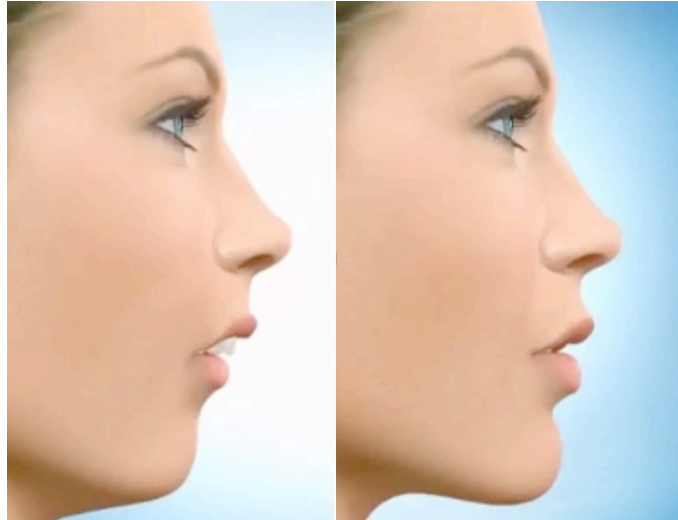


**Figure 2.10:** Correction of bone discrepancy (retrognathism) and restoration of dentofacial harmony. Note the alterations in the nose-lip-chin area.

**Orthognathic surgery has a dual purpose:**

- **functional: achieving stable and durable anatomical dental occlusion.**
- **esthetic: restoring facial harmony**

In order to reach these goals, three consecutive steps are mandatory:

- **planning:** after having diagnosed the site of the anomaly and the magnitude of the deformity, the surgeon uses patient's radiographs to plan where bone cuts need to be performed and how bone segments shall be positioned
- **simulation:** assessment of postoperative patient's facial morphological outcome is useful to provide validation of the operative strategy and to collect patient's consent.
- **transfer of surgical planning** to the operating theatre during surgery to ensure that the actual result matches the planning.

There has been a great technological leap since 3D Computed Tomography (CT) scans have been widely available in combination with advances in computer sciences. Therefore, the way surgeons perform these steps have drastically changed (Neumann et al. 1999).

Of course, the next scientific breakthrough will come from bio-engineering and the ability to generate new growth centers among the facial skeleton.

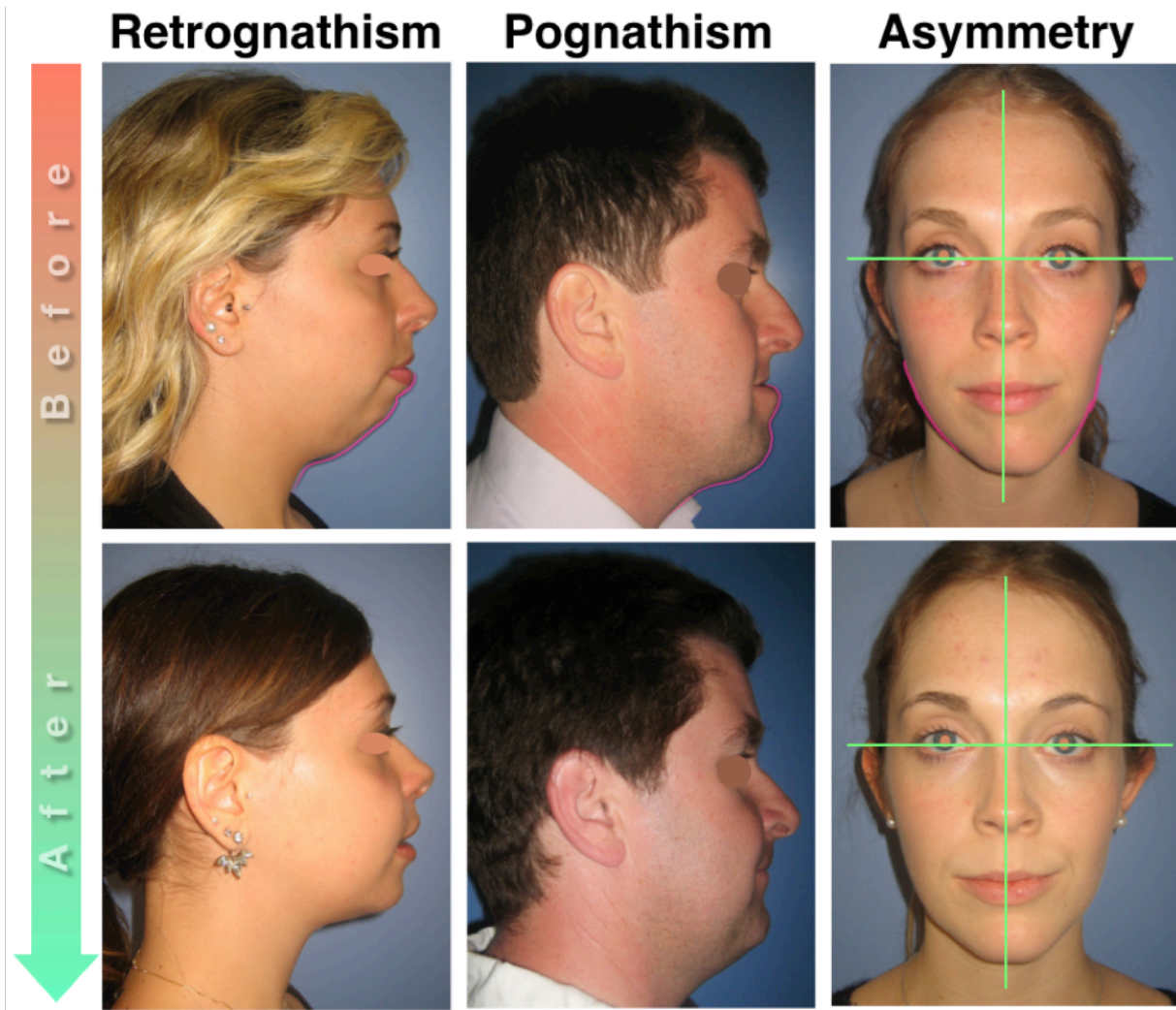


**Figure 2.11:** Preoperative (before, top row) and postoperative (after, bottom row) clinical aspects in terms of facial morphology of retrognathism (left), prognathism (middle) and asymmetry (right). Vertical midline and horizontal line are featured in green in the asymmetry case.

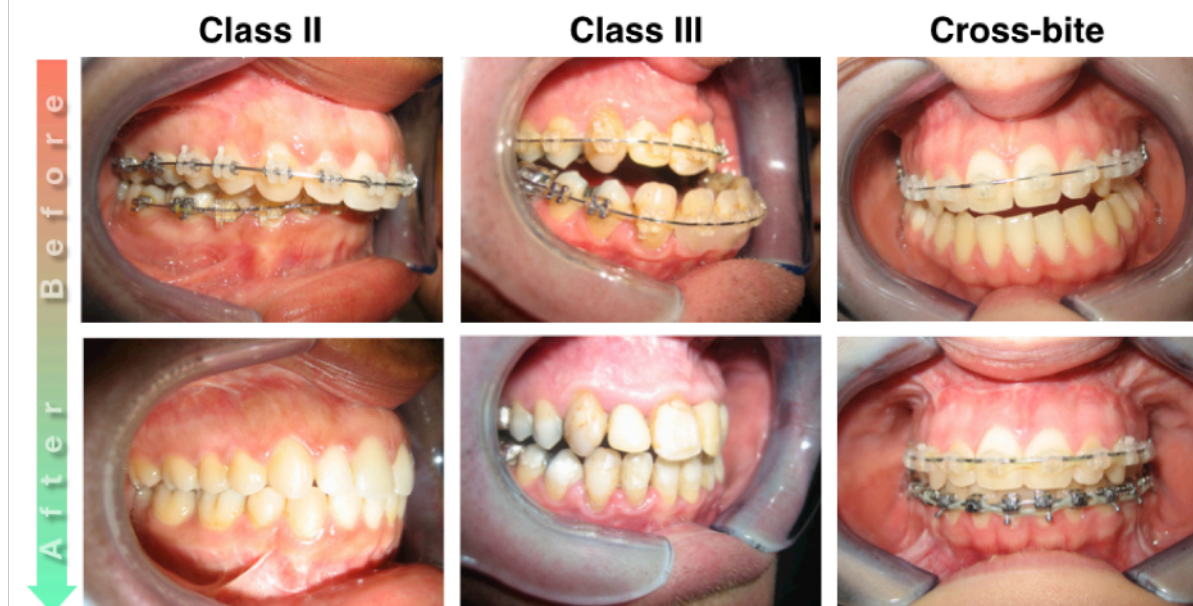


**Figure 2.12:** Preoperative (before, top row) and postoperative (after, bottom row) clinical aspects in terms of dental occlusion of class II - retrognathism (left), class III - prognathism (middle) and cross-bite - asymmetry (right). Vertical midline and horizontal line are featured in green in the asymmetry case.

## 2.2. Issues in orthognathic surgery and existing solutions

### 2.2.1. Planning surgery

The first step in the surgical workflow is the diagnosis of the facial bone structure affected with the deformity and its quantification. Subsequently, the optimal position for the maxilla and the mandible can be assessed. For this purpose, surgical planning and simulation become crucial. The purpose of surgical planning is to visualize how and where bone cuts need to be performed and to determine the direction and range of movements applied to bone segments. Additionally, surgical planning shall provide clear explanation of the procedure to the patient.

Classically, such planning relies on 2D lateral cephalometric radiographs (Rosen 1988) (Louis et al. 2001) (Betts et al. 1993) (Boulenguiez et al. 1991) (Jensen, Sinclair, and Wolford 1992) (Marşan et al. 2009) that display the facial skeleton as well as the soft tissue contour.

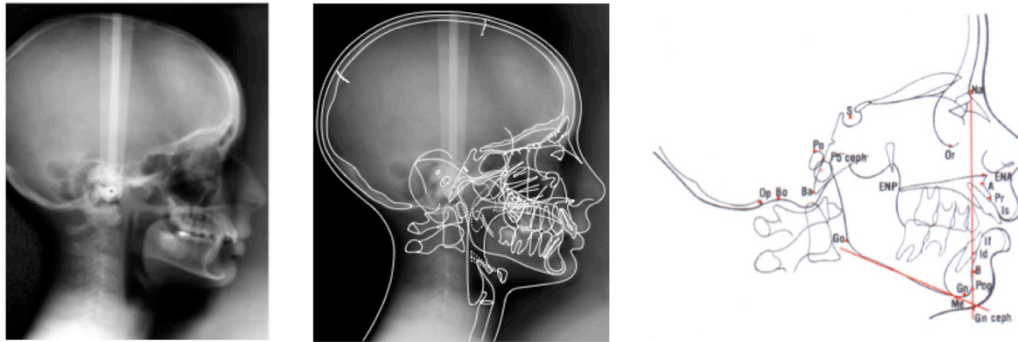


**Figure 2.13:** Conventional 2D analysis through cephalometry (left) and cephalometric tracings (right).

Tracing of the main bony structures as well as of the cutaneous profile are performed using tracing paper. Specific skeletal and cutaneous landmarks are then drawn (Cf. Figure 2.13). The resulting geometric construction is called **cephalometric analysis**. Numerous authors have suggested different types and concepts of such analysis among which the classical Delaire first described in 1971 and based on lateral cephalograms (Delaire, Schendel, and Tulasne 1981). Each of these analyses compare the geometrical data of the considered patient to anthropological standard ranges (Proffit, Fields, and Sarver 2013) (Turley 2015). Therefore, the site of the deformity is identified and the magnitude of surgical correction is determined.

Such planning based on 2D radiographs provides poor spatial resolution and may be inaccurate because of inherent errors. The soft tissues may not be observed clearly because of the low resolution of the radiographic image and the superimposition of bony structures on soft tissues. More significantly, it is unable to show the 3-dimensional changes of a 3D object (Soncul and Bamber 2004).

Olszewski et al. (Olszewski et al. 2007) validated in vitro (using 26 dry skulls) that cephalometry according to Delaire could be adapted to the **third dimension**. They

also proved that reproducibility of such analysis on 3D CT method was significantly superior to the one on 2D X-rays. Additionally, accuracy of measurements on 3D CT (ACRO 3D™ software) appeared identical to the ones directly made on the dry skulls.

Most important is the fact that 3D CT Scan allows better and easier assessment of maxillofacial deformities and provides with more didactical documents for patient information (Olszewski et al. 2007) (Caloss, Atkins, and Stella 2007) (McCance et al. 1992).

Therefore, nowadays, orthognathic surgical planning is performed on software packages using patient-specific 3D CT scans or Cone-Beam Computed Tomography (CBCT) input data (Neumann et al. 1999) (Gwen R. J. Swennen and Schutyser 2006) (G. R. J. Swennen et al. 2009) (Moerenhout et al. 2009).

**One of the main drawbacks is the complexity of handling such software for a surgeon who often has no qualification in computer science. This step is often complex and time-consuming.**

### 2.2.2. Simulating the facial morphological outcome resulting from surgery

Simulation allows evaluating the morphological surgical outcome on the patient's soft tissues. Therefore, the surgeon can validate the procedure he has planned and patients can have an idea of what their postoperative appearance would be.

Before computers were involved, surgeons could only rely on their experience to assess postoperative result. They used to show their patients photographs of individuals taken before and after surgical treatment of similar deformities.

Today, numerous software packages provide simulation of the postoperative result on the patient's face, provided surgery is performed according to the planning. This critical step consists of the visual simulation of the soft tissue behavior subsequent to the virtual movement of bone structures achieved through planning.

**Two-dimensional simulation software** have been developed as early as 1984 (Bhatia and Sowray 1984) based on data provided by Engel et al. (Engel, Quan, and Chaconas 1979). Computer-generated spontaneous simulation appeared later (Walters and Walters 1986) based on Freihofer's data (Freihofer 1984). In 1988, Sarver et al. merge a photography to 2D simulation (Sarver, Johnston, and Matukas 1988): video-imaging was born. It allowed processing a photograph of patients' profile in order to simulate the postoperative result (Quick-Ceph® Software) (Verdonck et al. 1993), therefore expressing a more realistic outcome. Such technology became rapidly improved (Sinclair et al. 1995; Chunmaneechote and Friede 1999; Smith, Thomas, and Proffit 2004) until providing rendering more esthetic than the actual postoperative result (Chew et al. 2008).

Contemporary 2D planning software are commonly based on retrospective studies and mostly use linear ratios of soft tissue response depending on the type and magnitude of surgical bone movements (Chew, Sandham, and Wong 2008). Systematic literature reviews have evaluated the relevance of esthetic outcome prediction using 2D software (Kaipatur and Flores-Mir 2009). On the seven studies selected in this review, none was prospective. These studies showed inaccuracy in the vertical and horizontal planes. The lower lip area was the one subject to the most statistically significant errors. The degree of reliability of mono-maxillary procedures was greater than the one of bimaxillary surgical procedures. In the end, this systematical review did not mention the direction of surgical movements, which could be a variable of great importance.

If two-dimensional simulation is based on linear ratios, **three-dimensionnal simulation** is extraordinary more difficult, since the challenge is to build a mathematical model mimicking the own biomechanical behavior of facial soft tissues. Many software including orthognathic 3D planning and a simulation module are commercially available (Cf. Figure 2.14). The five most cited software in scientific literature are:

- **3dMD Vultus™** (3dMD™, USA)<sup>6</sup> (Becker et al. 2013; Eder et al. 2013)(Khambay and Ullah 2015; Ullah, Turner, and Khambay 2015)
- **Dolphin 3D Surgery™** (Dolphin Imaging & Management Solutions™, Chatsworth, CA, USA)<sup>7</sup> (Becker et al. 2013; Stokbro et al. 2014a)(Alexandre Meireles Borba et al. 2016; Zhang et al. 2016a)
- **Maxilim™** (Medicim™, Sint-Niklass, Belgium)<sup>8</sup> (Gwen R. J. Swennen, Mollemans, and Schutyser 2009) (Gwen R. J. Swennen 2014)(Jeroen Liebrechts et al. 2014; J. Liebrechts et al. 2016a; Baan et al. 2016)
- **SimPlant OMS™** (Materialise™, Leuven, Belgium)<sup>9</sup> (Chang et al. 2015; Nam and Hong 2015)
- **SurgiCase CMF™** (Materialise™, Belgique)<sup>10</sup> (X. Wang et al. 2013)

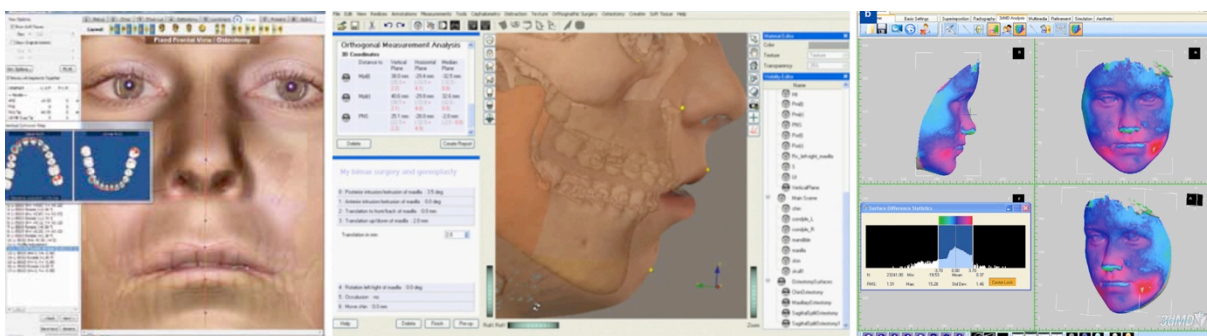


**Figure 2.14: Screen captures of 3D simulation software:** Dolphin 3D Surgery™<sup>7</sup> (left) Maxilim™<sup>8</sup> (middle) and 3dMD Vultus™<sup>6</sup> (right).

<sup>6</sup> <http://www.3dmd.com/3dmd-systems/4d/3dmdvultus/>

<sup>7</sup> <http://www.dolphinimaging.com>

<sup>8</sup> <http://www.medicim.com/en/products/orthognathic-Surgery>

<sup>9</sup> <http://www.materialise.com/Dental>

<sup>10</sup> <http://www.materialise.com/en/medical/software/materialise-surgicase>

Schendel's and Swennen's university teams contributed to the development of respectively 3dMD Vultus™ and Maxilim™, whereas Dolphin 3D Surgery™ originates from the computerized 2D profile cephalometric analysis. Simplant OMS™ derives from guided dental implant surgery.

The scientific bases of these software are scarce among literature. We found that Xia et al. (J. Xia et al. 2000) have successfully used, among other data, 3D CT Scans to perform soft-tissue evaluation in order to predict soft tissue deformation by means of specific algorithms (Surface Normal-based Model Deformation and Ray Projection-based Model Deformation). Specific algorithms are also applied to CT Data in order to predict the three-dimensional changes that will occur in soft tissues, in Caloss' review (Caloss, Atkins, and Stella 2007).

**In the end, due to the complexity of facial anatomy (bone, cutaneous muscles, fat, skin) and the variety of physical properties (elasticity, viscosity) of the tissues involved, simulation of soft-tissue changes is quite challenging (Chabanas et al. 2004). Clinical experience and controversial literature both show that these modifications are more critical in the nose-lip area (Rosen 1988) (Louis et al. 2001) (Betts et al. 1993) (Boulenguiez et al. 1991) (Honrado et al. 2006) (Jensen, Sinclair, and Wolford 1992) (Chabanas et al. 2004), especially in the case of maxillary advancement or vertical movement which relocates the anterior nasal spine, bony key point of surface anatomy.**

**Subsequently, contemporary software packages seem suited to provide an assessment of postoperative result, but numerous studies pinpoint the inconsistencies between the simulated and the actual surgical result (Kaipatur and Flores-Mir 2009).**

### **2.2.3. Transferring surgical planning to the operating theatre and role of navigation**

The main issue in orthognathic surgery is to achieve appropriate positioning of the maxilla, since it is usually the first step of the procedure and will greatly influence the quality of the outcome, especially in terms of facial aesthetics and smile harmony (Kretschmer et al. 2009). Such appropriate surgical positioning aims at achieving centering, symmetry and horizontality of the maxilla in relation to the rest of the skull.

If the assessment of symmetry and horizontality of the occlusal plane can be achieved basing on the clinical analysis of an awoken patient facing the surgeon (using, for instance the horizontal line passing through the pupils), this becomes quite uneasy intraoperatively, since the patient is asleep, lying on the back, his face equipped with various probes and covered by surgical drapes (Cf. Figure 2.15).

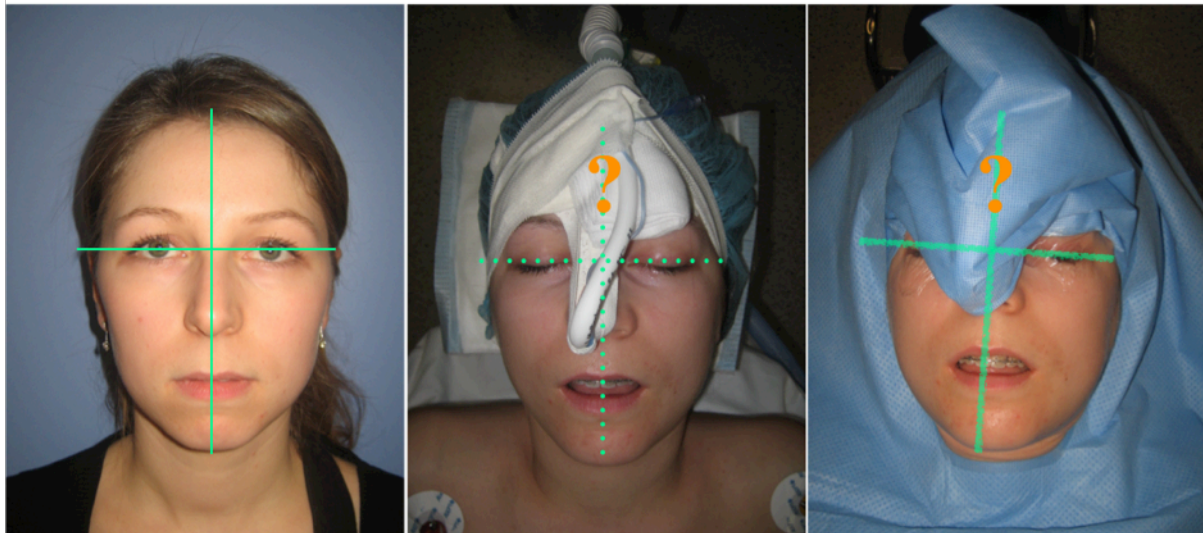


**Figure 2.15: Illustration of clinical landmarks loss** to assess symmetry and horizontality between an awoken patient (left) and the same patient once intubated (middle) then draped (right).

This step of maxilla repositioning is traditionally planned prior to surgery thanks to a set-up manufactured in the prosthodontics laboratory. This set-up uses a specific support mimicking the jaws, namely an articulator, to fix patient-specific dental casts (models) made from imprints of his dental arches. Such a set-up is meant to reproducing the surgical movements.

During the planning of complex movements, such as bimaxillary or asymmetry surgical procedures, the position of dental arches in relation to the skull is registered thanks to a face-bow. Then, different tracings allow, thanks to the potential use of a modified Boley gauge (Henry 1990), to establish landmarks of the simulated bone movements onto the set-up.

In a bimaxillary surgical procedure, the maxillary model is sectioned first, and then moved according to the planning designed by the surgeon, potentially based on lateral cephalometric radiographs (Cf. 2.2.2).

The mandibular model is then also cut and place in proper dental occlusion. This pattern, traditionally described in literature, can however be inverted since the advent of rigid internal fixation (osteosynthesis plating systems) (A.M. Borba et al. 2016).

The reliability of such a burdensome task first depends on the recording of the maxilla position thanks to the face-bow. **The literature analyzing the accuracy of transfer reports significant discrepancies between the measurements performed on the set-up and the cephalometric analysis (Ellis, Tharanon, and Gambrell 1992; Gateno, Forrest, and Camp 2001; Zizelmann et al. 2012). Also, the set-up is not an actual surgical simulation, since it does not consider the cranio-facial complex. Osteotomy lines are also neglected and only the movement of dental arches is determined.**

**If translational movements are easily conceivable, complex tridimensional motions are less likely without appropriate mathematical computation (Kim et al. 2015).**

Once the appropriate anatomical relation is determined between teeth from the upper and the lower jaw, namely proper occlusion has been restored, this position is recorded by means of custom-made acrylic splint. This splint is then used intraoperatively to fix the cut maxilla onto the uncut mandible to reproduce the ideal position established in the prosthodontics laboratory.

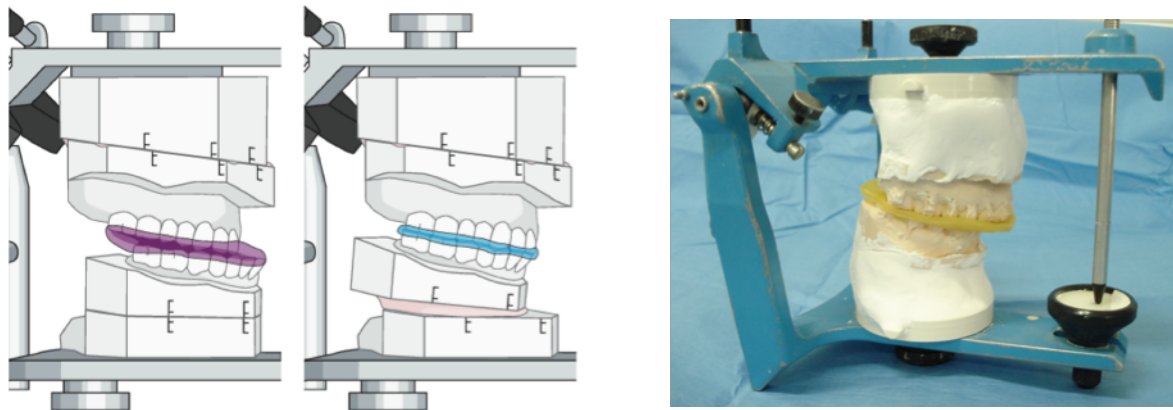


**Figure 2.16:** Schematic (left) and photographic (right) illustration of intermediate dental splint process (due to the courtesy of M. BENASSAROU, M.D. and J-Y CLIET).

Monomaxillary procedures only require one intraoperative repositioning splint, whereas bimaxillary procedures imply the use of an additional **intermediate splint** (Ellis 1999). The usual sequence is indeed:

- the repositioning of the maxilla guided by a splint placed on the uncut mandible
- then the mandibular osteotomy, controlled through the use of a second splint carried by the maxilla, once fixed in its new position.

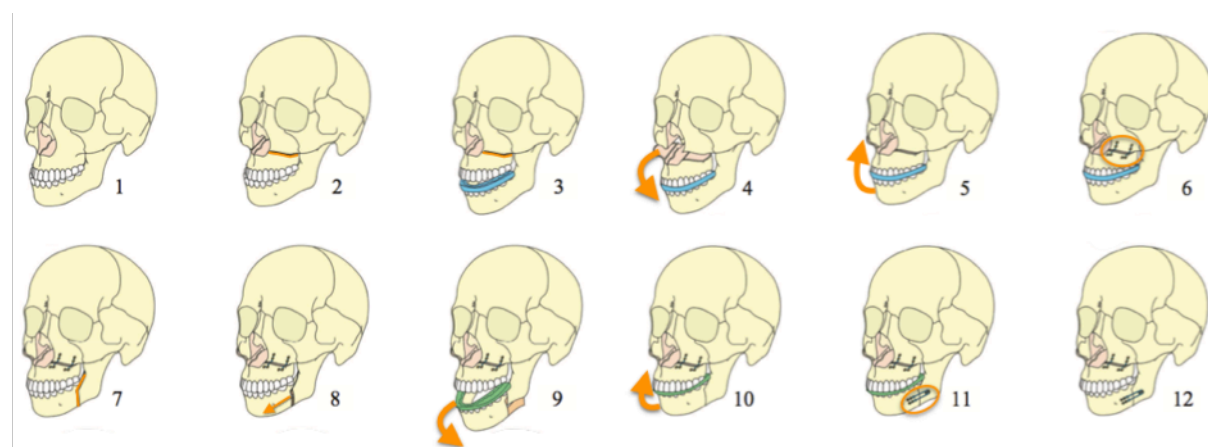


**Figure. 2.17:** Schematic illustration of surgical planning transfer using an intermediate (blue) and final dental splint (green) for intraoperative positioning of the maxilla. (due to the courtesy of M. BENASSAROU, M.D.)



These intermaxillary transfer splints are designed at the same time as the manufacturing of the surgical set-up. During a “Le Fort I” osteotomy, the transversal and horizontal position of the maxilla is controlled by the transfer splint, whereas its vertical position is determined on the basis of extra-oral landmarks (Ellis 1990). Approaches based on intra-oral landmarks (Stanchina et al. 1988; Gil et al. 2007) have been described in literature, but are less accurate (Van Sickels, Larsen, and Triplett 1986; Polido, Ellis, and Sinn 1991).

**We have seen that such a process requires specific training and time-consuming careful preparation. The workflow consists of many steps (dental imprints from the patient, plaster models, surgical set-up). This method allows the placement of an appropriate relation between the maxilla and the mandible. Nevertheless, it is quite difficult to determine the position of the maxilla relatively to the whole facial skeleton.**

Finally, it must be emphasized that the maxilla can be repositioned without any intermediate splint (Lapp 1999), that is, without the help of a mandibular reference, but no study is yet available in order to evaluate the accuracy of such a method.

**In practice, due to the complexity and the time consumed for preoperative set-up and splint design, numerous expert surgeons chose not to use any intermediate splint and to only rely on their experience and visual evaluation to set the ideal pitch, yaw and roll of the maxilla.**

Modern improvements have allowed splints to be generated using computer-assisted design (CAD) and computer-assisted manufacturing (CAM) (Chen et al. 2016). Literature has proved that these processes, such as stereolithography provide an in vitro configuration which as accurate as the one obtained using the traditional method (dental casts) (Gateno et al. 2003) (Schouman et al. 2015). Whether any of these two similar methods are used, the accuracy of bone position actually relies on centric relation<sup>11</sup>, which achievement is intraoperatively uncertain. Therefore, in order to overcome such inconveniencies (Ow and Cheung 2009), as well as to monitor the vertical dimension, some teams have developed patient-specific repositioning guides (Gateno et al. 2007; Polley and Figueroa 2013; Shehab et al. 2013; Kang et al. 2014; Farrell, Franco, and Tucker 2014; Y. Li et al. 2015) (Cf. Figure 2.18). Such guides are fixed onto facial bone structures unaffected by the osteotomy, and are therefore independent from the centric relation.

Furthermore, rapid prototyping allows manufacturing of patient-specific pre-shaped fixation plates (Farrell, Franco, and Tucker 2014) and osteotomy guides (B. Li et al. 2013; Mazzoni et al. 2015), that can reduce the risks of nerve injury (Mensink et al. 2014) and prove helpful in complex surgical cases.

---

<sup>11</sup> In dentistry, **centric relation** is the mandibular jaw position in which the head of the mandibular condyle is situated as far anteriorly and superiorly as it possibly can within the mandibular fossa/glenoid fossa.

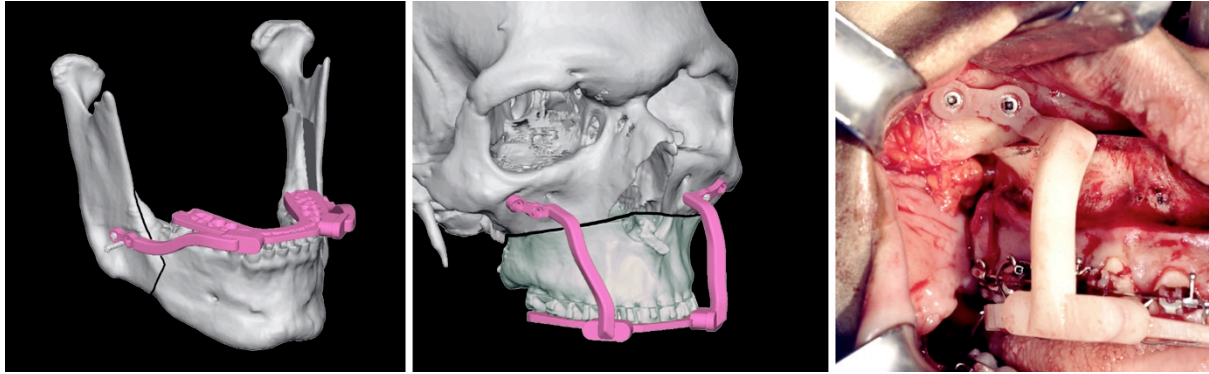


**Figure 2.18: CAD/CAM intramaxillary positioning guides** (Polley and Figueroa 2013). Virtual design of mandibular guide (left), maxillary guide (middle). Intraoperative use of maxillary guide (right).

## 2.3. Drawbacks of existing solutions

### 2.3.1. Drawbacks in planning

Numerous **planning** software, relying on similar data processes from computed tomography (CT) scan, allow preoperative orthognathic surgical planning and are today widely spread (Neumann et al. 1999) (Smith, Thomas, and Proffit 2004) (Kaipatur and Flores-Mir 2009) (Gwen R. J. Swennen, Mollemans, and Schutyser 2009).

These software allow visualization of a patient-specific 3D model and provide computer tools to measure distances and angles (Oz, Orhan, and Abe 2011) in order to achieve a tridimensional cephalometric analysis. Such cephalometry will help identify the site and magnitude of the deformity and therefore determine the surgical movements required to achieve proper dental occlusion and facial harmony, namely, surgical planning. Computer tools allow choosing cutting planes and moving bone segments to perform virtual surgery.

As well as regarding 2D profile cephalometry (Durão et al., others 2013), relevant scientific proofs concerning 3D cephalometry are scarce. Indeed, Smektala et al.'s literature review (Smektala et al. 2014) could not confirm the hypothesis of an accurate and reproducible technique. Pittayapat et al.'s review (Pittayapat et al. 2014) underlines the difficulty in achieving an objective synthesis due to the too large methodological heterogeneity of the selected studies. Lisboa et al. (Lisboa et al. 2015) conclude that, despite an acceptable reliability in identifying certain landmarks, there is still no cephalometric analysis established on normative known parameters even if CBCT is increasingly used in this purpose. Finally, according to Hassan (Hassan et al. 2013), interactive positioning of landmarks can prove rather time-consuming.

Additionally, specific issues arise in 3D cephalometry which does not prove as simple as adding a third dimension to a 2D profile cephalometric analysis.

Indeed, reference planes, such as the Frankfurt plane (Cf. Figure 2.1) and the parasagittal one, are usually traced thanks to two anatomical landmarks selected on a 2D profile radiograph. When shifting to 3D, since structures are bilateral, a total of four landmarks are subsequently available. However, due to frequent facial asymmetry in the general population, it is less likely that all four points are located in the same plane (Gateno, Xia, and Teichgraeber 2011). Subsequent troublesome technical choices need to be made consisting either in suppressing one point or averaging all points. This prevents normalization, which is the basis of a reference system.

The second issue is that, in case of asymmetry, these planes would impact all the measurements resulting from their placement. In this case, the solution would be to use an external referential, such as the natural head position aiming at setting an independent system consisting of a median sagittal plane, a transversal and a frontal one.

Third, tridimensional cephalometric measurements do not have the same significance as their 2D equivalents. Tridimensional measurements are directly influenced by the reference system, which can cause interpretation errors. Subsequently, local coordinate systems are required for the measurements of every anatomical unit, such as the maxilla and the mandible. Therefore, the size and shape of structures can be analyzed regardless of the space they lie into (J.J. Xia, Gateno, Teichgraeber, Yuan, Li, et al. 2015). On the contrary, their position, orientation and symmetry require a main reference system and several local reference systems. Indeed, a symmetrical structure must qualify for both, intrinsic symmetry (local coordinate system) and a symmetrical position in relation to the median sagittal plane (main coordinate system).

### 2.3.2. Drawbacks in simulation

Detailed protocols of such software are quite deficient among literature (Cf. Table 2.1). Two systematic literature reviews, namely Stokbro et al.'s in 2014 (Stokbro et al. 2014b) and Haas et al.'s in 2015 (Haas Jr., Becker, and de Oliveira 2015) sought evaluating clinical trials regarding reliability of tridimensional planning and simulation. They conclude that tridimensional planning and simulation seems accurate and reproducible enough, but also that its **validity lacks a strong level of evidence due to the too poor quality of selected studies**. Their systematic research, however, have been closed in June 2012 and January 2014, yet it is a domain in which progress is likely to occur rapidly and approximately 30 % of potential publications are written later than January 1<sup>st</sup>, 2014.

## 2.3. Drawbacks of existing solutions

	3dMD Vultus™ (Schendel 2015)	Dolphin 3D Surgery™ (Zhang et al. 2016b)	Maxilim™ (Gwen R.J. Swennen, Mollemans, and Schutyser 2009)	SimPlant OMS™ (Hsu et al. 2013)	SurgiCase CMF™ (Marchetti et al. 2011)
<b>Acquisition</b>					
skin surface	•	•	•	NS	•
bone structures	•	•	•	•	•
dental arches	•	•	•	•	NS
natural head position	NS <sup>12</sup>	NS	•	•	NS
<b>Fusion</b>					
skin surface / bone structures	surface (Xin et al. 2013)	NS	surface (Naudi et al. 2013)	NS	NS
bone structures / dental arches	surface (Lin et al. 2013)	NS	point (Gwen R. J. Swennen et al. 2007) surface (de Waard et al. 2016) voxel <sup>13</sup>	point <sup>14</sup>	NS
skin surface / dental arches	NS	NS	surface (Rangel et al. 2008)	NS	NS
skin surface / bone structures / dental arches	NS	NS	NS	NS	NS
<b>Deformity analysis</b>					
structure recognition	•	•	•	•	•
reference values	NS	NS	•	NS	NS
<b>Surgical simulation</b>					
soft tissues	MSM	NS	MTM	NS	FEM
hard tissues	•	•	•	•	•
<b>Intraoperative assistance</b>					
intermaxillary guides	•	•	•	•	•
intramaxillary guides	NS	•	NS	•	•
navigation <sup>15</sup>	NS	NS	NS	• (Bell 2011)	•

**Table 2.1: Specifications of the main tridimensional planning and simulation software.**

(Source: "L'apport de la troisième dimension dans la planification d'un traitement associant orthodontie et chirurgie orthognathique", Dental Thesis by P. MOULIN).

<sup>12</sup> NS : non specified.

<sup>13</sup> Triple CBCT protocol developed by Swennen *et al.* (Gwen R. J. Swennen et al. 2009).

<sup>14</sup> Protocol developed by Gateno et Xia (J.J. Xia, Gateno, Teichgraeber, Yuan, Chen, et al. 2015).

<sup>15</sup> Navigation thanks to third party software such as eNlite™ (Stryker™, Germany), Stealth Station™ (Medtronic-Xomed™, USA), Stryker Navigation System™ (Stryker-Leibinger™, USA) or Vector vision™ (BrainLab™, USA).

We were able to find 11 studies about reliability of soft tissue simulation in literature. All software were evaluated except Dolphin 3D Surgery™. Among all studies, except Nam et al.'s (Nam and Hong 2015), the potential inaccuracy of surgical bone repositioning is subtracted from the soft tissue evaluation. The majority of them report an average error ranging from 0 to 2 mm, when quantitative analysis based on regional surfaces methods are preferred to other methods. The inter-alar width and the chin area are best simulated whereas **the lips or the subnasal areas feature more inaccuracies. Analysis of cephalometric measurements however, show higher errors** (Jeroen Liebrechts et al. 2014; J. H. F. Liebrechts et al. 2014) **and great discrepancy exist between the results of different studies**. Mc Neil, in 1972, was the first author to try and study the soft-tissue response subsequent to orthognathic surgery (McNeill, Proffit, and White 1972). Nowadays, this issue remains difficult to solve in such a way that it could be explained by the proper characteristics of soft tissues. Furthermore, **the degree of freedom of lips regarding incisive support makes the reliability of simulation more complicated**. The presence of orthodontical appliances on the teeth impacts this degree of freedom in such a way that their removal has been considered at the time of follow-up acquisition in 4 studies of the systematic literature review (J. H. F. Liebrechts et al. 2014; Jeroen Liebrechts et al. 2014; J. Liebrechts et al. 2016b; Bianchi et al. 2010).

Indeed, this variable could generate discrepancy among results (up to 1.4 mm regarding lips and labial commissure (Jeon et al. 2013).

Additionally, **the individual response would also be important** (Eidson et al. 2012).

In the end, two authors have compared the reliability of tridimensional soft tissue simulation compared to the two-dimensional one. Thus, Van Hemelen et al.'s randomized, double-blind control study (Van Hemelen et al. 2015) reports that the accuracy of soft tissue tridimensional simulation is greater in sagittal directions (1.48 mm versus an average of 2.29 mm) and vertical ones (1.46 mm versus an average of 2.07 mm). Nadjmi et al.'s study (Nadjmi et al. 2013) also concludes that soft tissue tridimensional simulation is more reliable but without any statistically significant difference.

### **2.3.3. Drawbacks in surgical transfer of the planning and of navigation**

We have seen that the conventional workflow based on dental splints consists of many time-consuming steps (dental imprints from the patient, plaster models, surgical set-up) also requiring specific training. If such a method allows restoring an appropriate relation between the maxilla and the mandible, it still makes it difficult to determine the position of the maxilla relatively to the whole facial skeleton.

These elements have 2 consequences:

- In practice, numerous expert surgeons chose not to use any intermediate splint and to only rely on their experience and visual evaluation to reposition the maxilla.
- Alternate methods have been proposed on the basis of CAD/CAM in order to provide either splints or osteotomy and positioning guides.

The major drawback of such CAD/CAM surgical repositioning guides is the total lack of adaptability. Indeed, any flaw in preoperative design or any change in the surgical workflow makes them useless.

Subsequently, **Surgical navigation**, initially developed for neurosurgery appeared as a relevant tool to replace the methods based on physical devices (splints, osteotomy and positioning guides). Indeed, surgical navigation allows accurate surgical transfer of the preoperative planning, while providing the surgeon with intraoperative freedom to adapt his procedure (Lin and Lo 2015) especially regarding critical anatomical structures (Shim et al. 2013). Surgical navigation both provides accurate information about 3D position of bone segments notably in reference to the rest of patient's skull and assists the surgeon regardless of the last-minute decision he makes. As opposed to physical guiding methods, he can always decide whether to follow the information provided by navigation.

Surgical navigation is based on the **registration** between the CT Scan based 3D model onto which virtual planning is conducted and the real patient lying in the OR, thanks to sensors or fiducials fixed to the patient.

Until now, the navigation systems used in maxillofacial surgery mostly rely on optical-based tracking systems (Cf. Figure 2.19) (Zinser et al. 2013a) (Bettega et al. 1996; Bettega and Leitner 2013).

**Their main disadvantages are the bulk of optical fiducials and the disruption of line of sight where intraoral surgical exposure is so critical** (Benassarou, Benassarou, and Meyer 2013) (Cf. Figure 2.20).

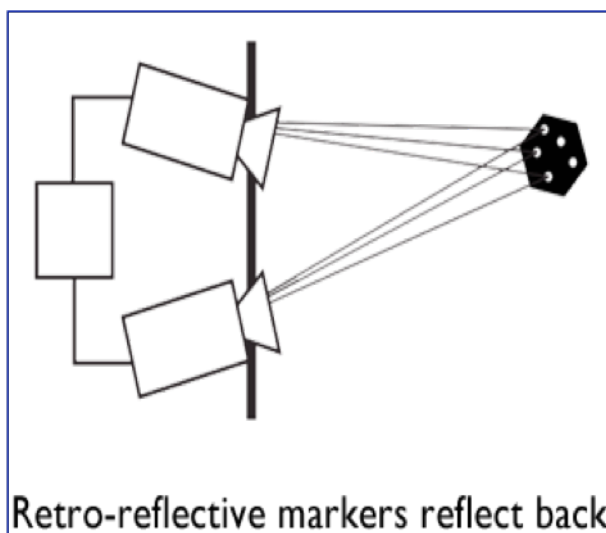


**Figure 2.19:** Scheme depicting the **principle in optical-based tracking** and required line of sight integrity.



**Figure 2.20:** Intraoperative photography depicting the **bulk of optical fiducials in orthognathic surgical navigation** (Benassarou, Benassarou, and Meyer 2013).

Despite the progress made from the conventional workflow, some issues still exist and are the purpose of ongoing research. Such research nowadays mainly focuses on:

- planning: providing user-friendly 3D cephalometric analysis and solving the coordinate system-related problems (Terajima, Furuichi, et al. 2009; Terajima, Nakasima, et al. 2009).
- simulation: providing realistic soft-tissue predictability through dedicated algorithms (J. Xia et al. 2000)(Mollemans et al. 2007; Barbarino et al. 2009; S. Wang, Yang, and Gee 2009; S. Wang and Yang 2010; Mazza and Barbarino 2011; Lou et al. 2012; Pan et al. 2012)
- navigation:
  - o adapting optical-based tracking systems initially developed for neurosurgery and ENT (Zinser et al. 2013b)(Benassarou, Benassarou, and Meyer 2013) (B. Li et al. 2014) to maxillofacial surgery
  - o developing user-friendly interface : augmented virtuality, augmented reality (Mischkowski et al. 2006), hybrid interface (Traub, Stefan, Heining, Riquarts, et al. 2006; Traub, Stefan, Heining, Sielhorst, et al. 2006)

## **2.4. Summary of existing problems and improvements necessary for practical medical use**

### **2.4.1. Planning software**

Most of the available software require **time-consuming pre-processing time**: the surgeon, who often has no specific computer skills, needs to achieve a segmentation procedure in order to generate patient-specific 3D models from CT Scan DICOM raw data. Either an intuitive and fast segmentation-based pipeline shall be developed or an external ready-to-use service can be chosen.

If virtual tools are already available to achieve cuts and movements on facial bones, they are scarcely user-friendly. Intuitive features and ergonomic interface would be great improvements.

Three-dimensional cephalometric analysis is a controversial topic on its own that we decide to not address any further in our research.

### **2.4.2. Simulation software**

Expected postoperative morphology of patient's face shall be realistic and close to the actual surgical result. This is often not the case, especially in the nose-lip area due to the diversity of parameters. New algorithms need to be developed and confronted to clinical databases in order to provide optimal prediction.

### **2.4.3. Navigation system**

Such system shall be non-invasive and user-friendly. Initial set-up shall be quick in order not to increase procedure duration under general anesthesia. Fiducials shall be inconspicuous and compatible with restricted operating sight. The system shall be 1mm accurate and remain effective even in case of occultation by surgeon's hand. User interface shall be intuitive and relevant to provide actual improvement in procedure accuracy and duration.



## 2.5. Specification goals of our development and scientific choices

Our ultimate purpose is to provide the surgeon with navigation software to improve accuracy, operative time and safety. In order to be able to provide such navigation software, it is mandatory that we define the target position of facial segments that the surgeons shall reach in order to match the result they have planned. Therefore, a preliminary step of our work is to address planning issues.

### 2.5.1. Planning

Since planning is achieved on patient-specific numerical models from CT Scan DICOM raw data, we would initially need to propose a fast segmentation-based **modeling** pipeline providing ready-to-use 3D models in order to spare the surgeons' precious time as we will see in Chapter 3.

Additionally, we would need to develop **planning tools** that allow cutting the facial skeleton and moving bone segments similarly to the way it is performed in the operating theatre. Mathematical modeling of the surgical steps, such as bone section and displacement would therefore be addressed in the first part of Chapter 4.

### 2.5.2. Simulation

Once ideal preoperative planning is achieved on a virtual model, it becomes quite relevant to try and predict patient's postoperative facial morphological outcome. Such **simulation** would thus favorably provide:

- the patients with explicit information based on their specific virtual model,
- the surgeons with confirmation that their clinical assessment is relevant and able to achieve adequate morphological result,
- the students with comprehensive explanation about the morphological impact of every surgical step.

We therefore decided to analyze scientific literature in order to determine which physical models could be used to provide relevant simulation of facial soft tissue response. We chose a mechanical model and proposed a simulation method in order to understand the issues of providing realistic simulation in the nose-lip area, as we will detail in the second part of Chapter 4.

### 2.5.3. Navigation: surgical transfer of the planning

Once preoperative planning has been processed, **navigation** software could be developed in order to provide the surgeons with according intraoperative guidance. In order for such a system to provide increased accuracy and safety, reduced operative time and conformity with the planned procedure, it should be suited to routine clinical practice and feature appropriate specifications.

The system specifications shall include:

- Swift preoperative set-up
- Elements compatible with asepsis constraints
- Inconspicuous fiducials
- Preservation of the restricted operative sight
- Freedom of movement for the surgeon

Particularly, the software shall display:

- 3D views of patient's virtual model
- The maxillary cutting plane
- The planned surgical position of the maxilla
- The actual position of the maxilla, based on real-time registration
- Specific interface allowing real-time intuitive apprehension of 3D movements applied to bone segments

As explained by Nicolau (Stéphane Nicolau et al. 2011), there are two kinds of computer guiding systems: the first one is called **Augmented Virtuality (AV)** and displays a virtual environment, which is controlled by real information. The second one, called **Augmented Reality (AR)**, displays virtual information onto real images of the patient.

In the context of minimally invasive surgery, it seems natural to use **Augmented Reality** techniques to superimpose in the endoscopic view structures, which are not visible by direct camera view, but are visible in the pre-operative image.

In our field of maxillofacial application, the structures are directly accessible to the surgeon's sight but he needs assistance to achieve precise movements and to set accurate positions. Surgical research teams (Zinser et al. 2013c; Badiali et al. 2014) have recently used such method in orthognathic surgery (Cf. Figure 2.21).



**Figure 2.21: Augmented reality-based surgical navigation** according to Mischkowski *et al.* (Mischkowski et al. 2006b) and Zinser *et al.* (Zinser, Sailer, et al. 2013). Registration system (left), augmented reality display (middle), on-screen superimposition of surgical planning onto the patient's maxilla.

On the other hand, **Augmented Virtuality (AV)** in orthognathic surgery would consist in displaying maxillary motions performed in the real world onto a virtual image, namely, the patient's CT scan (Cf. Figure 2.23).

Aiming at achieving such computer guiding systems, we proceeded through different steps in order to choose the technology we finally based our research on.

### 2.5.3.1. Interactive Augmented Reality: manual registration using visual landmarks

We have conducted some tests of such software on real patients in the OR (Cf. Figure 2.22). This initial step consisted in developing a first version of an Augmented Reality software based on an external view of the patient provided by a camera embedded into the handle of the operation lamp. The purpose of this software was, first, to display the preoperative model of the patient's skull onto which the maxillary cutting plane was indicated. Second, we loaded a patient model displaying the planned maxillary position (expected target position of the maxilla after bone section). We used existing IRCAD Software allowing to process a patient model and to display the bone section line.

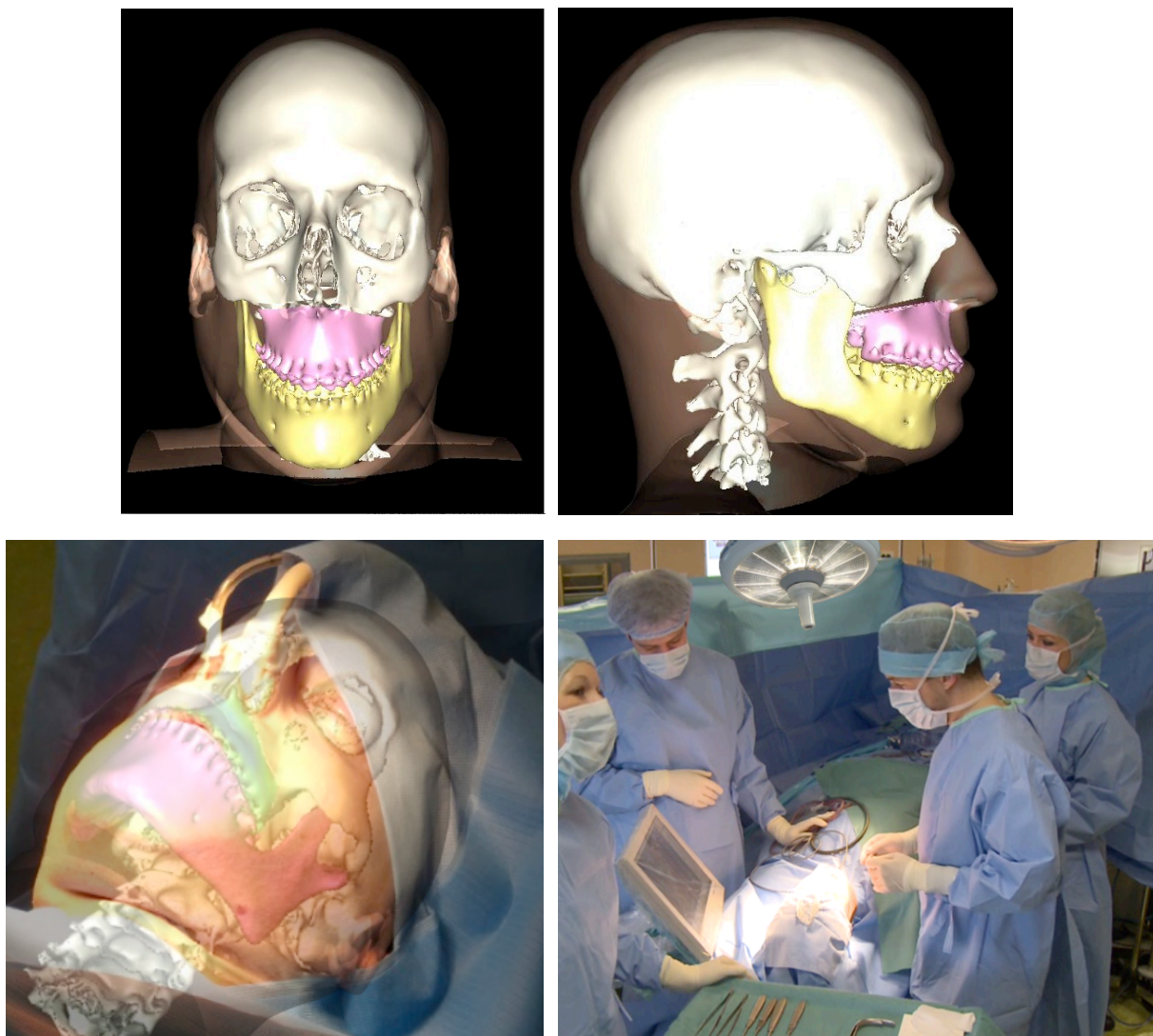


**Figure 2.22: Interactive Augmented Reality System we developed and tested in the OR.** Preoperative virtual model (Top left and right). Interface displaying the preoperative model onto which the maxillary cutting line is indicated (bottom left). System set-up in the OR (bottom right). Note the camera embedded into the handle of the operation lamp.

An **interactive** registration of the model into the preoperative video image was conducted by the operator thanks to visual anatomical landmarks (Marescaux et al. 2004). The definition of optimal anatomical landmarks, one rigid in relation to the other, will be a subject of research that will be used for a further version of the software.

**The problem of such a system relies in its operator-dependency and its lack of reproducibility.**

### **2.5.3.2. Automated Augmented Reality: automated registration of head movements, and of the maxilla using a tracking system.**

The main drawback of the previous system was, on the one hand, that it relied on a manual registration therefore restrained by the user's accuracy, and, on the other hand, that it had to be started over every time that the patient's head changed position in the camera field of view. Such head movements usually occur secondary to the surgeon's manipulations during surgery and it is not reasonable to consider that the patient's head can remain perfectly steady throughout the whole procedure. In order for the system to be used in clinical routine, it was therefore mandatory to provide an automated head tracking method. This was the purpose of a second step of our preliminary work.

We first established a 3D/2D registration procedure based on the interactive pairing of visual anatomical landmarks, both in the preoperative image and in the intraoperative video image (S. Nicolau et al. 2005). Once the registration of the preoperative model conducted, we used an electromagnetic-based system to achieve real-time tracking of head movements. Such an electromagnetic system is able to track the position and orientation of miniaturized electromagnetic coils (8x2 mm). Thanks to fixation of a coil onto the patient's head, it was possible to achieve real-time tracking.

The main advantage of this system was the low bulk of the coil, which could be placed anywhere on the head, underneath operative drapes, or even into a probe placed inside the patient. On the other hand, it was prerequisite to calibrate the position of electromagnetic system in relation to the camera in order to provide an Augmented Reality view (Feuerstein et al. 2009) (Stéphane Nicolau et al. 2011; Stéphane Nicolau, Soler, and Marescaux 2012; Soler et al. 2014; Pessaux et al. 2015).

The purpose of the software provided thanks to this step is the same as previously, that is, to achieve a real-time display of the maxillary cutting plane, then displaying its ideal planned position once it is relocated.

The advantage of this system compared to the previous is that it only requires a sole registration at the beginning of surgery.

In order to provide the operator with an additional assistance, we proposed real-time software assistance when maxillary repositioning and fixation occurs. To reach this goal, we had to be able to achieve an independent tracking of the maxilla, once it was cut. Therefore, we developed a dental-borne splint embedding an electromagnetic sensor. This splint was also designed to allow physical repositioning of the mandible onto the maxilla. Thus, we were able to display real-time position of the maxilla in relation to the skull, therefore making easier the monitoring of the preoperative planning with a 1 mm accuracy (Berger et al. 2015; Lutz et al. 2015).

We will detail in Chapter 5 the work achieved to design the splint as well as to conceive ergonomic software adequate to transfer relevant information to the surgeon.

In the preliminary steps described above, we used **Augmented Reality**, which consisted in displaying the virtually planned ideal position of the maxilla into a video of the **real world**, either using interactive or automated registration. **Augmented Reality** appeared uneasy, since calibration and tracking of the camera, as well as registration of the virtual image in relation to the real world were required.

**If we found an outcome rather visually flattering, we also concluded that all these calibration and registration steps, required for Augmented Reality view, were sources of additional errors. Such augmented reality based on the use of a video camera caused also visualization ergonomic issues, mainly since the surgeon's point of view differs from the one of the camera, which induces a bothersome visual discrepancy.**

An alternate option for interfacing consists in displaying the position of the automatically tracked maxilla into the virtual world, which is the 3D model of the real world, so called **Augmented Virtuality**. **Such a method has the great advantage of restraining the number of registration steps and providing satisfactory visualization.**

**Since our purpose was to provide an optimal system in terms of accuracy in maxillary repositioning, we chose to base our development onto Augmented Virtuality. We will detail the development of this system and its evaluation in Chapter 5.**

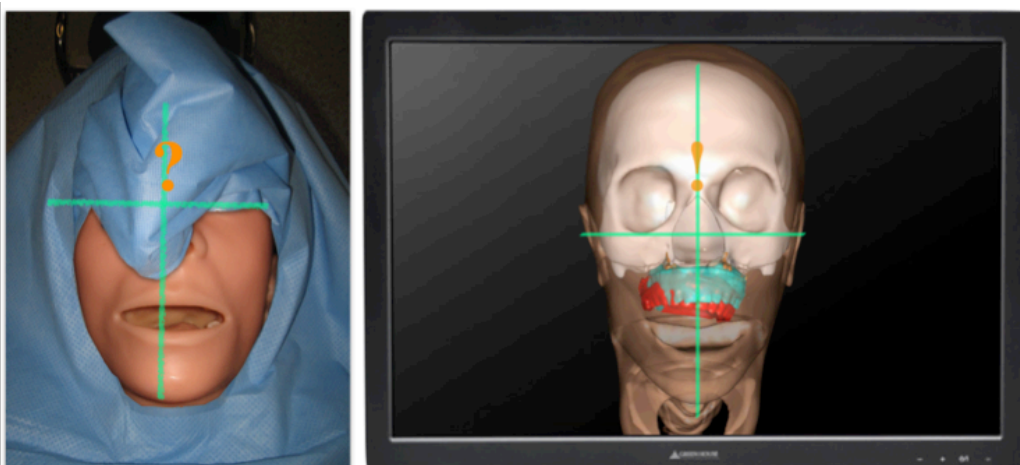


**Figure 2.23:** Illustration of the principle of our Augmented Virtuality navigation software.

## **2.6. Conclusion**

Throughout this chapter, we have analyzed the issues encountered in the routine practice of orthognathic surgery. We have identified the surgeon's needs for improvement in every step of patient care, from preoperative planning, simulation to intraoperative assistance.

We explained that, in order to reach the ultimate goal of intraoperative navigation, the surgeon needs to perform previous virtual surgery, which is favorably conducted in a context and environment free of asepsis and time constraints, allowing him to carefully anticipate anatomical pitfalls: namely virtual planning. Such planning is achieved on a virtual patient-specific model of his head. The initial mandatory step consists in achieving such a model, keeping in mind that surgeons are not necessarily computer experts and that their precious time shall be focused towards patient care.

Therefore, considering these requirements, we will detail in the following chapter 3 the part of our research dedicated to modeling.

## REFERENCES

1. Baan, Frank, Jeroen Liebrechts, Tong Xi, Ruud Schreurs, Martien de Koning, Stefaan Bergé, and Thomas Maal. 2016. "A New 3D Tool for Assessing the Accuracy of Bimaxillary Surgery: The OrthoGnathicAnalyser." Edited by Gururaj Arakeri. *PLOS ONE* 11 (2): e0149625. doi:10.1371/journal.pone.0149625.
2. Badiali, Giovanni, Vincenzo Ferrari, Fabrizio Cutolo, Cinzia Freschi, Davide Caramella, Alberto Bianchi, and Claudio Marchetti. 2014. "Augmented Reality as an Aid in Maxillofacial Surgery: Validation of a Wearable System Allowing Maxillary Repositioning." *Journal of Cranio-Maxillo-Facial Surgery: Official Publication of the European Association for Cranio-Maxillo-Facial Surgery* 42 (8): 1970–76. doi:10.1016/j.jcms.2014.09.001.
3. Barbarino, G. G., M. Jabareen, J. Trzewik, A. Nkengne, G. Stamatias, and E. Mazza. 2009. "Development and Validation of a Three-Dimensional Finite Element Model of the Face." *Journal of Biomechanical Engineering* 131 (4): 041006. doi:10.1115/1.3049857.
4. Becker, Otávio Emmel, Neimar Scolari, Marcelo Fernandes Santos Melo, O. L. Haas Junior, Rafael Linard Avelar, and others. 2013. "Three-Dimensional Planning in Orthognathic Surgery Using Cone-Beam Computed Tomography and Computer Software." *J Comput Sci Syst Biol* 6: 311–16.
5. Bell, R. Bryan. 2011. "Computer Planning and Intraoperative Navigation in Orthognathic Surgery." *Journal of Oral and Maxillofacial Surgery* 69 (3): 592–605. doi:10.1016/j.joms.2009.06.030.
6. Benassarou, M, A Benassarou, and C Meyer. 2013. "[Computer-assisted navigation in orthognathic surgery. Application to Le Fort I osteotomy]." *Revue de stomatologie, de chirurgie maxillo-faciale et de chirurgie orale*, August. doi:10.1016/j.revsto.2013.06.004.
7. Berger, Moritz, Sebastian Kallus, Igor Nova, Oliver Ristow, Urs Eisenmann, Hartmut Dickhaus, Reinald Kuhle, Jürgen Hoffmann, and Robin Seeberger. 2015. "Approach to Intraoperative Electromagnetic Navigation in Orthognathic Surgery: A Phantom Skull Based Trial." *Journal of Cranio-Maxillofacial Surgery* 43 (9): 1731–36. doi:10.1016/j.jcms.2015.08.022.
8. Bettega, G, and F Leitner. 2013. "[Computer assisted orthognathic surgery: Condyle repositioning]." *Revue de stomatologie, de chirurgie maxillo-faciale et de chirurgie orale*, July. doi:10.1016/j.revsto.2013.06.001.
9. Bettega, G., V. Dessenne, B. Raphaël, and P. Cinquin. 1996. "Computer-Assisted Mandibular Condyle Positioning in Orthognathic Surgery." *Journal of Oral and Maxillofacial Surgery: Official Journal of the American Association of Oral and Maxillofacial Surgeons* 54 (5): 553–58.

10. Betts, N. J., K. W. Vig, P. Vig, P. Spalding, and R. J. Fonseca. 1993. "Changes in the Nasal and Labial Soft Tissues after Surgical Repositioning of the Maxilla." *The International Journal of Adult Orthodontics and Orthognathic Surgery* 8 (1): 7–23.
11. Bhatia, S. N., and J. H. Sowray. 1984. "A Computer-Aided Design for Orthognathic Surgery." *The British Journal of Oral & Maxillofacial Surgery* 22 (4): 237–53.
12. Bianchi, Alberto, Louis Muyldermans, Mirko Di Martino, Lorenzo Lancellotti, Sara Amadori, Alessandro Sarti, and Claudio Marchetti. 2010. "Facial Soft Tissue Esthetic Predictions: Validation in Craniomaxillofacial Surgery With Cone Beam Computed Tomography Data." *Journal of Oral and Maxillofacial Surgery* 68 (7): 1471–79. doi:10.1016/j.joms.2009.08.006.
13. Borba, A.M., A.H. Borges, P.S. Cé, B.A. Venturi, M.G. Naclério-Homem, and M. Miloro. 2016. "Mandible-First Sequence in Bimaxillary Orthognathic Surgery: A Systematic Review." *International Journal of Oral and Maxillofacial Surgery* 45 (4): 472–75. doi:10.1016/j.ijom.2015.10.008.
14. Borba, Alexandre Meireles, Dustin Haupt, Leiliane Teresinha de Almeida Romualdo, André Luis Fernandes da Silva, Maria da Graça Naclério-Homem, and Michael Miloro. 2016. "How Many Oral and Maxillofacial Surgeons Does It Take to Perform Virtual Orthognathic Surgical Planning?" *Journal of Oral and Maxillofacial Surgery*, March. doi:10.1016/j.joms.2016.03.013.
15. Boulenguiez, M., R. Garcia, E. Hadjean, & B. Négrier. 1991. "[Esthetic impact of the Le Fort I type osteotomy]." *L' Orthodontie Française* 62 Pt 3: 899–919.
16. Caloss, Ron, Kevin Atkins, and John P. Stella. 2007. "Three-Dimensional Imaging for Virtual Assessment and Treatment Simulation in Orthognathic Surgery." *Oral and Maxillofacial Surgery Clinics of North America* 19 (3): 287–309, v. doi:10.1016/j.coms.2007.04.006.
17. Chabanas, M, Ch Marécaux, F Chouly, F Boutault, and Y Payan. 2004. "Evaluating Soft Tissue Simulation in Maxillofacial Surgery Using Preoperative and Postoperative CT Scans.", 419–24.
18. Chang, Hsin-Wen, Hsiu-Hsia Lin, Peerasak Chortrakarnkij, Sun Goo Kim, and Lun-Jou Lo. 2015. "Intraoperative Navigation for Single-Splint Two-Jaw Orthognathic Surgery: From Model to Actual Surgery." *Journal of Cranio-Maxillofacial Surgery* 43 (7): 1119–26. doi:10.1016/j.jcms.2015.06.009.
19. Chen, Xiaojun, Lu Xu, Yue Yang, and Jan Egger. 2016. "A Semi-Automatic Computer-Aided Method for Surgical Template Design." *Scientific Reports* 6 (February): 20280. doi:10.1038/srep20280.
20. Chew, Ming Tak, Chay Hui Koh, Andrew Sandham, and Hwee Bee Wong. 2008. "Subjective Evaluation of the Accuracy of Video Imaging Prediction Following Orthognathic Surgery in Chinese Patients." *Journal of Oral and Maxillofacial Surgery* 66 (2): 291–96. doi:10.1016/j.joms.2007.06.629.



21. Chew, Ming Tak, Andrew Sandham, and Hwee Bee Wong. 2008. "Evaluation of the Linearity of Soft- to Hard-Tissue Movement after Orthognathic Surgery." *American Journal of Orthodontics and Dentofacial Orthopedics* 134 (5): 665–70. doi:10.1016/j.ajodo.2006.12.017.
22. Chunmaneechote, P., and H. Friede. 1999. "Mandibular Setback Osteotomy: Facial Soft Tissue Behavior and Possibility to Improve the Accuracy of the Soft Tissue Profile Prediction with the Use of a Computerized Cephalometric Program: Quick Ceph Image Pro: V. 2.5." *Clinical Orthodontics and Research* 2 (2): 85–98.
23. Delaire, J., S. A. Schendel, and J. F. Tulasne. 1981. "An Architectural and Structural Craniofacial Analysis: A New Lateral Cephalometric Analysis." *Oral Surgery, Oral Medicine, and Oral Pathology* 52 (3): 226–38.
24. Durão, Ana R., Pisha Pittayapat, M. I. Rockenbach, Raphael Olszewski, Suk Ng, Afonso P. Ferreira, and Reinhilde Jacobs, others. 2013. "Validity of 2D Lateral Cephalometry in Orthodontics: A Systematic Review." *Prog Orthod* 14 (1): 31–42.
25. Eder, Maximilian, Gernot Brockmann, Alexander Zimmermann, Moschos A. Papadopoulos, Katja Schwenzer-Zimmerer, Hans Florian Zeilhofer, Robert Sader, Nikolaos A. Papadopoulos, and Laszlo Kovacs. 2013. "Evaluation of Precision and Accuracy Assessment of Different 3-D Surface Imaging Systems for Biomedical Purposes." *Journal of Digital Imaging* 26 (2): 163–72. doi:10.1007/s10278-012-9487-1.
26. Eidson, Lindsey, Lucia H.S. Cevidanes, Leonardo Koerich de Paula, H. Garland Hershey, Gregory Welch, and P. Emile Rossouw. 2012. "Three-Dimensional Evaluation of Changes in Lip Position from before to after Orthodontic Appliance Removal." *American Journal of Orthodontics and Dentofacial Orthopedics* 142 (3): 410–18. doi:10.1016/j.ajodo.2012.01.018.
27. Ellis, E. 1990. "Accuracy of Model Surgery: Evaluation of an Old Technique and Introduction of a New One." *Journal of Oral and Maxillofacial Surgery: Official Journal of the American Association of Oral and Maxillofacial Surgeons* 48 (11): 1161–67.
28. Ellis, E. 1999. "Bimaxillary Surgery Using an Intermediate Splint to Position the Maxilla." *Journal of Oral and Maxillofacial Surgery: Official Journal of the American Association of Oral and Maxillofacial Surgeons* 57 (1): 53–56.
29. Ellis, E., W. Tharanon, and K. Gambrell. 1992. "Accuracy of Face-Bow Transfer: Effect on Surgical Prediction and Postsurgical Result." *Journal of Oral and Maxillofacial Surgery: Official Journal of the American Association of Oral and Maxillofacial Surgeons* 50 (6): 562–67.
30. Engel, G. A., R. E. Quan, and S. J. Chaconas. 1979. "Soft-Tissue Change as a Result of Maxillary Surgery. A Preliminary Study." *American Journal of Orthodontics* 75 (3): 291–300.

31. Farrell, Brian B., Peter B. Franco, and Myron R. Tucker. 2014a. "Virtual Surgical Planning in Orthognathic Surgery." *Oral and Maxillofacial Surgery Clinics of North America* 26 (4): 459–73. doi:10.1016/j.coms.2014.08.011.
32. Feuerstein, Marco, Tobias Reichl, Jakob Vogel, Joerg Traub, and Nassir Navab. 2009. "Magneto-Optical Tracking of Flexible Laparoscopic Ultrasound: Model-Based Online Detection and Correction of Magnetic Tracking Errors." *IEEE Transactions on Medical Imaging* 28 (6): 951–67. doi:10.1109/TMI.2008.2008954.
33. Freihofer, H. P. 1984. "Latitude and Limitation of Midface Movements." *The British Journal of Oral & Maxillofacial Surgery* 22 (6): 393–413.
34. Gateno, Jaime, Kim K. Forrest, and Brian Camp. 2001. "A Comparison of 3 Methods of Face-Bow Transfer Recording: Implications for Orthognathic Surgery." *Journal of Oral and Maxillofacial Surgery* 59 (6): 635–40. doi:10.1053/joms.2001.23374.
35. Gateno, Jaime, James J. Xia, and John F. Teichgraeber. 2011. "New 3-Dimensional Cephalometric Analysis for Orthognathic Surgery." *Journal of Oral and Maxillofacial Surgery* 69 (3): 606–22. doi:10.1016/j.joms.2010.09.010.
36. Gateno, Jaime, James J. Xia, John F. Teichgraeber, Andrew M. Christensen, Jeremy J. Lemoine, Michael A.K. Liebschner, Michael J. Gliddon, and Michaelanne E. Briggs. 2007. "Clinical Feasibility of Computer-Aided Surgical Simulation (CASS) in the Treatment of Complex Cranio-Maxillofacial Deformities." *Journal of Oral and Maxillofacial Surgery* 65 (4): 728–34. doi:10.1016/j.joms.2006.04.001.
37. Gateno, Jaime, James Xia, John F. Teichgraeber, Andrew Rosen, Bruce Hultgren, and Tim Vadnais. 2003. "The Precision of Computer-Generated Surgical Splints." *Journal of Oral and Maxillofacial Surgery* 61 (7): 814–17.
38. Gil, J.N., J.D.P. Claus, R. Manfro, and S.M. Lima. 2007. "Predictability of Maxillary Repositioning during Bimaxillary Surgery: Accuracy of a New Technique." *International Journal of Oral and Maxillofacial Surgery* 36 (4): 296–300. doi:10.1016/j.ijom.2006.10.015.
39. Haas Jr., O.L., O.E. Becker, and R.B. de Oliveira. 2015. "Computer-Aided Planning in Orthognathic Surgery—systematic Review." *International Journal of Oral and Maxillofacial Surgery* 44 (3): 329–42. doi:10.1016/j.ijom.2014.10.025.
40. Hassan, B., P. Nijkamp, H. Verheij, J. Tairie, C. Vink, P. van der Stelt, and H. van Beek. 2013. "Precision of Identifying Cephalometric Landmarks with Cone Beam Computed Tomography in Vivo." *The European Journal of Orthodontics* 35 (1): 38–44. doi:10.1093/ejo/cjr050.

41. Hemelen, Geert Van, Maarten Van Genechten, Lieven Renier, Maria Desmedt, Elric Verbruggen, and Nasser Nadjmi. 2015. "Three-Dimensional Virtual Planning in Orthognathic Surgery Enhances the Accuracy of Soft Tissue Prediction." *Journal of Cranio-Maxillo-Facial Surgery: Official Publication of the European Association for Cranio-Maxillo-Facial Surgery* 43 (6): 918–25. doi:10.1016/j.jcms.2015.04.006.
42. Henry, Charles H. 1990. "Modified Boley Gauge for Use as a Reference Plane in Orthognathic Surgery." *Journal of Oral and Maxillofacial Surgery* 48 (5): 535–39.
43. Honrado, Carlo P, Samson Lee, Dale S Bloomquist, and Wayne F Larrabee Jr. 2006. "Quantitative Assessment of Nasal Changes after Maxillomandibular Surgery Using a 3-Dimensional Digital Imaging System." *Archives of Facial Plastic Surgery* 8 (1): 26–35. doi:10.1001/archfaci.8.1.26.
44. Hsu, Sam Sheng-Pin, Jaime Gateno, R. Bryan Bell, David L. Hirsch, Michael R. Markiewicz, John F. Teichgraeber, Xiaobo Zhou, and James J. Xia. 2013. "Accuracy of a Computer-Aided Surgical Simulation Protocol for Orthognathic Surgery: A Prospective Multicenter Study." *Journal of Oral and Maxillofacial Surgery* 71 (1): 128–42. doi:10.1016/j.joms.2012.03.027.
45. Hutton, Tim J., Bernard F. Buxton, Peter Hammond, and Henry W. W. Potts. 2003. "Estimating Average Growth Trajectories in Shape-Space Using Kernel Smoothing." *IEEE Transactions on Medical Imaging* 22 (6): 747–53. doi:10.1109/TMI.2003.814784.
46. Jensen, A. C., P. M. Sinclair, and L. M. Wolford. 1992. "Soft Tissue Changes Associated with Double Jaw Surgery." *American Journal of Orthodontics and Dentofacial Orthopedics: Official Publication of the American Association of Orthodontists, Its Constituent Societies, and the American Board of Orthodontics* 101 (3): 266–75. doi:10.1016/0889-5406(92)70096-S.
47. Jeon, H, S. J. Lee, T. W. Kim, and R. E. Donatelli. 2013. "Three-Dimensional Analysis of Lip and Perioral Soft Tissue Changes after Debonding of Labial Brackets: Three-Dimensional Soft Tissue Change after Debonding." *Orthodontics & Craniofacial Research* 16 (2): 65–74. doi:10.1111/ocr.12006.
48. Kaipatur, Neelambar R, and Carlos Flores-Mir. 2009. "Accuracy of Computer Programs in Predicting Orthognathic Surgery Soft Tissue Response." *Journal of Oral and Maxillofacial Surgery: Official Journal of the American Association of Oral and Maxillofacial Surgeons* 67 (4): 751–59. doi:10.1016/j.joms.2008.11.006.
49. Kang, Sang-Hoon, Moon-Key Kim, Bong Chul Kim, and Sang-Hwy Lee. 2014. "Orthognathic Y-Splint: A CAD/CAM-Engineered Maxillary Repositioning Wafer Assembly." *British Journal of Oral and Maxillofacial Surgery* 52 (7): 667–69. doi:10.1016/j.bjoms.2014.01.023.

50. Khambay, B., and R. Ullah. 2015. "Current Methods of Assessing the Accuracy of Three-Dimensional Soft Tissue Facial Predictions: Technical and Clinical Considerations." *International Journal of Oral and Maxillofacial Surgery* 44 (1): 132–38. doi:10.1016/j.ijom.2014.04.007.
51. Kim, Sung-Jin, Kee-Joon Lee, Hyung-Seog Yu, Young-Soo Jung, and Hyoung-Seon Baik. 2015. "Three-Dimensional Effect of Pitch, Roll, and Yaw Rotations on Maxillomandibular Complex Movement." *Journal of Cranio-Maxillofacial Surgery* 43 (2): 264–73. doi:10.1016/j.jcms.2014.11.022.
52. Kretschmer, W. B., W. Zoder, G. Baciut, Mihaela Bacuit, and K. Wangerin. 2009. "Accuracy of Maxillary Positioning in Bimaxillary Surgery." *British Journal of Oral and Maxillofacial Surgery* 47 (6): 446–49. doi:10.1016/j.bjoms.2009.06.004.
53. Lapp, Thomas H. 1999. "Bimaxillary Surgery without the Use of an Intermediate Splint to Position the Maxilla." *Journal of Oral and Maxillofacial Surgery* 57 (1): 57–60.
54. Li, Biao, Lei Zhang, Hao Sun, Steve G F Shen, and Xudong Wang. 2014. "A New Method of Surgical Navigation for Orthognathic Surgery: Optical Tracking Guided Free-Hand Repositioning of the Maxillomandibular Complex." *The Journal of Craniofacial Surgery* 25 (2): 406–11. doi:10.1097/SCS.0000000000000673.
55. Li, Biao, Lei Zhang, Hao Sun, Jianbing Yuan, Steve G.F. Shen, and Xudong Wang. 2013. "A Novel Method of Computer Aided Orthognathic Surgery Using Individual CAD/CAM Templates: A Combination of Osteotomy and Repositioning Guides." *British Journal of Oral and Maxillofacial Surgery* 51 (8): e239–e244. doi:10.1016/j.bjoms.2013.03.007.
56. Li, Yunfeng, Yangmei Jiang, Nan Zhang, Rui Xu, Jing Hu, and Songsong Zhu. 2015. "Clinical Feasibility and Efficacy of Using Virtual Surgical Planning in Bimaxillary Orthognathic Surgery Without Intermediate Splint." *The Journal of Craniofacial Surgery*, February. doi:10.1097/SCS.0000000000001530.
57. Liebrechts, J., T. Xi, R. Schreurs, B. van Loon, S. Bergé, and T. Maal. 2016a. "Three-Dimensional Virtual Simulation of Alar Width Changes Following Bimaxillary Osteotomies." *International Journal of Oral and Maxillofacial Surgery*, June. doi:10.1016/j.ijom.2016.05.012.
58. Liebrechts, Jeroen H.F., Maarten Timmermans, Martien J.J. De Koning, Stefaan J. Bergé, and Thomas J.J. Maal. 2014. "Three-Dimensional Facial Simulation in Bilateral Sagittal Split Osteotomy: A Validation Study of 100 Patients." *Journal of Oral and Maxillofacial Surgery*, November. doi:10.1016/j.joms.2014.11.006.
59. Liebrechts, Jeroen, Tong Xi, Maarten Timmermans, Martien de Koning, Stefaan Bergé, Theo Hoppenreijns, and Thomas Maal. 2014. "Accuracy of Three-Dimensional Soft Tissue Simulation in Bimaxillary Osteotomies." *Journal of*

*Cranio-Maxillo-Facial Surgery: Official Publication of the European Association for Cranio-Maxillo-Facial Surgery*, December. doi:10.1016/j.jcms.2014.12.012.

60. Lin, Hsiu-Hsia, Wen-Chung Chiang, Lun-Jou Lo, Sam Sheng-Pin Hsu, Chien-Hsuan Wang, and Shu-Yen Wan. 2013. "Artifact-Resistant Superimposition of Digital Dental Models and Cone-Beam Computed Tomography Images." *Journal of Oral and Maxillofacial Surgery* 71 (11): 1933–47. doi:10.1016/j.joms.2013.06.199.
61. Lin, Hsiu-Hsia, and Lun-Jou Lo. 2015. "Three-Dimensional Computer-Assisted Surgical Simulation and Intraoperative Navigation in Orthognathic Surgery: A Literature Review." *Journal of the Formosan Medical Association = Taiwan Yi Zhi* 114 (4): 300–307. doi:10.1016/j.jfma.2015.01.017.
62. Lisboa, Cinthia de Oliveira, Daniele Masterson, Andréa Fonseca Jardim Motta, and Alexandre Trindade Motta. 2015. "Reliability and Reproducibility of Three-Dimensional Cephalometric Landmarks Using CBCT: A Systematic Review." *Journal of Applied Oral Science* 23 (2): 112–19. doi:10.1590/1678-775720140336.
63. Lou, H. D., Si Chen, Gui Chen, T. M. Xu, and Q. G. Rong. 2012. "Patient-Specific Modeling of Facial Soft Tissue Based on Radial Basis Functions Transformations of a Standard Three-Dimensional Finite Element Model." *Chin Med J* 125 (22): 4066–71.
64. Louis, P J, R B Austin, P D Waite, and C S Mathews. 2001. "Soft Tissue Changes of the Upper Lip Associated with Maxillary Advancement in Obstructive Sleep Apnea Patients." *Journal of Oral and Maxillofacial Surgery: Official Journal of the American Association of Oral and Maxillofacial Surgeons* 59 (2): 151–56. doi:10.1053/joms.2001.20485.
65. Lutz, Jean-Christophe, Stéphane Nicolau, Vincent Agnus, Frédéric Bodin, Astrid Wilk, Catherine Bruant-Rodier, Yves Rémond, and Luc Soler. 2015. "A Novel Navigation System for Maxillary Positioning in Orthognathic Surgery: Preclinical Evaluation." *Journal of Cranio-Maxillofacial Surgery* 43 (9): 1723–30. doi:10.1016/j.jcms.2015.08.001.
66. Marchetti, C., A. Bianchi, L. Muyltermans, M. Di Martino, L. Lancellotti, and A. Sarti. 2011. "Validation of New Soft Tissue Software in Orthognathic Surgery Planning." *International Journal of Oral and Maxillofacial Surgery* 40 (1): 26–32. doi:10.1016/j.ijom.2010.09.004.
67. Marescaux, Jacques, Francesco Rubino, Mara Arenas, Didier Mutter, and Luc Soler. 2004. "Augmented-Reality-Assisted Laparoscopic Adrenalectomy." *JAMA* 292 (18): 2214–15. doi:10.1001/jama.292.18.2214-c.
68. Marşan, G., E. Oztaş, S. V. Kuvat, N. Cura, and U. Emekli. 2009. "Changes in Soft Tissue Profile after Mandibular Setback Surgery in Class III Subjects." *International Journal of Oral and Maxillofacial Surgery* 38 (3): 236–40. doi:10.1016/j.ijom.2008.12.005.

69. Mazza, Edoardo, and Giuseppe Giovanni Barbarino. 2011. "3D Mechanical Modeling of Facial Soft Tissue for Surgery Simulation." *Facial Plastic Surgery Clinics of North America* 19 (4): 623–637, viii. doi:10.1016/j.fsc.2011.07.006.
70. Mazzoni, Simona, Alberto Bianchi, Giulio Schiariti, Giovanni Badiali, and Claudio Marchetti. 2015. "Computer-Aided Design and Computer-Aided Manufacturing Cutting Guides and Customized Titanium Plates Are Useful in Upper Maxilla Waferless Repositioning." *Journal of Oral and Maxillofacial Surgery* 73 (4): 701–7. doi:10.1016/j.joms.2014.10.028.
71. McCance, A. M., J. P. Moss, W. R. Fright, D. R. James, and A. D. Linney. 1992. "A Three Dimensional Analysis of Soft and Hard Tissue Changes Following Bimaxillary Orthognathic Surgery in Skeletal III Patients." *The British Journal of Oral & Maxillofacial Surgery* 30 (5): 305–12.
72. McNeill, R. W., W. R. Proffit, and R. P. White. 1972. "Cephalometric Prediction for Orthodontic Surgery." *The Angle Orthodontist* 42 (2): 154–64. doi:10.1043/0003-3219(1972)042<0154:CPFOS>2.0.CO;2.
73. Mensink, Gertjan, Peter J.J. Gooris, J. Eelco Bergsma, Erik van Hooft, and J.P. Richard van Merkesteyn. 2014. "Influence of BSSO Surgical Technique on Postoperative Inferior Alveolar Nerve Hypoesthesia: A Systematic Review of the Literature." *Journal of Cranio-Maxillofacial Surgery* 42 (6): 976–82. doi:10.1016/j.jcms.2014.01.019.
74. Mischkowski, Robert A, Max J Zinser, Alexander C Kübler, Barbara Krug, Ulrich Seifert, and Joachim E Zöller. 2006. "Application of an Augmented Reality Tool for Maxillary Positioning in Orthognathic Surgery - a Feasibility Study." *Journal of Cranio-Maxillo-Facial Surgery: Official Publication of the European Association for Cranio-Maxillo-Facial Surgery* 34 (8): 478–83. doi:10.1016/j.jcms.2006.07.862.
75. Moerenhout, Bernard A. M. M. L., Frederik Gelaude, Gwen R. J. Swennen, Jan W. Casselman, Jos Van Der Sloten, and Maurice Y. Mommaerts. 2009. "Accuracy and Repeatability of Cone-Beam Computed Tomography (CBCT) Measurements Used in the Determination of Facial Indices in the Laboratory Setup." *Journal of Cranio-Maxillofacial Surgery* 37 (1): 18–23. doi:10.1016/j.jcms.2008.07.006.
76. Mollemans, W, F Schutyser, N Nadjmi, F Maes, and P Suetens. 2007. "Predicting Soft Tissue Deformations for a Maxillofacial Surgery Planning System: From Computational Strategies to a Complete Clinical Validation." *Medical Image Analysis* 11 (3): 282–301. doi:10.1016/j.media.2007.02.003
77. Nadjmi, Nasser, Azita Tehranchi, Niloufar Azami, Bahram Saedi, and Wouter Mollemans. 2013. "Comparison of Soft-Tissue Profiles in Le Fort I Osteotomy Patients with Dolphin and Maxilim Softwares." *American Journal of Orthodontics and Dentofacial Orthopedics* 144 (5): 654–62. doi:10.1016/j.ajodo.2013.06.019.

78. Nam, Ki-Uk, and Jongrak Hong. 2015. "Is Three-Dimensional Soft Tissue Prediction by Software Accurate?" *The Journal of Craniofacial Surgery* 26 (8): e729–733. doi:10.1097/SCS.0000000000002234.
79. Naudi, K.B., R. Benramadan, L. Brocklebank, X. Ju, B. Khambay, and A. Ayoub. 2013. "The Virtual Human Face: Superimposing the Simultaneously Captured 3D Photorealistic Skin Surface of the Face on the Untextured Skin Image of the CBCT Scan." *International Journal of Oral and Maxillofacial Surgery* 42 (3): 393–400. doi:10.1016/j.ijom.2012.10.032.
80. Neumann, P., D. Siebert, A. Schulz, G. Faulkner, M. Krauss, and T. Tolxdorff. 1999. "Using Virtual Reality Techniques in Maxillofacial Surgery Planning." *Virtual Reality* 4 (3): 213–22. doi:10.1007/BF01418157.
81. Nicolau, S., A. Garcia, X. Pennec, L. Soler, and N. Ayache. 2005. "An Augmented Reality System to Guide Radio-Frequency Tumour Ablation." *Computer Animation and Virtual Worlds* 16 (1): 1–10. doi:10.1002/cav.52.
82. Nicolau, Stéphane, Luc Soler, and Jacques Marescaux. 2012. "Augmented Reality." In *Medical Robotics*, Chapter 4:101–39. ISTE and Wiley.
83. Nicolau, Stéphane, Luc Soler, Didier Mutter, and Jacques Marescaux. 2011. "Augmented Reality in Laparoscopic Surgical Oncology." *Surgical Oncology* 20 (3): 189–201. doi:10.1016/j.suronc.2011.07.002.
84. Olszewski, R., F. Zech, G. Cosnard, V. Nicolas, B. Macq, and H. Reyhler. 2007. "Three-Dimensional Computed Tomography Cephalometric Craniofacial Analysis: Experimental Validation in Vitro." *International Journal of Oral and Maxillofacial Surgery* 36 (9): 828–33. doi:10.1016/j.ijom.2007.05.022.
85. Ow, Andrew, and Lim Kwong Cheung. 2009. "Skeletal Stability and Complications of Bilateral Sagittal Split Osteotomies and Mandibular Distraction Osteogenesis: An Evidence-Based Review." *Journal of Oral and Maxillofacial Surgery* 67 (11): 2344–53. doi:10.1016/j.joms.2008.07.003.
86. Oz, U., K. Orhan, and N. Abe. 2011. "Comparison of Linear and Angular Measurements Using Two-Dimensional Conventional Methods and Three-Dimensional Cone Beam CT Images Reconstructed from a Volumetric Rendering Program in Vivo." *Dento Maxillo Facial Radiology* 40 (8): 492–500. doi:10.1259/dmfr/15644321.
87. Pan, Binbin, James J. Xia, Peng Yuan, Jaime Gateno, Horace HS Ip, Qizhen He, Philip KM Lee, Ben Chow, and Xiaobo Zhou. 2012. "Incremental Kernel Ridge Regression for the Prediction of Soft Tissue Deformations." In *International Conference on Medical Image Computing and Computer-Assisted Intervention*, 99–106. Springer. [http://link.springer.com/chapter/10.1007/978-3-642-33415-3\\_13](http://link.springer.com/chapter/10.1007/978-3-642-33415-3_13).

- 
88. Pessaux, Patrick, Michele Diana, Luc Soler, Tullio Piardi, Didier Mutter, and Jacques Marescaux. 2015. "Towards Cybernetic Surgery: Robotic and Augmented Reality-Assisted Liver Segmentectomy." *Langenbeck's Archives of Surgery* 400 (3): 381–85. doi:10.1007/s00423-014-1256-9.
89. Pittayapat, P., N. Limchaichana-Bolstad, G. Willems, and R. Jacobs. 2014. "Three-Dimensional Cephalometric Analysis in Orthodontics: A Systematic Review." *Orthodontics & Craniofacial Research* 17 (2): 69–91. doi:10.1111/ocr.12034.
90. Polido, W. D., E. Ellis, and D. P. Sinn. 1991. "An Assessment of the Predictability of Maxillary Repositioning." *International Journal of Oral and Maxillofacial Surgery* 20 (6): 349–52.
91. Polley, John W., and Alvaro A. Figueroa. 2013. "Orthognathic Positioning System: Intraoperative System to Transfer Virtual Surgical Plan to Operating Field During Orthognathic Surgery." *Journal of Oral and Maxillofacial Surgery* 71 (5): 911–20. doi:10.1016/j.joms.2012.11.004.
92. Proffit, W.R., W.F. Fields, and D.M. Sarver. 2013. "Chapter 6: Orthodontic Diagnostic: The Problem-Oriented Approach." In *Contemporary Orthodontics*, Mosby, Fifth Edition, 150–219.
93. Rangel, Frits A., Thomas J.J. Maal, Stefaan J. Bergé, Olivier J.C. van Vlijmen, Joanneke M. Plooi, Filip Schutyser, and Anne Marie Kuijpers-Jagtman. 2008. "Integration of Digital Dental Casts in 3-Dimensional Facial Photographs." *American Journal of Orthodontics and Dentofacial Orthopedics* 134 (6): 820–26. doi:10.1016/j.ajodo.2007.11.026.
94. Raphaël, Bernard, Jacques Lebeau, and B Morand. 2002. "Ostéotomies Maxillomandibulaires. Introduction et Principes Généraux." In *Techniques Chirurgicales - Chirurgie Plastique Reconstructrice et Esthétique*, Editions Scientifiques et Médicales Elsevier SAS, Paris. Vol. 45–600. Encycl Méd Chir.
95. Richter, M, Patrick Goudot, François Laurent, A Jacquinet, and L Bidaut. 1998. "Chirurgie Correctrice Des Malformations Ou Dysmorphies Maxillomandibulaires: Bases Chirurgicales." In , Editions Scientifiques et Médicales Elsevier SAS, Paris, Stomatologie 22-066-E-10:24 P. Encycl Méd Chir.
96. Rosen, H. M. 1988. "Lip-Nasal Aesthetics Following Le Fort I Osteotomy." *Plastic and Reconstructive Surgery* 81 (2): 171–82.
97. Sarver, David M., Mark W. Johnston, and Victor J. Matukas. 1988. "Video Imaging for Planning and Counseling in Orthognathic Surgery." *Journal of Oral and Maxillofacial Surgery* 46 (11): 939–45.
98. Schendel, S.A. 2015. "Computer Simulation in the Daily Practice of Orthognathic Surgery." *International Journal of Oral and Maxillofacial Surgery* 44 (12): 1451–56. doi:10.1016/j.ijom.2015.05.022.



99. Schouman, Thomas, Philippe Rouch, Benoît Imholz, Jean Fasel, Delphine Courvoisier, and Paolo Scolozzi. 2015. "Accuracy Evaluation of CAD/CAM Generated Splints in Orthognathic Surgery: A Cadaveric Study." *Head & Face Medicine* 11 (1). doi:10.1186/s13005-015-0082-9.
100. Shehab, Mohamed F., Ahmed A. Barakat, Khaled AbdElghany, Yehia Mostafa, and Dale A. Baur. 2013. "A Novel Design of a Computer-Generated Splint for Vertical Repositioning of the Maxilla after Le Fort I Osteotomy." *Oral Surgery, Oral Medicine, Oral Pathology and Oral Radiology* 115 (2): e16–e25. doi:10.1016/j.oooo.2011.09.035.
101. Shim, Byung Kwan, Ho Seong Shin, Seung Min Nam, and Yong Bae Kim. 2013. "Real-Time Navigation-Assisted Orthognathic Surgery." *Journal of Craniofacial Surgery* 24 (1): 221–25. doi:10.1097/SCS.0b013e318267bb76.
102. Sickels, J. E. Van, A. J. Larsen, and R. G. Triplett. 1986. "Predictability of Maxillary Surgery: A Comparison of Internal and External Reference Marks." *Oral Surgery, Oral Medicine, and Oral Pathology* 61 (6): 542–45.
103. Sinclair, P. M., P. Kilpelainen, C. Phillips, R. P. White, L. Rogers, and D. M. Sarver. 1995. "The Accuracy of Video Imaging in Orthognathic Surgery." *American Journal of Orthodontics and Dentofacial Orthopedics: Official Publication of the American Association of Orthodontists, Its Constituent Societies, and the American Board of Orthodontics* 107 (2): 177–85.
104. Smektała, T., M. Jędrzejewski, J. Szyndel, K. Sporniak-Tutak, and R. Olszewski. 2014. "Experimental and Clinical Assessment of Three-Dimensional Cephalometry: A Systematic Review." *Journal of Cranio-Maxillofacial Surgery* 42 (8): 1795–1801. doi:10.1016/j.jcms.2014.06.017.
105. Smith, J. Dempsey, Paul M. Thomas, and William R. Proffit. 2004. "A Comparison of Current Prediction Imaging Programs." *American Journal of Orthodontics and Dentofacial Orthopedics: Official Publication of the American Association of Orthodontists, Its Constituent Societies, and the American Board of Orthodontics* 125 (5): 527–36. doi:10.1016/S0889540604001210.
106. Soler, Luc, Stephane Nicolau, Patrick Pessaux, Didier Mutter, and Jacques Marescaux. 2014. "Real-Time 3D Image Reconstruction Guidance in Liver Resection Surgery." *Hepatobiliary Surgery and Nutrition* 3 (2): 73–81. doi:10.3978/j.issn.2304-3881.2014.02.03.
107. Soncul, Murat, and Mohammad Anwar Bamber. 2004. "Evaluation of Facial Soft Tissue Changes with Optical Surface Scan after Surgical Correction of Class III Deformities." *Journal of Oral and Maxillofacial Surgery: Official Journal of the American Association of Oral and Maxillofacial Surgeons* 62 (11): 1331–40.
108. Stanchina, R., E. Ellis, W. J. Gallo, and R. J. Fonseca. 1988. "A Comparison of Two Measures for Repositioning the Maxilla during Orthognathic Surgery." *The International Journal of Adult Orthodontics and Orthognathic Surgery* 3 (3): 149–54.

- 
109. Stokbro, K., E. Aagaard, P. Torkov, R. B. Bell, and T. Thygesen. 2014a. "Virtual Planning in Orthognathic Surgery." *International Journal of Oral and Maxillofacial Surgery* 43 (8): 957–65. doi:10.1016/j.ijom.2014.03.011.
110. Swennen, G. R. J., M. Y. Mommaerts, J. Abeloos, C. De Clercq, P. Lamoral, N. Neyt, J. Casselman, and F. Schutyser. 2009. "A Cone-Beam CT Based Technique to Augment the 3D Virtual Skull Model with a Detailed Dental Surface." *International Journal of Oral and Maxillofacial Surgery* 38 (1): 48–57. doi:10.1016/j.ijom.2008.11.006.
111. Swennen, Gwen R. J. 2014. "Timing of Three-Dimensional Virtual Treatment Planning of Orthognathic Surgery: A Prospective Single-Surgeon Evaluation on 350 Consecutive Cases." *Oral and Maxillofacial Surgery Clinics of North America* 26 (4): 475–85. doi:10.1016/j.coms.2014.08.001.
112. Swennen, Gwen R. J., Wouter Mollemans, Calix De Clercq, Johan Abeloos, Philippe Lamoral, Frank Lippens, Nathalie Neyt, Jan Casselman, and Filip Schutyser. 2009. "A Cone-Beam Computed Tomography Triple Scan Procedure to Obtain a Three-Dimensional Augmented Virtual Skull Model Appropriate for Orthognathic Surgery Planning." *The Journal of Craniofacial Surgery* 20 (2): 297–307. doi:10.1097/SCS.0b013e3181996803.
113. Swennen, Gwen R. J., Wouter Mollemans, and Filip Schutyser. 2009. "Three-Dimensional Treatment Planning of Orthognathic Surgery in the Era of Virtual Imaging." *Journal of Oral and Maxillofacial Surgery, Accelerated Orthognathic Surgery and Increased Orthodontic Efficiency—A Paradigm Shift: A Special Series Part I*, 67 (10): 2080–92. doi:10.1016/j.joms.2009.06.007.
114. Swennen, Gwen R. J., Maurice Y. Mommaerts, Johan Abeloos, Calix De Clercq, Philippe Lamoral, Nathalie Neyt, Jan Casselman, and Filip Schutyser. 2007. "The Use of a Wax Bite Wafer and a Double Computed Tomography Scan Procedure to Obtain a Three-Dimensional Augmented Virtual Skull Model." *The Journal of Craniofacial Surgery* 18 (3): 533–39. doi:10.1097/scs.0b013e31805343df.
115. Swennen, Gwen R. J., and Filip Schutyser. 2006. "Three-Dimensional Cephalometry: Spiral Multi-Slice vs Cone-Beam Computed Tomography." *American Journal of Orthodontics and Dentofacial Orthopedics* 130 (3): 410–16. doi:10.1016/j.ajodo.2005.11.035.
116. Swennen, Gwen R.J., Wouter Mollemans, and Filip Schutyser. 2009. "Three-Dimensional Treatment Planning of Orthognathic Surgery in the Era of Virtual Imaging." *Journal of Oral and Maxillofacial Surgery* 67 (10): 2080–92. doi:10.1016/j.joms.2009.06.007.
117. Terajima, Masahiko, Yoshihide Furuichi, Yoshimitsu Aoki, Tazuko K. Goto, Kenji Tokumori, and Akihiko Nakasima. 2009. "A 3-Dimensional Method for Analyzing Facial Soft-Tissue Morphology of Patients with Jaw Deformities." *American Journal of Orthodontics and Dentofacial Orthopedics* 135 (6): 715–22. doi:10.1016/j.ajodo.2007.06.017.

118. Terajima, Masahiko, Akihiko Nakasima, Yoshimitsu Aoki, Tazuko K. Goto, Kenji Tokumori, Noriko Mori, and Yoshihiro Hoshino. 2009. "A 3-Dimensional Method for Analyzing the Morphology of Patients with Maxillofacial Deformities." *American Journal of Orthodontics and Dentofacial Orthopedics* 136 (6): 857–67. doi:10.1016/j.ajodo.2008.01.019.
119. Traub, Joerg, Philipp Stefan, Sandro M. Heining, Christian Riquarts, Tobias Sielhorst, Ekkehard Euler, and Nassir Navab. 2006. "Towards a Hybrid Navigation Interface: Comparison of a Slice Based Navigation System with In-Situ Visualization." In *Medical Imaging and Augmented Reality*, edited by Guang-Zhong Yang, TianZi Jiang, Dinggang Shen, Lixu Gu, and Jie Yang, 179–86. Lecture Notes in Computer Science 4091. Springer Berlin Heidelberg. [http://link.springer.com/chapter/10.1007/11812715\\_23](http://link.springer.com/chapter/10.1007/11812715_23).
120. Traub, Joerg, Philipp Stefan, Sandro Michael Heining, Tobias Sielhorst, Christian Riquarts, Ekkehard Euler, and Nassir Navab. 2006. "Hybrid Navigation Interface for Orthopedic and Trauma Surgery." *Medical Image Computing and Computer-Assisted Intervention: MICCAI ... International Conference on Medical Image Computing and Computer-Assisted Intervention* 9 (Pt 1): 373–80.
121. Turley, Patrick K. 2015. "Evolution of Esthetic Considerations in Orthodontics." *American Journal of Orthodontics and Dentofacial Orthopedics* 148 (3): 374–79. doi:10.1016/j.ajodo.2015.06.010.
122. Ullah, R., P.J. Turner, and B.S. Khambay. 2015. "Accuracy of Three-Dimensional Soft Tissue Predictions in Orthognathic Surgery after Le Fort I Advancement Osteotomies." *British Journal of Oral and Maxillofacial Surgery* 53 (2): 153–57. doi:10.1016/j.bjoms.2014.11.001.
123. Verdonck, A., E. Jorissen, C. Carels, and J. Van Thillo. 1993. "The Interaction between Soft Tissues and the Sagittal Development of the Dentition and the Face." *American Journal of Orthodontics and Dentofacial Orthopedics: Official Publication of the American Association of Orthodontists, Its Constituent Societies, and the American Board of Orthodontics* 104 (4): 342–49.
124. Waard, Olivier de, Frank Baan, Luc Verhamme, Hero Breuning, Anne Marie Kuijpers-Jagtman, and Thomas Maal. 2016. "A Novel Method for Fusion of Intra-Oral Scans and Cone-Beam Computed Tomography Scans for Orthognathic Surgery Planning." *Journal of Cranio-Maxillofacial Surgery* 44 (2): 160–66. doi:10.1016/j.jcms.2015.11.017.
125. Walters, H., and D. H. Walters. 1986. "Computerised Planning of Maxillo-Facial Osteotomies: The Program and Its Clinical Applications." *The British Journal of Oral & Maxillofacial Surgery* 24 (3): 178–89.
126. Wang, Shengzheng, and Jie Yang. 2010. "Simulating Cranio-Maxillofacial Surgery Based on Mixed-Element Biomechanical Modelling." *Computer Methods in Biomechanics and Biomedical Engineering* 13 (3): 419–29. doi:10.1080/10255840903317386.

127. Wang, Shengzheng, Jie Yang, and James C. Gee. 2009. "Advances in Collision Detection and Non-Linear Finite Mixed Element Modelling for Improved Soft Tissue Simulation in Craniomaxillofacial Surgical Planning." *The International Journal of Medical Robotics and Computer Assisted Surgery*, n/a–n/a. doi:10.1002/rcs.286.
128. Wang, Xue, Norimasa Okafuji, Yoshiyasu Yoshikawa, Tomoko Uozumi, Guirong Zhang, Jiqiang Li, Jihui Liu, Mingliang Yang, and Yang Zhanb. 2013. "Application of SurgiCase-CMF Software for Patients with Facial Asymmetry in Orthognathic Surgery." *Journal of Hard Tissue Biology* 22 (4): 507–12.
129. Xia, J, N Samman, R W Yeung, D Wang, S G Shen, H H Ip, and H Tideman. 2000. "Computer-Assisted Three-Dimensional Surgical Planing and Simulation. 3D Soft Tissue Planning and Prediction." *International Journal of Oral and Maxillofacial Surgery* 29 (4): 250–58.
130. Xia, J.J., J. Gateno, J.F. Teichgraeber, P. Yuan, K.-C. Chen, J. Li, X. Zhang, Z. Tang, and D.M. Alfi. 2015. "Algorithm for Planning a Double-Jaw Orthognathic Surgery Using a Computer-Aided Surgical Simulation (CASS) Protocol. Part 1: Planning Sequence." *International Journal of Oral and Maxillofacial Surgery* 44 (12): 1431–40. doi:10.1016/j.ijom.2015.06.006.
131. Xia, J.J., J. Gateno, J.F. Teichgraeber, P. Yuan, J. Li, K.-C. Chen, A. Jajoo, M. Nicol, and D.M. Alfi. 2015. "Algorithm for Planning a Double-Jaw Orthognathic Surgery Using a Computer-Aided Surgical Simulation (CASS) Protocol. Part 2: Three-Dimensional Cephalometry." *International Journal of Oral and Maxillofacial Surgery* 44 (12): 1441–50. doi:10.1016/j.ijom.2015.06.007.
132. Xia, James J., Carl V. Phillips, Jaime Gateno, John F. Teichgraeber, Andrew M. Christensen, Michael J. Gliddon, Jeremy J. Lemoine, and Michael A.K. Liebschner. 2006. "Cost-Effectiveness Analysis for Computer-Aided Surgical Simulation in Complex Cranio-Maxillofacial Surgery." *Journal of Oral and Maxillofacial Surgery* 64 (12): 1780–84. doi:10.1016/j.joms.2005.12.072.
133. Xin, Pengfei, Hongbo Yu, Huanchong Cheng, Shunyao Shen, and Steve G. F. Shen. 2013. "Image Fusion in Craniofacial Virtual Reality Modeling Based on CT and 3dMD Photogrammetry." *The Journal of Craniofacial Surgery* 24 (5): 1573–76. doi:10.1097/SCS.0b013e3182688ed7.
134. Zhang, Nan, Shuguang Liu, Zhiai Hu, Jing Hu, Songsong Zhu, and Yunfeng Li. 2016a. "Accuracy of Virtual Surgical Planning in Two-Jaw Orthognathic Surgery: Comparison of Planned and Actual Results." *Oral Surgery, Oral Medicine, Oral Pathology and Oral Radiology* 122 (2): 143–51. doi:10.1016/j.oooo.2016.03.004.

135. Zinser, Max J, Robert A Mischkowski, Timo Dreiseidler, Oliver C Thamm, Daniel Rothamel, and Joachim E Zöller. 2013a. "Computer-Assisted Orthognathic Surgery: Waferless Maxillary Positioning, Versatility, and Accuracy of an Image-Guided Visualisation Display." *The British Journal of Oral & Maxillofacial Surgery* 51 (8): 827–33. doi:10.1016/j.bjoms.2013.06.014.
136. Zizelmann, Christoph, Beat Hammer, Nils-Claudius Gellrich, Rainer Schwestka-Polly, Majeed Rana, and Peter Bucher. 2012. "An Evaluation of Face-Bow Transfer for the Planning of Orthognathic Surgery." *Journal of Oral and Maxillofacial Surgery* 70 (8): 1944–50. doi:10.1016/j.joms.2011.08.025.

## Chapter 3

### Modeling

#### Segmentation: from DICOM data to the virtual model

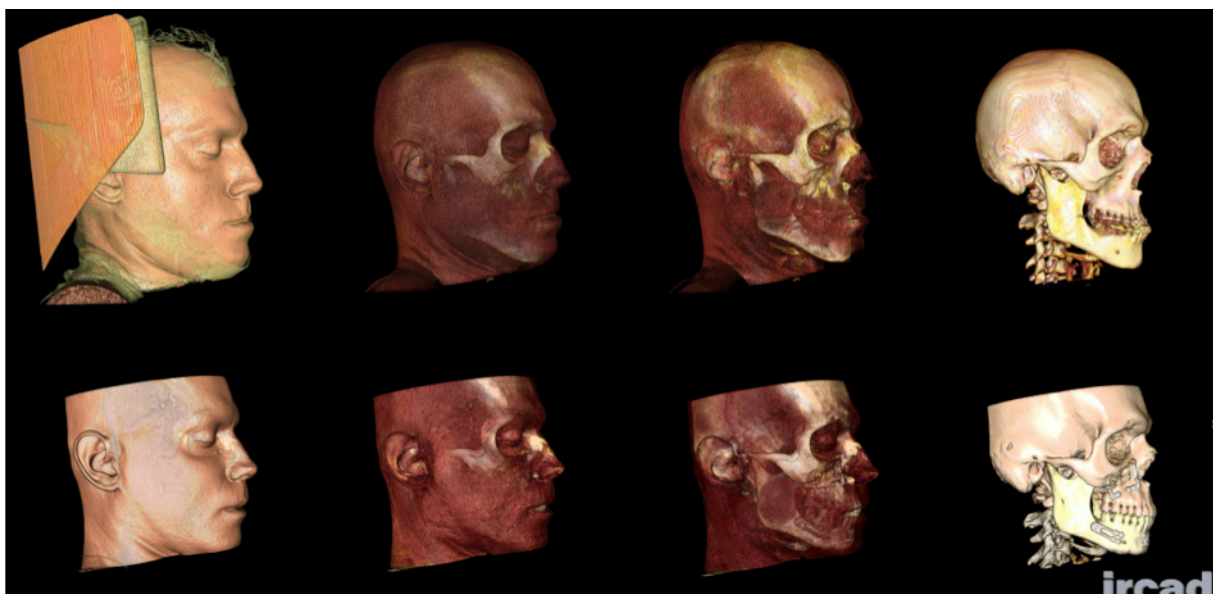
---

*In order to achieve navigation and simulation, it is mandatory to start from the virtual preoperative planning of the surgical procedure. Such planning is ideally conducted on the patient's 3D model.*

*Therefore, in this Chapter, we start describing how raw input data consisting of DICOM images from patients' head CT scans have been computed in order to obtain a 3D virtual model. The virtual craniofacial model was achieved through a **segmentation**<sup>16</sup> step.*

*Our goal was to achieve a fully automated segmentation pipeline for facial bones and skin. In order to identify the issues that would need to be considered for automation, we first conducted an interactive segmentation procedure. This preliminary step helped us consider how metal artifacts were a problem and allowed us to determine the ground truth in terms of processing time. Second, we elaborated an automated segmentation pipeline addressing the issues identified in the previous step and aiming at reducing processing time.*

---



Source: IRCAD® France, courtesy of Pr. Solier

---

<sup>16</sup> In computer vision, image segmentation is the process of partitioning a digital image into multiple segments (sets of pixels, also known as super-pixels). The goal of segmentation is to simplify and/or change the representation of an image into something that is more meaningful and easier to analyze.

This automated segmentation pipeline was based on image processing operators. Then, evaluation of the segmentation procedure was conducted through the comparison of masks from respectively, the interactive segmentation and the automated one: the percentage of voxel difference between these two masks was computed. Additionally, processing time could be compared between the two methods.

Once the virtual model was achieved, we were able to address the planning of the surgical procedure, that is, the motion of facial bone segments and their quantification. Finally, we could consider simulating the alterations of facial soft tissues resulting from the motion of the underlying skeleton. Planning and simulation will be addressed in Chapter 4.

### 3.1. Definition

Image segmentation is the process of partitioning a digital image into multiple regions. The goal of segmentation is to labelize voxels of a medical image into one class among two or more classes, allowing the definition of binary **image masks**, which are a set of connected voxels corresponding to one or more anatomical or pathological structures.

Due to the large amount of data contained within the masks, it is often more convenient to consider the surface of such masks. Indeed, since the surface is locally planar, it can be represented using 3D triangles, consisting of a **3D mesh**, which greatly reduces the amount of data and allows faster processing.

Such a mesh results in a virtual model, which can be used for diagnosis, planning, simulation and navigation purposes.

Our segmentation is based on image processing operators (notably, threshold and mathematical morphological operators,...).

**Annex I** describes the VR-med Software and explains the mathematical bases of the filters we have used.

### 3.2. Structures of interest

In order to achieve orthognathic surgical planning, it is mandatory to obtain 3D modeling of both, bones and skin. Since the surgeon will perform cuts through the maxilla as well as through the mandible, each of these teeth-bearing bones must be extracted independently. Indeed, surgical repositioning of the lower segment of the cut maxilla is of utmost importance to achieve satisfactory smile esthetics, therefore providing a successful outcome.

Segmentation greatly depends on the density of the different tissues considered. As opposed to CBCT (Spin-Neto, Gotfredsen, and Wenzel 2014; Pauwels et al. 2013), multi-slice computed tomography (MSCT) provides a medical image in which the density of the different anatomical and pathological structures have different levels of grey, which can be accurately measured using Hounsfield Units. In Figure 3.1., we briefly remind the average density of tissues in Hounsfield Units (HU), whereas Figure 3.2. details the anatomical components of the tooth and its surrounding structures.

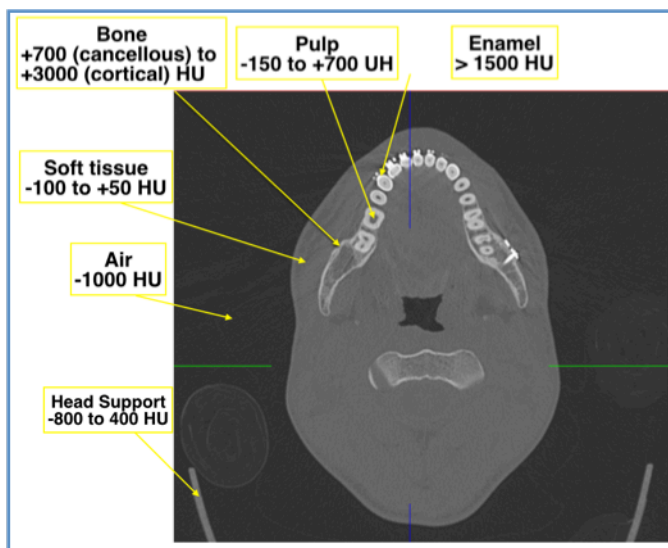


**Figure 3.1:** Average densities in Hounsfield Unit in a Head CT scan.

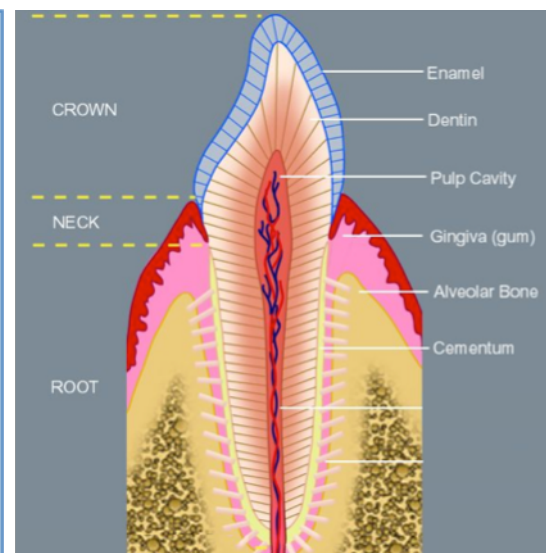


**Figure 3.2:** Sagittal section of a tooth.



### 3.3. Issues

#### 3.3.1. Continuum between the maxilla and the mandible

Dental occlusion<sup>17</sup> is a key point in orthognathic surgery. Indeed, one of the purposes of surgical repositioning of the jaws is to achieve appropriate relations between the upper and the lower teeth. In order to assess dental occlusion prior to surgery, CT scan is usually acquired in biting position (Cf. Figure 3.3). For the same reason, if a postoperative CT scan is intended for evaluation, acquisition shall occur in biting position as well. The resulting contact between the upper and the lower teeth creates a continuum between the maxilla and the mandible. Because of this continuum, the use of a basic segmentation workflow would result in one whole model consisting of the maxilla together with the mandible.



**Figure 3.3:** CT scan acquired in dental occlusion (volume rendering). (Schendel and Jacobson 2009)

#### 3.3.2. Dental metal artifacts

Artifacts are commonly encountered on head CT scans. They are usually referred to as streak artifacts.

On pre-operative CT scans, these artifacts are caused:

- mainly by the metal used for dental restoration in the treatment of cavities
- to a smaller extent, by the metallic appliances fixed to the teeth by the orthodontist. Indeed, orthognathic surgery is often prepared with preoperative orthodontics.

On post-operative CT scans, additional artifacts can be caused by the titanium metal of fixation plates or screws used to stabilize osteotomies (Cf. Figure 3.4).

---

<sup>17</sup> Dental occlusion: biting position resulting in contact between the upper (maxillary) and lower (mandibular) dental arches.

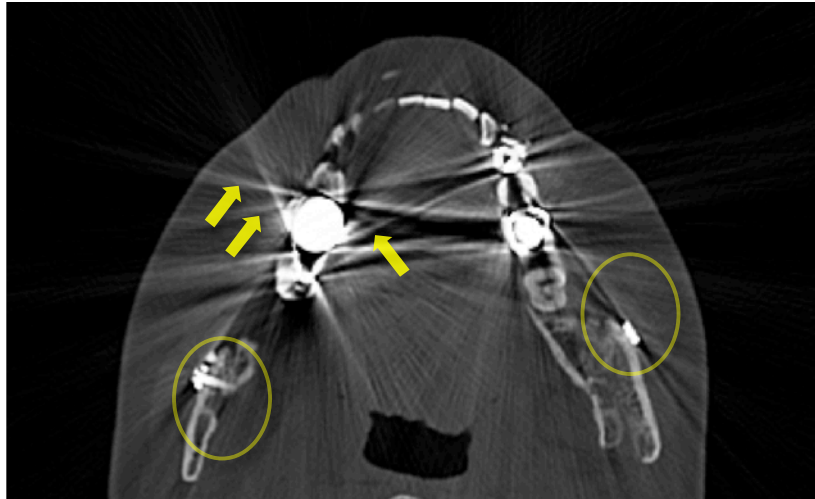


**Figure 3.4: Native postoperative CT scan slice featuring streak metal artifacts** due to both, metallic dental restorations (arrows) and titanium fixation screw (circle).

Dental metal artifacts represent a significant obstacle for 2 reasons:

1. They greatly disturb segmentation between the maxilla and the mandible.
2. They lead to data loss affecting skin segmentation especially in the nose-lip area, crucial in orthognathic surgical assessment. Indeed, the achievement of esthetical harmony in the nose-lip area is one of the primary concerns in orthodontics and orthognathic surgery.

This issue has not been addressed in most of the studies on soft tissue changes using CT scan.

From a physical point of view, metal artifacts are due to

- a poor signal-to-noise ratio in the detector area of the metal shadow
- a higher proportion of the scattered radiation to the primary radiation
- beam hardening (Buzug and Oehler 2007)

Although the mechanism is clear, the standard that is used in the field does not appear as an appropriate procedure to cope with the inconsistencies in the Radon space. Furthermore, the very low signal-to-noise situation cannot be easily improved by an increase of the scanning parameters due to dose considerations (Buzug and Oehler 2007).

Over the recent years, Cone Beam Computed Tomography (CBCT) has become widely available. One great advantage of such technology is the low X-ray dose delivered to the patient, 10 times less than a standard CT scan. However, the metal artifacts affecting the images resulting from a CBCT are more important than the ones affecting standard CT scan (Y. Zhang et al. 2007) and can propagate along 5 cm (Nardi et al. 2015). Additionally, acquisition time ranging from 5 to 40 seconds requires head fixation using a frontal strap and a chin support that can alter facial morphology. In the end, when the maxillo-facial complex requires a large acquisition field, only 20% of CBCT commercialized in 2013 were able to cover a volume of 15 X 21 cm (Nemtoi et al. 2013).

Different solutions meant to reduce dental metal artifacts have been suggested in the literature. The methods initially addressed some fields different from maxillo-facial surgery such as orthopedics for metal hip prosthesis and oncology for radiation treatment planning.

### **Solution using specific algorithms**

**In standard CT scans**, Jung et al. (Jung, Kim, and Baek 2009) remove blurring artifact from metal brackets using the “polygon mesh deleting” function, after Oehler et al. (Buzug and Oehler 2007) claimed that the iterative maximum likelihood reconstruction seemed to be the most promising. Details of structures within the images are therefore much more visible. **The main drawback is the grained appearance of the reconstructed images which are not as smooth as those reconstructed with the filtered back projection.**

Yazdi et al. (Yazdi et al. 2005) note that, when the raw projection data (sinogram) are inspected, no artifact is present. Therefore, their approach of metal artifact reduction is based on interpolation of missing projections. First, the missing projections are automatically detected on the sinogram. Then, an advanced interpolation algorithm is used to fill the missing projections, preserving the structure of adjacent projections. Thus, additional artifacts due to destruction of the boundary structure of other objects in the area of the interpolated projections (normally produced by a simple interpolation) were reduced. According to the authors, this procedure was successfully used in clinical cases.

Yu et al. (Yu et al. 2007) and Zhang et al. (Y. Zhang et al. 2007) use segmentation-based interpolation methods.

Yu et al. use an original mean-shift filtering technique in the computer vision field to improve the accuracy of the metallic object (surgical clip) segmentation. Then forward projection is performed followed by projection interpolation comprising a feedback strategy to adjust the interpolated value. The authors claim their method reduces metal artifacts by 20-40% compared to previously designed segmentation-based methods allowing better assessment of soft and osseous tissues surrounding surgical clips. **The main disadvantage of this procedure is the long computational time needed: 10 minutes to process one 512 X 512 CT slice mostly due to the forward-projection step.** This does not actually represent a bothersome obstacle.

Zhang worked on cone-beam CT (CBCT) images where the impact of metal artifacts in the soft-tissue region is increased because of lower soft-tissue contrast in CBCT. In their approach, two projections need to be selected by the user who needs to annotate the positions of the metal shadows in the beginning. The algorithm described then consists in 3D voxel planning from 2 projections, metal shadow segmentation using threshold method and binary post processing, and, at last, metal shadow replacement with boundary values. Based on Laplacian diffusion method. **The main drawbacks of this procedure is the fact that it is non-automatic and that it has its limits for irregularly-shaped objects, which is often the case in dental amalgams.**

Wang et al. (Wang, Frei, and Vannier 2000) worked on the speed problem that burdened Yu's method. Wang used a fast iterative algorithm adapted from the row-action/ordered subset (expectation maximization) formula, known as slow. In each iteration of this algorithm, both reprojection from an intermediate image and back projection from discrepancy data were performed. **It proved faster and the residual effects of metal objects were much less disturbing than the results seen with filtered backprojection. Nevertheless, image noise and edge rings still increase with the number of iterations.**

All 4 above methods were assessed on physical phantoms and real patient datasets and, nonetheless, proved efficient.

### **Solution using MRI**

Goto et al (Goto et al. 2007) proved in their publication that the accuracy of 3D vite MRI sequence, determined from the data of 2 volunteers, was high compared to direct measurements on dry mandibles (in vitro study), which is important in orthognathic surgery. This accuracy also appeared similar to the one using CT. Most interestingly, they pointed out that there was no incidence of artifacts that severely disturbed MRI image interpretation in the volunteers although they had restorations on their teeth.

Other benefits were the absence of X-radiation hazard and the almost same required time for data processing as for CT.

**The limitations were that MRI segmentation for bones is subjective and needed to be performed manually because of the difficulty to segment some parts. Also, their study was performed on dry mandible only, which is less complex than a skull for orthognathic surgery.**

Ramos-Cabrer et al. (Ramos-Cabrer et al. 2004) studied MRI regarding artifacts caused by hip prosthesis. **Images completely free of distortions were obtained but only in vitro using a very specific MRI method called single-point imaging (SPI).** Conventional MRI methods, which require several milliseconds for signal preparation and acquisition, fail to image solid materials because NMR signal from these systems vanishes before it can be completely recorded (ultra-short T2 values). In SPI, this problem is solved by acquiring only one point of the free induction decay as soon as possible following excitation. This way of signal acquisition makes SPI immune to image distortions arising from changes in signal intensity that occur during acquisition of multiple k-space points.

**Unfortunately, there are many limitations that prevent the authors' promising result from being implemented in vivo, among which: gradient amplitudes must be large in SPI but have to be limited in vivo for safety reasons; heating of the metallic material is an undesired consequence of the fast succession of powerful radiofrequency pulses and hazardous in vivo; intolerable acoustic noise produced by fast switching of large gradients.**

In conclusion, the use of MRI for data assessment that could appear at first as an easy way to solve artifacts does not prove as obvious as expected regarding literature. Additionally, if MRI is particularly suited for the study of soft tissues, its resolution is much poorer towards bone compared to CT. Therefore, bone segmentation using MRI would be less accurate than using CT.

### **Solution using surface imaging**

Surface imaging consists in laser scanning and 3D surface scanning.

These procedures can be used for acquisition of the skin, and/or the surface of the dental arches, providing artifact-free images.

Some authors (Nkenke et al. 2004) therefore thought of the fusion of CT data and optical 3D surface images. The CT data of the dental arches were replaced by optical 3D images acquired either through intra-oral scanning or laser scanning of the patient's dental casts, therefore suppressing the dental metal artifacts (Wiranto et al. 2013; De Luca Canto et al. 2015; Vogel et al. 2015). These optical dental data are then merged using registration with the patient's skull CT scan

Surface imaging can also achieve skin surface acquisition.

**Laser scanning** is widely used for industrial purposes and considered *in vitro* as the gold standard (Kusnoto and Evans 2002). However, it is not quite appropriate for medical imaging, since acquisition time can reach from 8 to 20 seconds (Kau et al. 2007; Djordjevic et al. 2014) which can lead to artifacts caused by breathing motion.

Three-dimensional surface scanning is based on different types of technology, such as **structured light** and passive (Catherwood et al. 2011) (Plooij et al. 2009), active or hybrid **stereophotogrammetry**<sup>18</sup> (Tzou et al. 2014). When a light beam of structured light is projected onto an object, its deformation can be analyzed, therefore allowing the object surface to be recorded. **Acquisition is then sequential, which can compromise recording accuracy (Lane and Harrell 2008).**

Active stereophotogrammetry is quite similar. Cameras are used to record the deformation of a pattern projected onto the face allowing a 3D image to be generated thanks to a triangulation procedure. The advantage of such procedure is the independence from ambient lighting (Lane and Harrell 2008). On the contrary, passive stereophotogrammetry merges several high-resolution 2D photographs without any projected pattern. The fusion process between the different captures is then more complex and requires perfectly controlled lighting conditions (Lane and Harrell 2008).

At last, hybrid stereophotogrammetry uses both, the active and passive technologies in order to provide improved volumetric and texture accuracy.

---

<sup>18</sup> Stereophotogrammetry: The construction of a three-dimensional model based on the positions of recognizable points or landmarks in several different photographs.

All these methods provide high reliability and accuracy lower than 1 millimeter (Weinberg et al. 2006; Hoevenaren et al. 2015; Oliveira-Santos et al. 2013; Catherwood et al. 2011). Additionally, the patient is not exposed to X-rays thanks to these technologies.

**The main drawbacks of such technologies are the long calibration time, the artifacts induced by hairiness (Metzger et al. 2013), and the difficult recording of the sub nasal and mental areas (Heike et al. 2010) (requiring head extension during acquisition).**

If multi-modal imaging thus seems to reach a consensus in 2017, it still requires time-consuming fusion steps and interactive operations. Therefore, most of the companies providing orthognathic simulation software propose additional acquisition of patient-specific dental casts. The resulting image is free of any artifacts and can be merged to the patient's cranio-facial CT scan (Swennen et al. 2007; Swennen et al. 2009; Rangel et al. 2008; Joda and Gallucci 2015). However, the accuracy of the data fusion process is itself significantly reduced due to the metal artifacts.

In conclusion, we became aware that dental metal artifacts is a priority issue to be addressed at the time of cranio-facial modeling. We have therefore developed a dedicated segmentation pipeline allowing to partially overcome the limit of the artifacts.

## 3.4. Computation

### 3.4.1. Tools

#### 3.4.1.1. Hardware

The hardware we used was based on an Intel Core i7 @ 2.5 GHz, 8 Go of RAM running on Windows 7 Professional (64 bits version). On this version of Windows, a maximum of 2 Go could be dedicated per application, therefore restricting processing time.

#### 3.4.1.2. VR-Med Software (Cf. ANNEX I)

We used the VR-Med software v.1.3.2 based on the Framework for Software Processing Line (Fw4spl<sup>19</sup>). This framework has been developed by IRCAD for fast and easy creation of applications, mainly in the medical imaging field. It includes various features such as 2D and 3D digital image processing, visualization, augmented reality and medical interaction simulation. It runs on many different environments (Windows, linux, OSX), is written in C++, and features rapid interface design using XML files. It is freely available under open source license (LGPL). This software has been developed for processing of CT scans of thorax and abdomen. Nevertheless, it is perfectly suited for the analysis of head CT scans. VR-Med has some specific features that we will describe. We detail its specifications and features in Annex I.

### 3.4.2. Process

As mentioned in the introduction of this chapter, we decided to first conduct an interactive segmentation in order to both, identify the issues that would need to be considered for automation (e.g. artifacts), and to determine the ground truth in terms of processing time.

In a second step, we elaborated an automated segmentation pipeline addressing the issues identified in the first step and aiming at reducing processing time.

#### 3.4.2.1. Interactive bone segmentation

Our purpose here is to use **basic tools** in order to obtain distinct segmentations of the maxilla, on one hand, and the mandible, on the other hand.

The image source consists of Dicom data from patient CT scan . After conducting an initial anonymization step of patient data for ethical purposes, we create a new workflow, which combines various operators (Cf. Figure 3.5). The mathematical bases of the operators we used are described in Annex I.

---

<sup>19</sup>fw4spl: FrameWork for Software Processing Line - <https://github.com/fw4spl-org/fw4spl>

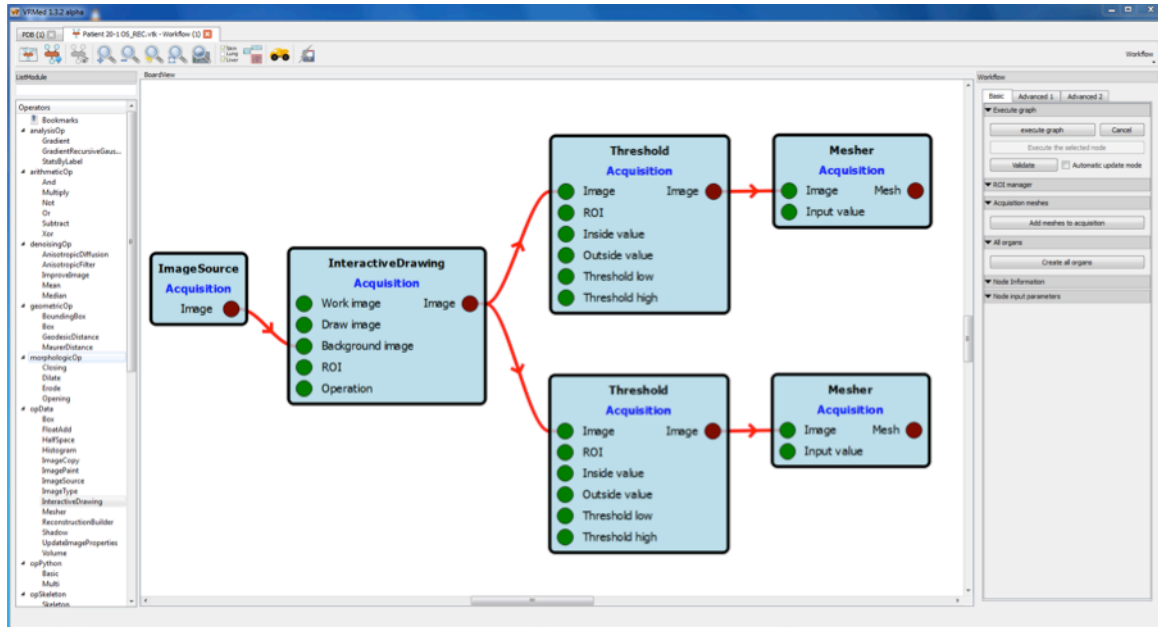


**Figure 3.5: Interactive bone segmentation pipeline designed on VR-Med (Cf. Annex I).** The operators are represented as light blue boxes and their chaining illustrated by red connectors.

### a. Interactive segmentation tools (min/max propagation, eraser, paint bucket 3D)

This toolkit provides a **min/max propagation tool**. Using it by clicking on one point of the cortical bone of either the maxilla or the mandible resulted in propagation to the whole facial skeleton, since upper and lower teeth are usually in contact (Cf. Figures 3.3, 3.6 and 3.7).



**Figure 3.6: Propagation (in red) affecting the whole facial skeleton**, since the skull and the mandible are linked due to contact between the upper and lower teeth, especially in this case where dental metal artifacts affect the image.



Obviously, if CT Scan were acquired on a patient in opened mouth position, the seed would have only propagated to the adjacent structure, i.e.: either the maxilla or the mandible.

In order to separate maxilla from mandible, we then used the standard **eraser**, with a thickness of 2.00 (pixels). In order for this operation to be successful, it was crucial to meticulously erase any pixel, which connected the maxilla to the mandible. Therefore, to be complete, it was mandatory to conduct this operation in the axial, frontal and sagittal axes, especially in cases of important overlapping between upper and lower teeth, and/or when dental metal artifacts were numerous.

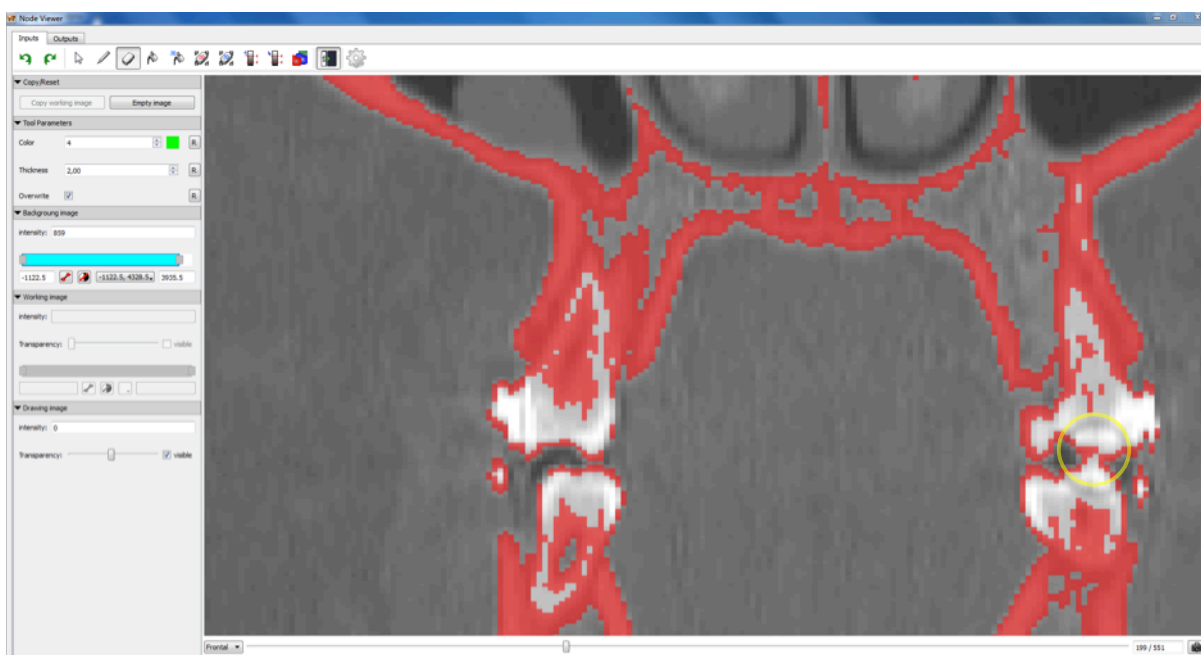


**Figure 3.7:** Detail of the contact between the upper and lower teeth due to one voxel (yellow circle) causing propagation (in red) from the skull to the mandible.

Once the maxilla is separated from the mandible, we use the **paint bucket 3D** in order to apply a different color (i.e.: a scalar label) mask to the mandible (Cf. Figure 3.8).

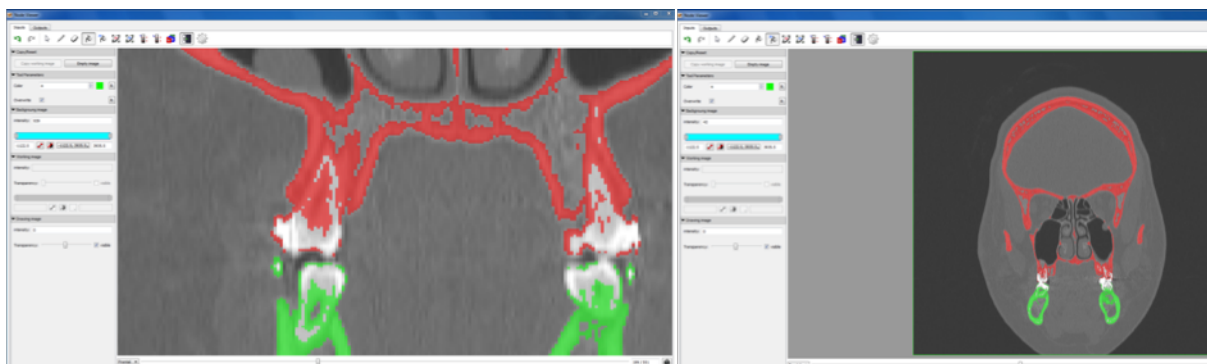


**Figure 3.8:** Detail of the separation between the upper and lower teeth achieved using eraser and the different color mask (green) applied to the mandible using paint bucket 3D (left: zoom, right: whole skull).

### b. Threshold

Two such photometric operators are applied to the output from the interactive drawing in order to facilitate selection either of the maxilla or the mandible thanks to the different scalar labels (Cf. Figure 3.9).

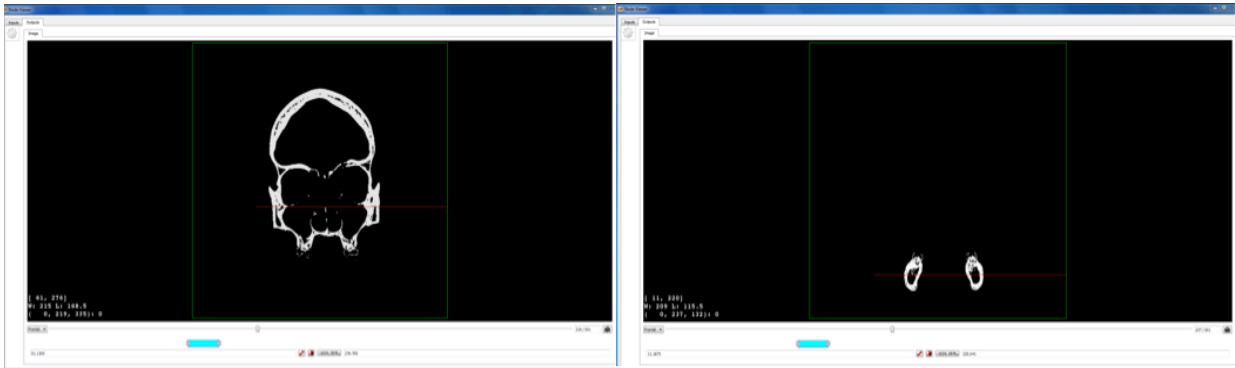


**Figure 3.9:** Result of two different thresholds applied to respectively the upper facial skeleton (left) and the mandible (right). (Cf. Pipeline Fig. 3.5 p. 11)

### c. Mesher

Among the different meshers available from the toolkit, we used a marching cube algorithm-based **mesher (opVTK)**, since this mesher provided more processing stability (Cf. Figure 3.10).

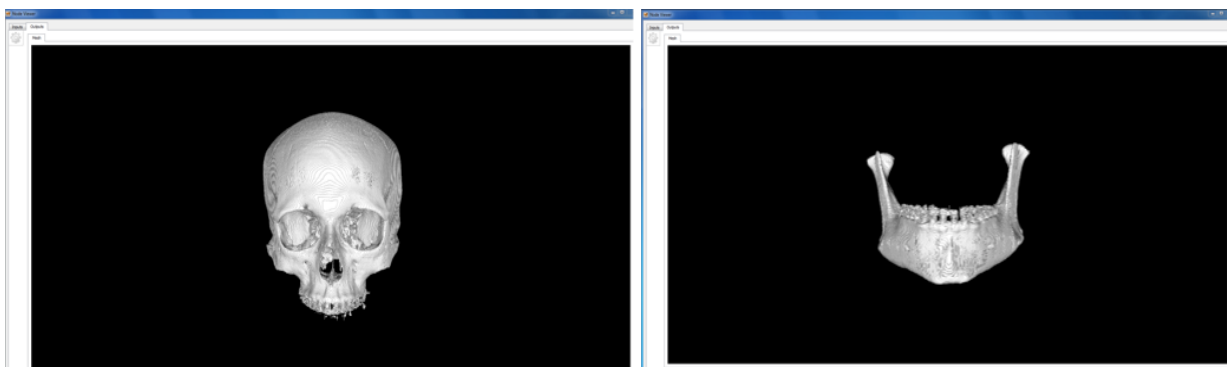


**Figure 3.10:** The two distinct virtual models of respectively the upper facial skeleton (left) and the mandible (right) resulting from op vtk mesher. (Cf. Pipeline Fig. 3.5 p. 11)

We end up with two distinct models of the facial bones (**Cf. Figure 3.10**) suitable as input data for virtual planning, which is the next step.

It must be underlined that this interactive workflow was quite fastidious and time consuming (2 hours/case), especially when images contained many dental artifacts. By the end of this procedure, only bone segmentation was achieved. Since our ultimate goal is to achieve simulation and planning of the facial outcome, skin segmentation is another required input data. Skin segmentation has been conducted in a further step.

All segmented cases are saved using a dedicated format (.mwz13 fwXML compressed archive), which allowed saving the whole workflow and not only the final result. Using “export medical workspace” function therefore generated a backup for every single operation.

We repeated this interactive bone segmentation procedure of the maxilla and the mandible in 8 CT scans as shown in **Table 3.1**. Everyone of the 4 patients patient was anonymized using a number. Preoperative CT scans were distinguished from postoperative ones using the mark “-1” for preoperative and “-2” for postoperative. Most acquisitions were conducted on a patient in biting position (i.e.: mouth closed), yet, 2 patients (i.e.: 4 CT scans) had their mouth opened.

<b>Anonymized patient réf.</b>	<b>Segmentation</b> Maxilla= MX Mandible=MD	<b>Voxel size (mm)</b>	<b>Artifacts</b>	<b>Mouth</b>	<b>Segmentation total duration (min)</b>
<b>12-1</b>	<b>MD</b>	0.53 x 0.53 x 0.30	Many	closed	130
	<b>MX</b>	0.53 x 0.53 x 0.30	Many		
<b>12-2</b>	<b>MD</b>	0.48 x 0.48 x 0.30	∅	closed	121
	<b>MX</b>	0.48 x 0.48 x 0.30	∅		
<b>18-1</b>	<b>MD</b>	0.43 x 0.43 x 0.30	Few	opened	105
	<b>MX</b>	0.43 x 0.43 x 0.30	Few		
<b>18-2</b>	<b>MD</b>	0.41 x 0.41 x 0.30	∅	opened	97
	<b>MX</b>	0.41 x 0.41 x 0.30	∅		
<b>20-1</b>	<b>MD</b>	0.49 x 0.49 x 1	∅	closed	103
	<b>MX</b>	0.49 x 0.49 x 1	∅		
<b>20-2</b>	<b>MD</b>	0.45 x 0.45 x 0.30	∅	closed	90
	<b>MX</b>	0.45 x 0.45 x 0.30	∅		
<b>33-1</b>	<b>MD</b>	0.49 x 0.49 x 1	Few	closed	115
	<b>MX</b>	0.49 x 0.49 x 1	Few		
<b>33-2</b>	<b>MD</b>	0.44 x 0.44 x 0.30	Many	closed	117
	<b>MX</b>	0.44 x 0.44 x 0.31	Many		

**Table 3.1:** Interactive segmentation duration of anonymized patients (number 12 to 33) preoperative (-1) or postoperative (-2) CT Scans.

Our results showed that there is a learning curve, since the last segmentations were achieved in less time than the first ones. It is also obvious that when CT Scans are acquired in an opened mouth position, interactive segmentation is much shorter. In the end, the average interactive segmentation time was at 110 minutes, which is not acceptable for a surgeon in routine practice. Therefore, we aimed at developing an automated segmentation pipeline in order to reduce processing time and compared it to the interactive procedure.

### 3.4.2.2. Automated bone and skin segmentation pipeline

Our purpose was to provide distinct segmentations of the bones (maxilla, on the one hand, and mandible, on the other hand), and skin, using a fully automated global pipeline.

We were able to achieve such a result using a unique semi-automated algorithm with few interactive entries. This pipeline was built as a combination of mathematical morphological operators applied to the image source. For didactical reasons, we have parted the pipeline in different blocks and steps as depicted in **figure 3.11**. There are two large blocks, bone and teeth segmentation on the one hand, and skin segmentation on the other. In the following sections, we will detail the steps used in every block and explain the output of every operator. For clarity purposes, in each corresponding section, we will reprint **figure 3.11** as a small footer scheme, using a red rectangle to outline the area of the pipeline on which we were focusing.

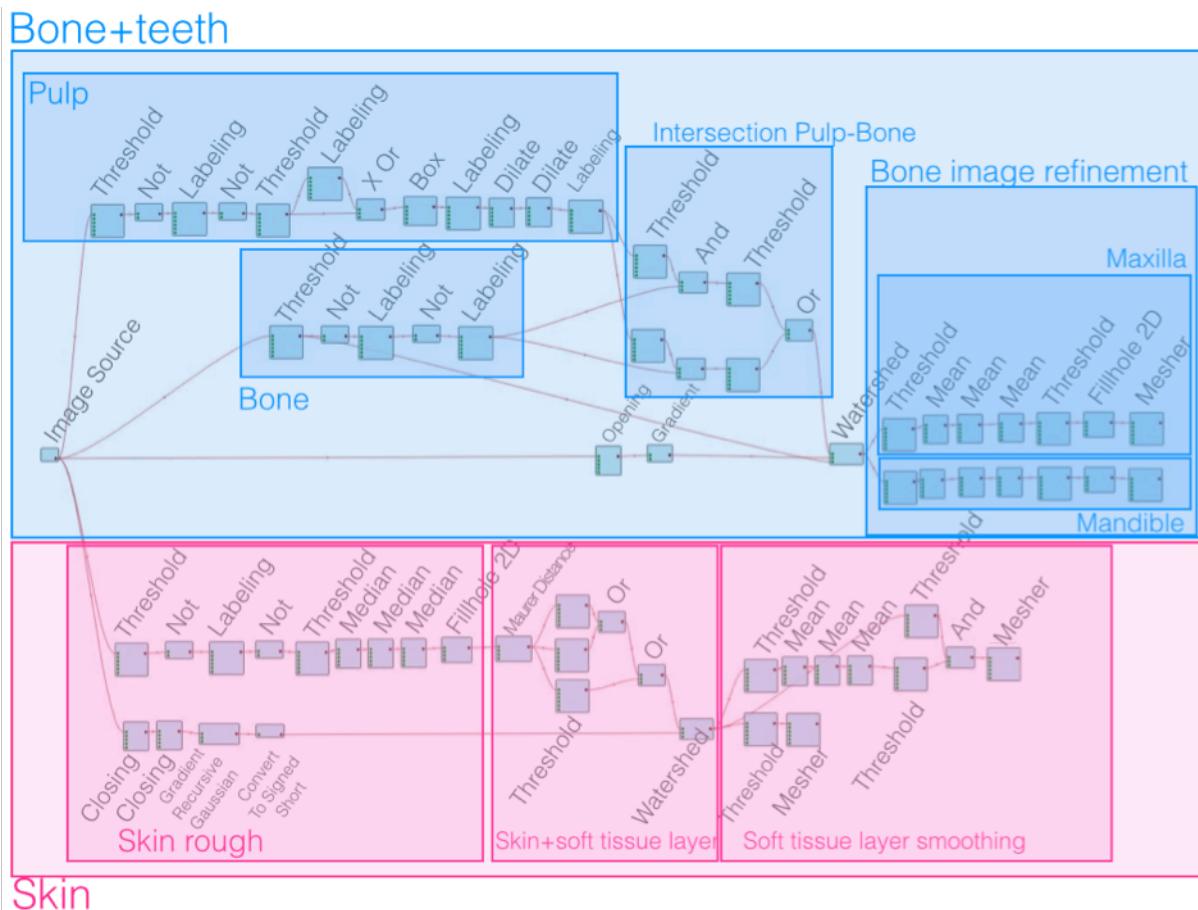


**Figure 3.11: Scheme illustrating our global semi-automated segmentation pipeline and its partition.** The operators are identified by small light blue rectangles with their names above and are connected to one another with red lines. The large bone + teeth segmentation block (blue) is parted into 4 steps and 2 substeps. The large Skin segmentation block (pink) is parted into 3 steps.

### 3.4.2.2.1. Bone and teeth segmentation method

In order to achieve bone and teeth segmentation, we proceeded in 4 steps, outlined with a red rectangle in Figure 3.12:

- Step 1: Rough **segmentation of the bones** without distinction between the upper and the lower teeth. (Cf. rectangle “Bone” in Figure 3.12)
- Step 2: **Segmentation of the pulp** since the pulp from the upper teeth can easily be discriminated from the one of the lower teeth. (Cf. rectangle “Pulp” in Figure 3.12)
- Step 3: **Intersection bone-pulp** is then conducted in order to discriminate the maxilla from the mandible. (Cf. rectangle “Intersection Pulp-Bone” in Figure 3.12)
- Step 4: **Image refinement** of respectively the maxilla and the mandible (2 substeps). (Cf. rectangle “Bone image refinement” in Figure 3.12)

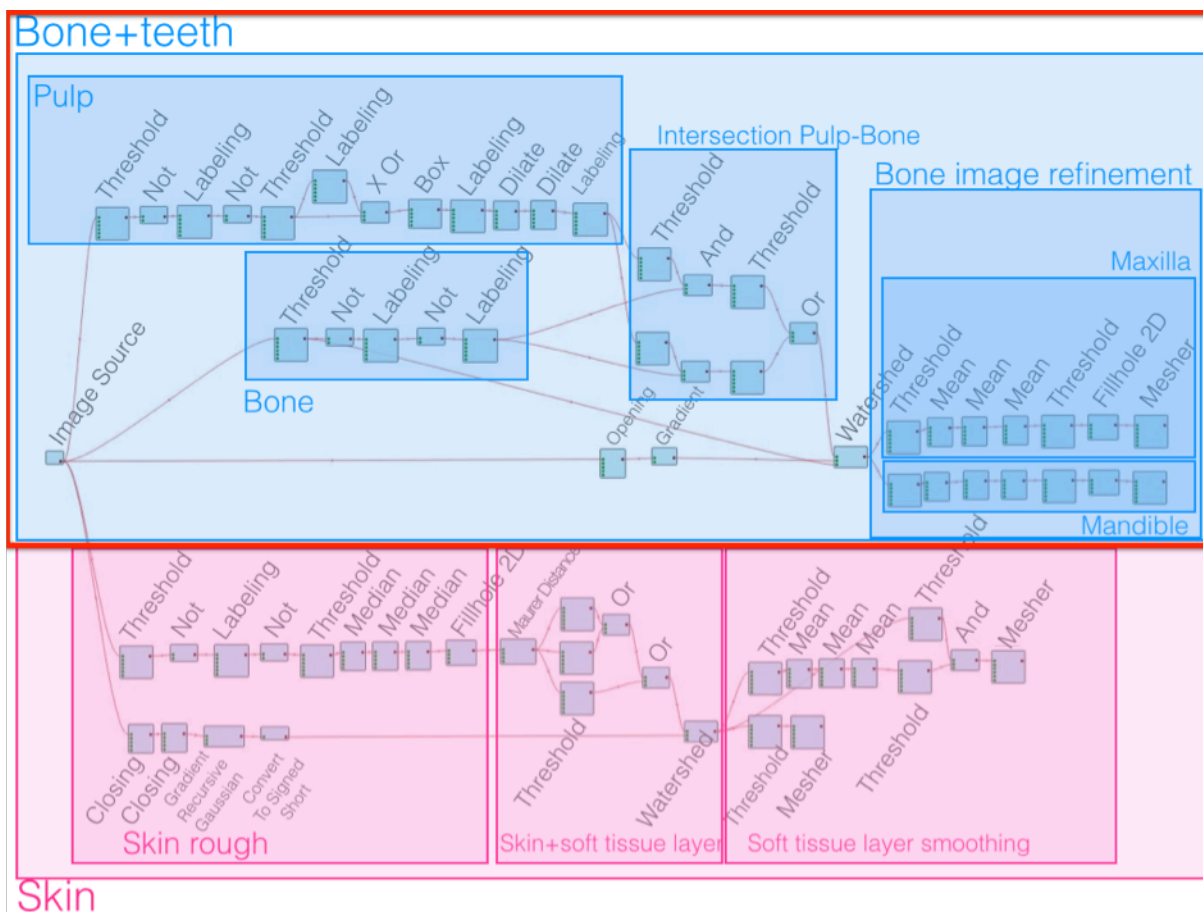


**Figure 3.12:** Footer scheme illustrating the part of the global pipeline addressing bone and teeth segmentation (red rectangle) through 4 steps.

In the following sections, we will detail the combination of operators used to build every step of the bone + teeth segmentation pipeline. **Figure 3.13** summarizes this part of the pipeline using output images from some key steps.

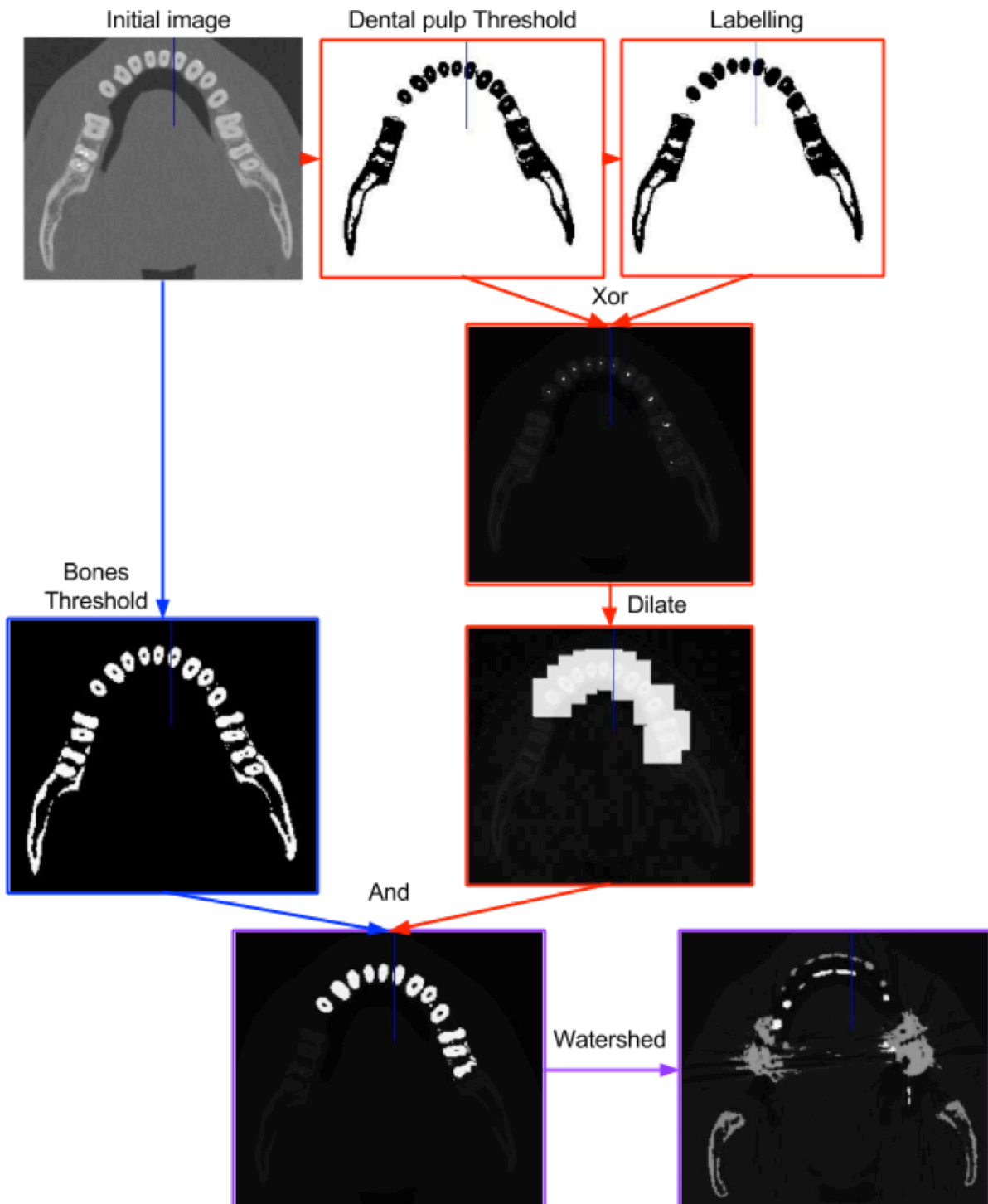


**Figure 3.13:** Scheme summarizing the bone and teeth part of the segmentation pipeline through output images of key steps.

## a. Bone segmentation

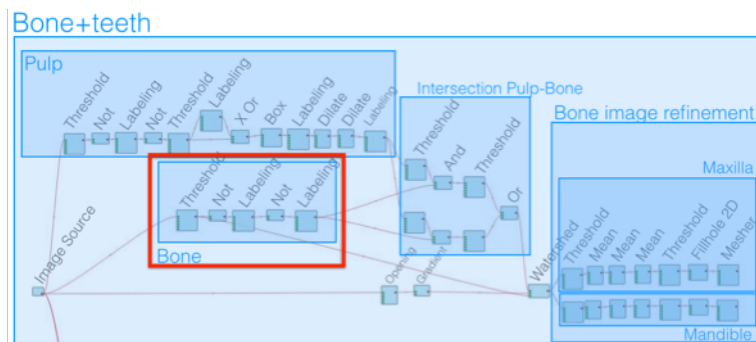


**Figure 3.14:** Footer scheme illustrating the part of the bone + teeth segmentation pipeline addressing bone segmentation (red rectangle).

In this first step, our purpose was to achieve rough segmentation of the bones without distinction between the upper and the lower teeth, yet considering two pitfalls:

- metal dental artifacts which greatly disturb data as already addressed in chapter 3.3.2.
- vicinity between the skull and a head support. Indeed, in order to prevent artifacts due to movements during acquisition, the patient is placed in a head support. However, the head support has similar levels of grey as the facial bones. Until then, since segmentation was interactive, the head support was not an obstacle. It could become one at the time of automation.

At this stage, we needed to keep in mind that the ultimate aim of bone segmentation was to provide 2 distinct masks, respectively one for the maxilla and one for the mandible. Yet, we have previously emphasized that these bones were connected through the upper and lower teeth (Cf. Chap. 3.3.1, 3.4.2.1 and Figure 3.7). Therefore, in order to separate maxilla from mandible as accurately as possible, we searched for intact areas (no artifacts) that could help us identify automatically the teeth. We came up with the idea of using **dental pulp** (Cf. Figures 3.1 et 3.2) for two empirical reasons found in most of the cases:

1. the pulp can be extracted from artifact-free healthy teeth.
2. the pulp from the upper teeth is always distinguishable from the one of lower teeth.

The initial substep of the bone segmentation pipeline aimed at keeping the dense structures only. Therefore, we first apply a **“Threshold”** to the original image. The threshold parameters needed to be chosen considering the density of artifacts in order for the output image not to be affected by artifacts. Indeed, the pulp and the dark part of the artifacts have similar levels of grey. Therefore, we chose as threshold value, the level of grey of the **pulp-dentin junction** (Cf. Figure 3.15), which is quite higher than the one of the pulp.

After analyzing 10 images, we found that 1615 was a suitable value to characterize the pulp-dentin junction. Of course, it would have been elegant to compute a dedicated algorithm that would automatically pick this threshold value as the level of grey of the pulp-dentin junction. Unfortunately, the version of the software we used did not allow replacing a value by a dedicated algorithm that would compute it. Therefore, we proceeded empirically in our automated pipeline and set the threshold parameters to keep only the voxels which density was higher than 1615. Such parameters were Threshold low= 1615 Threshold high= 4095, Inside value= 255, Outside value=0.

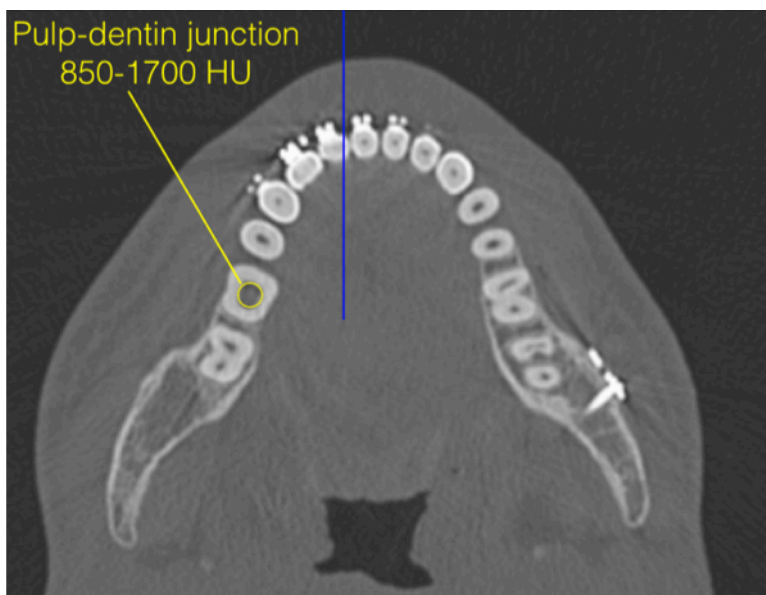


**Figure 3.15:** Radiological anatomy and density (Hounsfield Units = HU) of the pulp-dentin junction in a Head CT scan.

As depicted in Figure 3.16, the image resulting from such a threshold yet featured the bones but also some non-dense internal components described as “holes”. The image also showed parts of the head support.

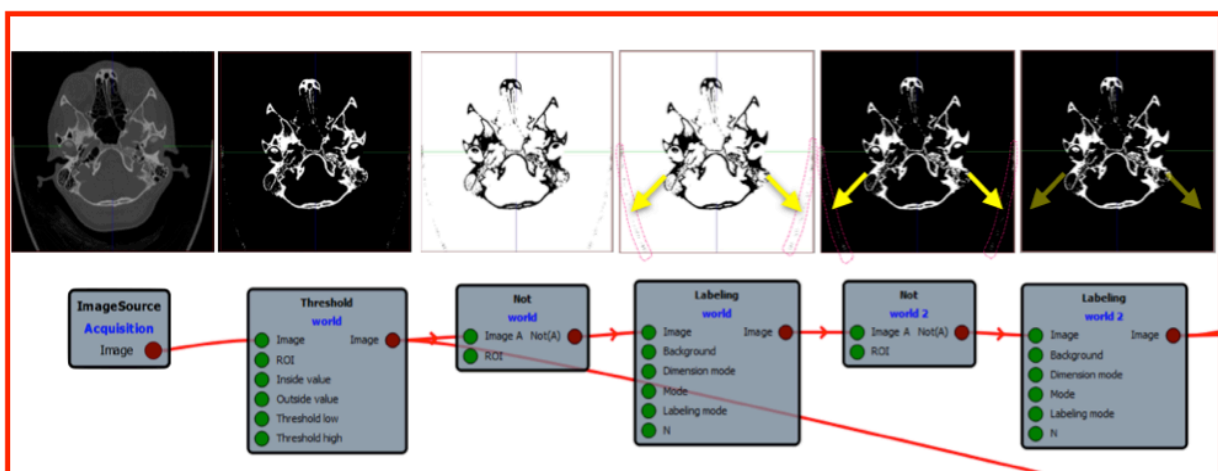


**Figure 3.16:** Detail of bone segmentation pipeline (Abstract from global pipeline –Cf. Figure 3.14) Yellow arrows point at the head support that gets removed in the last image after labeling.



In order to obtain filled bones, we had to suppress the non-dense small internal components (holes). Since labeling is only able to extract the connected component different from 0 (i.e.: white pixels), we decided to work in the dual space<sup>20</sup> by applying a **not** operator followed by a **labeling**. We therefore kept the largest connected component (soft tissue and air) and removed all non-dense internal structures, such as the pulp and parts of cancellous bone. Another **not** was applied in order to retrieve the filled bones, then, a final **labeling** was applied to remove the head support.

### b. Pulp segmentation

In the previous section, we have achieved rough segmentation of the bones without distinction between the upper and the lower teeth. We emphasized why the pulp from the upper teeth could easily be discriminated from the one of the lower teeth. In this section, we describe how we processed pulp segmentation (Cf. Figures 3.17 and 3.18).

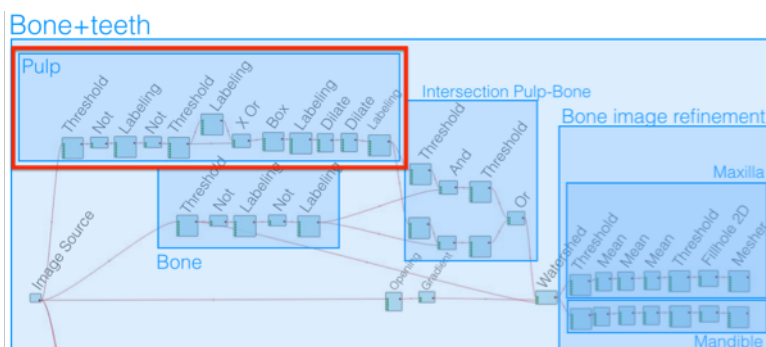


**Figure 3.17:** Footer scheme illustrating the part of the bone + teeth segmentation pipeline addressing pulp segmentation (red rectangle).

Through interactive measurements, we concluded that the pulp consisted in small, not very dense structures. Therefore, in order to extract them, we first remove dense and large structures (bones), then, we remove the air. For technical reasons, it was easier to work on the dual space.

Thus, the first five operators of our pulp segmentation pipeline are dedicated to suppressing all dense areas, which are bones and teeth. The hypotheses we have used are:

- structures are dense, i.e.  $> 1615$  HU
- structures are large.
- we seek segmenting either 1 or 2 two structures (skull and/or mandible) depending on whether the skull and the mandible are in contact (i.e. the patient has his mouth closed during acquisition).

<sup>20</sup> Dual space: in mathematics, any vector space  $V$  has a corresponding dual (vector) space consisting of all linear functionals on  $V$  together with a naturally induced linear structure. In our case, working in the dual space results in converting all black densities into white and *vice versa*.

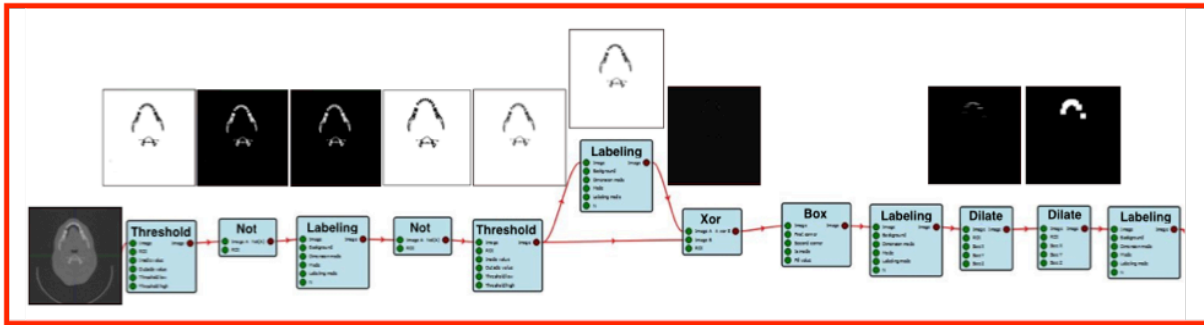


Figure 3.18: Detail of Pulp segmentation pipeline (Abstract from global pipeline Cf. Fig. 3.17).

The purpose of every operator appearing in Figure 3.18 is detailed chronologically:

1. We use the **“Threshold”** operator to transform the image from 256 levels of gray to black and white image, having the dark shades in white and the light shades in black (Cf. Figure 3.19). Image analysis showed that the pulp had a level of gray at 1615.  
The parameters were: Threshold low=0; Threshold high=1615; Inside value=255; Outside value = 0  
I.e.: anything between 0 (black) and 1615 (air, soft tissues and pulp) is converted into value 255 (white), the rest gets value 0.

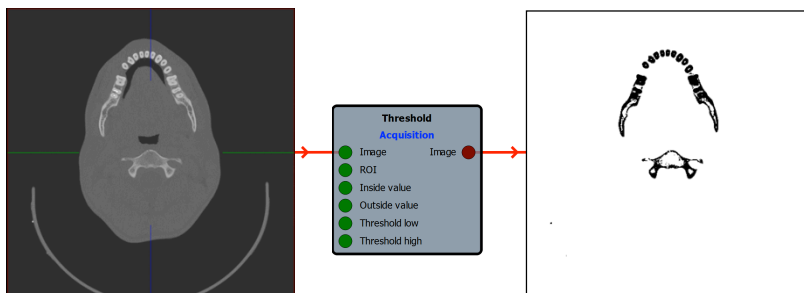


Figure 3.19: Output (right) resulting from a **threshold** operator applied to the image source (left).

2. We then applied a **“NOT”** operator in order to keep dense structures only (Cf. Figure 3.20). This results in inverting black and white. Of course, we could have set the threshold in order to obtain this result from the start, but we decided to proceed this way for didactical purposes.

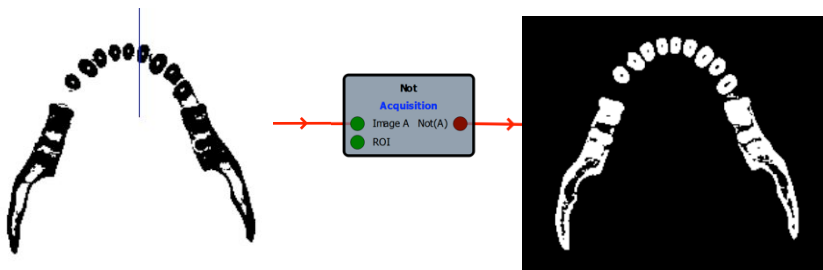


Figure 3.20: Output (right) resulting from a **NOT** operator.

3. We then used a **“Labeling”** to select only the two largest white regions (the two main connected components) (In the case where there is only one white region, we would extract the whole skull. If there are 2 regions, i.e.: when mouth is opened, we would extract respectively the maxilla and mandible) (Cf. Figure 3.21).

4. A second “**NOT**” operator was applied in order for our structure of interest (the pulp) to get back to value=1, as 1 is the input value which was to be considered in further operators. Output results in only two values, 0 or 1 (Cf. Figure 3.21).

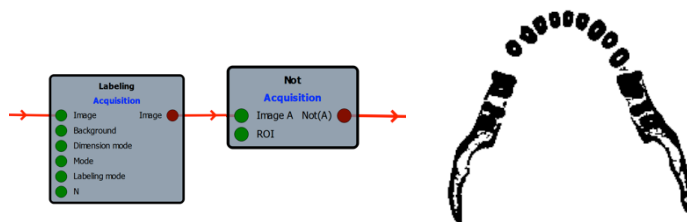


Figure 3.21: Output resulting from **Labeling** (step 3) and **NOT** (step 4) operators.

5. A “**Threshold**” was used in order to spread the binary values from 0 to 1 to 0 to 255, since 255 will be the input value in the next operator (Cf. Figure 3.22).  
In the current image, we have, in white, the pulp and the air.
6. A “**Labeling**” kept the larger set of voxels and therefore eliminates the pulp area. It results in keeping the air only (Cf. Figure 3.22).
7. After, a “**Xor**” operator was applied to images resulting respectively from step 5 and from step 6. Such “**Xor**” operator kept the differences between these two images and results in displaying the pulp only as well as small neighboring areas. Indeed, the 2 previous labeling operations have kept the larger connected component. Due to the “**Xor**” operation, only the smaller connected components are kept (Cf. Figure 3.22).

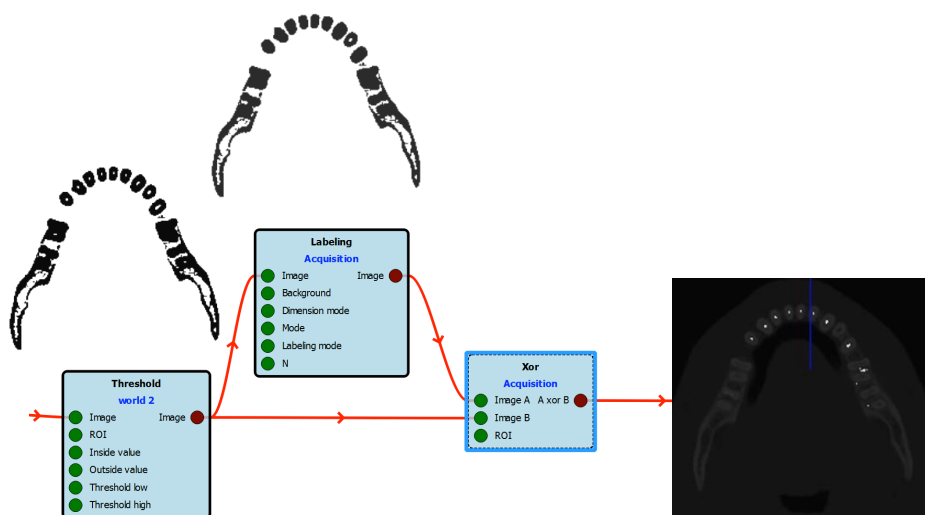


Figure 3.22: Output (right) resulting from **Threshold** (step 5), **Labeling** (step 6) and **XOR** (step 7) operators. Please note that, on the right image, we have placed a mask of the native image for localization purposes.

8. “**BOX**” is an operator, which allows defining a box-shape region of interest in order to keep the voxels in this area. It is applied in order to focus on the dental area containing the pulp and to neglect the other small voxels that have the same

level of gray and are not to be considered for our purpose. Typically, these areas consisted in the cancellous bone in the skull (parietal, temporal, frontal bones). These parameters need to be set interactively choosing the slices on the image.

Remark: we did not apply this Box operator from the beginning of the pipeline, since it would have changed our initial hypothesis. Indeed, our hypothesis was that the skull and the air were the largest connected component. After a Box operator, that would not be true anymore.

In the next section, we used as hypothesis that the pulp area are rather close to one another. We therefore, use pseudo-connectivity algorithms.

9. **“Labeling”**: In the resulting image, we set to 100, the number of largest connected components to be kept in order to only consider the pulp of the teeth and not the other small voxels that may be left within the box. Indeed, value 100 was based on the number of teeth (32) considering an additional safety margin.
10. **“Dilate”**: in order to determine a teeth-bearing area based on the pulp, we try and connect the pulp areas between one another. We use 2D Dilatation within every axial plane in order to dilate the pulp so that the lower teeth are connected with each other, as well as the upper teeth. This operator is **applied twice (successively)** for 2 reasons:
  - a. in plane x, then plane y in order to keep the separation between the upper and the lower dental arches (which would be compromised if considering the z-axis)
  - b. for processing speed concerns.
11. **“Labeling”**: We label the two main components extracted (in terms of number of voxels) in order to give a different label to the two remaining sets representing the upper and lower teeth (Cf. Figure 3.23).

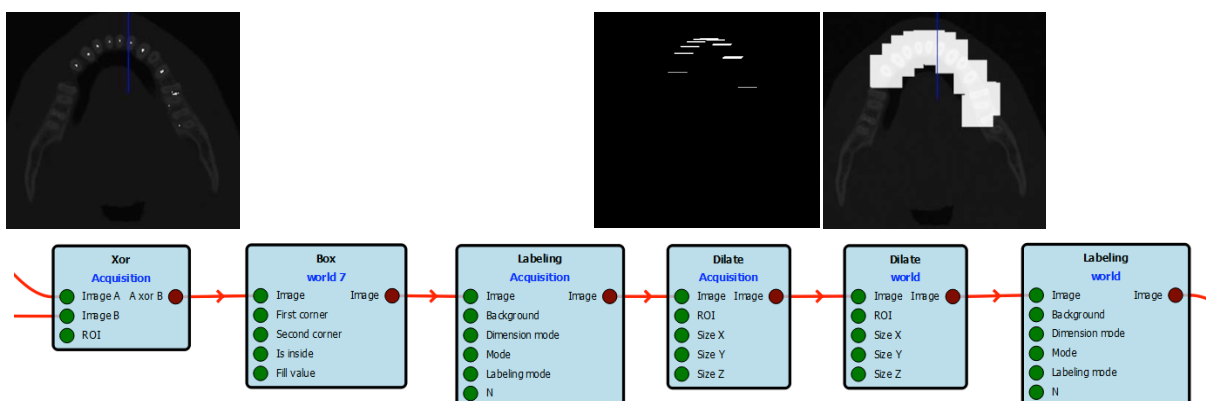


**Figure 3.23:** Output (right) resulting from **Box** (step 8), **Labeling** (step 9), **Dilate** (step 10) and **Labeling** (step 11) operators.

### c. Intersection pulp-bone

Our ultimate purpose was to merge the upper teeth to the maxilla, on the one hand, and to merge the lower teeth to the mandible, on the other hand. To do so, we needed to first determine the intersection between pulp and bone, which actually resulted in differentiating the upper teeth from the lower ones, based on pulp discrimination. Therefore, we generated, two parallel pipelines (Cf. Figures 3.24 and 3.25). We used as input image, the one resulting from the above step 11 (“Labeling”). This image contained two sets of voxels matching the position of the upper and lower teeth. Every set of voxel had a different label (label 1 for the largest set of voxel (maxilla) and label 2 for the other one (mandible)).

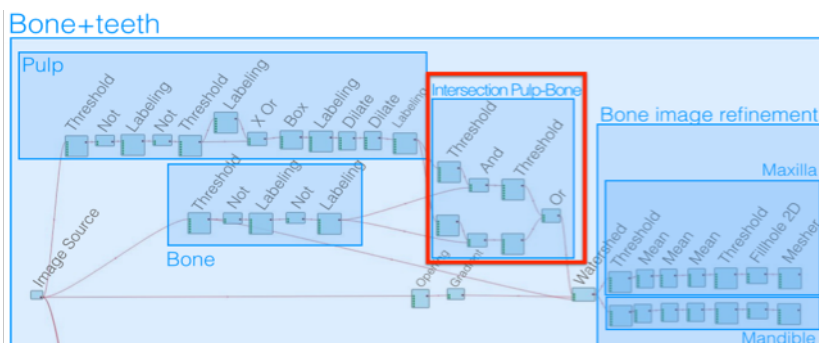


**Figure 3.24:** Footer scheme illustrating the part of the bone + teeth segmentation pipeline addressing intersection pulp-bone (red rectangle).

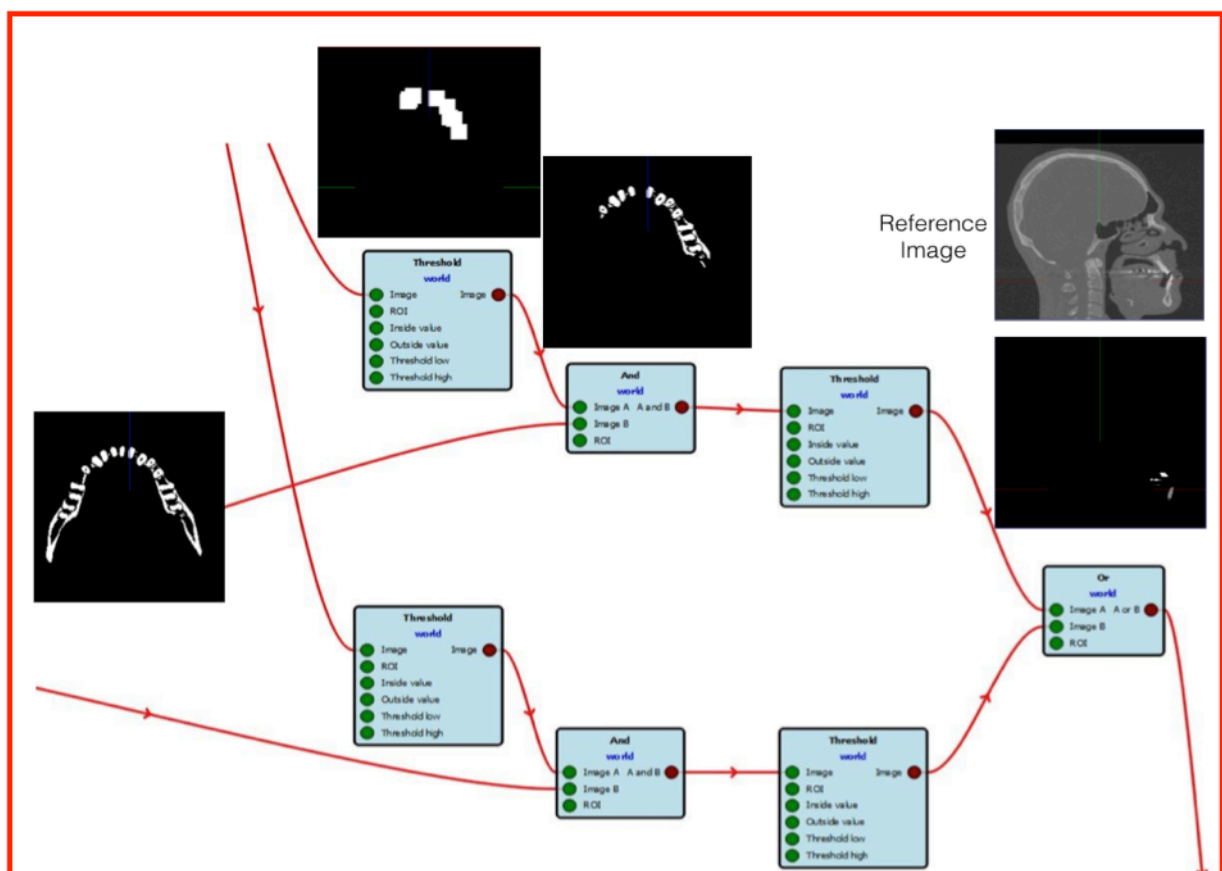


**Figure 3.25:** Detail of Intersection Bone-pulp segmentation pipeline (Abstract from global pipeline –Cf. Fig 3.12 ). Note that the reference image has been recalled above the last image resulting from the “Or” operator for localization purposes i.e.: to demonstrate that only the upper or the lower teeth are extracted at the end of this computational step.)

For every label (i.e.: either label 1 for the largest set of voxel or label 2 for the other one), we applied a **“Threshold”** in order to isolate the related connected component. Then, we computed its intersection with the bone segmentation thanks to an **“And”** operator. We merged these two intersections with the **“Or”** operator. The resulting image consisted of two seeds that were further used in a **“Watershed”** as we will describe in the next section. In this **“Watershed”**, the bones were set as **“Region of interest”** (the watershed only propagates in the region of interest) to propagate our teeth labels to the bones. Both, the maxilla and the mandible were present in the same image but each of them had a different label.

#### d. Bone image refinement

On the basis of already segmented bones, our purpose was yet to process a smooth and realistic mask of the maxilla, on the one hand and of the mandible, on the other. There again, we used two identical parallel pipelines.

In every pipeline, we use a **“Threshold”** to separate the mandible (threshold value=2) from the maxilla (threshold value = 1), since every bone was provided a different value thanks to a previous labeling operator (Cf. "c."). An optional **“Interactive drawing”** operator can be inserted in order to remove the remaining artifacts. The contour was smoothed using a series of three **“Mean operators”**, everyone along an axis (respectively, x, y, z). The parameters we used were respectively, Size X=10, Size Y=0, Size Z=0; Size X=0, Size Y=10, Size Z=0; Size X=0, Size Y=0, Size Z=10. The resulting image was a gradual image in which contours might be blurred. In order to retrieve contours close to the original image, we applied a **“Threshold”** (Threshold low=128; Threshold high=255; Inside value=255; Outside value = 0). In order to avoid the management of internal surface, we used a **“Fillhole 2D”** operator in the axial planes. Finally, once the mask was ready, we used the **“Mesher”** to get the bone mesh (Cf. Figures 3.26, 3.27, and 3.28).

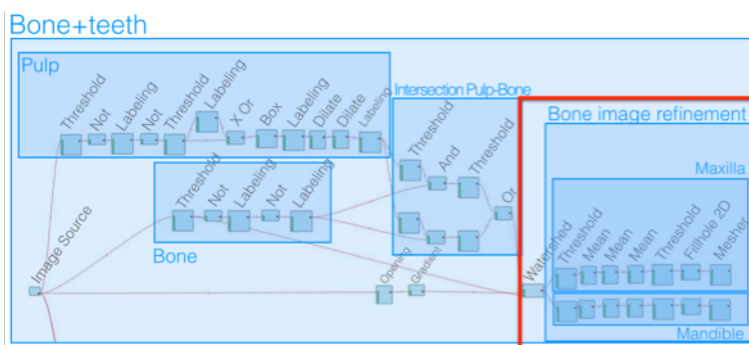


**Figure 3.26:** Footer scheme illustrating the part of the bone + teeth segmentation pipeline addressing bone image refinement (red rectangle).



Figure 3.27: Detail of Bone image refinement segmentation pipeline (Abstract from global pipeline –Cf. Fig 3.12).

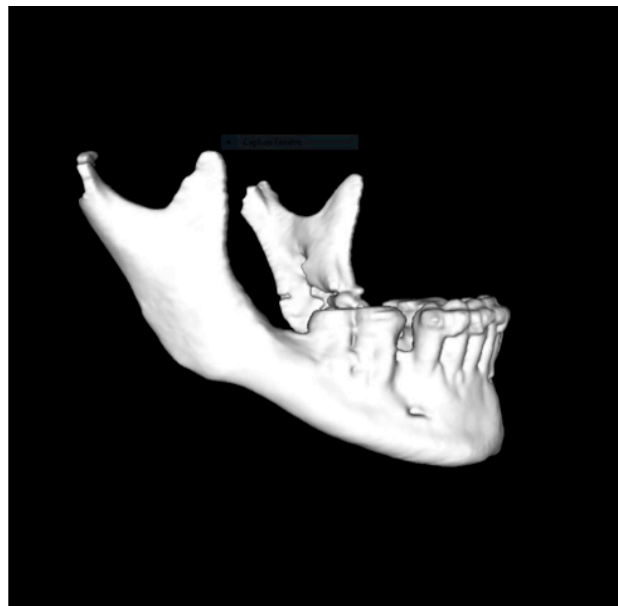
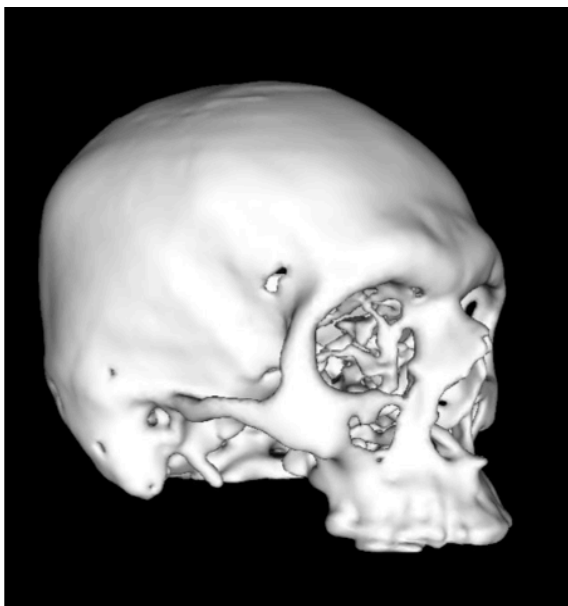
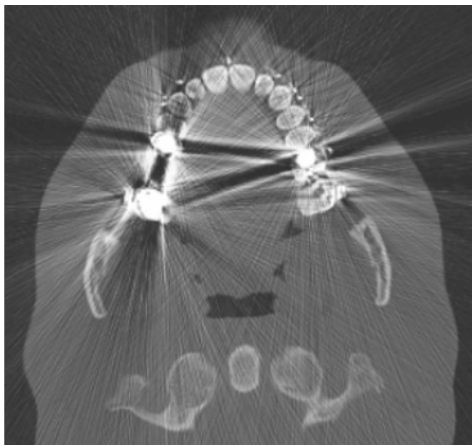


Figure 3.28: Surface meshes of respectively the maxilla+skull (left) and the mandible (right) resulting from the bone+teeth segmentation pipeline.

### 3.4.2.2. Skin and soft tissue layer segmentation method

Skin segmentation is a critical issue when it comes to simulation of the postoperative facial outcome. As we will detail in chapter 4, we needed to develop a soft tissue deformation method. Such a method will require as input data the surface meshes of patient's upper skull including the maxilla, the mandible, the skin surface and the soft tissue layer surface. After having described how the semi-automated segmentation pipeline provided surface meshes of facial bones, we will, in the next section, explain how we conducted segmentation of both, the complete facial soft tissue in its whole thickness (**soft tissue layer**), and the **skin surface**. We could think that the skin surface could be easily processed from the soft tissue segmentation through a single "Fillhole 2D". Actually, as explained in chapter 3.3.2, the problem with skin segmentation was mainly the artifacts creating holes in the skin shade of grey (Cf. Figure 3.29), so that we could not just use a single threshold to segment the skin.



**Figure 3.29:** Native postoperative CT scan slice featuring streak metal artifacts due to metallic dental restorations.

In order to achieve segmentation of both, the skin surface and the soft tissue layer considering disturbances due to metal dental artifacts, we proceeded in 3 steps, outlined with a red rectangle in Figure 3.30:

- **Step 1: Rough segmentation of the skin.** This step consisted of two parallel pipelines (Cf. rectangle "Skin rough" in Figure 3.32 and 3.33).
  - The bottom line aimed at extracting a smooth **contour gradient** even though artifacts could distort the image. From this smooth contour gradient, we would compute the final contour. This contour would be refined through a "**Watershed**" at the end of step 2. The "**Watershed**" required seeds.
  - The top line aimed at helping defining the seeds thanks to the **extraction of the rough skin outline**. The rough skin outline was extracted using different operators to address the artifacts.



- Step 2: **Skin and soft tissue layer segmentation**. Consisted in actually defining the seeds thanks to the extraction of the rough skin outline (top line of step 1) conducted using distance transform. A watershed was applied using the seeds, on the one hand, and the contour gradient map, on the other hand (bottom line of step 1) (Cf. rectangle “Skin + soft tissue layer” in Figure 3.32 and 3.33).
- Step 3: **Soft tissue layer smoothing**. Consisted in extracting the skin outer surface (bottom line) and smoothing the internal surface of the soft tissue layer (top line) (Cf. rectangle “Soft tissue layer smoothing” in Figure 3.32 and 3.33).

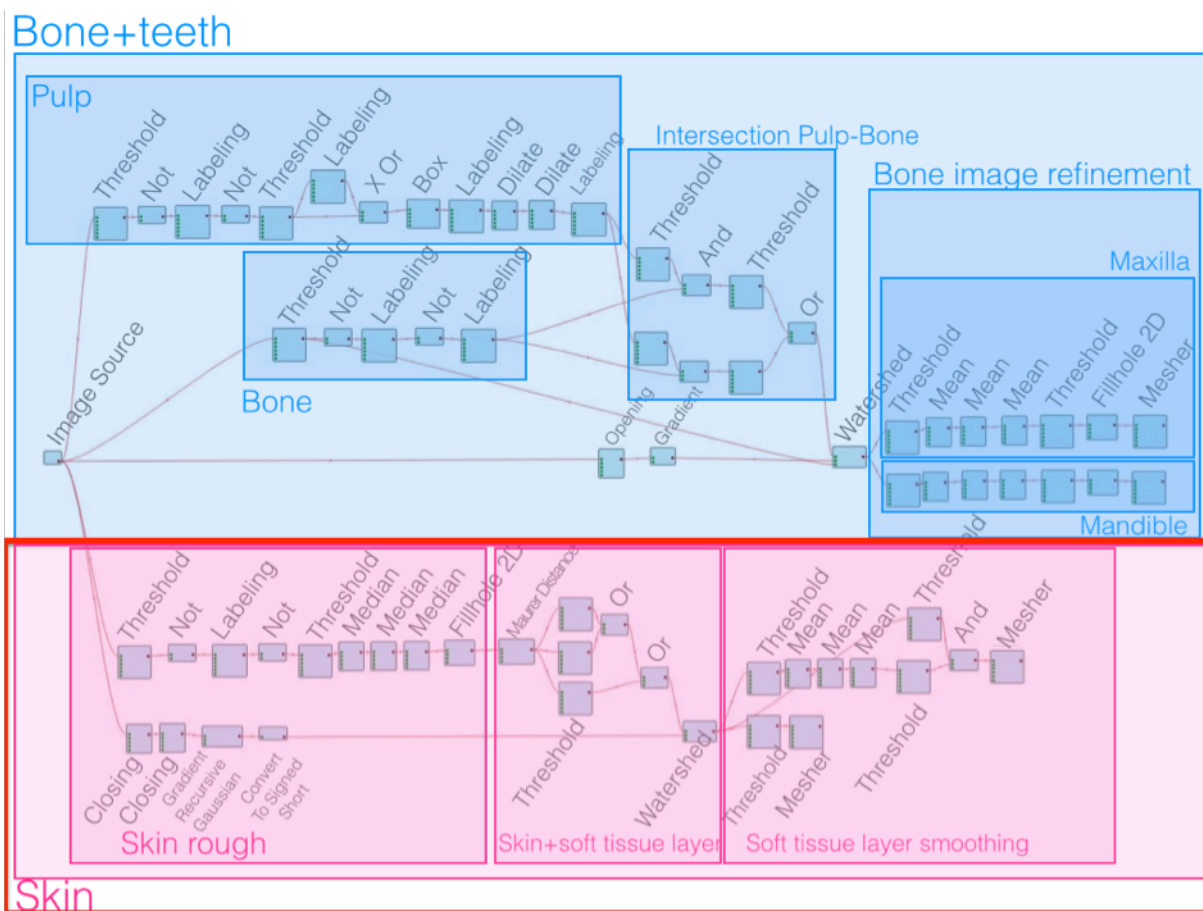


**Figure 3.30:** Footer scheme illustrating the part of the global pipeline addressing skin segmentation (red rectangle) through 3 steps.

In the following sections, we will detail the combination of operators used to build every step of the bone + teeth segmentation pipeline. Figure 3.31 summarizes this part of the pipeline using output images from some key steps.

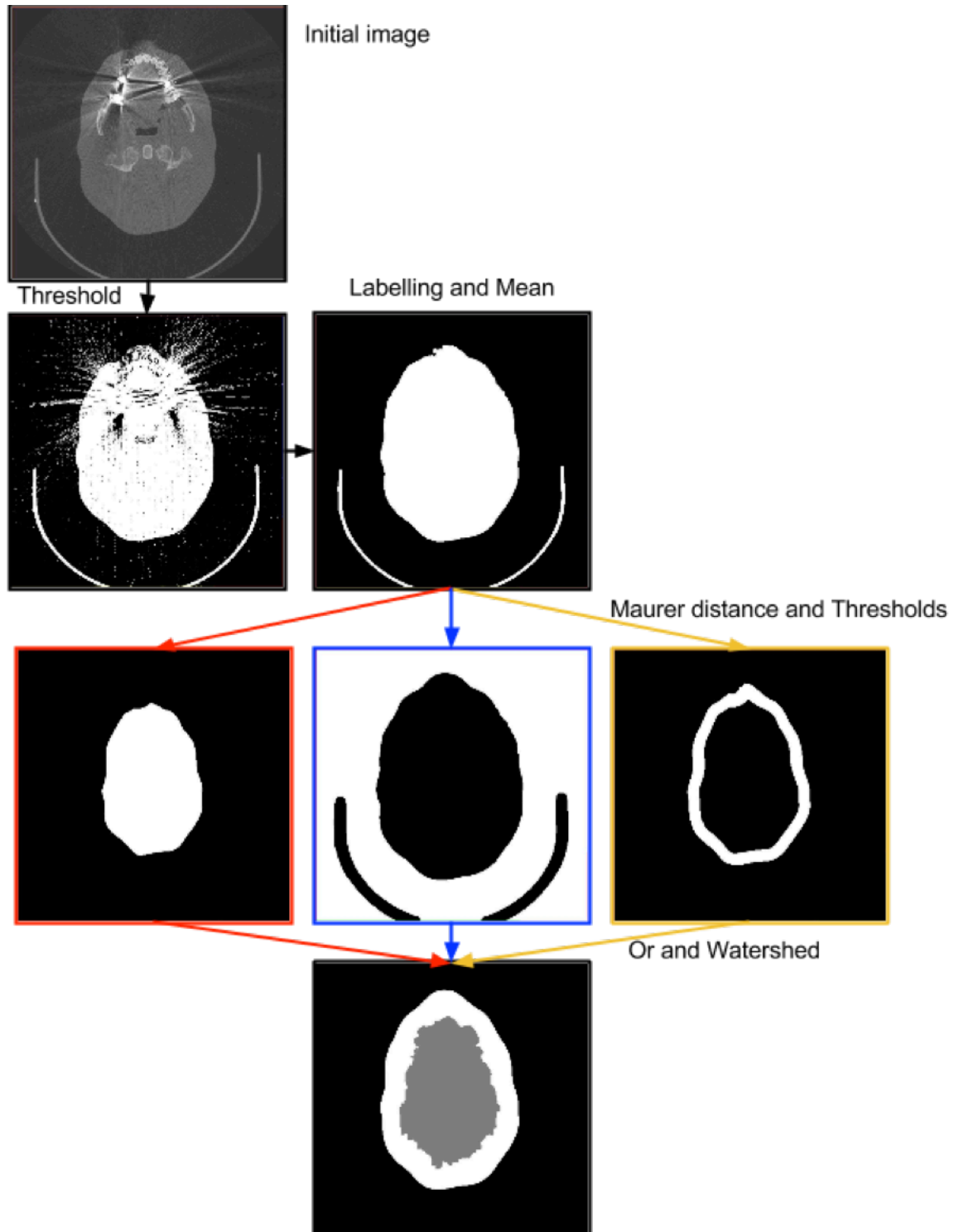


**Figure 3.31:** Scheme summarizing the skin and soft tissue layer part of the segmentation pipeline through output images of key steps (Cf. Figure 3.30).

a. Skin rough segmentation



Figure 3.32: Footer scheme illustrating the part of the skin segmentation pipeline addressing skin rough segmentation (red rectangle).

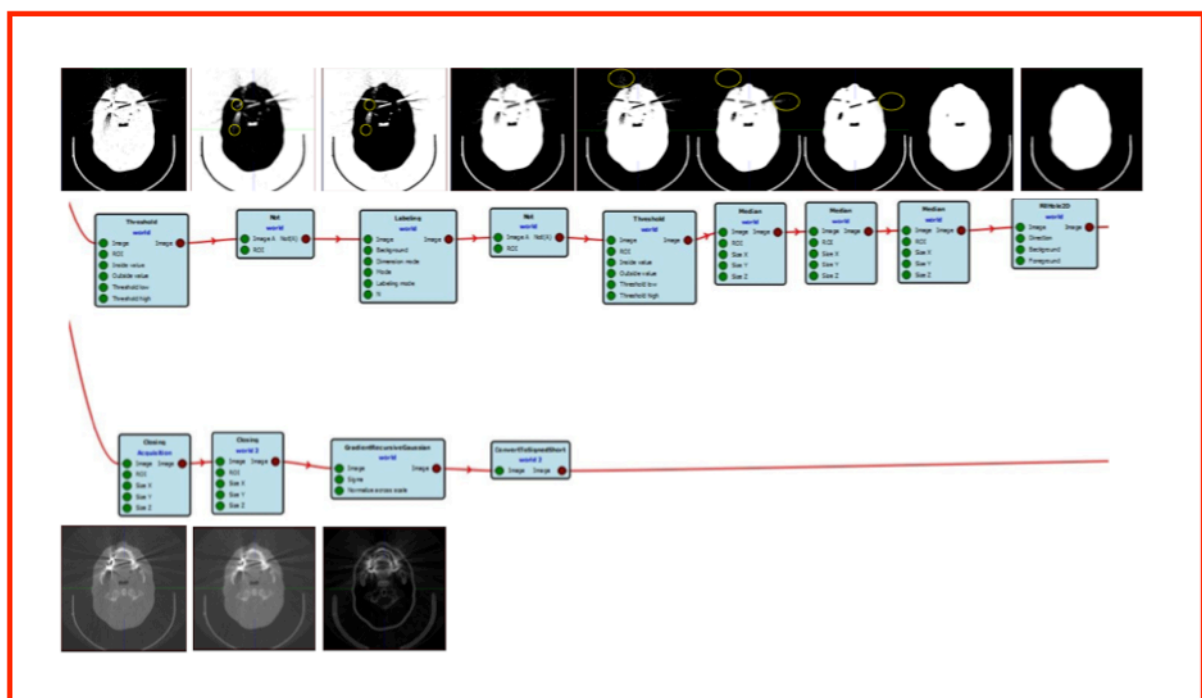
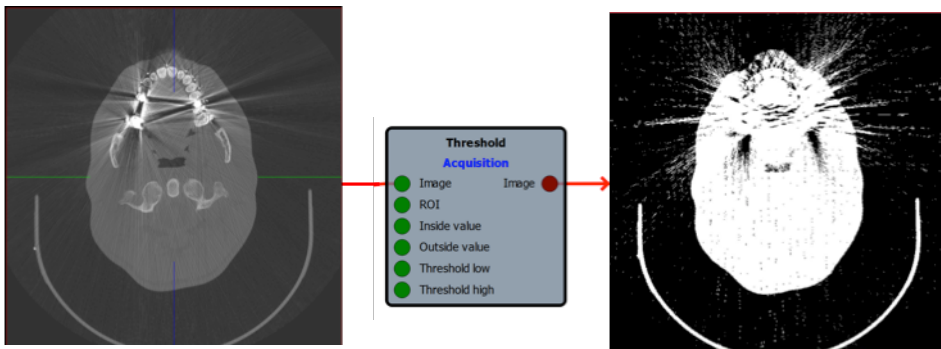


Figure 3.33: Detail of Skin rough segmentation pipeline. (Abstract from skin segmentation pipeline –Cf. Figure 3.32).

Our purpose was to keep the facial soft tissue outline without creating any hole due to dark streak artifacts. The idea behind the proposed pipeline was that artifacts were shaped as lines, which could be removed by “voting filters”, since such filters keep the most similar pixels (either black or white) within its neighborhood (Cf. Annex I, Median Filter). Therefore, we used a “Threshold” in order to get most of the skin, with the fewer artifacts possible but low enough to preserve the whole facial soft tissue outline (Cf. Figure 3.34). The parameters of the threshold operator were: threshold low=550, threshold high=4095, inside value=255, outside value=0. This step had to be conducted interactively after iterative measurements of image levels of grey.

As a result, some small spikes due to artifacts could still be encountered on the resulting image as depicted in Figure 3.34.



**Figure 3.34:** Output (right) resulting from a **Threshold** operator applied to the image source (left). Note the artifact-induced spikes disturbing the skin outline on the right image. Abstract of Skin rough segmentation pipeline (Cf. Figure 3.33).

According to the process described previously in section 3.4.2.2.1.a and b, the small dark internal connected components were suppressed thanks to a “**Not**” and a “**3D Labeling**” operator (Binary Mode, N=1). A second “**Not**” was applied to leave the dual space. A “**Threshold**” was applied again in order to obtain 256 levels of gray. The parameters of the threshold were threshold low=1, threshold high=1, inside value=255, outside value=0.

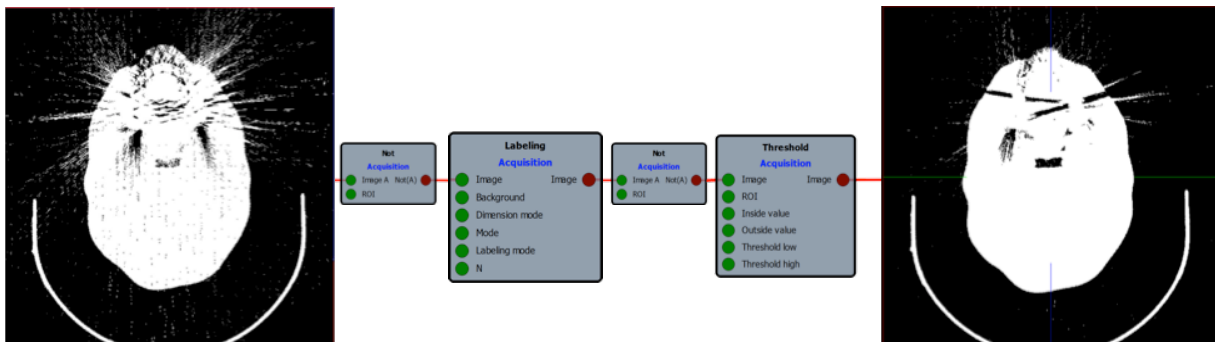


**Figure 3.35:** Output (right) resulting from a sequence of **Not-Labeling-Not-Threshold** operators applied to the output image in fig 3.34 (left). Note the artifact-induced spikes disturbing the skin outline on the right image were reduced. Abstract of Skin rough segmentation pipeline (Cf. Figure 3.33)

Then, the remaining spikes due to the artifacts were removed using a series of 3 “**Median**” operators, one on each axis.

The “**Median**” operator behaves as a voting filter, which keeps the most similar pixels (either black or white) within its neighborhood (Cf. Annex I).

Using such a filter on a binary image results in a binary image.

In the present case, we chose the value = 5, since the spikes were usually smaller than 2 pixels wide. The **parameters** of the “**Median**” operators were, respectively, Size X=5, Size Y=0, Size Z=0 ; Size X=0, Size Y=5, Size Z=0 ; Size X=0, Size Y=0, Size Z=5.

This appears quite relevant since artifacts are thin, therefore a voting filter easily removed them because their presence rate is low.

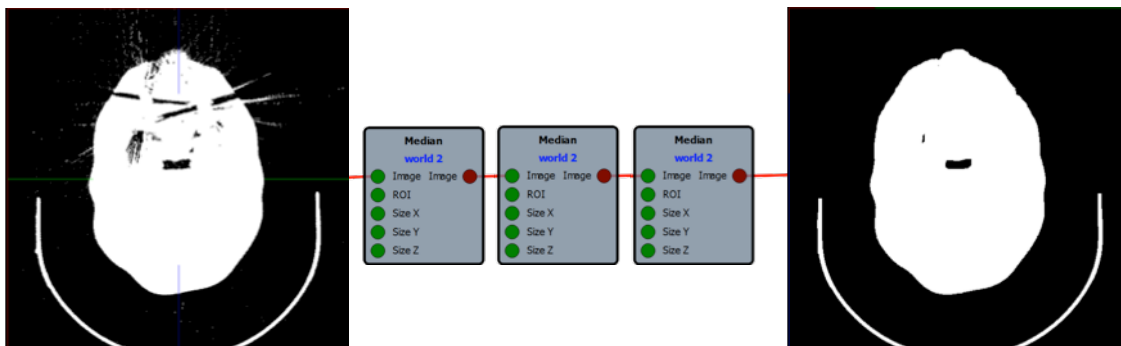


**Figure 3.36:** Output (right) resulting from a sequence of 3 **Median** operators applied to the output image in Figure 3.35 in order to remove the remaining spikes. Note the artifact-induced spikes disturbing the skin outline on the right image were suppressed. Abstract of Skin rough segmentation pipeline (Cf. Figure 3.33).

A “**Fillhole 2D**” (direction=axial, background =0, foreground=255) was then applied in order to fill concavities. The resulting image was binary and consisted of the air outside the patient in black (0) and a white (1) volume limited by the skin outline. At this stage, we have obtained a rough segmentation of the facial soft tissue.

**Such rough skin segmentation helped us subsequently define some seeds from which the thickness of the soft tissue layer was computed.**

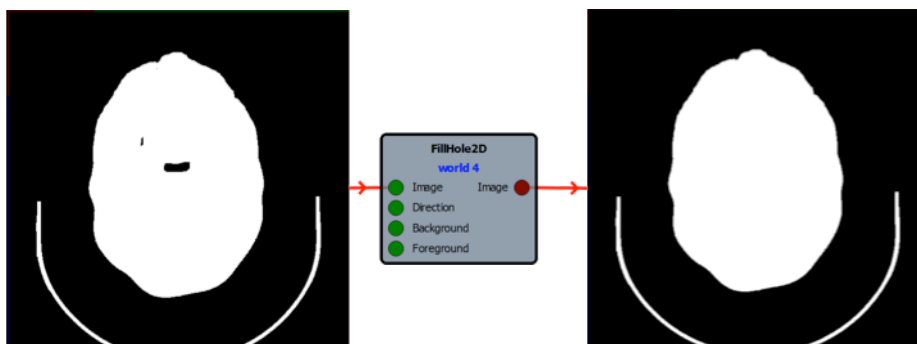


**Figure 3.37:** Output (right) resulting from a **Fillhole 2D** operator applied to the output image in Figure 3.36 providing the expected rough segmentation of the skin outline (right). Abstract of Skin rough segmentation pipeline (Cf. Figure 3.33).

As explained in the beginning of section 3.4.2.2.2, the next processing step, aiming at generating the skin and the soft tissue layer, was based on a **“Watershed”**. Such operator requires both, a gradient (to smoothen the skin and define the growth speed) and 3 seeds (Air, Soft tissue layer, Internal boundary of the soft tissue layer). We just described the **top line** of the skin rough segmentation meant to help define the seeds.

We will now detail **the bottom line** of the skin rough segmentation step, meant to obtain an input image suitable to define the **gradient** (Cf. Figures 3.38 and 3.39). In order to do so, we first removed the bright sparks thanks to two consecutive **“Closing”** operators. Every **“Closing”** operator was applied on an axis. Two consecutive operators were used due to processing time concerns (separable property of the operators). The parameters were respectively: Closing 1: Size X=2, Size Y=0, Size Z=0 ; Closing 2: Size X=0, Size Y=2, Size Z=0.

We then use the **“Gradient Recursive Gaussian”** (Parameter: sigma=2). Such operator achieves two simultaneous operations: smoothing and contour detection. Since watershed requires a signed pixel type as input data, we cast into Signed Short thanks to a dedicated operator (**“Convert to Signed Short”**).

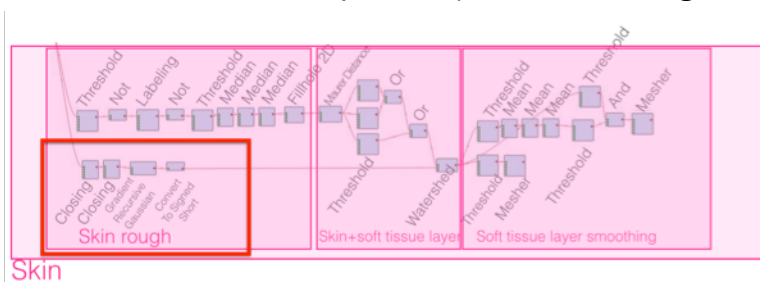


**Figure 3.38:** Footer scheme focusing on the bottom line (red rectangle) of the skin rough segmentation step, meant to extract a smooth contour gradient.

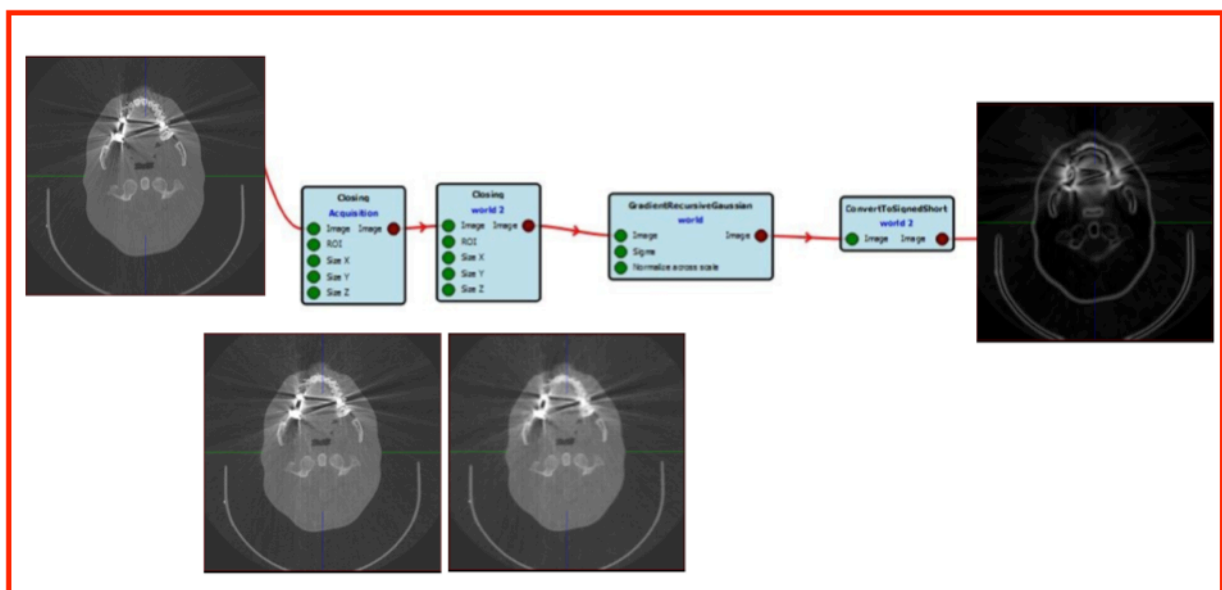


**Figure 3.39:** Detail of the **Bottom line of the Skin rough segmentation step**, meant to extract a smooth contour gradient. This smooth contour gradient is depicted in the right thumbnail. (Abstract from skin rough segmentation pipeline –Cf. Figure 3.38).

By the end of this step, we had both elements required to proceed further with a **“Watershed”**:

- The skin rough outline segmentation helping defining the seeds, thanks to the top line of this step.
- The smooth contour gradient, thanks to the bottom line of this step.

**b. Skin and soft tissue layer segmentation**



**Figure 3.40:** Footer scheme illustrating the part of the skin segmentation pipeline addressing skin and soft tissue layer segmentation (red rectangle).

The aim of this step was to generate a **soft tissue layer**. Therefore, we needed **3 seeds**, which were:

1. Air, which defines the external boundary constraint
2. The internal boundary constraint
3. The soft tissue layer, which grew between these two regions.

These seeds are defined using a distance transform (**“Maurer distance”** operator) on the rough segmentation of the head. Thanks to a **“Threshold”** operator for every seed, we can define the range (since grey level here represent distance to rough skin). The output value is used to set a label number for every seed. In order to merge all seeds in one labeled image, we combine them to a couple of cascaded **“Or”** operators.

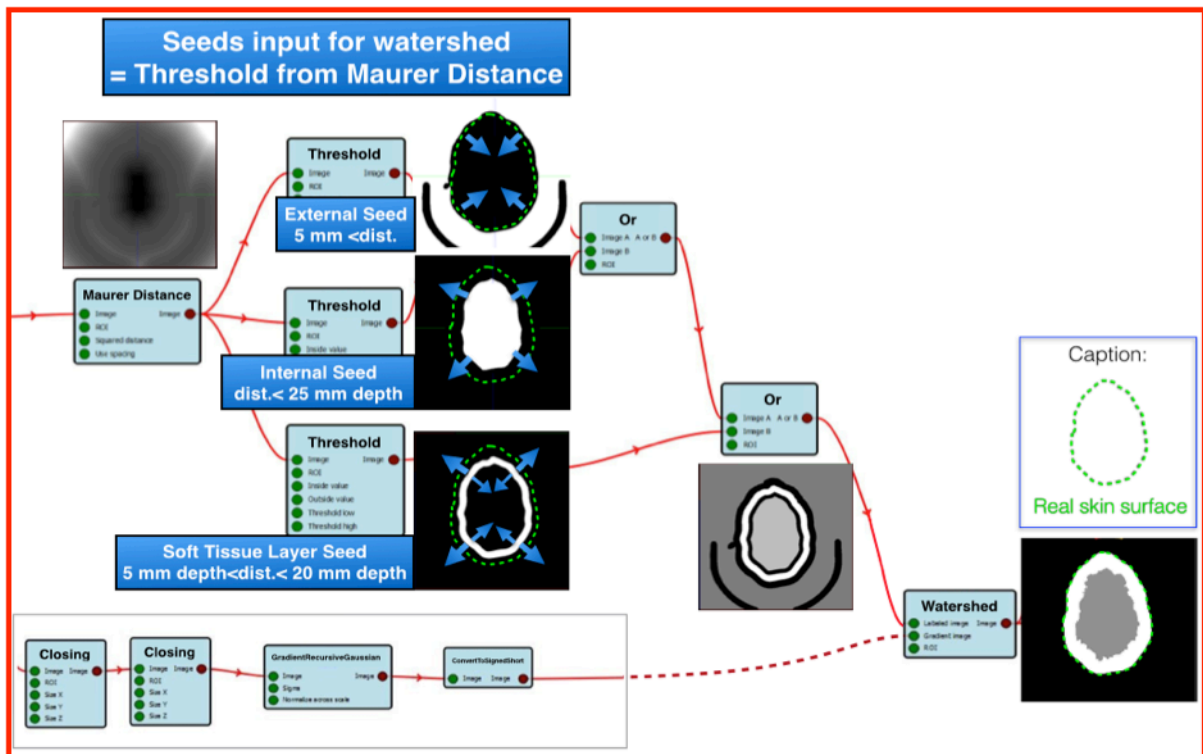


**Figure 3.41: Detail of Skin + Soft tissue layer segmentation pipeline.** Scheme illustrating the definition of 3 seeds to extract the soft tissue layer. Note the real skin surface illustrated as a green dashed line. (Abstract from skin segmentation pipeline –Cf. Figure 3.40). Note that a framed footer has been pasted in the bottom left corner. This footer consists of the bottom line of the previous “skin rough” segmentation step, as a reminder.

The parameters of the 3 thresholds are detailed in table 3.2, given that voxel size is nearly 0.5 X 0.5 X 0.5 mm (Cf. Table 3.1):

	threshold low (mm)	threshold high (mm)	inside value	outside value
<b>External seed</b>	5	500	255	0
<b>Internal seed</b>	-500	-25	255	0
<b>Soft Tissue Layer seed</b>	-20	-5	255	0

**Table 3.2:** Parameters chosen for the definition of the 3 seeds intended to extract the soft tissue layer (Cf. Figure 3.41).

For all the seeds, we considered a propagation space of 5 mm.

Concerning the soft tissue layer, we set a minimum thickness of 20 mm.

Actually, the value 500 mm was chosen to make sure that it is higher than the largest possible distance, since image size is equal to 512 pixels X 0.5 mm in every direction. So, in this image, the largest possible distance is the diagonal:

$\sqrt{3} \times 512 \times 0,5 = 443$  mm, which means that our extreme thresholds are sufficient.

We can see on Figure 3.42, that this pipeline allows getting the skin and the soft tissue layer. The “**Watershed**” generates an image composed of three different values: one value outside, one value for the soft tissue layer, and one value inside the skin. Every structure, particularly the skin surface can be further separated using a “**Threshold**”.

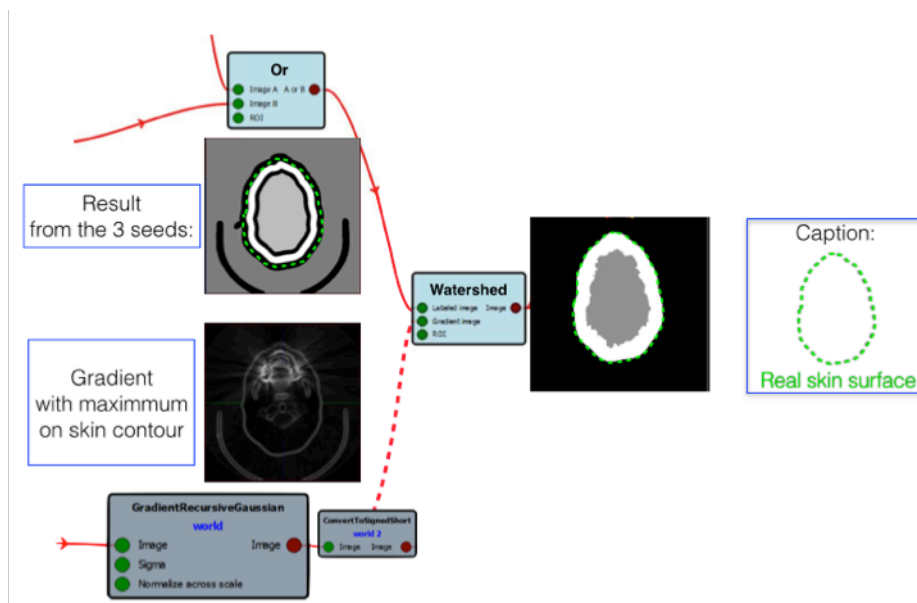


**Figure 3.42:** Abstract from Skin + Soft tissue layer segmentation pipeline (Cf. Fig 3.41) illustrating the two input images required for the watershed (2 thumbnails on the left side). The watershed results in the skin soft tissue layer (thumbnail on the right side). Note the real skin surface illustrated as a green dashed line.



### Discussion

Since the “skin rough” segmentation step, due to the operators applied to overcome artifacts, results in slight contour alteration and data loss (Cf. Figure 3.42, using a watershed operator became relevant).

Indeed, there were two advantages in using a “**Watershed**” in the process:

- Interface soft tissue layer-external seed: working on a smoothed input of the soft tissues (Cf. bottom line of the pipeline “Closing / Closing / Gradient Recursive Gaussian / Convert to signed short) allows **reducing artifact distortion**.
- Interface soft tissue layer-internal seed: the “**Watershed**” allows the soft tissue internal surface being close to the underlying bones, therefore providing different thickness, which approximates the “anatomical truth”.

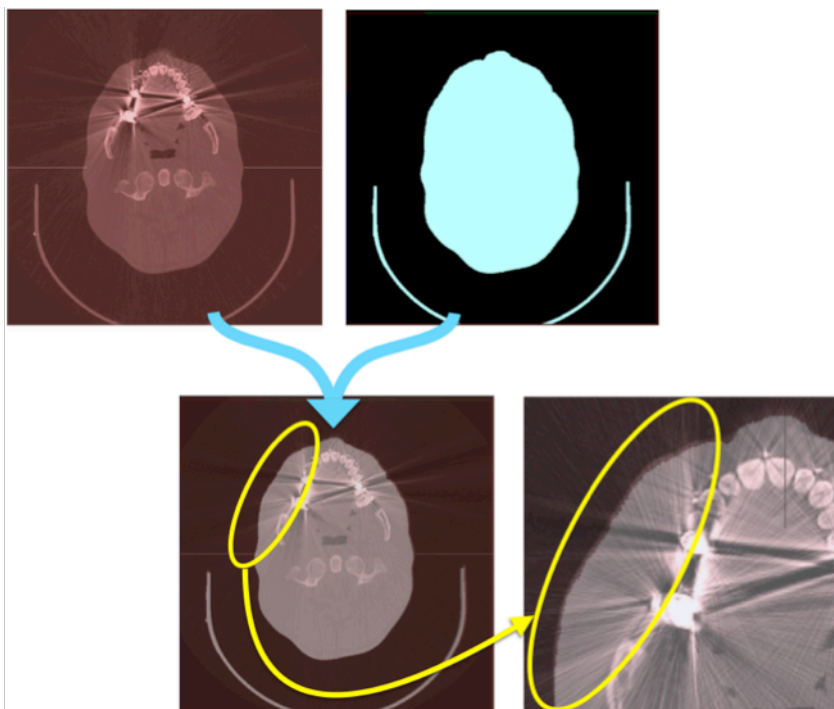


**Figure 3.43: Illustration of contour alteration secondary to rough skin segmentation.**

Top left: Patient's image in levels of grey artificially colored in redish.

Top right: Image mask resulting from rough skin segmentation artificially colored in cyan.

Bottom left: superimposition of the 2 images. Bottom right: detail showing contour alteration.

### c. Soft tissue layer smoothing

At the end of the previous step, we have obtained an approximation of the soft tissue layer (Cf. Figure 3.42). However, the internal surface featured a number of surface irregularities.

The aim of this next step was to conduct soft tissue layer smoothing. It consisted, on the one hand, in extracting the skin outer surface (bottom line) and, on the other hand, in smoothing the internal surface of the soft tissue layer (top line) (Cf. Figures 3.44 and 3.45).



**Figure 3.44:** Footer scheme illustrating the part of the skin segmentation pipeline addressing skin outer surface extraction and soft tissue layer smoothing (red rectangle).

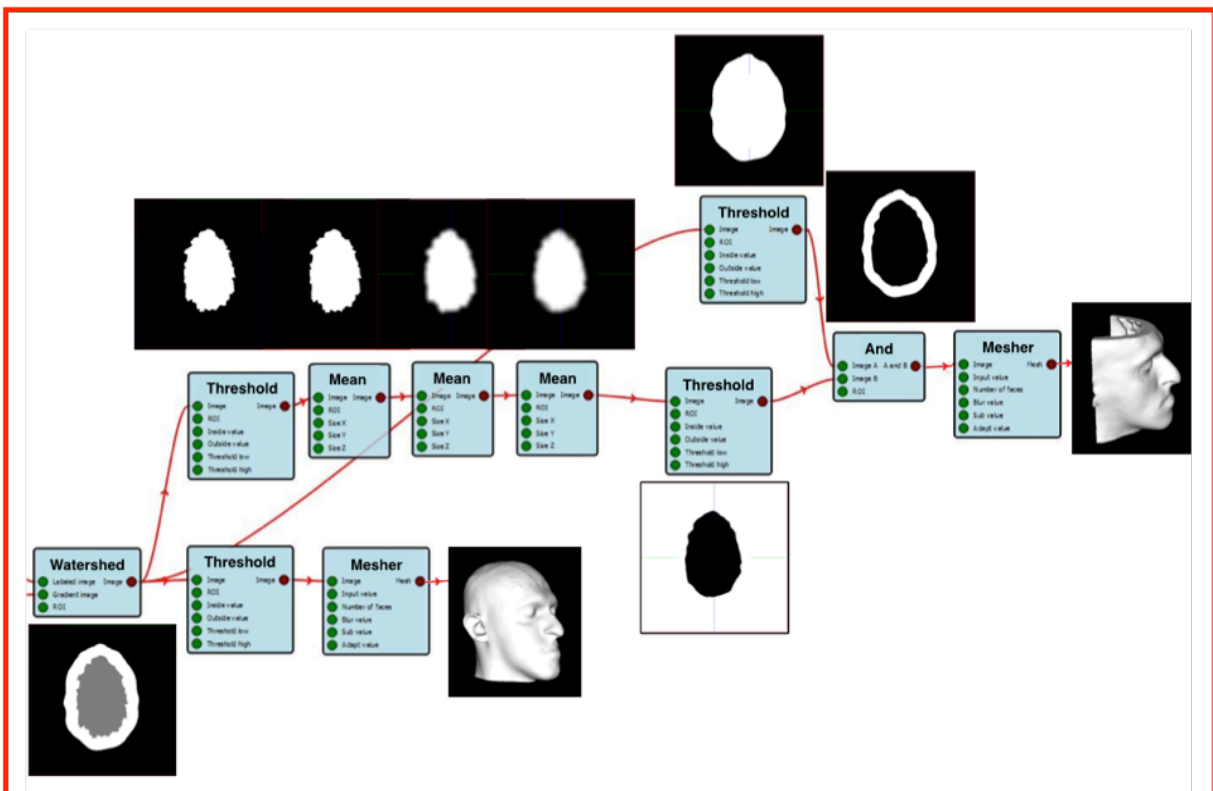


**Figure 3.45:** Detail of soft tissue layer smoothing pipeline. (Abstract from skin segmentation pipeline –Cf. Figure 3.32).

The bottom line (Watershed-Threshold-Mesher) consisted in extracting the skin outer surface. The top line (Threshold-Mean-Mean-Mean-Threshold-And-Mesher) resulted in smoothing the internal surface of the soft tissue layer.

**On the top line of this pipeline**, a first **“Threshold”** operator was used in order to extract the internal skin surface, from an input image displaying three levels of grey (Cf. Figure 3.45, and Table 3.2). These three levels of grey were respectively equal to 3 for the “inside” of the patient, to 2 for the soft tissue layer, and to 1 for the outside of the patient. Using a threshold=3 results in extracting the “inside of the patient, i.e.: the internal surface of the soft tissue layer. Therefore, the first “Threshold” used the following parameters: threshold low= 3, threshold high= 3, Inside value=255, outside value=0.

Then, we aimed at smoothing the irregularities of the internal surface of the soft tissue layer. To do so, we proposed applying 3 successive **“Mean”** operators. The parameters we used were respectively, Size X=10, Size Y=0, Size Z=0; Size X=0, Size Y=10, Size Z=0; Size X=0, Size Y=0, Size Z=10.

The **“Threshold”** following the 3 **“Means”** was applied to retrieve a binary image and used: threshold low= 25, threshold high= 255, Inside value=0, outside value=255. It was actually an “inverted” Threshold, resulting in inverting black and white for computation purposes.

The **“Threshold”** on the very top part of the pipeline (Cf. Figure 3.45) was applied to the image resulting from the watershed in order to retrieve the whole head (outside skin surface + soft tissue layer) and used: threshold low= 3, threshold high= 4, Inside value=255, outside value =0.

The bottom line of this pipeline consisted in extracting the outer skin surface thanks to a **“Threshold”** to apply a **“Mesher”**. Threshold parameters were threshold low=1, threshold high= 255, Inside value=255, outside value =1.

### 3.4.2.2.3 Discussion

Using a “**Watershed**” operator (Cf. 3.4.2.2.2.b) is useful to obtain the external skin surface. However, regarding the internal surface of the soft tissue layer, the results of this method did not meet our expectations (Cf. p. 30). We were only able to approximate the thickness consistency of the soft tissue layer. As a result, the position of the soft tissue layer internal surface did not match the external surface of the bones. Yet, as we will see in chapter 4.2.2, this point is of primary importance to allow the simulation of soft tissues. We therefore proposed an alternate and simpler method consisting in computing a **distance map (Maurer)** to “subtract” the bone surface to the soft tissue layer. Such distance map started from the skin surface and stopped inside the mask, at a distance defined by a “**Threshold**”, in order to match the required soft tissue thickness.

In order to segment the skin, we still use the same watershed approach, but only using 2 seeds (1 external, 1 soft tissue layer).

Once we have obtained the patient’s skin mask, we can apply a “**Threshold**” after a simple “**Maurer distance**” operator. Finally, we use a “**Box**” in order to limit the area of interest. This area of interest consists of the soft tissue part, which needs to be simulated, since it is affected by surgical movements of the underlying skeleton (Cf. Chapter 4). The advantages of this method are its simplicity and the shorter processing time required.

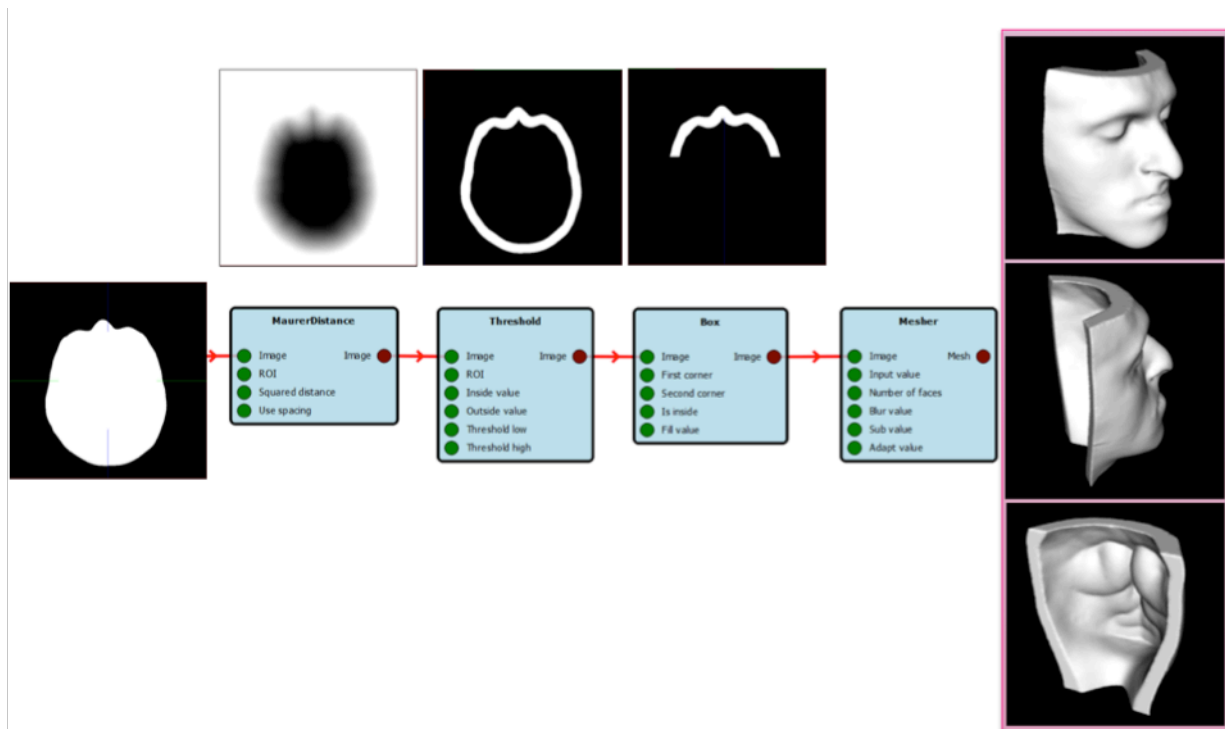


**Figure 3.46: Detail of the alternate skin + soft tissue layer pipeline.** This part of the pipeline was connected to the top line of the Skin rough segmentation step (Cf. Figure 3.32). The input image in this pipeline is the output one from the Fillhole 2D in the top right of Figures 3.33 and 3.36.

At the end of the global pipeline, we finally obtain the 4 segmentations needed as depicted in Figure 3.47.

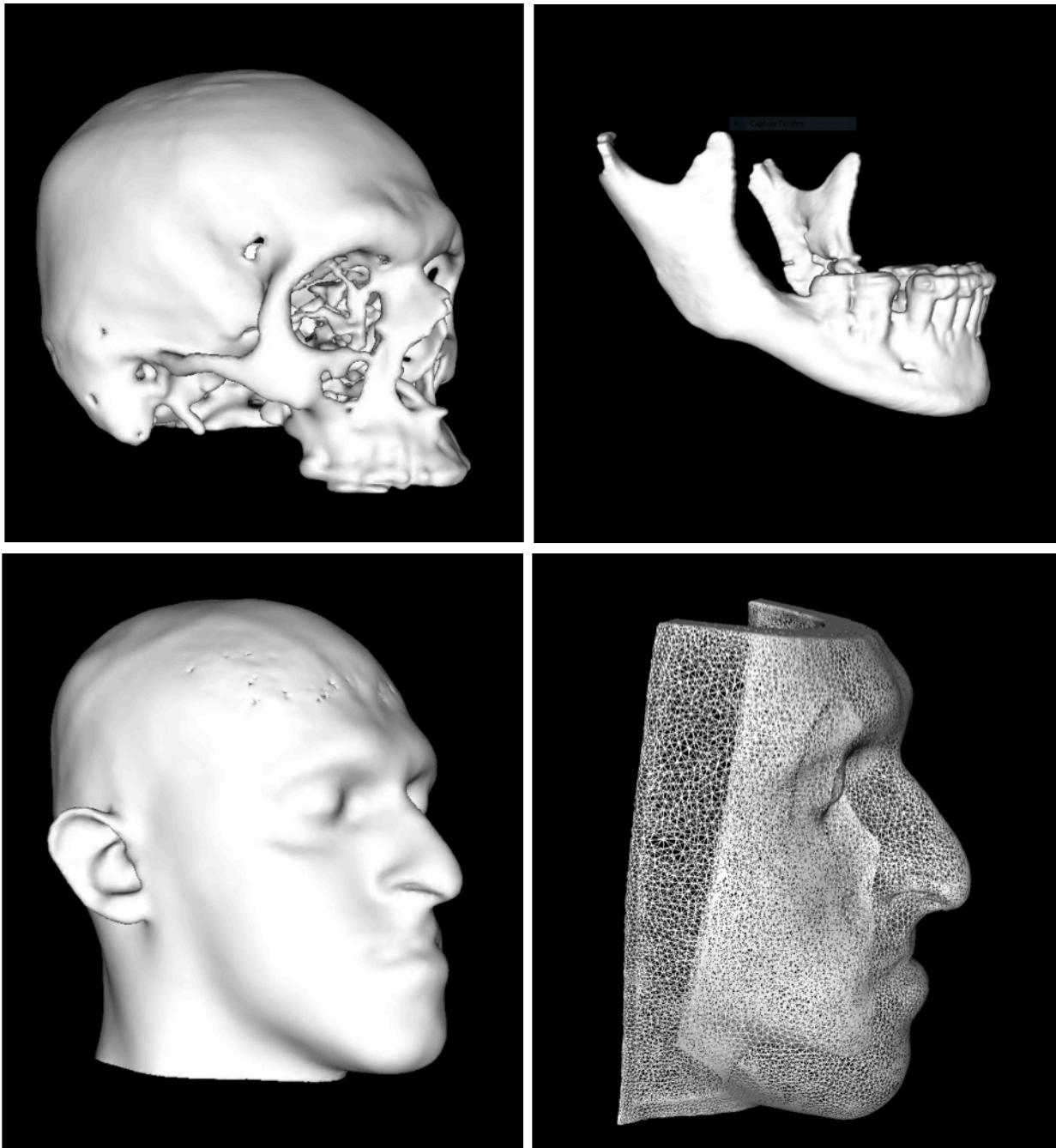


**Figure 3.47:** Surface meshes resulting from the 4 distinct segmentations of respectively, the maxilla attached to the skull (top left), the mandible (top right), the outside skin surface (bottom left) and the soft tissue layer (wire-frame, bottom right). Note the smooth aspect of the internal soft tissue layer (bottom right).

### **3.4.2.3. Conclusion**

We were able to implement a semi-automated global pipeline suited to provide distinct segmentation of the structures required as input data in the continuation of our work, which is simulation.

This pipeline was based on successive mathematical morphology operators in order to independently process image masks. Even if alternative methods exist to process simultaneously these mask images (Ronse and Agnus 2005), we were not able to use them because they are not yet implemented in the software version we have used.

Unfortunately, this pipeline is not fully automated, since it requires manual operations, especially to determine the values of the thresholds through interactive measurements. Automation of these steps would be a relevant topic that we maintain for further research, since the purpose of this thesis is focused on surgical navigation and soft tissue simulation rather than on the sole segmentation.

### 3.5. Segmentation evaluation

#### 3.5.1. Method

We conducted an evaluation of the automated (A) segmentation pipeline compared to the interactive (I) (manual) one using a database of 8 patient CT scans (Cf. Table 3.3).

Patient	Segmented Bone Maxilla=MX Mandible=MD	Voxel size (mm)	Artifacts	Mouth	Automated Segmentation total duration (min)	Interactive Segmentation total duration (min)
12-1	MD	0.53 x 0.53 x 0.30	Many	closed	29	130
	MX	0.53 x 0.53 x 0.30	Many			
12-2	MD	0.48 x 0.48 x 0.30	∅	closed	21	121
	MX	0.48 x 0.48 x 0.30	∅			
18-1	MD	0.43 x 0.43 x 0.30	Few	opened	09	105
	MX	0.43 x 0.43 x 0.30	Few			
18-2	MD	0.41 x 0.41 x 0.30	∅	opened	12	97
	MX	0.41 x 0.41 x 0.30	∅			
20-1	MD	0.49 x 0.49 x 1	∅	closed	17	103
	MX	0.49 x 0.49 x 1	∅			
20-2	MD	0.45 x 0.45 x 0.30	∅	closed	23	90
	MX	0.45 x 0.45 x 0.30	∅			
33-1	MD	0.49 x 0.49 x 1	Few	closed	18	115
	MX	0.49 x 0.49 x 1	Few			
33-2	MD	0.44 x 0.44 x 0.30	Many	closed	14	117
	MX	0.44 x 0.44 x 0.31	Many			

**Table 3.3:** Duration (min) of automated and interactive segmentation of 8 Patient CT scans.

We first measured the automated segmentation durations in order to compare them with the interactive ones.

We then decided to conduct an image-to-image comparison rather than mesh-to-mesh. Indeed, mesh generation induces both, sparse information and data shifting, therefore a bias.

Classical segmentation evaluation metrics are Jaccard index (Jaccard 1912) and DICE index (Dice 1945), which compute the ratio between the overlap of segmented areas and their respective size.

Let,

A, the image resulting from automated segmentation

I, the image resulting from interactive segmentation

These methods can be expressed as follows:

$$\text{Jaccard index} = \frac{A \cap I}{A \cup I}$$

$$\text{DICE index} = \frac{2|A \cap I|}{|A| + |I|}$$

If such methods are suited to compare two algorithms, they are not relevant in our practical clinical case, since they do not provide information that is easily interpreted.

We defined as accuracy metric, the border-to-border distance in the two voxel images. This method has the advantage of providing metrics in mm, which can be used as reference when further analyzing mesh similarity in Chap 4 (simulation evaluation).

We implemented a pipeline dedicated to evaluation (Cf. Figure 3.49). It started from one mask and processed an **erosion** on it. Then, it **subtracted** the eroded image from the original one, in order to obtain its internal border only.

We proceeded accordingly for respectively the interactive segmentation and the automated segmentation, in order to obtain a second border: in a second step, we applied a **distance transform** according to **Maurer** onto the other mask. Finally, we superimpose the distance transform with the other border. As a result, it is obvious to directly read the distance between the two segmentations, that we name “distance-to-border dataset”. Since this metric is not symmetrical (e.g.: the distance from interactive (I) to automated (A) segmentation is different from the distance from automated (A) to interactive (I) segmentation), we then swap the two segmentations, compute the second internal border and a second set of distances, and merge them in order to obtain a new “distance-to-border dataset” (Cf. Figure 3.48). In the end, we combine the two “distance-to-border datasets”. The metrics consist of statistical attributes (mean and standard deviation) of the distance distribution.

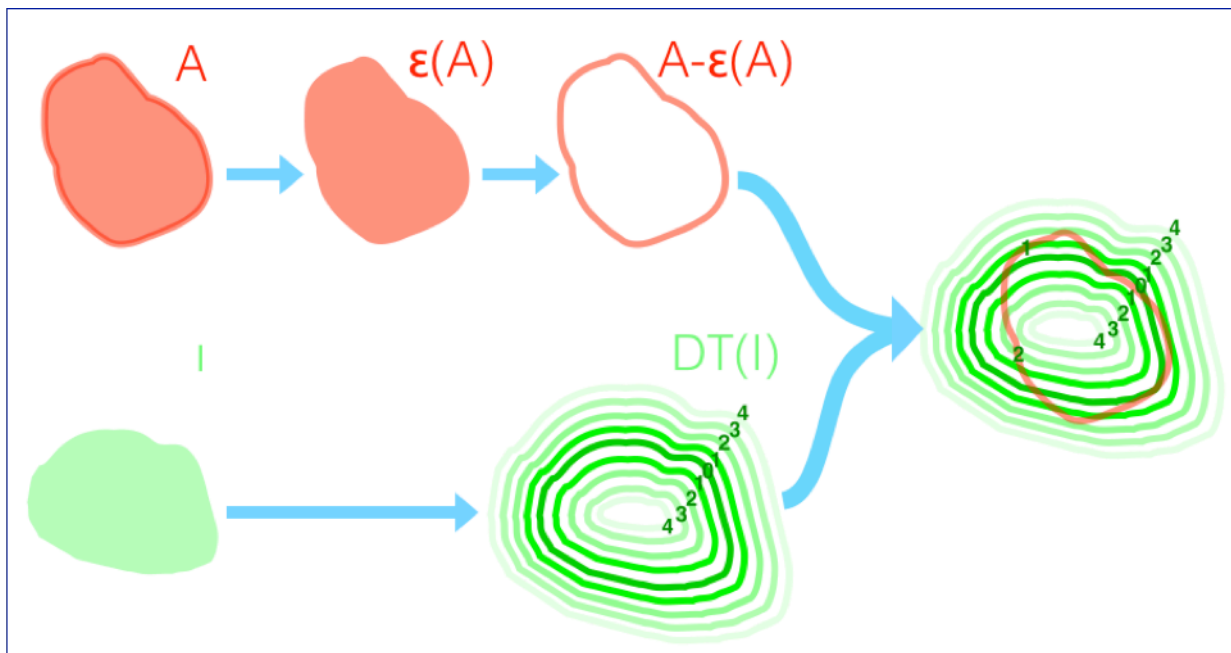


**Figure 3.48: Principles used to implement the evaluation pipeline** between the automated segmentation (A) and the interactive (I) one. Erosion is noted  $\epsilon$ . Distance transform is noted DT. Note the isodistance contours generated thanks to the distance transform of I allowing direct reading of the distance between the 2 segmentations.



Figure 3.49 details the operators used to build the segmentation evaluation pipeline.

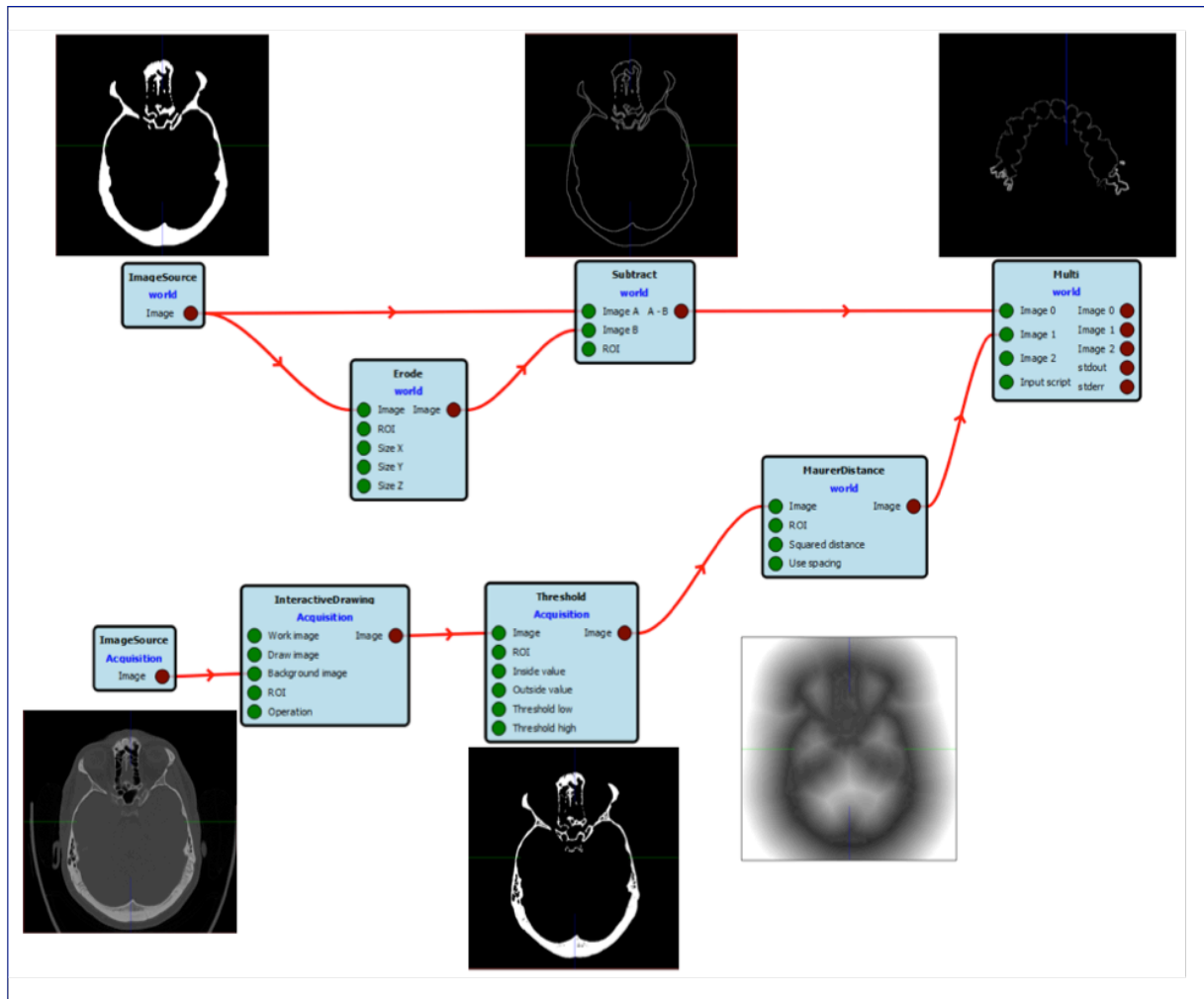


**Figure 3.49: Evaluation pipeline between the automated segmentation (A) and the interactive (I) one.** The top line is dedicated to the automated (A) segmentation. It details the **Erode** and the **Subtract** operators applied.

The bottom line starts from the image source. The **Interactive Drawing** operator stands for interactive segmentation. Then, a **Maurer Distance** transform was applied to the interactive (I) segmentation. The **Multi** operator compares the 2 resulting image from respectively the top and the bottom line and computes statistics. Note that the thumbnail in the top right corner of the figure is a zoom on the teeth area, since it is the most affected by distance errors.

### 3.5.2. Results

#### a) Duration

The average interactive segmentation duration was at 110 minutes compared to 18 minutes for the automated one. This shows an improvement in processing time by a factor of 6. We can note that during the automated process, interaction of the operator is extremely short, since he only needs to set a few parameters.

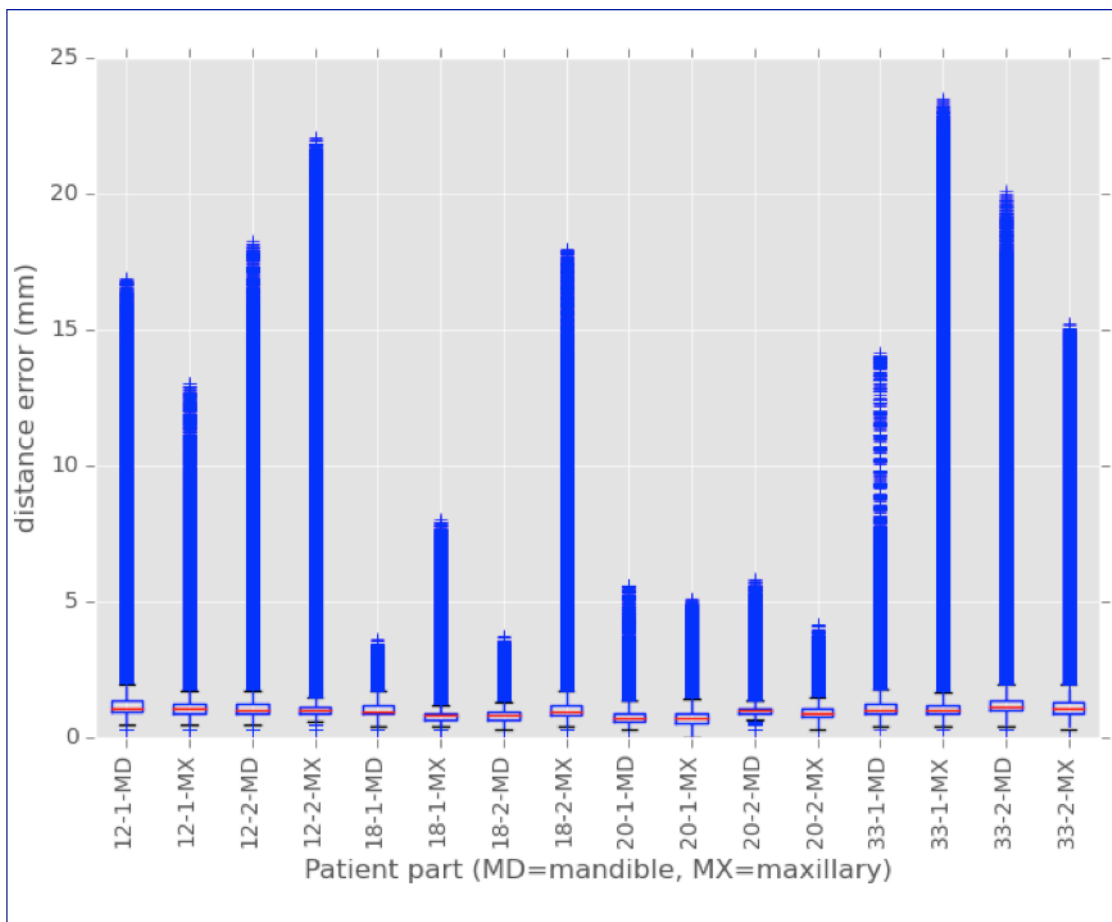
#### b) Accuracy

In Graph 3.1, we compare the interactive segmentation to the automated one.

The boxplots represent the statistical distribution of distance from border-to-border.

The highest, respectively, lowest, part of the box corresponds to the 75<sup>th</sup>, respectively 25<sup>th</sup>, percentile of the distance. The red line inside the box represents the median value. The whiskers represent 1.5 of inter-quartile range.

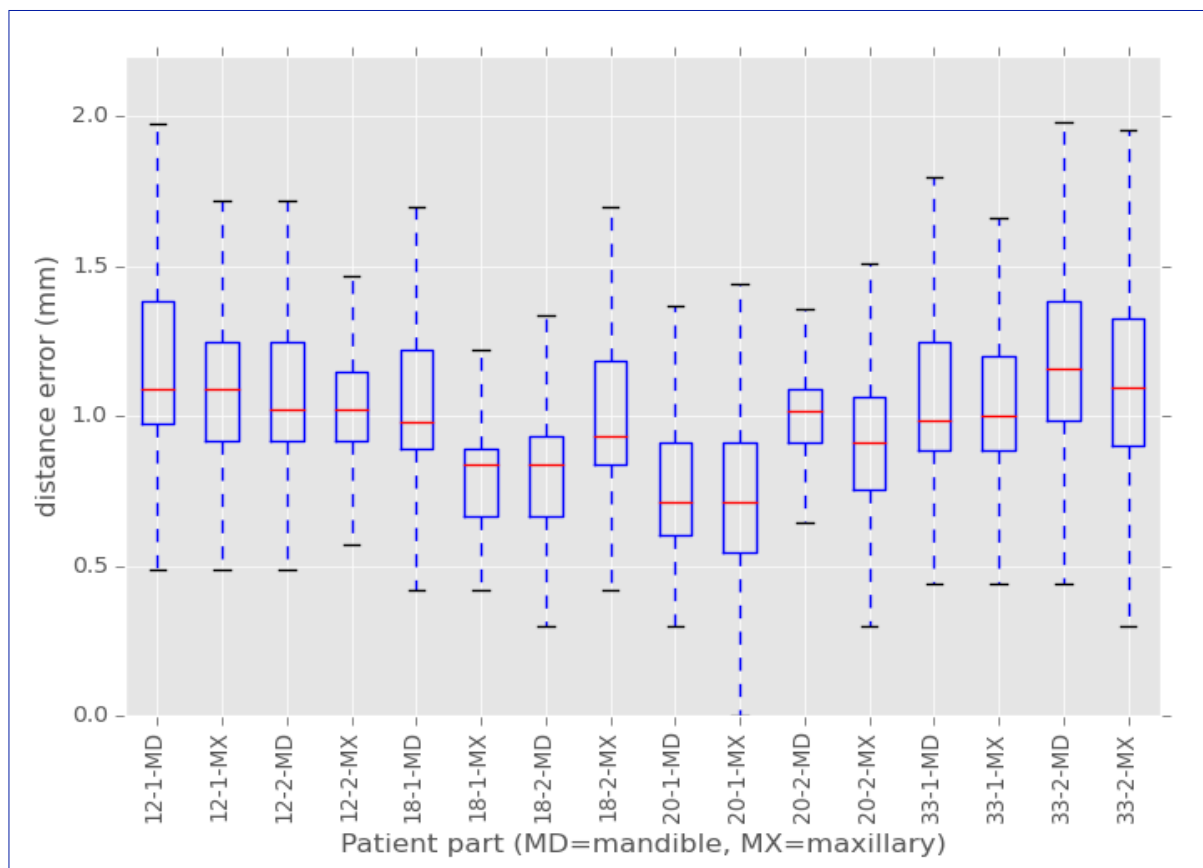
The distances outside the 25%-75% range (outliers) are displayed using blue crosses. Due to the vertical scale chosen to include all the outliers, the corresponding blue crosses merge into one another, therefore falsely appearing as a continuous blue bar (Cf. Graph 3.1). We generated Graph 3.2, which vertical scale is smaller (up till 2mm, rather than 25mm), therefore zooming on the whisker boxes. Table 3.4 displays the numerical results.



**Graph 3.1:** Boxplot graph illustrating the statistical distribution of border-to-border distance error (mm) between the automated segmentation and the interactive one for each segmented bone in every patient.

Target	mean (mm)	median (mm)	std (mm)	max (mm)
12-1-MD	1,36	1,09	1,48	16,89
12-1-MX	1,08	1,09	0,59	13,06
12-2-MD	1,36	1,02	1,55	18,25
12-2-MX	1,38	1,02	1,68	22,10
18-1-MD	1,04	0,98	0,22	3,64
18-1-MX	0,84	0,84	0,43	8,05
18-2-MD	0,81	0,84	0,26	3,74
18-2-MX	1,14	0,93	0,97	17,95
20-1-MD	0,77	0,71	0,29	5,61
20-1-MX	0,72	0,71	0,22	5,10
20-2-MD	1,03	1,02	0,33	5,81
20-2-MX	0,96	0,91	0,29	4,19
33-1-MD	1,08	0,99	0,59	14,14
33-1-MX	1,53	1,00	2,24	23,50
33-2-MD	1,68	1,16	2,07	20,11
33-2-MX	1,20	1,10	0,88	15,23

**Table 3.4:** Numerical results (in millimeters) of border-to-border distance error between the automated segmentation and the interactive one for each segmented bone in a patient. Mean, median, standard deviation (std) and maximum.



**Graph 3.2:** Detail of Boxplot graph illustrating the statistical distribution of border-to-border distance error (mm) between the automated segmentation and the interactive one for each segmented bone in every patient. The vertical scale is chosen at a maximum of 2 mm, neglecting some outliers but focusing on the whisker boxes. The highest, respectively, lowest, part of the box corresponds to the 75<sup>th</sup>, respectively 25<sup>th</sup>, percentile of the distance. The red line inside the box represents the median value. The whiskers represent 1.5 of inter-quartile range.

### 3.5.3. Discussion

From graphs 3.1 and 3.2, we can note that the number of outliers (distance error > 1.5 mm) do not exceed 25%. Many outliers occur in the posterior part of the dental arches (Cf. Figure 3.50) where artifacts are usually numerous (Cf. Figure 3.4). This is not a problem, since the clinical focus is on the external facial morphology and such errors have no impact on soft tissue segmentation.

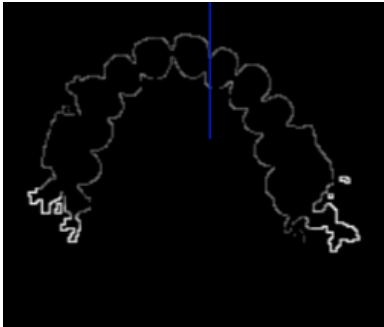


**Figure 3.50: Image detail from the evaluation pipeline displaying the distance error between interactive (manual) and automated segmentation.** The more the grey level intensity, the more distance errors. Note high intensity in the posterior dental arch.

Since voxel sizes are nearly 0.5 X 0.5 X 0.5 mm, seventy-five percent of distance errors are less than 3 pixels.

Moreover, such accuracy is quite satisfactory considering that the interpretation of the bone limit can vary depending on the windowing chosen by the operator. Indeed, the partial volume effect induces a smooth transition (typically 2 to 3 pixels) between bones and soft tissues (Cf. Figure 3.51).

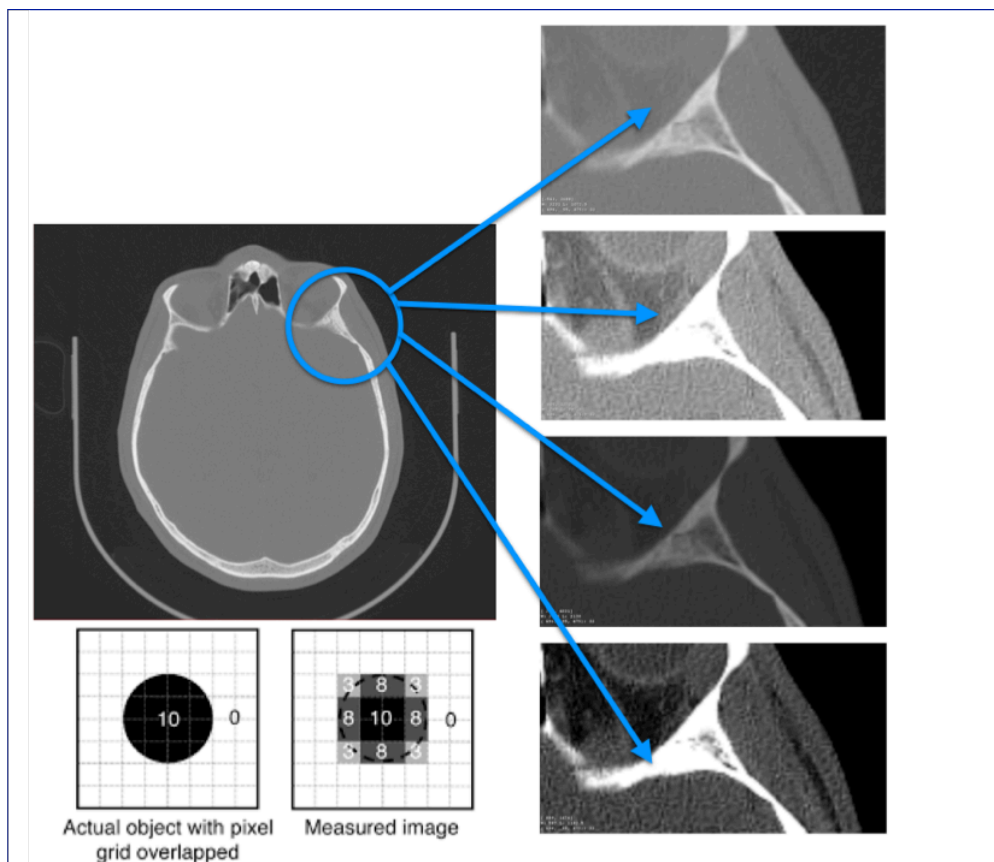


**Figure 3.51: Illustration of the partial volume effect.** Depending on the windowing applied to the image source (left), the bone limit can vary as shown in the 4 thumbnails (right).

In case 18, the distance error is low, since acquisition was performed on a patient with opened mouth therefore eliminating any contact between the maxilla and the mandible. As a result, segmentation becomes much more convenient.

Case 20-1 also showed very low distance error, which can be explained because there were few artifacts, making segmentation quite easy.

Of course, optimal evaluation would have involved iterative segmentations by the same operator as well as segmentation of the same image by different operators. Due to time and staff constraints, we seek conducting such study in further developments.

Considering partial volume effect and surgical accuracy of 1 mm, we can consider the 1.5 mm distance error we obtained between semi-automated and interactive segmentation is acceptable.

We have demonstrated that the proposed semi-automated segmentation pipeline could replace the interactive segmentation conducted by an expert in terms of accuracy.

The semi-automated pipeline also prevents from inter-operator discrepancy, therefore providing reproducibility. Thanks to the mainly automated pipeline, the great benefit is that it makes the surgeon available for more critical tasks.

---

**REFERENCES**

1. Buzug, Thorsten, and May Oehler. 2007. "Statistical Image Reconstruction for Inconsistent CT Projection Data." *Methods of Information in Medicine* 46 (3): 261–69. doi:10.1160/ME9041.
2. Catherwood, T., E. McCaughan, E. Greer, R. A. J. Spence, S. A. McIntosh, and R. J. Winder. 2011. "Validation of a Passive Stereophotogrammetry System for Imaging of the Breast: A Geometric Analysis." *Medical Engineering & Physics* 33 (8): 900–905. doi:10.1016/j.medengphy.2011.02.005.
3. Dice, Lee R. 1945. "Measures of the Amount of Ecologic Association Between Species." *Ecology* 26 (3): 297–302. doi:10.2307/1932409.
4. Djordjevic, J., B. M. Lewis, C. E. Donaghy, A. I. Zhurov, J. Knox, L. Hunter, and S. Richmond. 2014. "Facial Shape and Asymmetry in 5-Year-Old Children with Repaired Unilateral Cleft Lip And/or Palate: An Exploratory Study Using Laser Scanning." *The European Journal of Orthodontics* 36 (5): 497–505. doi:10.1093/ejo/cjs075.
5. Goto, Tazuko K., Satoko Nishida, Yuko Nakamura, Kenji Tokumori, Yasuhiko Nakamura, Koji Kobayashi, Yutaka Yoshida, and Kazunori Yoshiura. 2007. "The Accuracy of 3-Dimensional Magnetic Resonance 3D Vibe Images of the Mandible: An in Vitro Comparison of Magnetic Resonance Imaging and Computed Tomography." *Oral Surgery, Oral Medicine, Oral Pathology, Oral Radiology, and Endodontics* 103 (4): 550–59. doi:10.1016/j.tripleo.2006.03.011.
6. Heike, Carrie L., Kristen Upson, Erik Stuhaug, and Seth M. Weinberg. 2010. "3D Digital Stereophotogrammetry: A Practical Guide to Facial Image Acquisition." *Head Face Med* 6 (1): 18.
7. Hoevenaren, Inge A., J. Meulstee, E. Krikken, S. J. Bergé, D. J. O. Ulrich, and Thomas J. J. Maal. 2015. "Development of a Three-Dimensional Hand Model Using Three-Dimensional Stereophotogrammetry: Assessment of Image Reproducibility." Edited by Qinghui Zhang. *PLOS ONE* 10 (9): e0136710. doi:10.1371/journal.pone.0136710.
8. Jaccard, Paul. 1912. "The Distribution of the Flora in the Alpine Zone.1." *New Phytologist* 11 (2): 37–50. doi:10.1111/j.1469-8137.1912.tb05611.x.
9. Joda, Tim, and German O. Gallucci. 2015. "The Virtual Patient in Dental Medicine." *Clinical Oral Implants Research* 26 (6): 725–26. doi:10.1111/clr.12379

10. Jung, Yu-Jin, Myung-Jin Kim, and Seung-Hak Baek. 2009. "Hard and Soft Tissue Changes after Correction of Mandibular Prognathism and Facial Asymmetry by Mandibular Setback Surgery: Three-Dimensional Analysis Using Computerized Tomography." *Oral Surgery, Oral Medicine, Oral Pathology, Oral Radiology, and Endodontics* 107 (6): 763–771.e8. doi:10.1016/j.tripleo.2008.12.026.
11. Kau, Chung How, Stephen Richmond, Angela Incrapera, Jeryl English, and James Jiong Xia. 2007. "Three-Dimensional Surface Acquisition Systems for the Study of Facial Morphology and Their Application to Maxillofacial Surgery." *The International Journal of Medical Robotics and Computer Assisted Surgery* 3 (2): 97–110. doi:10.1002/rcs.141.
12. Kusnoto, Budi, and Carla A. Evans. 2002. "Reliability of a 3D Surface Laser Scanner for Orthodontic Applications." *American Journal of Orthodontics and Dentofacial Orthopedics* 122 (4): 342–48. doi:10.1067/mod.2002.128219.
13. Lane, Christopher, and William Harrell. 2008. "Completing the 3-Dimensional Picture." *American Journal of Orthodontics and Dentofacial Orthopedics: Official Publication of the American Association of Orthodontists, Its Constituent Societies, and the American Board of Orthodontics* 133 (4): 612–20. doi:10.1016/j.ajodo.2007.03.023.
14. Luca Canto, G. De, C. Pachêco-Pereira, M. O. Lagravere, C. Flores-Mir, and P. W. Major. 2015. "Intra-Arch Dimensional Measurement Validity of Laser-Scanned Digital Dental Models Compared with the Original Plaster Models: A Systematic Review." *Orthodontics & Craniofacial Research* 18 (2): 65–76. doi:10.1111/ocr.12068.
15. Metzger, Tasha E., Katherine S. Kula, George J. Eckert, and Ahmed A. Ghoneima. 2013. "Orthodontic Soft-Tissue Parameters: A Comparison of Cone-Beam Computed Tomography and the 3dMD Imaging System." *American Journal of Orthodontics and Dentofacial Orthopedics* 144 (5): 672–81. doi:10.1016/j.ajodo.2013.07.007.
16. Mollemans, W., F. Schutyser, N. Nadjmi, F. Maes, and P. Suetens. 2007. "Predicting Soft Tissue Deformations for a Maxillofacial Surgery Planning System: From Computational Strategies to a Complete Clinical Validation." *Medical Image Analysis* 11 (3): 282–301. doi:10.1016/j.media.2007.02.003.
17. Nardi, Cosimo, Claudia Borri, Francesco Regini, Linda Calistri, Alessandro Castellani, Chiara Lorini, and Stefano Colagrande. 2015. "Metal and Motion Artifacts by Cone Beam Computed Tomography (CBCT) in Dental and Maxillofacial Study." *La Radiologia Medica* 120 (7): 618–26. doi:10.1007/s11547-015-0496-2.
18. Nemtoi, A, C Czink, D Haba, and A Gahleitner. 2013. "Cone Beam CT: A Current Overview of Devices." *Dentomaxillofacial Radiology* 42 (8): 20120443. doi:10.1259/dmfr.20120443.

19. Nkenke, E., S. Zachow, M. Benz, T. Maier, K. Veit, M. Kramer, S. Benz, G. Häusler, F. Wilhelm Neukam, and M. Lell. 2004. "Fusion of Computed Tomography Data and Optical 3D Images of the Dentition for Streak Artefact Correction in the Simulation of Orthognathic Surgery." *Dento Maxillo Facial Radiology* 33 (4): 226–32. doi:10.1259/dmfr/27071199.
20. Oliveira-Santos, Thiago, Christian Baumberger, Mihai Constantinescu, Radu Olariu, Lutz-Peter Nolte, Salman Alaraibi, and Mauricio Reyes. 2013. "3D Face Reconstruction from 2D Pictures: First Results of a Web-Based Computer Aided System for Aesthetic Procedures." *Annals of Biomedical Engineering* 41 (5): 952–66. doi:10.1007/s10439-013-0744-3.
21. Pauwels, R, O Nackaerts, N Bellaiche, H Stamatakis, K Tsiklakis, A Walker, H Bosmans, et al. 2013. "Variability of Dental Cone Beam CT Grey Values for Density Estimations." *The British Journal of Radiology* 86 (1021): 20120135–20120135. doi:10.1259/bjr.20120135.
22. Plooij, J. M., G. R. J. Swennen, F. A. Rangel, T. J. J. Maal, F. A. C. Schutyser, E. M. Bronkhorst, A. M. Kuijpers–Jagtman, and S. J. Bergé. 2009. "Evaluation of Reproducibility and Reliability of 3D Soft Tissue Analysis Using 3D Stereophotogrammetry." *International Journal of Oral and Maxillofacial Surgery* 38 (3): 267–73. doi:10.1016/j.ijom.2008.12.009.
23. Ramos-Cabrer, P., J. P. M. van Duynhoven, A. Van der Toorn, and K. Nicolay. 2004. "MRI of Hip Prostheses Using Single-Point Methods: In Vitro Studies towards the Artifact-Free Imaging of Individuals with Metal Implants." *Magnetic Resonance Imaging* 22 (8): 1097–1103. doi:10.1016/j.mri.2004.01.061.
24. Rangel, Frits A., Thomas J.J. Maal, Stefaan J. Bergé, Olivier J.C. van Vlijmen, Joanneke M. Plooij, Filip Schutyser, and Anne Marie Kuijpers-Jagtman. 2008. "Integration of Digital Dental Casts in 3-Dimensional Facial Photographs." *American Journal of Orthodontics and Dentofacial Orthopedics* 134 (6): 820–26. doi:10.1016/j.ajodo.2007.11.026.
25. Ronse, Christian, and Vincent Agnus. 2005. "Morphology on Label Images: Flat-Type Operators and Connections." *Journal of Mathematical Imaging and Vision* 22 (2-3): 283–307. doi:10.1007/s10851-005-4895-1.
26. Spin-Neto, R, E Gottfredsen, and A Wenzel. 2014. "Variation in Voxel Value Distribution and Effect of Time between Exposures in Six CBCT Units." *Dentomaxillofacial Radiology* 43 (4): 20130376. doi:10.1259/dmfr.20130376.
27. Swennen, G. R. J., E. -L. Barth, C. Eulzer, and F. Schutyser. 2007. "The Use of a New 3D Splint and Double CT Scan Procedure to Obtain an Accurate Anatomic Virtual Augmented Model of the Skull." *International Journal of Oral and Maxillofacial Surgery* 36 (2): 146–52. doi:10.1016/j.ijom.2006.09.019.



28. Swennen, G.R.J., M.Y. Mommaerts, J. Abeloos, C. De Clercq, P. Lamoral, N. Neyt, J. Casselman, and F. Schutyser. 2009. "A Cone-Beam CT Based Technique to Augment the 3D Virtual Skull Model with a Detailed Dental Surface." *International Journal of Oral and Maxillofacial Surgery* 38 (1): 48–57. doi:10.1016/j.ijom.2008.11.006.
29. Tzou, Chieh-Han John, Nicole M. Artner, Igor Pona, Alina Hold, Eva Placheta, Walter G. Kropatsch, and Manfred Frey. 2014. "Comparison of Three-Dimensional Surface-Imaging Systems." *Journal of Plastic, Reconstructive & Aesthetic Surgery* 67 (4): 489–97. doi:10.1016/j.bjps.2014.01.003.
30. Vogel, A.B., F. Kilic, F. Schmidt, S. Rübél, and B.G. Lapatki. 2015. "Dimensional Accuracy of Jaw Scans Performed on Alginate Impressions or Stone Models: A Practice-Oriented Study." *Journal of Orofacial Orthopedics / Fortschritte Der Kieferorthopädie* 76 (4): 351–65. doi:10.1007/s00056-015-0296-2.
31. Wang, G., T. Frei, and M. W. Vannier. 2000. "Fast Iterative Algorithm for Metal Artifact Reduction in X-Ray CT." *Academic Radiology* 7 (8): 607–14.
32. Weinberg, Seth M., Sybill Naidoo, Daniel P. Govier, Rick A. Martin, Alex A. Kane, and Mary L. Marazita. 2006. "Anthropometric Precision and Accuracy of Digital Three-Dimensional Photogrammetry: Comparing the Genex and 3dMD Imaging Systems with One Another and with Direct Anthropometry." *The Journal of Craniofacial Surgery* 17 (3): 477–83.
33. Wiranto, Matthew G., W. Petrie Engelbrecht, Heleen E. Tutein Nolthenius, W. Joerd van der Meer, and Yijin Ren. 2013. "Validity, Reliability, and Reproducibility of Linear Measurements on Digital Models Obtained from Intraoral and Cone-Beam Computed Tomography Scans of Alginate Impressions." *American Journal of Orthodontics and Dentofacial Orthopedics* 143 (1): 140–47. doi:10.1016/j.ajodo.2012.06.018.
34. Yazdi, Mehran, Mehran Yazdia, Luc Gingras, and Luc Beaulieu. 2005. "An Adaptive Approach to Metal Artifact Reduction in Helical Computed Tomography for Radiation Therapy Treatment Planning: Experimental and Clinical Studies." *International Journal of Radiation Oncology, Biology, Physics* 62 (4): 1224–31. doi:10.1016/j.ijrobp.2005.02.052.
35. Yu, Hengyong, Kai Zeng, Deepak K. Bharkhada, Ge Wang, Mark T. Madsen, Osama Saba, Bruno Policeni, Matthew A. Howard, and Wendy R. K. Smoker. 2007. "A Segmentation-Based Method for Metal Artifact Reduction." *Academic Radiology* 14 (4): 495–504. doi:10.1016/j.acra.2006.12.015.
36. Zhang, Guangming, James J. Xia, Michael Liebschner, Xiaoyan Zhang, Daeseung Kim, and Xiaobo Zhou. 2016. "Improved Rubin–Bodner Model for the Prediction of Soft Tissue Deformations." *Medical Engineering & Physics* 38 (11): 1369–75. doi:10.1016/j.medengphy.2016.09.008.

37. Zhang, Yongbin, Lifei Zhang, X. Ronald Zhu, Andrew K. Lee, Mark Chambers, and Lei Dong. 2007. "Reducing Metal Artifacts in Cone-Beam CT Images by Preprocessing Projection Data." *International Journal of Radiation Oncology, Biology, Physics* 67 (3): 924–32. doi:10.1016/j.ijrobp.2006.09.045.



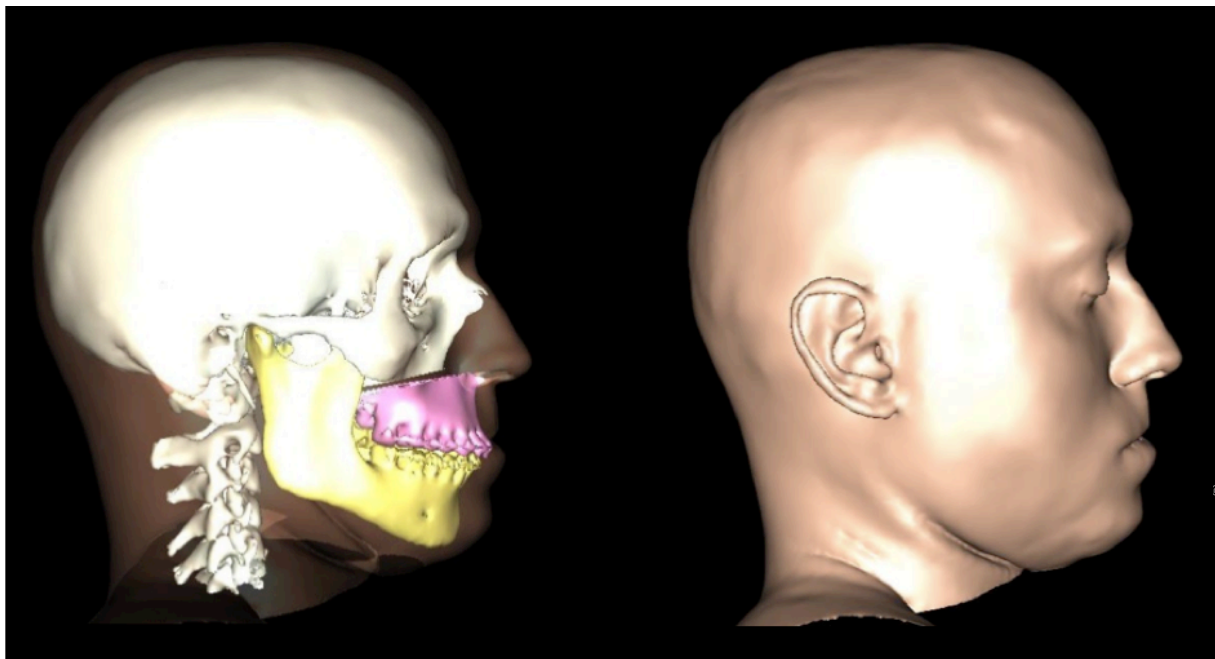
## Chapter 4

### Planning and Simulation

---

*In chapter 3, we have explained how a 3D virtual model of the patient's face was achieved thanks to a semi-automated segmentation pipeline based on mathematical morphological operators. Once modeling was achieved, we were able to address planning and simulation in Chapter 4, since simulation requires both, surface and volume meshes. On the one hand, **surface meshes** consist of patient facial anatomy. On the other hand, tetrahedron-based **volume meshes** are needed as input data for most mechanical engines.*

---



In a first part, we start describing how we achieved prerequisite surgical planning consisting in mathematically “converting” the surgical cutting plane, as well as specifying and quantifying the displacement of facial bone segments. This planning step is achieved using surface meshes.

To do so, we had to choose a set of anatomically relevant points in order to define cutting plane and axis of both rotation and translation. Once the cutting plane was defined, the mesh could be cut into two separate sub-meshes. Then, points and axes were defined in order to apply bone movements. For experimental purposes, planning was initially performed on a segmented CT-Scan from a plastic head model that has been actually cut for validation purposes of navigation, as we will see in chapter 6. Planning was then adapted to real patient CT Scans.

In a second part, we approach **simulation** through a state of the art of available methods especially the ones appropriate for orthognathic surgical simulation.

Then, in a third part, we will describe the methods available in IRCAD.

In a fourth part, we will explain how we developed a software program meant to **simulate** the alterations of facial soft tissues resulting from the surgical displacement of underlying bone segments. This step required volume meshes, which were processed from segmented DICOM images of patients’ CT-Scans using approaches described in Chapter 3.

In a last part, we will evaluate our simulation software through comparison of the simulation outcome with the ground truth consisting of surface meshes extracted from postoperative CT-Scans.

### 4.1 Surgical planning: cutting the bone mesh and moving bone segments

In a first part, we start describing how we achieved prerequisite surgical **planning** consisting in mathematically “converting” the surgical cutting plane, as well as specifying and quantifying the displacement of facial bone segments. This planning step is achieved using surface meshes.

To do so, we had to choose a set of anatomically relevant points in order to define the cutting plane. Once the cutting plane was defined, the mesh could be cut into two separate sub-meshes representing, respectively, the maxilla cut segment and the remaining upper facial skeleton. Then, points allowing defining axes were defined in order to apply bone displacement. For experimental purposes, planning was initially performed on a segmented CT-Scan from a plastic head model that has been actually cut for validation purposes of navigation, as we will see in Chapter 6. Planning was then adapted to actual patient CT Scans.

We used the 3D VSP software, then its evolved version VR-Planning (Koehl, Soler, and Marescaux 2002; Soler, Mutter, and Marescaux 2011).

The initial step relied on mathematically defining the displacement applied to the maxilla. It consisted in geometrically modeling the surgical displacements.

In order to do so, we needed to:

- model the cutting plane used for maxilla section.
- generate new models (surface meshes) of the resulting separated segments.
- select a set of reference points along the maxilla which defines axis of both translation and rotation allowing to mimic surgical displacements.
- convert the rotational surgical displacements (defined in clinical routine as a length in millimeters) (i.e.: pitch, yaw and roll), into an angle defined in degrees.
- apply the transformation (translation and rotation) to the meshes in relation to the previously defined axes.

#### 4.1.1 Cutting planes definition

Virtual section of the maxilla was planned to mimic as closely as possible the actual surgical procedure. Yet, the surgeon does not cut the maxilla along a unique pseudo-axial plane due to anatomical constraints. Indeed, only a restricted space is available laterally between the lower part of the zygomatic bone (cheekbone) cranially, and the roots of upper molar teeth, caudally. Medially, the osteotomy shall end in the lower part of the lateral wall of the piriform aperture (Cf. Figure 2.1). Subsequently, the osteotomy design consists in the combination of two planes symmetrical (in relation to the median sagittal plane). Each of these planes starts, on each side, from the maxillo-zygomatic pillar laterally, to the lower lateral part of the piriform aperture and the intersinuso-nasal wall medially. Additionally, a superior safety margin of 5mm must be applied above the dental apices all along the cutting plane in order to preserve teeth integrity (Cf. Chap 2, Fig 2.1).

Therefore, in order to model each of these two planes, three points had ideally to be interactively selected on the maxilla 3D surface mesh extracted from patients' CT. In such case, two points were selected along the lateral wall of the maxilla, and the third one chosen in order to mimic the appropriate angle allowing cutting the lower lateral part of the piriform orifice (Cf. Figure 4.1).

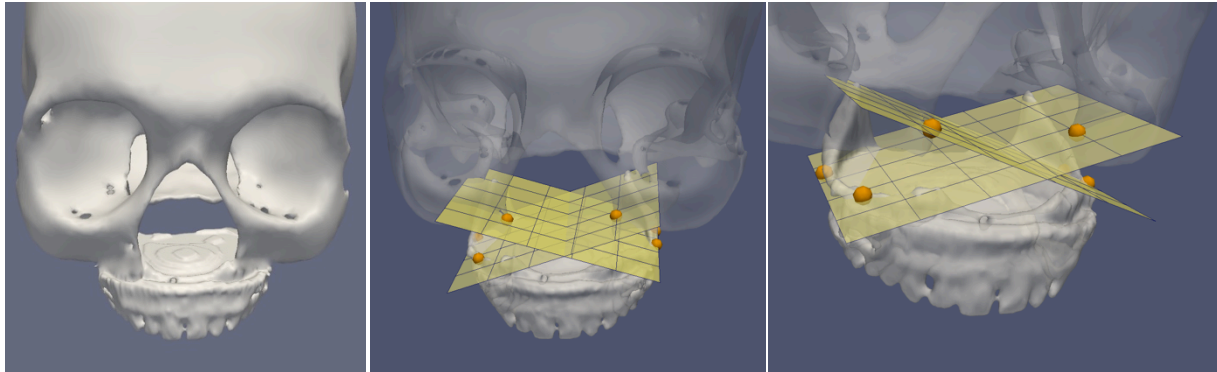


**Figure 4.1: Definition of the maxilla surgical cutting plane modeled as two symmetrical planes** (in relation to the median sagittal plane), each of them being defined by three points (orange) using segmented images from a plastic head model CT scan.

Subsequently, the 3D model was cut into two subsets according to the combination of the resection planes. Thanks to that, transformation could be applied to the cut maxillary in order to plan surgical-like target positions.

The next step was to compute modeling of the two maxillary subsets obtained after planning the cutting plane (Cf. Figure 4.2).

In order to generate two sub-meshes resulting from the section of the whole maxilla, two methods could be used: a **voxel-based** or a **mesh-based** approach.

The **voxel-based approach** consisted in using the maxilla mask. This mask was cut into a couple of voxel subsets. Then, every voxel subset was meshed independently.

The **mesh-based approach** consisted in separating the maxilla mesh into two parts. Subsequently, every mesh subset became opened along the section plane. These openings could optionally be closed through a “re-meshing step”.

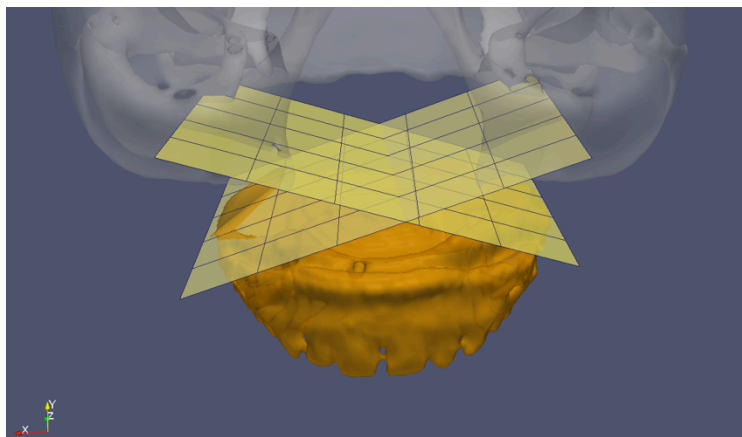


**Figure 4.2: Computing a new mesh subset of the maxilla (orange):** it is located under the combination of the cutting planes resulting from a mesh-based approach. This step allowed planning the surgical section of the lower maxilla.

Actually, in our software, we have implemented a mesh-based simplified approach, approximating the combination of the two cutting planes as a unique one. Such a mesh-cutting plane was thus defined by selecting three points. Therefore, the maxilla mesh was considered as the set of triangles located under this plane.

### 4.1.2 Software integration

**In practice, using our software (Cf. Figure 4.3),** when clicking on the “Cut by plan” button, the user needed to set a position to the three points defining the cutting plane. To do so, the user proceeded by clicking on the skull mesh while pressing the control key. Once the three points were positioned, another click would select and move the nearest already positioned point to the newly defined position.

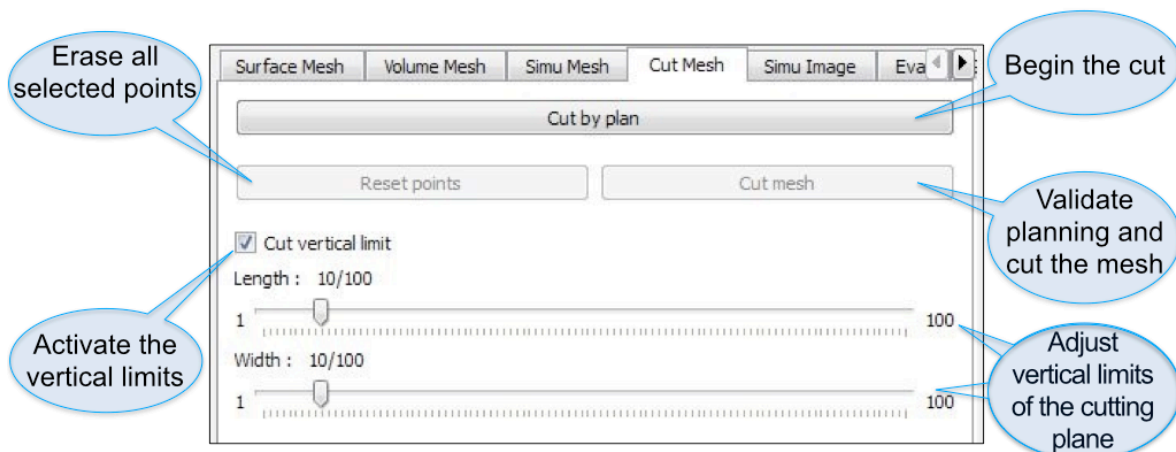


**Figure 4.3: Planning software interface** depicting the features used to define and apply the maxilla cutting plane.

Once the three points were positioned, the cutting plane appeared, and the user could click on the “Cut mesh” button to cut the skull mesh and create both, the maxilla cut segment and the remaining upper facial skeleton.

In case the plane cut off an unexpected piece of the skull, the “Cut vertical limit” checkbox could be used. The user could adjust the plane with the sliders and the cut was achieved with vertical limits corresponding to the displayed plane limits.

Additionally, we approximated the surgical displacement of the mandible (performed thanks to bilateral sagittal cuts through the ramus and corpus) as the displacement of the whole mandible.



### 4.1.3 Translation and rotation axes medical definition

#### 4.1.3.1 Translation medical definition

Postero-anterior **translation** is performed along an axis defined by the intersection of the two cutting planes simulating the actual surgical section of the maxilla (Cf. Figure 4.4).

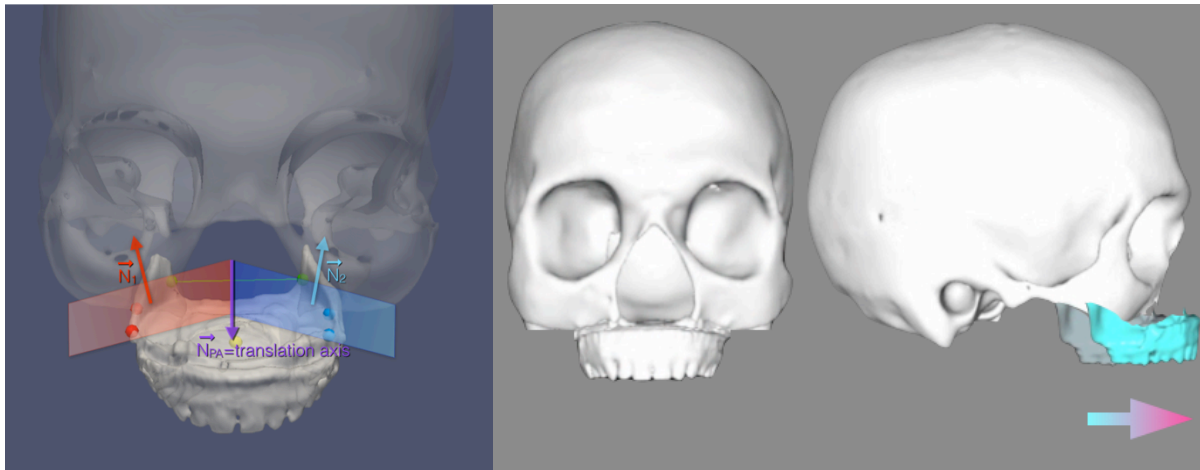


**Figure 4.4:** Postero-anterior translation axis was defined as vector  $N_{PA}$  which was computed as the vectorial product of the 2 resection plane normals ( $N_1$  and  $N_2$ ).

#### 4.1.3.2 Rotation medical definition

Axis passing through the red (respectively, blue) points defines the right (respectively, left) roll. The pitch is defined by the axis passing through the green points. Yaw is defined by the axis passing through the yellow point and normal to the plane defined by the red and green points (Cf. Figure 4.5), according to the formula:

$$\vec{n} = \overline{P_4P_5} \wedge \overline{P_1P_0}$$

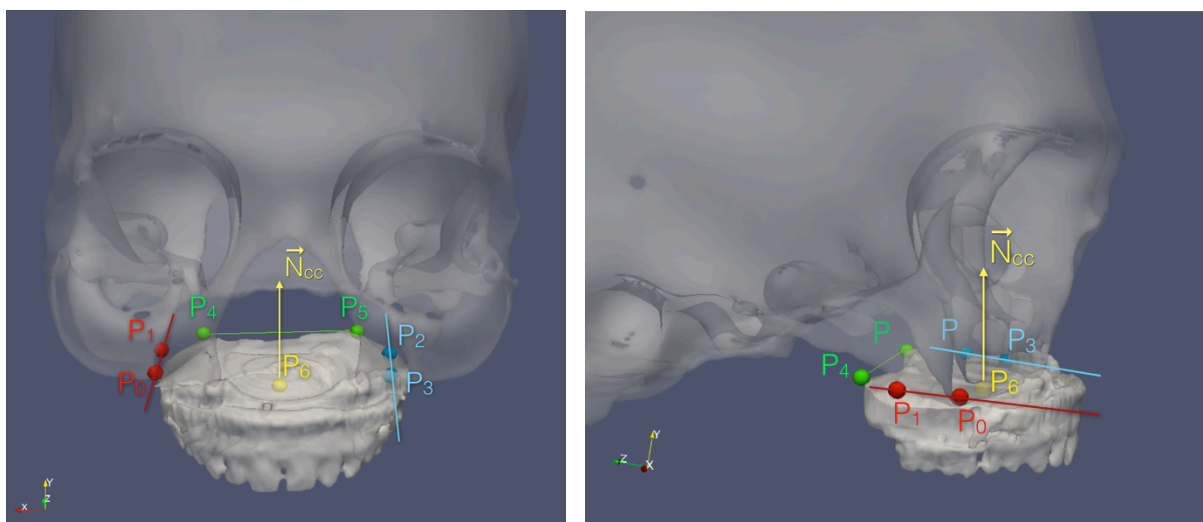


**Figure 4.5:** The set of 7 points interactively chosen to define 4 rotation axes allowing to plan for surgical movements in 3 dimensions. Axis passing through the red (respectively, blue) points define the right (respectively, left) roll (Cf. Fig 4.6 and 4.7). The pitch is defined by the axis passing through the green points. Yaw is defined by the axis passing through the yellow point and normal to the plane defined by the red and green points.

## 4.1. Surgical planning: cutting the bone mesh and moving bone segments

The yellow point (Cf. Figure 4.5) has been interactively placed at the center of the palate, which seemed logical according to the surgical workflow.

In order to convert the rotational contribution of the surgical displacement defined as a length in millimeters, into an angle defined in degrees (pitch, yaw and roll), we computed anatomical metrics thanks to the selected points as follows:

$$\text{Maxillary postero-anterior length} = \frac{P_0P_4 + P_5P_3}{2}$$

$$\text{Maxillary radius} = \frac{P_6P_1 + P_6P_0 + P_6P_2 + P_6P_3}{4}$$

$$\text{Maxillary lateral width} = \frac{P_2P_1 + P_0P_3}{2}$$

Subsequently, angles can be computed:

$$\text{Pitch angle} = \arcsin \frac{\text{pitch(mm)}}{\text{maxillary posteroanterior length}}$$

$$\text{Yaw angle} = \arcsin \frac{\text{yaw(mm)}}{\text{maxillary radius}}$$

$$\text{Roll angle} = \arcsin \frac{\text{roll(mm)}}{\text{maxillary lateral width}}$$

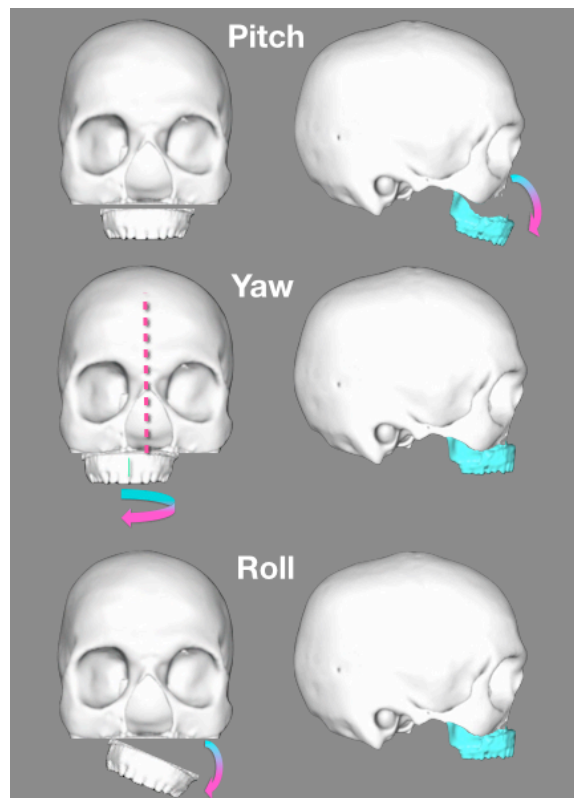


**Figure 4.6: Definitions of rotational displacements of the maxilla.**

#### 4.1.4 Mathematical conversion of the medical definition of maxillary model displacements

In our software, we actually used a simplified approach, using conventional rotational axes: longitudinal, transversal and sagittal ones (Cf. Figure 4.7). Therefore we used the pitch, yaw and roll of the maxilla.

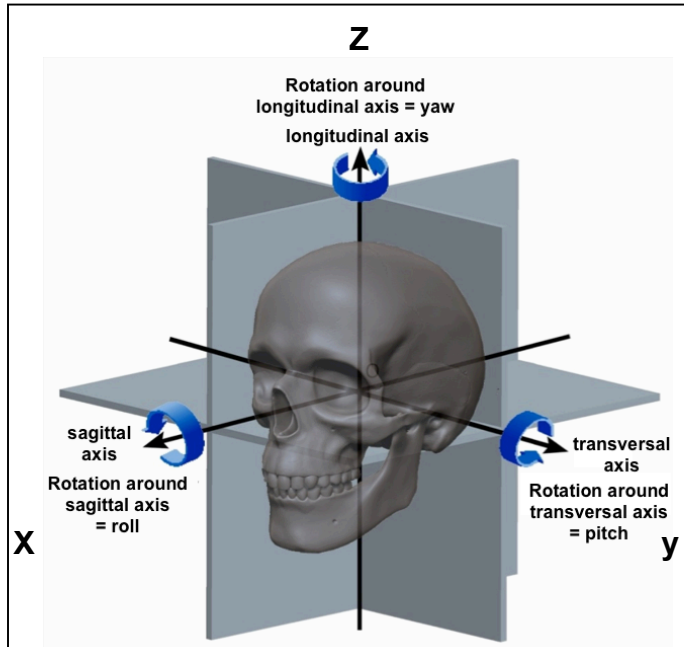


Figure 4.7: Schematic representation of the 3 axes and definition of the elementary rotational displacements. (Roll along X axis, Pitch along Y axis, Yaw along Z axis).

##### 4.1.4.1 Translation:

Postero-anterior translation axis was still computed as the vectorial product of the 2 resection plane normals.

Let  $N$  be this unit vector of the displacement,  $d$  the value of the displacement expressed in mm, therefore the matrix corresponding to this displacement is:

$$T(d,N) = \begin{bmatrix} 1 & 0 & 0 & dN_{PAx} \\ 0 & 1 & 0 & dN_{PAy} \\ 0 & 0 & 1 & dN_{PAz} \\ 0 & 0 & 0 & 1 \end{bmatrix}$$

#### 4.1.4.2 Rotation

Using the classical basis of a direct coordinate system XYZ (cf. Fig 4.7)<sup>21</sup>, we were therefore able to establish the matrices for rotation around every axis.

##### Pitch (Y-axis)

$$R_y(\theta) = \begin{bmatrix} \cos\theta & 0 & \sin\theta & 0 \\ 0 & 1 & 0 & 0 \\ -\sin\theta & 0 & \cos\theta & 0 \\ 0 & 0 & 0 & 1 \end{bmatrix}$$

##### Yaw (Z-axis)

$$R_z(\theta) = \begin{bmatrix} \cos\theta & -\sin\theta & 0 & 0 \\ \sin\theta & \cos\theta & 0 & 0 \\ 0 & 0 & 1 & 0 \\ 0 & 0 & 0 & 1 \end{bmatrix}$$

##### Roll (X-axis)

$$R_x(\theta) = \begin{bmatrix} 1 & 0 & 0 & 0 \\ 0 & \cos\theta & -\sin\theta & 0 \\ 0 & \sin\theta & \cos\theta & 0 \\ 0 & 0 & 0 & 1 \end{bmatrix}$$

---

<sup>21</sup> source : [http://inside.mines.edu/fs\\_home/gmurray/ArbitraryAxisRotation](http://inside.mines.edu/fs_home/gmurray/ArbitraryAxisRotation)

Any motion can be described using a 4x4 matrix. The above matrices consist in rotation around the origin of the coordinate system. Each of these matrices can easily be combined (ie: multiplied) in order to define translation and rotation around any axis. Therefore, rotation  $\theta$  around an axis defined by the vector which coordinates are  $(u, v, w)$ , is defined by:

$$R(\text{axis,angle}) = \begin{bmatrix} \frac{u^2 + (v^2 + w^2)\cos\theta}{u^2 + v^2 + w^2} & \frac{uv(1 - \cos\theta) - w\sqrt{u^2 + v^2 + w^2}\sin\theta}{u^2 + v^2 + w^2} & \frac{uw(1 - \cos\theta) + v\sqrt{u^2 + v^2 + w^2}\sin\theta}{u^2 + v^2 + w^2} & 0 \\ \frac{uv(1 - \cos\theta) + w\sqrt{u^2 + v^2 + w^2}\sin\theta}{u^2 + v^2 + w^2} & \frac{v^2 + (u^2 + w^2)\cos\theta}{u^2 + v^2 + w^2} & \frac{vw(1 - \cos\theta) - u\sqrt{u^2 + v^2 + w^2}\sin\theta}{u^2 + v^2 + w^2} & 0 \\ \frac{uw(1 - \cos\theta) - u\sqrt{u^2 + v^2 + w^2}\sin\theta}{u^2 + v^2 + w^2} & \frac{vw(1 - \cos\theta) + u\sqrt{u^2 + v^2 + w^2}\sin\theta}{u^2 + v^2 + w^2} & \frac{w^2 + (u^2 + v^2)\cos\theta}{u^2 + v^2 + w^2} & 0 \\ \frac{0}{0} & \frac{0}{0} & \frac{0}{0} & 1 \end{bmatrix}$$

Thanks to these mathematical conversions of elementary geometrical movements, we were able to define a set of positions that were further used for navigation evaluation (Cf. Figure 4.8 and table 4.1).

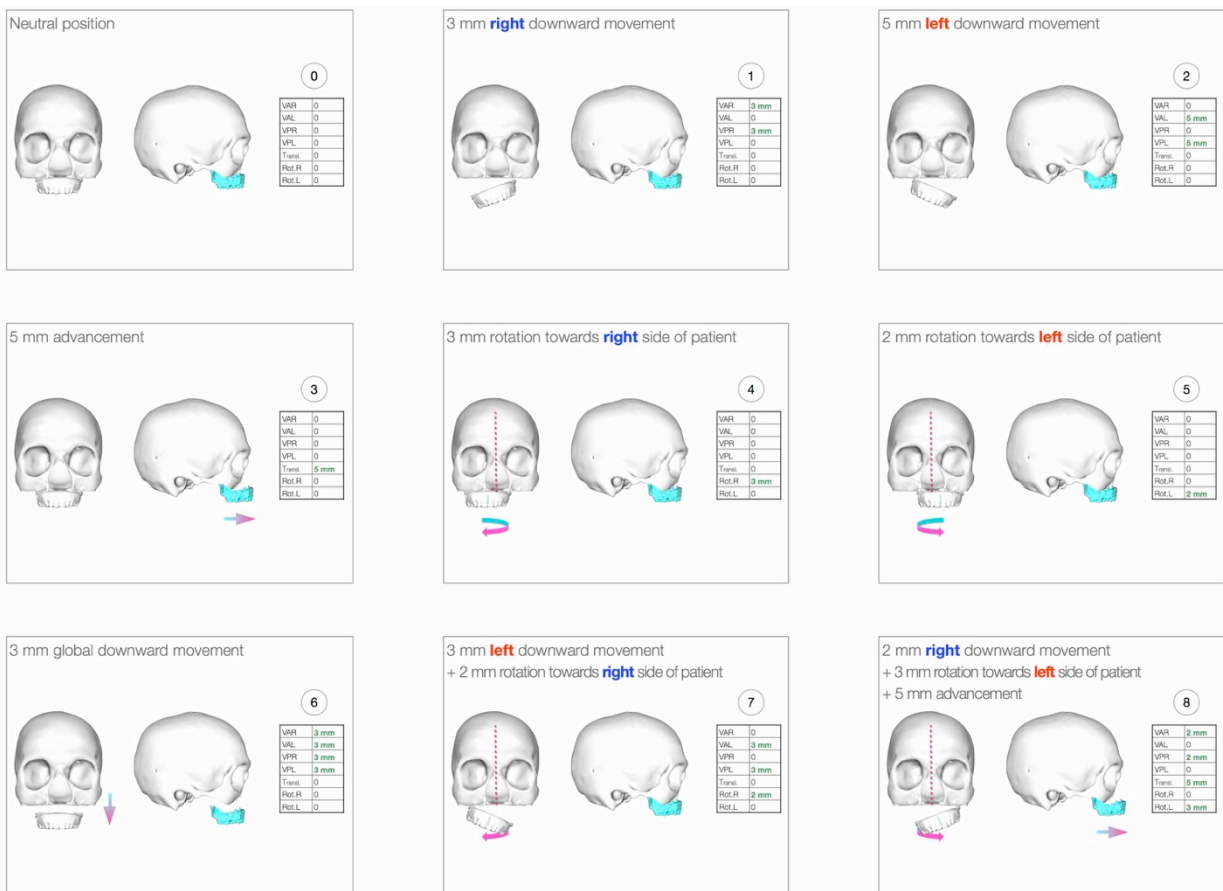


**Figure 4.8: Examples of common surgical movements, from simple ones along one axis, to complex ones along 3 different axes.**

## 4.1. Surgical planning: cutting the bone mesh and moving bone segments

### 4.1.4.3 Examples

Task Ref	Maxillary target position	Maxillary displacement	Transformation Matrix	Vertical dimension (mm)				Translation (mm)	Rotation (mm)	
				Anterior		Posterior			Postero anterior	towards Right side of patient
			<b>R(Axis, Angle)</b> <b>T</b>	Right	Left	Right	Left			
0	Neutral position		Matrix 4x4 identity	0	0	0	0	0	0	0
1	3 mm right downward movement	Roll 3mm Right	$R(P_1P_0, \text{roll\_angle}(3\text{mm}))$	3	0	3	0	0	0	0
2	5 mm left downward movement	Roll 5mm Left	$R(P_2P_3, \text{roll\_angle}(5\text{mm}))$	0	5	0	5	0	0	0
3	5 mm advancement	Translation postero anterior 5 mm	$T(N, 5\text{mm})$	0	0	0	0	5	0	0
4	3 mm right rotation	Yaw 3mm Right	$R(\text{normal to the point } P_6, 3\text{mm})$	0	0	0	0	0	3	0
5	2 mm left rotation	Yaw 5mm Left	$R(\text{normal to the point } P_6, -5\text{mm})$	0	0	0	0	0	0	2
6	3 mm global downward movement		$T([0.0, -1], 3\text{mm})$	3	3	3	3	0	0	0
7	3 mm left downward movement + 2 mm right rotation	Roll 3mm Left + Yaw 2mm Right	$R(\text{normal to the point } P_6, 3\text{mm}) \times R(P_2P_3, \text{roll\_angle}(3\text{mm}))$	0	3	0	3	0	2	0
8	2 mm right downward movement + 3 mm left rotation + 5 mm advancement	Roll 2mm Right + Yaw 3mm Left + Translation postero anterior 5mm	$R(P_1P_0, \text{roll\_angle}(3\text{mm})) \times R(\text{normal to the point } P_6, -3\text{mm}) \times T(N, 5\text{mm})$	2	0	2	0	5	0	3

**Table 4.1:** Numerical example of the conversion of 8 surgical target positions into mathematical language using transformation matrices.

## 4.2. Simulation in orthognathic surgery

### 4.2.1. State of the art

In this chapter, we will propose a quick state of the art about the different methods in real-time simulation of living tissues that could be applied to our purpose. We remind here that our goal is to compute the deformation of the facial soft tissues secondary to the surgical displacement of the underlying facial skeleton. Thanks to the analysis of these methods confronted to our goal, we will choose one of them and explain why it was not suited to our purpose.

Soft tissue modeling has already been the subject of many articles and thesis.

When simulation is considered, two constraints become crucial: computational efficiency and accuracy. Indeed, accuracy requires time consuming calculations. The highest the accuracy is required, the more the real-time feature is compromised. If real-time interaction is crucial in a training simulator, it is accuracy which prevails in surgical planning (Nisansala et al. 2015; Herve Delingette and Ayache, n.d.).

Cevitanes (Cevitanes et al. 2010) summarizes the methods that attempt to predict facial soft-tissue changes resulting from skeletal displacement. He explains that “such methods use approximation models, since direct formulation and analytic resolution of the equations of continuum mechanics are impossible with such geometric complexity”. Several models have been proposed.

The modeling methods for living tissues consist of **geometrical models** and **physical models**. As opposed to physical models, the behavior of geometrical models is not based on the laws of physics, but exclusively on mathematical concepts.

The standard **geometrical** method is the **chain mail method** (Chapter 4.2.1.1). Among the family of **physical** simulation methods, two categories can be separated: the **discrete** (heuristic) models and the **continuum**-mechanics-based models (Chapter 4.2.1.2).

The main types of discrete models are the **mass-spring models**. The method used in these models can be generalized to describe the connected particles systems. The main continuum-mechanics-based methods are the **finite difference method**, the **finite elements method**, the **mass-tensor method**, and the **finite volume method**. There are many other methods that cannot obviously be applied to our purpose, such as the boundary element method (James and Pai 1999; Monserrat et al. 2001; James and Pai 2003), or the long element method (Monserrat et al. 2001; K. Sundaraj, Mendoza, and Laugier 2002; Balaniuk and Salisbury 2003; Kenneth Sundaraj 2004).

#### 4.2.1.1 Geometrical models

As stated previously, these methods are not based on the laws of physics, but exclusively on mathematical concepts.

In these models, the displacements of soft-tissue vertices are estimated with the movements of neighboring hard-tissue vertices, (Schutyser et al. 2000) or bone-displacement vectors are simply applied on the vertices of the soft-tissue mesh (Xia et al. 2000).

The main geometrical method is the **Chain mail model**. This method has been designed in order to allow real-time simulation of deformable objects with which interaction is possible. A **2D Chain mail** algorithm, initially proposed by Gibson et al. (Gibson et al. 1997), has later been improved several times (Schill et al. 1998; Li and Brodlie 2003).

As implied by its name, this model can be compared to a chain mail (Cf. Figure 4.9). The considered volume is divided into small rigid elements that can have a movement in relation to their neighbors. These movements are determined by laws that constraint minimum and maximum distances between two neighboring links. If the movement applied to the initial link does not qualify for the distance constraints, the position of its neighbors is modified in order to find a position compatible with the model. Therefore, the movement propagates from one element to another in order to achieve a satisfactory global balance. The implementation of the minimum and maximum distance constraint values allows modifying the rigidity of the simulated object. At last, it is possible to implement the specifications of the distance constraints according to the direction of the links, therefore making the model sensitive to the orientation of the movements it is subject to.

Thanks to its extreme simplicity, this model is very fast and allows real-time applications for rather large objects. Nevertheless, the behavior of tissues simulated on this basis is far from being realistic, particularly because this method implies that the deformation remains localized. If it is possible to adapt this model in order to confer a more elastic behavior, this requires, in some steps of the algorithm, imposing an elastic relaxation between the links, which is costly in terms of processing time. The position of the different elements is modified accordingly in order to reach a configuration of minima energy.

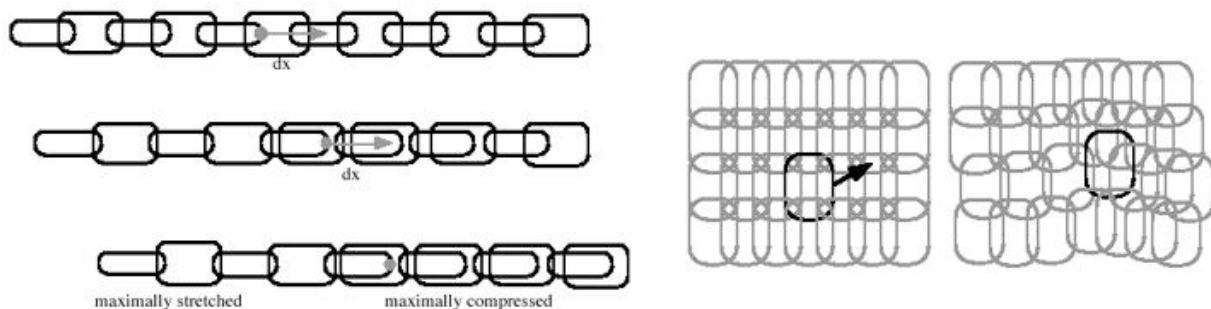


**Figure 4.9: Illustration of the 2D Chain mail deformation model.** When a chain link is moved, the distance constraints are applied to its neighbours. Source: Gibson et al. 1997.



Complementary research (Frisken-Gibson 1999) have shown that it was possible to simulate several types of elastic behavior, by implementing both, the distance constraints and their relaxation, but only in the unidirectional case. In addition, such modifications can induce laws that are no longer linear.

**The 3D Chain mail algorithm** is a novel algorithm based on the linked volumetric representation (Nisansala et al. 2015). It is also used in several medical simulations, since it allows the fast propagation of deformation. In chain mail, a list is maintained with each element's current position and old positions. When a selected element is moved, its old position and element indicator is updated in the list of moved elements. Accordingly, its neighbors in top, left, right and bottom are added to the lists of candidate for movement. The lists of candidate elements are processed until the entire candidate list is exhausted. The candidate lists are processed in right, left, top, bottom order. It begins with the first element in the list. The element is moved until it satisfies the stretch and shear constraints between sponsoring element and the list element.

In the end, the model parameters being apart from measurable physical properties, an empirical approach is required in order to adjust the different constants. Furthermore, the computed deformations are not always realistic, which makes it elusive to use such method in a predictive application.

### 4.2.1.2 Physical models

Terzopoulos et al were the first to use the laws of mechanics to animate graphic scenes of deformable objects (Demetri Terzopoulos et al. 1987). Their models were suited to react to external biasing such as forces, constraints or even contacts. Therefore, these are **active** models. Before Terzopoulos' research was published, physical models only consisted of **passive** models, also called **cinematic** models. Indeed, the cinematic models are built from geometric primitives and the models' points moved along trajectories defined by purely mathematical functions (Parke 1982).

Terzopoulos' initial model (Cf. Figure 4.10) is built from a lagrangian formulation of the elasticity theory and uses object discretization through finite elements. It allows representing 3D deformable objects. Such physical modeling is very general and non-linear, which requires small size computation steps, therefore long computational time. Additionally, stability of the method is not always guaranteed.

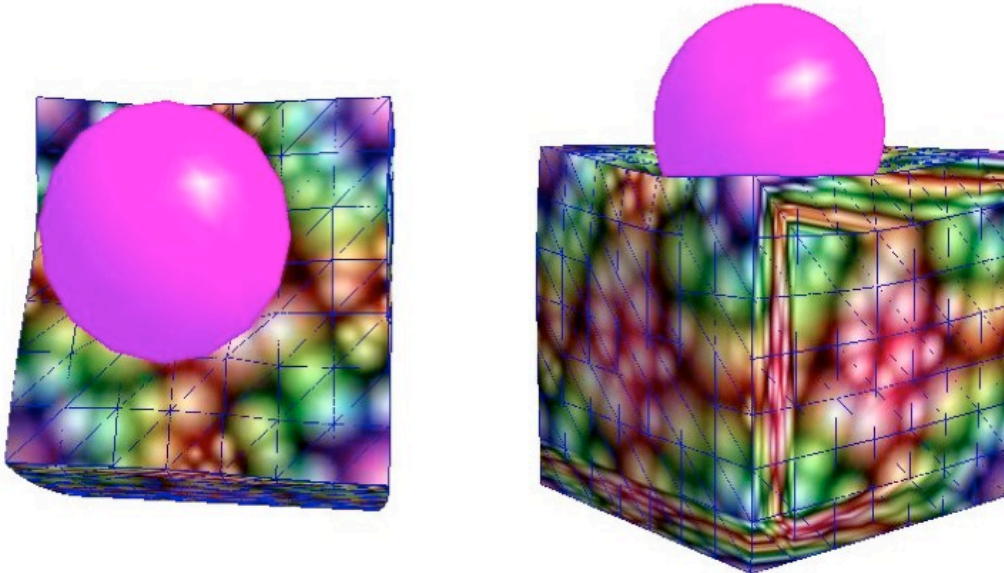


**Figure 4.10: A rigid sphere resting on a deformable solid.**

Source: M. Kelager and A. Fleron, Implementation of Deformable Objects, Department of Computer Science, University of Copenhagen, DIKU

Under Terzopoulos et al.'s impulsion, modeling based on physical principles lead to numerous studies seeking for faster methods and algorithms. Within the family of physical simulation methods, two categories can be separated: the **discrete (heuristic)** models and the **continuum-mechanics-based** models.

#### 4.2.1.2.1 Discrete methods

##### a. Mass-spring models

Mass-spring models (MSS) consist in the discretization of objects in the form of a surface or volume mesh. A mass is assigned to every node of the mesh. Possible interactions between two neighboring node are usually modeled using linear relationships. In such models, matter is not represented under a continuum fashion but under a 3D generalization of a 1D model. When describing the dynamic relations that govern movement, we obtain the following system of differential equations:

$$m_i \ddot{x}_i + d_i \dot{x}_i + g_i = f_i$$

With,

$m_i$  , the mass of the  $i^{\text{th}}$  node ,

$x_i$  , the vectorial coordinates of the  $i^{\text{th}}$  node ,

$d_i$  , the friction coefficient associated with the  $i^{\text{th}}$  node ,

$g_i$  , the internal forces applied to the  $i^{\text{th}}$  node,

$f_i$  , the external forces applied to the  $i^{\text{th}}$  node,

The internal forces that are applied to the  $i^{\text{th}}$  node are computed from the neighboring nodes:

$$g_i = \sum_{j=0}^{j<n} c_j^i e_j^i$$

With,

$n$  , the number of neighbors of the  $i^{\text{th}}$  node,

$c_j^i$  , the link rigidity value of the  $j^{\text{th}}$  neighbor of the  $i^{\text{th}}$  node,

$e_j^i$  , the deformation vector (in relation to its initial position) of the  $j^{\text{th}}$  neighbor of the  $i^{\text{th}}$  node.

The mass-spring models have been used in numerous medical applications, particularly in the simulation of the facial skin movements (Cf. Figure 4.11) (Lee, Terzopoulos, and Waters 1995), to model human expressions (Platt and Badler 1981; Waters 1987), and in facial surgery (Koch et al. 1996).

According to Nisansala (Nisansala et al. 2015), different spring constants were used to model the different tissue types based on their properties. Craniofacial simulations are one of the common simulations which use MSS (Keeve et al. 1998). Not only the deformable tissues, MSS facilitate modeling wide variety of objects including cloth, hair and deformable solid (Nedel and Thalmann 1998). Nedel and Thalmann carried out an extensive research on simulating muscles using springs. Elasticity was enhanced using theory of elasticity, especially concerning linear spring and Hooke's spring theory to calculate the force produced by linear springs. In this research they have simulated muscles only by their surfaces not the volumetric details, which could save the computing time (Granados 2008).

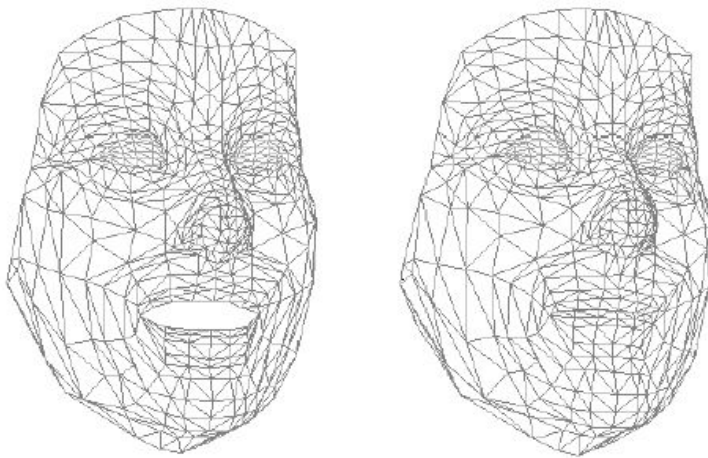


**Figure 4.11: Two faces animated by a mass-spring model.**

Source: Lee, Terzopoulos, and Waters 1995

Mass-spring models are well suited to the real-time simulation of elastic deformation, however, the mechanical behavior can be unrealistic, when only surface meshes are used.

**b. Connected particles system**

The connected particles system results from generalization of the mass-spring model. The difference here relies on the definition of elastic forces based on deformation energies (E. Promayon, P. Baconnier, C. Puech 1996; Baraff and Witkin 1998; Teschner et al. 2004). Therefore, the value of the forces that are applied to every particle can be related to particle position and to an energy function defined such that the energy is minimal in resting position:

$$f_i = -\frac{\delta E}{\delta x_i}$$

With,

$f_i$  , the force applied to the  $i^{\text{th}}$  particle

$x_i$  , the vectorial coordinates of the  $i^{\text{th}}$  particle

$E$  , the energy associated with the  $i^{\text{th}}$  particle as a function of strain.

There are a certain number of extensions and improvements depending on the method used to compute the energy. In facial soft tissue modeling, elasticity can be defined through shape memory. The non-linear property of some soft tissues can be considered through the use of maximum or minimum elongation conditions. Indeed, classical mass-spring models do not allow the simulation of realistic behavior whenever they are locally subject to important strains. Additionally, some existing models consider the non-linear relationship between the force intensity and the value of mesh nodes displacement. D'Aulignac et al. developed a model of human thigh (Cf. Figure 4.12), using these methods (d' Aulignac, Balaniuk, and Laugier 2000). The use of several sorts of springs (structural springs, shear springs, flexion springs) allows to also model more complex behavior. In particular, muscles contraction could be simulated (Chen et al. 1998). By favoring some directions of the springs, it is possible to generate an anisotropic behavior (F. B. D. Casson and Laugier 2000; F. B. de Casson 2000). Indeed, the behavior of a mass-spring model depends on the position and the direction of the edges linking the different mesh nodes. Finally, thanks to the use of generalized springs, it becomes possible to preserve distances, surfaces and even volumes. This allows submitting an object to incompressibility strains, which is the case of soft tissues (Teschner et al. 2004).

The connected particles system appears more appropriate than the mass-spring model, but the number of vertices remains a limitation regarding processing speed of the simulation.

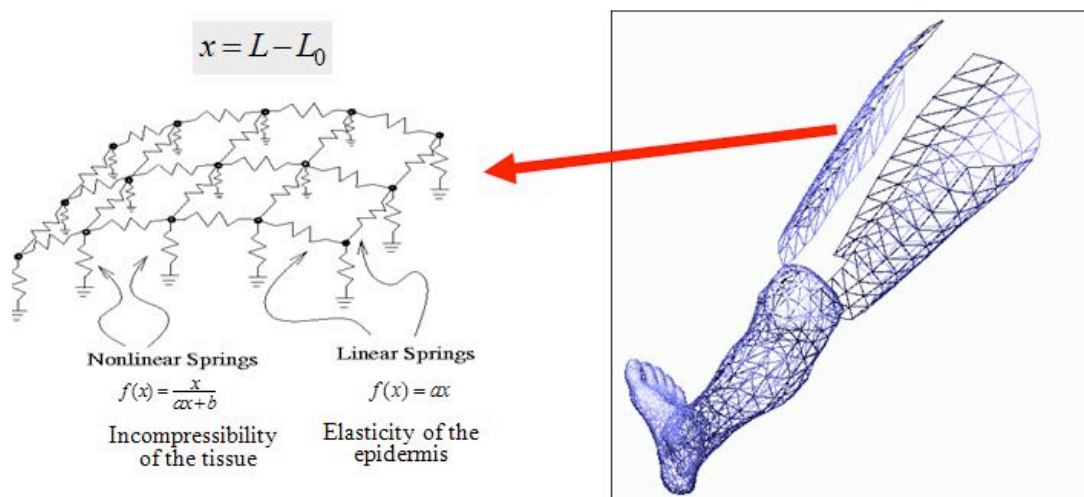


Figure 4.12: Thigh model defined through a mass-spring method.

Source : d' Aulignac, Balaniuk, and Laugier 2000

#### 4.2.1.2.2 Continuum-based methods

##### a. Finite difference method

The finite difference method can be applied when object discretization is conducted using a regular grid. In this case, movement equations are discretized through this method that allows approximating the local variations of a function using its own discretization. Nodes are defined at every intersection between the regular grid and the three-dimensional model (Demetri Terzopoulos et al. 1987). Every node is assigned with a physical property and movement equations. This therefore allows discretization of deformation energy.

The finite difference method relying on the use of a regular grid (Fig. 4.13), it is not possible to use a locally refined mesh without significantly increasing processing time. Subsequently, boundaries cannot be defined with satisfactory accuracy, which is not compatible with the requirements of our application.

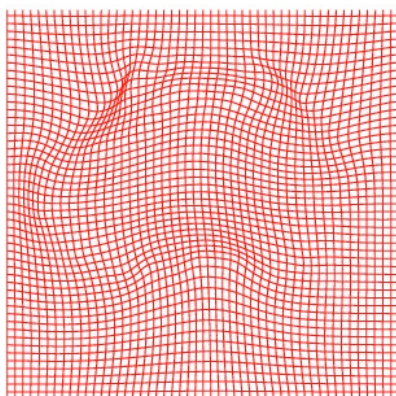


Figure 4.13: Deformation grid.

Source : Additional Results for Joint Segmentation/Registration model by shape alignment via Weighted Total Variation Minimization and Nonlinear Elasticity (Solène Ozeré, Christian Gout, Carole Le Guyader)  
<http://lmi2.insa-rouen.fr/~m2num/Ozere/resultats.html>

**b. Finite elements method**

As opposed to the finite difference method, the finite elements method consists in discretizing a continuous object using a mesh, which is not necessary regular, but consisting of cells with identical specifications (triangles, tetrahedrons, cubes, etc...). The object is discretized into small basic volumes in which it is possible to compute the result of continuum-mechanics equations. The global solution is then computed from polynomial interpolation formulas. These interpolation formulas allow evaluating the local value of strains and deformations. This method is quite versatile, since it is possible to implement computation accuracy and therefore processing speed. Indeed, the choice of the interpolation function can be modified while the initial mesh is preserved. In the case of a linear plastic mechanical model, discretization of the continuum into  $n$  nodes generates a linear system of equations such as:

$$\mathbf{K}\mathbf{u} = \mathbf{f}$$

With:

$\mathbf{K}$ , the system's stiffness matrix

$\mathbf{u}$ , the field of motion

$\mathbf{f}$ , the field of external forces applied to the system

The finite elements method has been for a long time incompatible with real-time applications. However, a number of methods have been developed in order to accelerate its resolution, therefore making it compatible with real-time constraints. For example, condensation techniques (Morten Bro-Nielsen and Cotin 1996; M. Bro-Nielsen 1998) seek at restricting the computation to the only surface nodes. We therefore obtain:

$$\mathbf{K}_{ss}\mathbf{u}_s = \mathbf{f}_s$$

Since only the vertices of the surface are subject to non-null external forces and that we are only interested in the deformation of these vertices, it is possible to simplify the following equation by removing all the null terms or the ones we have no interest in:

$$\mathbf{u}_s = \mathbf{k}_{ss}^{-1}\mathbf{f}_s$$

therefore becomes:

$$\mathbf{u} = \mathbf{k}^{-1}\mathbf{f}$$

This system then becomes quite simpler than the previous one.

It should be noted that this behavior is quasi-static, since we suppose the system to be at equilibrium. It is however possible to provide the system with a dynamic behavior by turning the initial equation into a dynamic equation:

With, 
$$\mathbf{M}\ddot{\mathbf{u}} + \mathbf{D}\dot{\mathbf{u}} + \mathbf{K}\mathbf{u} = \mathbf{f}$$

$\mathbf{M}$ , the matrix of values of the system's nodes mass

$\mathbf{D}$ , the matrix of the attenuation or friction coefficients.

The main problem remains the resolution speed. Using here again condensation and inversion methods (M. Bro-Nielsen 1998; Cotin, Delingette, and Ayache 1999; Wu and Heng 2004), or multi-resolution (Cf. Figure 4.14) (Debunne 2000), it is possible to accelerate system resolution.

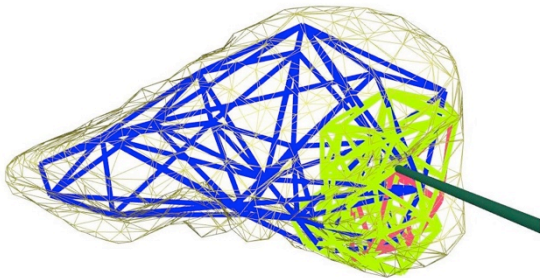


**Figure 4.14: Multi-resolution model** whose behavior is compatible with real-time applications.  
Source : Debunne 2000

Nevertheless, these methods require providing some parameters such as Young's modulus or Poisson's ratio. These values allow building the law of the medium behavior. These values can be extracted from tissue samples (Fung 1993). However, mechanical properties of tissues, particularly Young's modulus and Poisson's ratio, vary rapidly whenever the tissue no longer lies in its usual living environment, that is when it is no longer *in-vivo* but rather *in-vitro*. Characterization of *in-vivo* tissues is quite difficult due to accessibility, hygiene and tissue motion (Nava et al. 2008; Samur et al. 2007). Particularly in our case, tissues constituting the facial mask are quite numerous (skin, fat, muscles) and different (D. Terzopoulos and Waters 1990).

The finite elements method would be suited to our problem, since it is fast enough to be adapted to our application focusing on various facial tissues and numerous points. However, the specifications of the different tissues should be known, which would not be an easy task. Interesting research dedicated to maxillo-facial surgery is lead on this path by the UTC team and aims at performing facial mimics simulation using subject specific data derived from MRI technique. Zygomaticus major muscle is modeled as a transversely isotropic hyperrealistic material. Then the resulting effect of its shortening and lengthening process on the facial mimics simulation was performed using Finite Element Analysis (Dao et al. 2013) (Dakpé et al. 2016).

However, we based our research on CT scan acquisition, which prevented us to proceed in such an interesting direction.



### c. Mass-tensor method

The mass-tensor method proposes local rewriting of finite elements equations. The point of such method is to allow fast resolution through iterative process for a similar cost to the one of mass-spring method. The resulting equation system has the following form:

$$f_i = K_{ii}u_i + \sum_{j \neq i} K_{ij}u_j$$

With,

$f_i$  , the total force applied to the  $i^{\text{th}}$  node,

$K_{ii}$  , the sum of contributions of the  $i^{\text{th}}$  node, in all the tetrahedrons adjacent to the  $i^{\text{th}}$  node,

$K_{ij}$  , the sum of contributions of the other  $j$  nodes, in all the tetrahedrons adjacent to the  $i^{\text{th}}$  node.

The  $K_{ij}$  can be computed once and for all along the pre-computation step, since they only depend on the initial geometry and on the mechanical properties of the medium. We can then introduce this force into a local dynamic equation in order to compute the field of motion of the next time point, through an iterative process:

$$m_i \ddot{u}_i = -d_i \dot{u}_i + f_i$$

With,

$m_i$  , the mass associated with the  $i^{\text{th}}$  node,

$d_i$  , the attenuation coefficient associated with the  $i^{\text{th}}$  node.

The initial method has been used to develop a surgical simulator dedicated to liver surgery (H. Delingette, Cotin, and Ayache 1999b). An extension of this model, based on St. Venant-Kirchhoff elasticity, allows considering the geometric non-linearity and therefore qualifies for a hyper-elastic class of material (Picinbono, Delingette, and Ayache 2003). The incompressibility strain is introduced through a function that penalizes volume changes. Such modifications allow an 80% reduction of the conventional mass-tensor method processing time.

Interestingly, an existing application concerning the simulation of facial soft tissue (Wouter Mollemans et al. 2003), consists in optimizing the biomechanical parameters of the model using experimental data (Wouter Mollemans et al. 2006) (W. Mollemans et al. 2007).

For purposes of computational time decrease, the two methods can be combined into a hybrid model (H. Delingette, Cotin, and Ayache 1999a). The hybrid model allows preserving a global behavior computed from a quasi-static resolution, whereas the specific mass-tensor method is only used locally.

#### d. Finite volume method

Like the finite elements method, the finite volume method uses discretization of the modeled object. The difference lies in the fact that, in the finite volume method, strain tensors designated as  $\sigma$  are used, whereas, in the finite elements method, forces derived from the deformation energy are applied to every node of the mesh. The strain tensor allows computing the internal force  $F$  by surface unit in a plane giving by the following relation:

$$F = \sigma n$$

With,

$n$ , the normal to the considered plane.

Subsequently, the total force, designated as  $F_s$  of surface facet  $S$  of a finite element, has a value of:

$$F_s = \int_s \sigma dS$$

In the case where form functions that are used are not linear, the strain tensor is constant within one element. The previous relation then becomes:

$$F_s = S\sigma n$$

The value of the force applied to every node is computed from the sum of the different contributions of the aspects adjacent to every node.

Such method has been used to model material subject to large deformations, but rarely in the case of soft tissue deformation (such method allowed simulation of muscle deformation (Cf. Figure 4.15)) (Teran et al. 2003). Subsequently, it does not seem relevant to use such method in our topic.

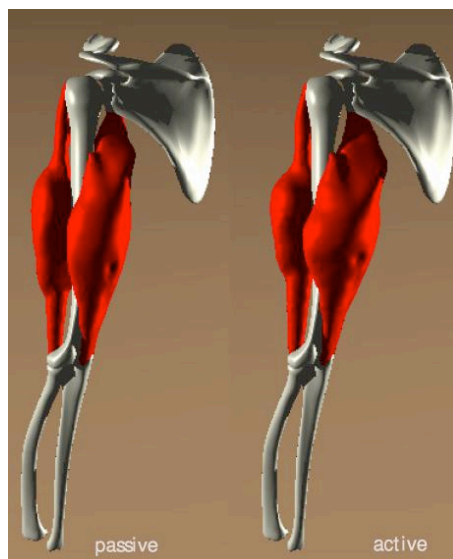


**Figure 4.15: Deformation of arm muscles through the finite volume method.**

Source: Teran et al. 2003

### 4.2.2 Preliminary Conclusion

Throughout literature, we have seen that many methods can be used for facial soft tissue simulation, as stated by Cevidanés (Cevidanés et al. 2010):

1. Purely geometric models: In these models, the displacements of soft-tissue vertices are estimated with the movements of neighboring hard-tissue vertices, (Schutyser et al. 2000) or bone-displacement vectors are simply applied on the vertices of the soft-tissue mesh (Xia et al. 2000).
2. Multi-layer mass-spring models: These models rely on the assumption that the material of an anatomic structure can be represented by a set of discrete elements, each having individual properties. Each discrete element bears a mass, and relationships between these masses are characterized by stiffness values. These models have stability problems, lack of conservation of volume, and a certain mismatch between model parameters and real physical properties (Teschner, Girod, and Girod 2001; Avril and Evans 2016; W. Mollemans et al. 2007).
3. Finite element models: These models are intensively used for the analysis of biomechanical systems. The finite element method (FEM) can offer a numeric approximation of viscoelastic deformation problems. FEM models consist of a discretization of the geometry in a set of discrete sub-domains, for which continuum mechanics equations can be formulated. In this way, the partial differential equation characterizing the deformation can be written as a matrix equation that can be solved by the computer. Although the problem is broken down in simpler elements, the number of necessary elements to obtain results of satisfying accuracy can be elevated; this usually entails substantial computation times and resources (W. Mollemans et al. 2007; Westermarck, Zachow, and Eppley 2005; Chabanas, Luboz, and Payan 2003; Schendel and Montgomery 2009).
4. Mass tensor models: These are a mixture of the easy architecture of the multilayer mass-spring models and the biomechanical relevance of FEM (Taylor 1996; W. Mollemans et al. 2007).

**Geometrical methods** can achieve realistic behavior of soft tissues using strictly mathematical or geometric principles, yet not any physical principle. However, their behavior cannot be reproduced from one patient to the other. Therefore, it is impossible to generalize their use without conducting whole new empirical calibration of the method.

Yet, **physical methods** allow simulating an accurate soft tissue behavior, yet processing speed and required specifications generally prevent from an easy achievement.

Because of their solid physical base, FEM models and mass tensor models are the most likely to provide reliable simulation results.

However, mass-spring models are suitable enough for the real-time simulation of elastic deformation, since facial soft tissue alterations are small (usually around 5 mm).

Additionally, standard mass-spring engines are widely available and their use consensual.

However, the mechanical behavior can be unrealistic, when only surface meshes are used. Subsequently, we decided to use volume mesh. We will therefore use an approach generating high quality volume meshes dedicated to mechanical engine use.

We shall emphasize that the global behavior of an object modeled through the **mass-spring method** greatly depends on the way object discretization has been conducted and on the position of the links between the different nodes. When multiplying the number of elements in order to refine the mesh, the resulting decrease of processing speed disqualifies its use for real-time applications. Since in our topic, real-time is not a critical issue, we can use numerous and dense meshes considering the deformed area.

Actually, the goal of this Thesis is neither to create a new simulation method, nor to optimize an existing one. Yet, our purpose is to provide a complete workflow (segmentation, planning, simulation and evaluation) to facilitate orthognathic surgery.

### 4.3 Methods available in IRCAD

#### 4.3.1 Language, Frameworks, library

Development of our dedicated software used the C++ programming language and was based on the IRCAD framework **fw4spl**<sup>22</sup> (FrameWork for Software Production Line).

The C++ is a programming language that offers many paradigm choices as procedural, generic, or object-oriented programming.

The fw4spl framework has been developed by IRCAD and is mainly dedicated to medical software development. Numerous libraries, such as the TetGen and the Bullet physics library are integrated in this framework.

TetGen<sup>23</sup> is written in C++ and meant to generate tetrahedral meshes from any surface mesh made of triangles. TetGen generates exact constrained Delaunay tetrahedralizations, boundary conforming Delaunay meshes, and Voronoi partitions. TetGen provides various features to generate good quality and adaptive tetrahedral meshes suitable for numerical methods, such as finite element or finite volume methods.

Bullet is a free library belonging to the category of physics engines. It is used to simulate the deformation and interactions of several soft tissues. In our case, the skin deformation results from bone displacements.

The fw4spl framework and the Bullet library are cross-platforms, that means our software runs under Linux, Windows and Mac OsX.

---

<sup>22</sup> For more details about the fw4spl framework, please consult the documentation on: <https://code.google.com/p/fw4spl/wiki/Description?wl=en>

<sup>23</sup> TetGen : <http://wias-berlin.de/software/tetgen/>

### 4.3.2 Code organization

To develop a fw4spl application, one must proceed according to the framework structure. It consists of:

- Data
- Services
- Bundles
- Communication links

A **Data** can be a single data, like an image or a video, or a data container called Composite.

A **Service** is a functionality that will work on a Data. It is always associated to a particular Data. For example, an Image has Reader, Writer and Visualization Services.

A **Bundle** is a set of **Services** having similar functionalities. For example, an in/out Bundle might group all the **Services** allowing to read or write.

**Services** associated to the same **Data** can communicate with each other thanks to the **Communication links** (Cf. Figure 4.16). A link connects a **Service** to a special service called **Edition Service**. Each **Data** has its own **Edition Service** (Cf. Figure 4.17). When a **Service** sends a message, the message goes to the **Edition Service** that relays it to the other connected **Services**.

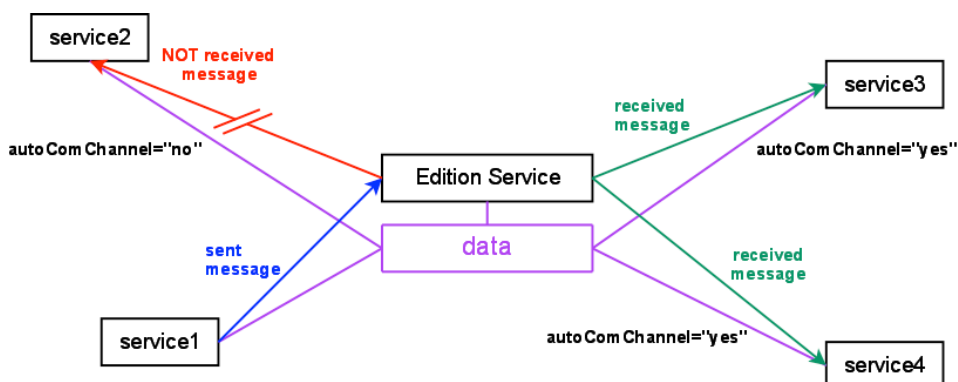


Figure 4.16: Service communication diagram

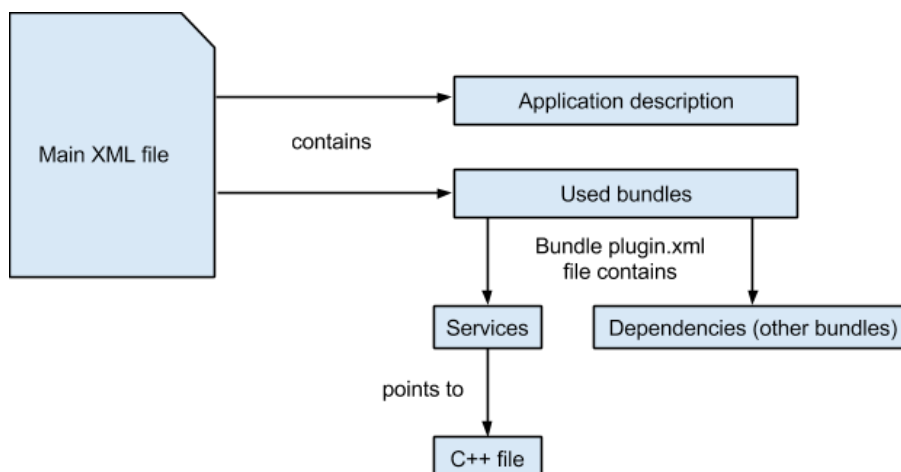
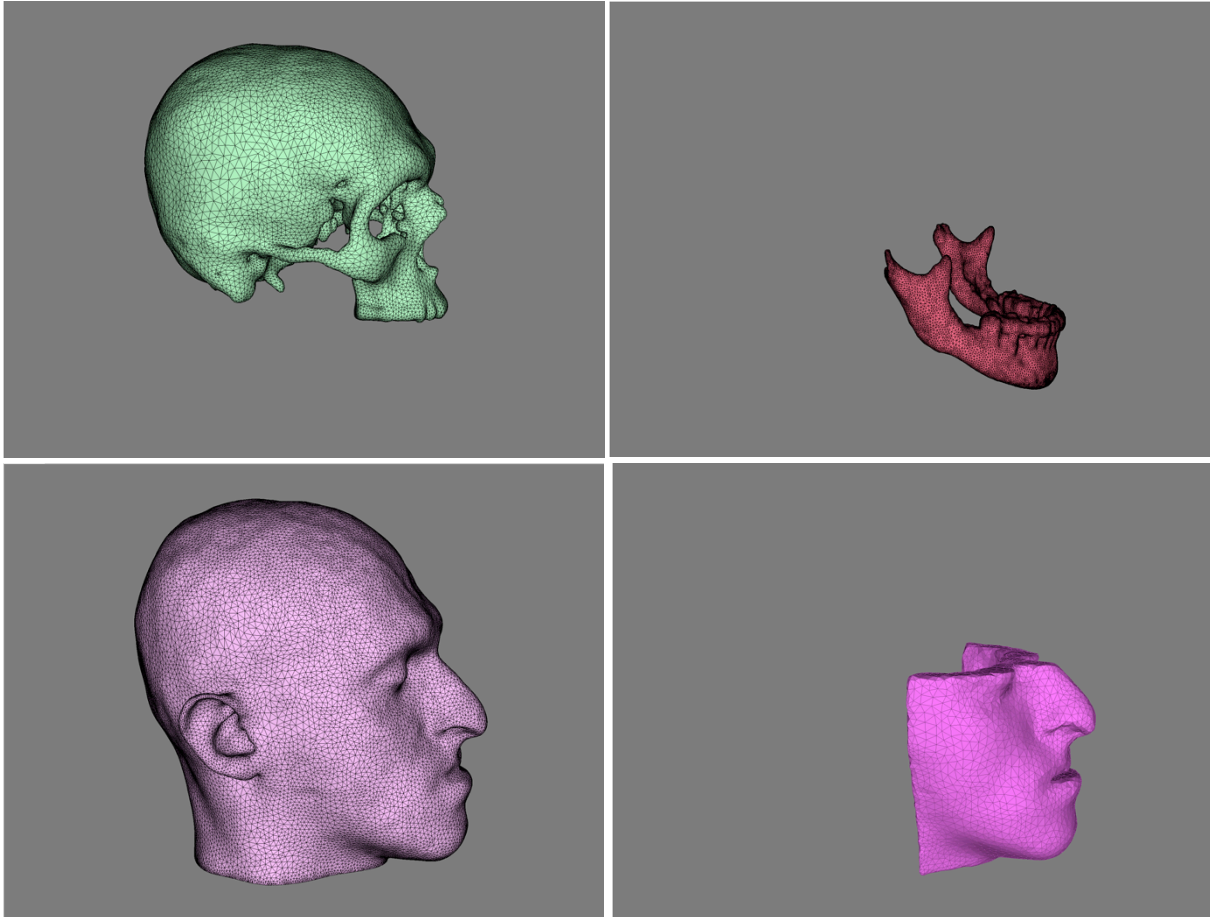


Figure 4.17: Application organization diagram

## 4.4. Description of our software

### 4.4.1 Input data

The Bullet mechanical engine uses tetrahedron-based **volume meshes**. Yet, at this stage, we only have computed **surface meshes** (cf. Figures 4.18, 4.19). A surface mesh is a set of triangles representing only the envelop of the object, whereas a volume mesh is a set of tetrahedra representing the whole object volume.



**Figure 4.18:** Surface meshes of the patient's upper skull including the maxilla (top left), the mandible (top right), the skin surface (bottom left) and the soft tissue layer surface. Note that, at this stage, meshes only consist of triangles.

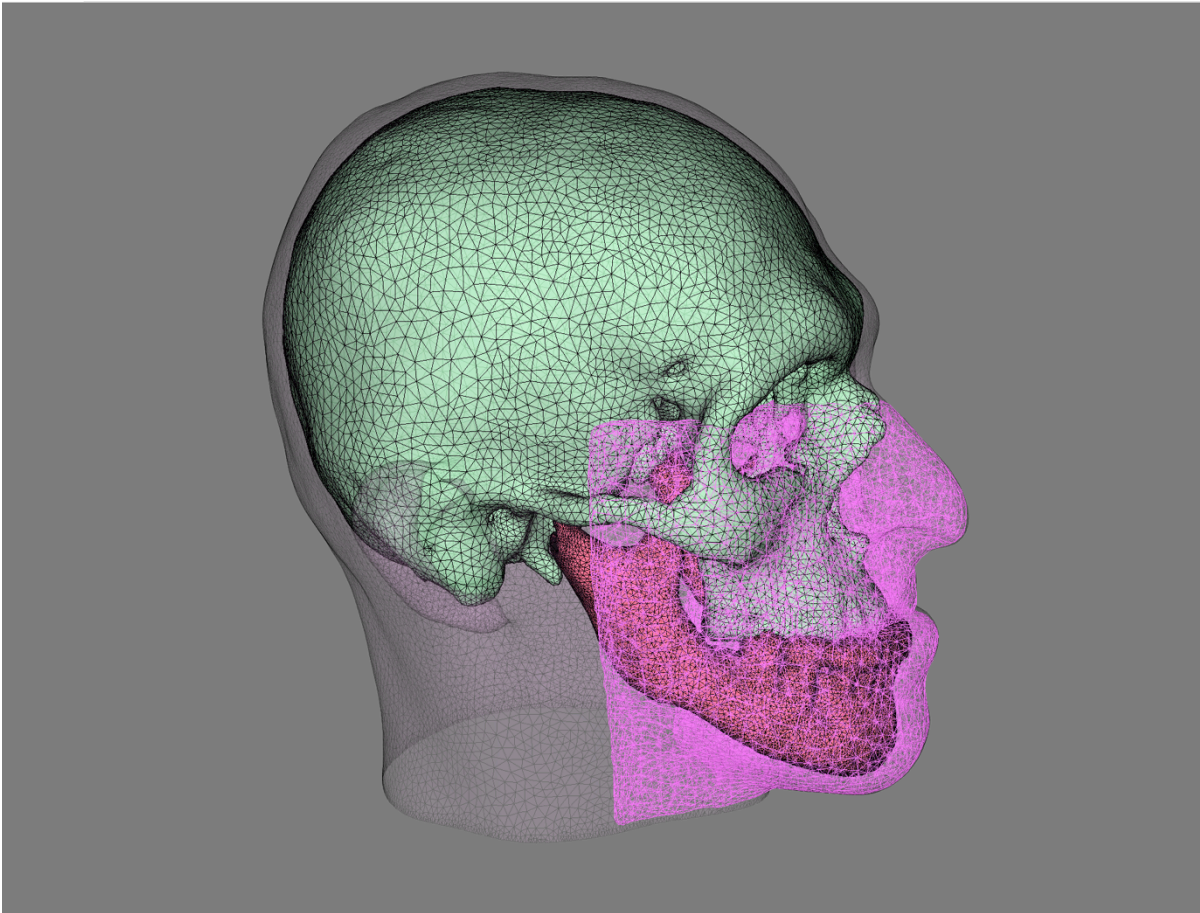


**Figure 4.19: Superimposition of all surface meshes** of the patient (maxilla, mandible, skin surface and soft tissue layer). Note that meshes consist of triangles.

Therefore, in order to compute the **volume meshes** as required input data, we use the framework-integrated library called **TetGen**. This library has been integrated into the VRTools software (Cf. Figures 4.21 and 4.22), using fw4spl. Thus, we can process a volume mesh from the surface mesh representing the soft tissue layer surface obtained at the end of chapter 3.

Processing of the surface mesh into a volume mesh using the **TetGen** integrated library is depicted in the following Figure 4.20.

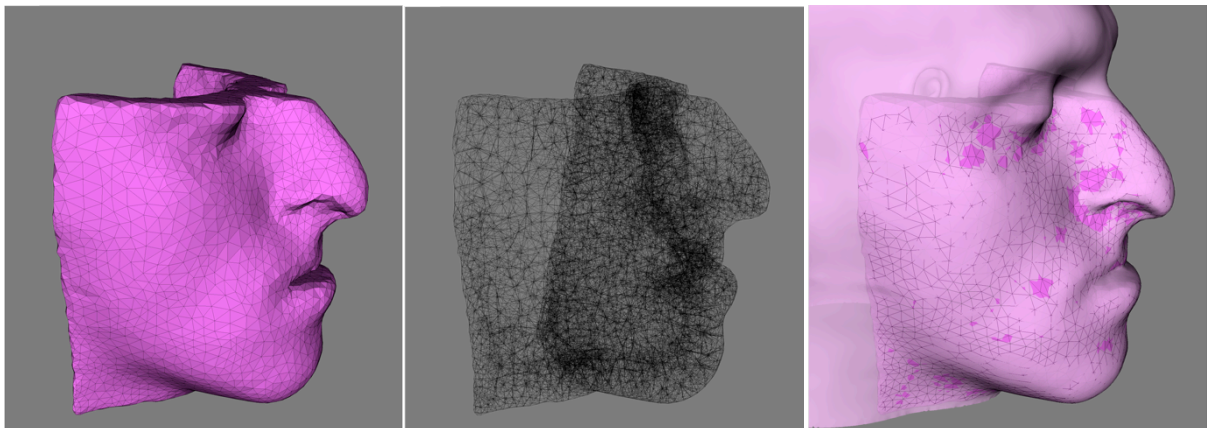


**Figure 4.20: Result of surface mesh conversion into a volume mesh.** This was achieved using the TetGen Library. We can see the **surface** mesh of the soft tissue layer (left), the **volume** mesh of the soft tissue layer (middle) and the superimposition of the whole skin surface onto the **volume** mesh (right).



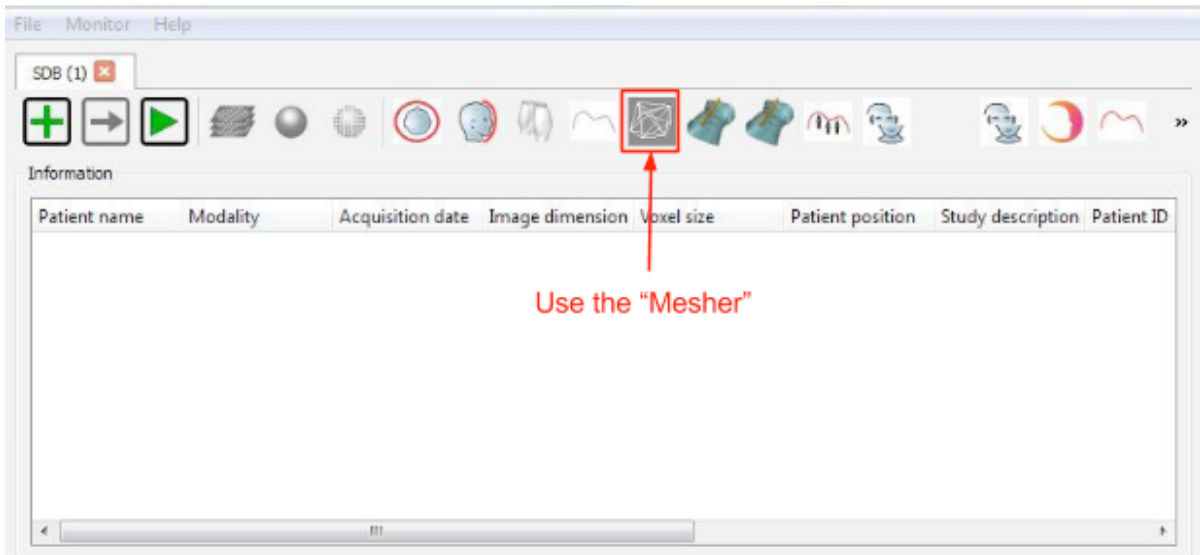


Figure 4.21 : VRTools main view.

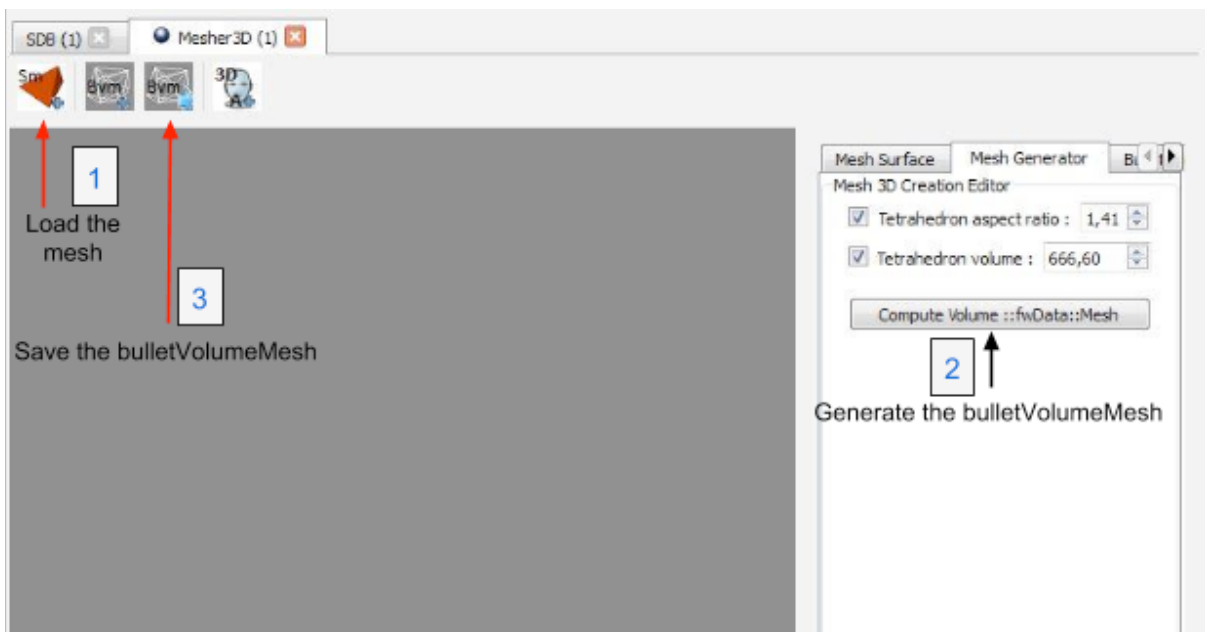


Figure 4.22: Mesher 3D main view.

### 4.4.2 Simulation

In order to simulate soft tissue deformation, we used the Bullet **mechanical engine**. Bullet<sup>®</sup> Physics is a **professional open source** collision detection, rigid body and **soft body** dynamics **library** written in portable **C++**. This library was primarily designed for use in games, visual effects and robotic simulation.

The main useful feature for us was: soft body dynamics for cloth, rope and deformable volumes with two-way interaction with rigid bodies, including constraint support.

The code is **Open source C++** under ZLib license and **free for any commercial** use on all platforms including PLAYSTATION 3<sup>®</sup>, XBox 360<sup>®</sup>, Wii<sup>®</sup>, **PC**<sup>®</sup>, **Linux**<sup>®</sup>, **Mac OSX**<sup>®</sup>, Android<sup>®</sup> and iPhone<sup>®</sup>. Therefore, it seemed to be a suitable enough engine to address facial surgical induced simulation compatible with the **fw4spl environment**. Furthermore, the Bullet<sup>®</sup> Physics library is under active development in collaboration with many professional game developers, movie studios, as well as academia and students.

The main author and project leader is Erwin Coumans, who started the project at Sony<sup>®</sup> Computer Entertainment America US R&D then at Advanced Micro Devices<sup>®</sup> and now at Google<sup>®</sup>.

#### 4.4.2.1 Mechanical approach

As previously explained, a mechanical engine requires that a volume mesh had been previously generated. In the Bullet<sup>®</sup> library, this is called the **soft body**. **The associated soft body mechanical model of Bullet<sup>®</sup> we have decided to use was based on mass-spring system**. Indeed, regarding the small alteration induced by facial surgery compared to the displacement induced onto tissues, such a physic modeling appeared suitable.

In this context, The Bullet<sup>®</sup> soft body could be used through two different ways:

- 1) Forces were applied on some vertices of the volume mesh and, at every computation step, the mechanical engine computed the forces induced onto the other neighboring vertices. Then, the mechanical engine computed the displacement, and therefore the new positions of the other vertices, which allowed the mechanical model to reach a state of mechanical equilibrium.
- 2) A new position was imposed to some vertices of the volume mesh and, at every computation step, the mechanical engine computed the forces induced onto the other neighboring vertices. Then the mechanical engine computed the displacement, and therefore the new positions of the other vertices, which allowed mechanical model to reach a state of mechanical equilibrium.

We decided to use both approaches to evaluate the efficiency of each one.

#### 4.4.2.2 Boundary conditions

We first needed to define which vertices would be imposed a future position or applied a force onto. We chose the vertices, which were located at the intersection between the **volume** mesh of the facial soft tissue and the volume represented by the **surface** mesh of facial bones (Cf. Figure 4.23). Indeed, it is the position of facial bones, which is affected by surgery, whereas the alteration of soft tissues is only the consequence. We had anticipated the requirement of meshes intersection in chapter 3.4.2.2.2 (Skin segmentation method). Actually, the segmentation we had conducted resulted in a soft tissue layer model which was slightly thicker than on the actual patient in order to make sure that the soft tissue mask either comes in close contact with, or interpenetrates the bone surface mesh.

Indeed, simulation becomes possible as long as an intersection exists between the two meshes (ie: the volume and the surface mesh). Even if the inside surface of the soft tissue layer goes deeper than the outside surface of the bone mesh, this would not represent a problem. On the contrary, if soft tissue layer had been too thin, simulation could not have been conducted. Indeed, this procedure guaranteed that facial bone movements would impact soft tissues.

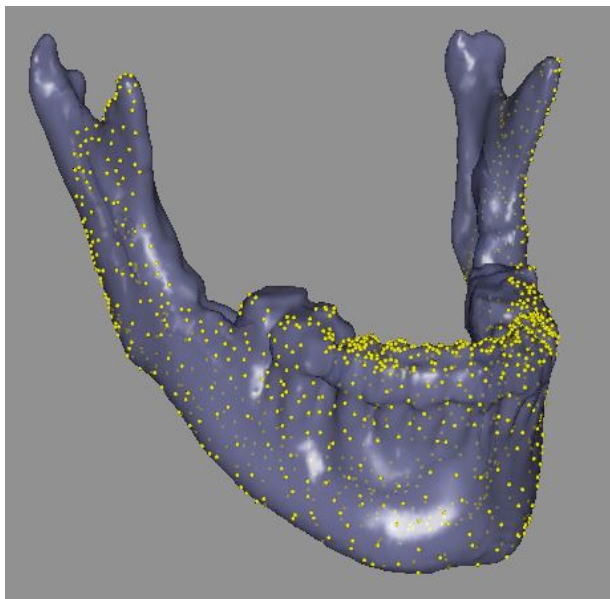


**Figure 4.23:** Vertices of the mandible (yellow spheres) linked to the closest ones belonging to the soft tissue layer.

We thus needed to identify the vertices of the soft tissue layer volume mesh, which belonged to the different surface volume meshes (i.e.: mandible, maxilla and skull). We then processed these 3 sets of points as follows:

- Maxilla and mandible sets: we applied the transformation matrix used to move the surface mesh (corresponding to the bone motion surgically induced) to the considered vertices of the volume mesh.
- Skull: we set a fixed position to these vertices, since the position of the skull was unchanged and therefore considered as a steady reference of the coordinate system.

Once we have modified the position of the vertices belonging to the volume mesh, this displacement induced forces responsible for the motion of the others vertices belonging to the soft body. Furthermore, Bullet<sup>®</sup> allowed to choose keeping constant the volume of the soft body, which is globally the case considering soft tissues.

### 4.4.2.3 Software integration

In this paragraph, we will detail the concrete implementation of our approach. Indeed, this approach had to take into account some important technical points, such as:

- The description of the tools implemented to facilitate the skull section in order to release the maxilla from the skull.
- The concrete cutting step of the maxilla from the skull.
- The linking between the soft tissue layer and both, the mandible and the maxilla, while the relative sliding motion between each bone remained possible.

In order to allow relative motion between the soft tissues linked to the mandible and the ones linked to the maxilla, we had to create an artificial separation corresponding to the mouth opening.

Subsequently, such an implementation allowed sliding of the soft tissues belonging to the upper and lower part of the unique soft tissues layer used for simulation.

We also implemented a few additional features (Cf. Figure 4.24). In practice:

The “Find teeth” button approximately identified the teeth on the skull meshes, in order not to attach the soft tissue layer to the teeth. Not using this option resulted in unattached teeth.

The “Link mandible” button associated each vertex of the soft tissue layer volume mesh to the nearest vertex of the mandible mesh, if the distance between them was inferior to 5 mm. This approach allowed easier association, avoiding the use of bone masks (respectively of the maxilla and the mandible).

The same process was used regarding the maxilla. The “Link skull” button associated each vertex of the soft tissue layer volume mesh to the nearest vertex of the skull and maxilla mesh, if the distance between them was inferior to 5mm.

The “Display PolySphere” checkbox (Cf. Figure 4.23 and 4.24) could be used to visualize the vertices belonging to the soft tissue layer linked to the mandible or to the maxilla. This was a useful tool to evaluate the area of attachment between soft and hard tissues.

Once the soft tissue layer was linked to the bones, we could apply a translation or a rotation to the mandible or the maxilla by selecting the axis expected to move along (translation) or around (rotation), through clicking on the “+” or “-” buttons. This very simple interface facilitated the understanding and the use of such software. x

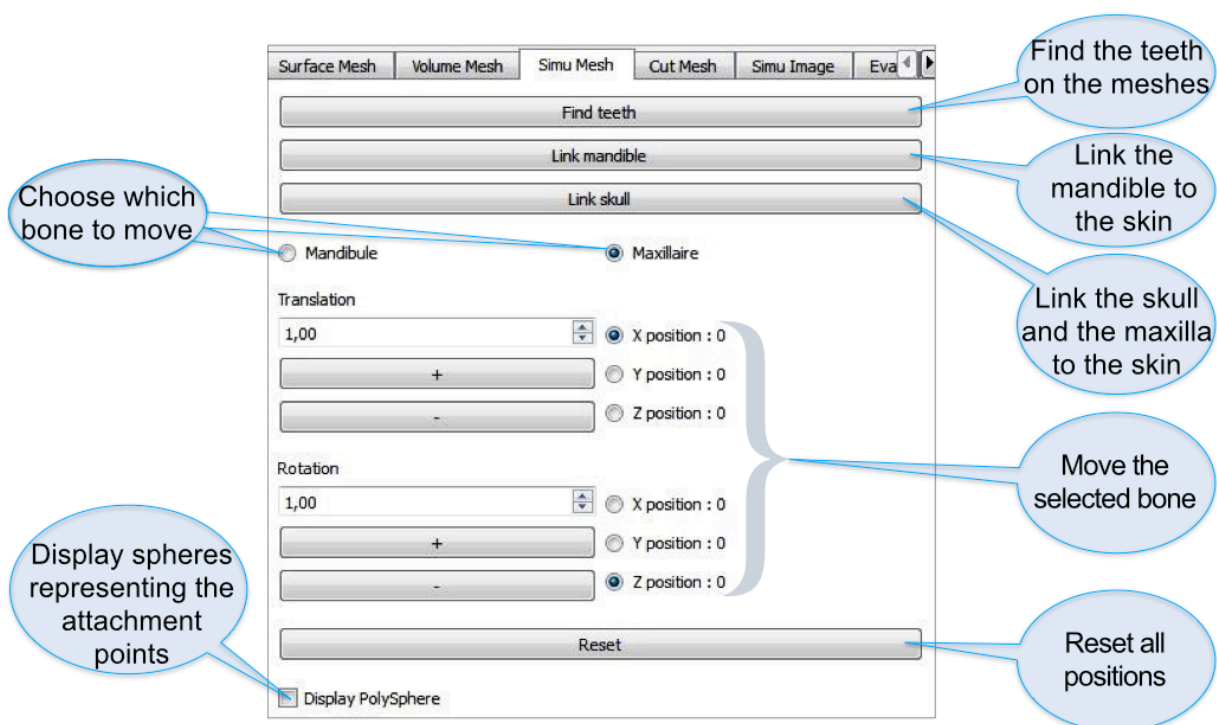


**Figure 4.24: Simulation software interface** depicting the features used to apply bone displacements and simulate soft tissue alterations.

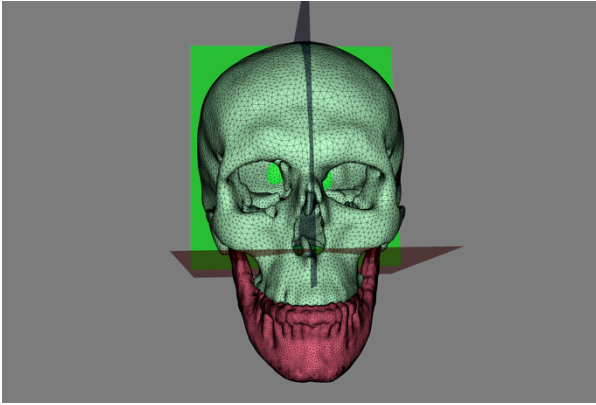


**Figure 4.25:** Surface bone meshes and reference planes (frontal view).

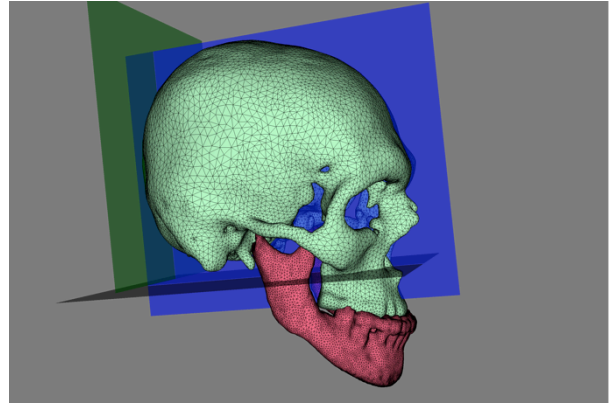


**Figure 4.26:** Surface bone meshes and reference planes (right lateral view).

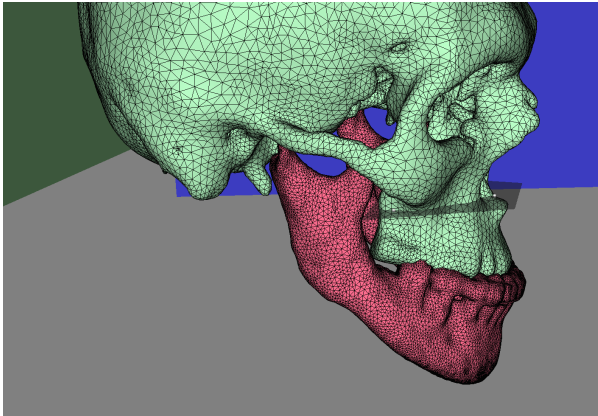


**Figure 4.27:** Surface bone meshes and **maxillary section plane** (right lateral view).

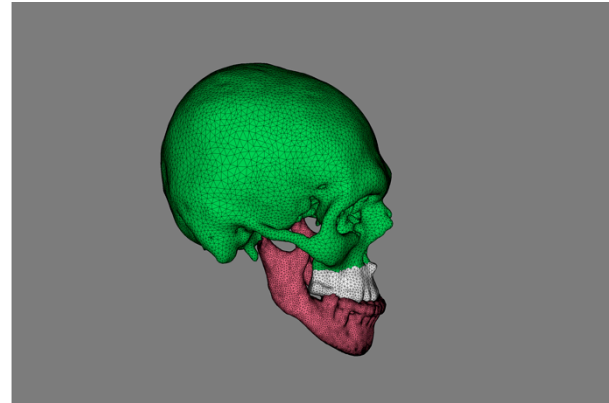


**Figure 4.28:** Surface bone meshes of the upper facial skeleton (green) and the **maxillary segment (white) after section** (right lateral view).

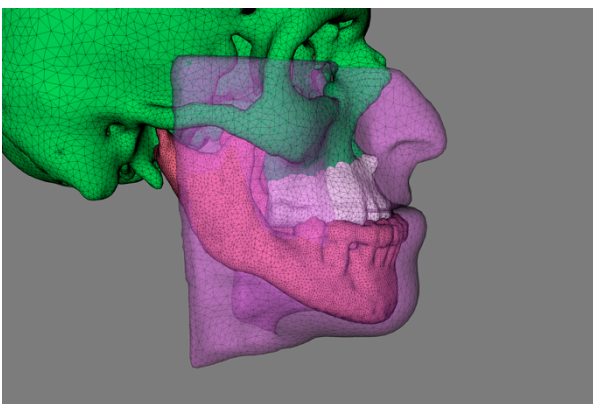


**Figure 4.29:** Surface bone meshes of the upper facial skeleton (green), the maxillary segment (white) after section and the **attachment of the simulated soft tissue layer volume mesh** (pink) (right lateral view).

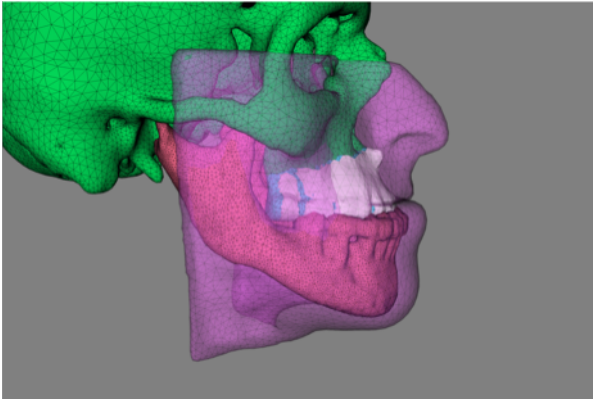


**Figure 4.30:** Surface bone meshes of the upper facial skeleton (green), the maxillary segment (white) after osteotomy and the **attachment of the simulated soft tissue layer volume mesh** (pink). The **anterior movement of the maxillary segment is depicted (white)** after section in relation to the phantom of the neutral position (cyan) (right lateral view).

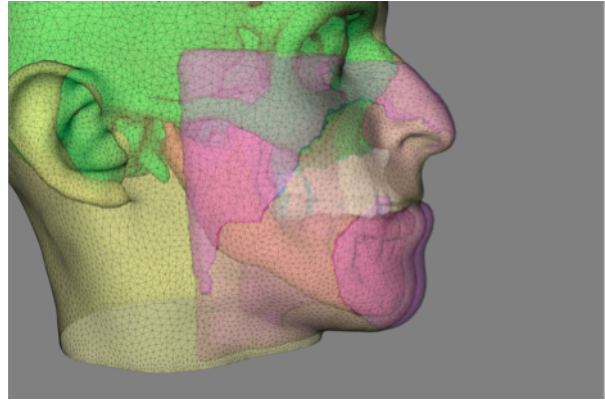


**Figure 4.31:** Surface bone meshes of the upper facial skeleton (green), the maxillary segment (white) after osteotomy and the **attachment of the simulated soft tissue layer volume mesh** (pink). The **anterior movement of the maxillary segment is depicted (white)** after section in relation to the phantom of the neutral position (cyan). The **postoperative skin surface mesh is added (yellow)** (right lateral view).

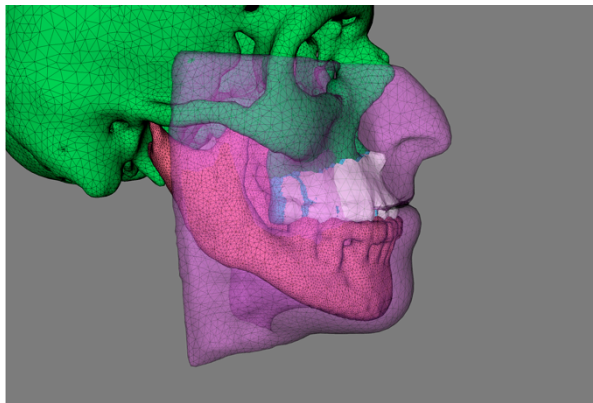


**Figure 4.32:** Surface bone meshes of the upper facial skeleton (green), the maxillary segment (white) after section and the **attachment of the simulated soft tissue layer volume mesh** (pink). A **posterior movement of the mandible has been performed** (right lateral view).

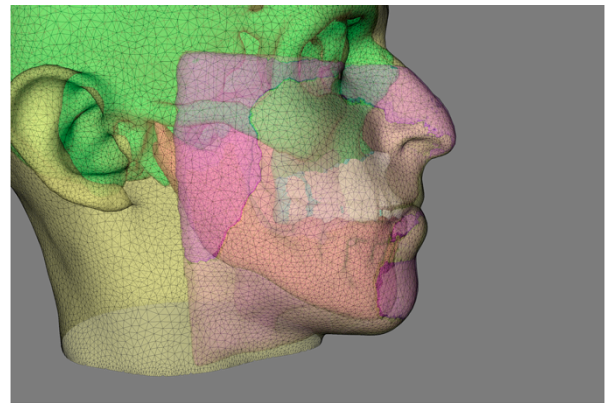


**Figure 4.33:** Surface bone meshes of the upper facial skeleton (green), the maxillary segment (white) after section and the **attachment of the soft tissue layer volume mesh** (pink). A **posterior movement of the mandible has been performed**. The **postoperative skin surface mesh is added (yellow)** (right lateral view).

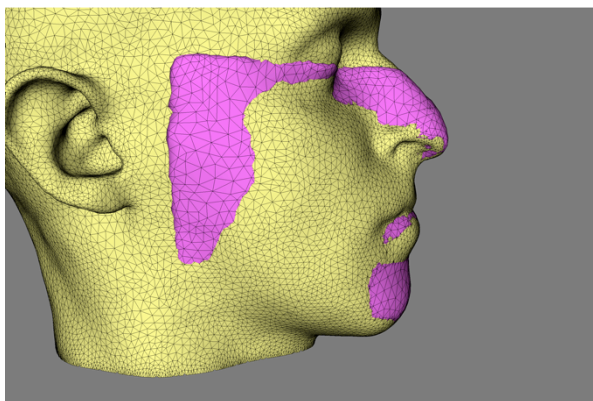


**Figure 4.34:** Superimposition of the simulated skin mesh (pink) and the real postoperative skin surface mesh (yellow) (right lateral view).

## 4.5. Evaluation

### 4.5.1 Evaluation protocol

In this section, we present the quantitative evaluation results of our simulation. The evaluation of our method accuracy necessarily depends on the choice of a comparison criterion.

The evaluation was based on the comparison of two surfaces position. These two surfaces were, on the one hand, the part of the soft tissue layer surface mesh in contact with patient's skin surface (once simulation has been completed) (Cf. Figure 4.35), and, on the other hand, the surface mesh position associated to the patient skin surface extracted from the postoperative CT scan (representing the ground truth) in order to limit the evaluation to the surgically altered part of patient skin.

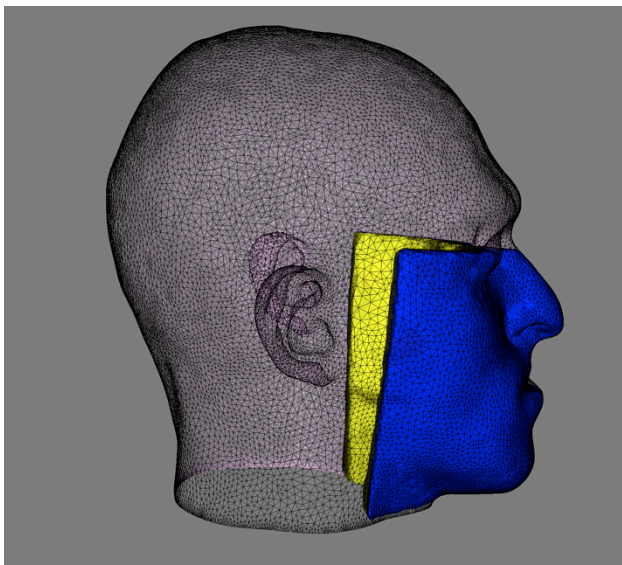


**Figure 4.35: The two surfaces used to evaluate our method accuracy.** The external surface of the soft tissue layer (simulated mesh), in blue is compared to the surface mesh of the patient skin surface extracted from the postoperative CT scan (considered as the ground truth) displayed as a pinkish wire-frame. Note that the internal surface of the soft tissue layer is colored in yellow.

In order to compare our simulated skin with the one extracted from the postoperative CT scan, we first need to interactively apply a rigid transformation to one out of two images, in order to **register the patient skull** in both images. Once this initial registration is achieved, the only part of patient face, which differs, is the surface altered by surgery.

In order to make sure that our simulation of the patient bone displacement is equivalent to the actual surgical one, we used a retro-planning approach. This approach consisted in interactively moving the **bone segments** from their original position in order to superimpose them onto the mask of their actual postoperative position (extracted from the postoperative CT scan). Indeed, the postoperative surgical outcome can slightly differ from the theoretical initial planning. From this step, the software provided the facial soft tissues simulated volume mesh.



First of all, a rough registration step could be conducted using 3D models in the 3D space (Cf. Figures 4.36-4.39)

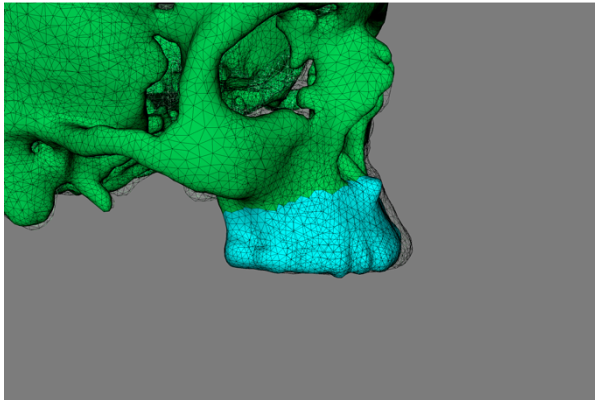


**Figure 4.36:** Surface bone meshes of the upper facial skeleton (green), the maxillary segment (cyan) after section and the **phantom of the postoperative maxillary position (black wire-frame)** (Right lateral view).

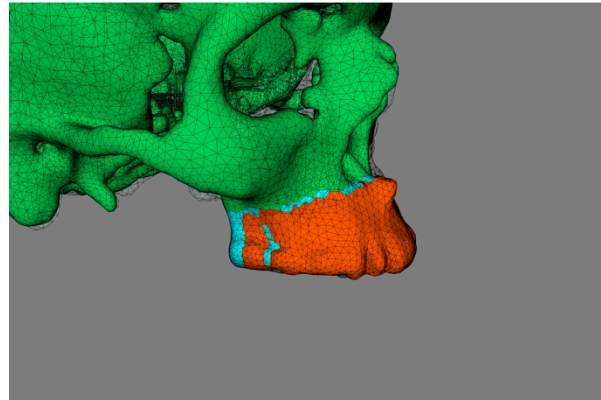


**Figure 4.37:** Surface bone meshes of the upper facial skeleton (green), the maxillary segment (cyan) after section and the **maxilla interactively moved to the postoperative position (orange)** (Right lateral view).

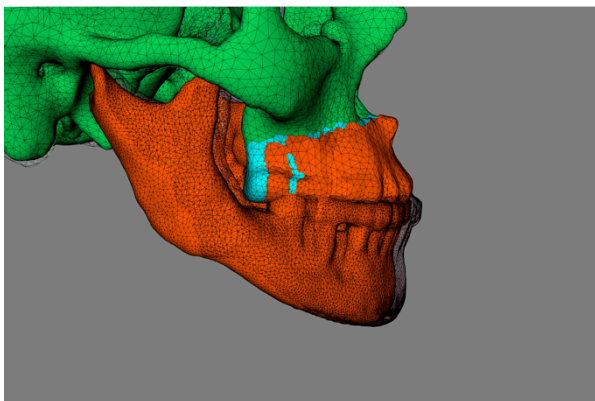


**Figure 4.38:** Surface bone meshes of the upper facial skeleton (green), the maxillary segment (cyan) after section and the maxilla interactively moved to the postoperative position (orange). **The mandible has been moved from its original position (black wire-frame) to its postoperative position (orange)** (Right lateral view).

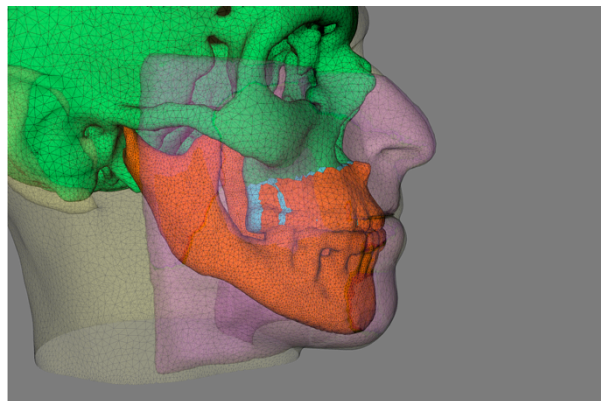


**Figure 4.39:** Surface bone meshes of the upper facial skeleton (green), the maxillary segment (cyan) after section and the maxilla interactively moved to the postoperative position (orange). **The mandible has been moved from its original position (black wire-frame) to its postoperative position (orange). The attachment of the simulated soft tissue layer volume mesh (pink) is displayed as well as the postoperative skin surface mesh (yellow)** (Right lateral view).

To ensure accuracy, a refinement step was computed using 2D visualization of the intersection between the bone surface and a slice from the postoperative 3D image. This approach allowed us to see in real-time this relative position and ensured to match the real surgical displacement.

Thanks to such **2D mesh intersection**, an accurate 2D interactive registration is achieved using the postoperative image (Cf. Figure 4.40). Of course, this approach required the bone meshes to have been segmented in the postoperative image.

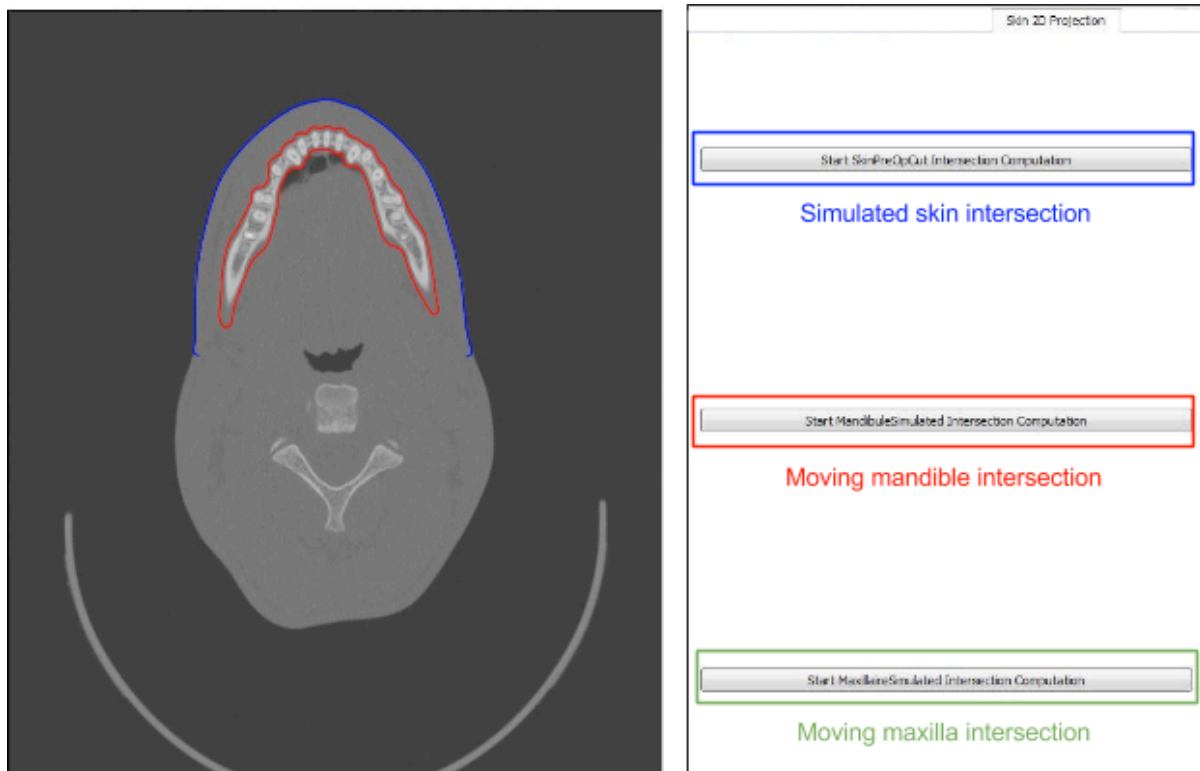


**Figure 4.40: Image and mesh intersection view.** One can see the 2D intersections between the bones surgically displaced and the postoperative 3D image. The three buttons on the right displayed the intersection of the simulated skin, the moving mandible and the moving maxilla with the medical image.

### 4.5.2 Computation methods and reference values

In order to quantitatively evaluate our approach, we have chosen to compare the actual and the simulated position of mesh surfaces using different methods. We achieved measurements of the point-to-point error, of the point-to-surface error and of the point to weighted-surface error. The measurement of the point-to-point error consists of the distance mean between every node of the first mesh and the first closest node belonging to the second mesh. The measurement of point to surface error consists of the mean value between the nodes of the first mesh and the surface of the second one. The measurement of point to weighted-surface error considers the size of the triangles in order to weight the distance value between the vertex and a triangle using the surface of the triangle from which this point originates. These three methods are detailed in the following section.

#### 4.5.2.1 Point-to-point error

Measurement of the point-to-point error, noted as  $\varepsilon_p$ , consists in computing the mean value of the minimal Euclidian distance existing between each point of a first mesh and the closest point of the second mesh. This is the most basic comparison method between two meshes.

Let,  $\{R_0, R_1, R_2, \dots, R_{n-1}\}$ , the set of  $n$  geometrical points belonging to a real organ mesh, noted  $\Psi_r$ .

Let,  $\{S_0, S_1, S_2, \dots, S_{m-1}\}$ , the set of  $m$  geometrical points belonging to a simulated organ mesh, noted  $\Psi_s$ .

Let,  $\varepsilon_p^{\Psi_s/\Psi_r}$  the point-to-point error of the  $\Psi_s$  simulated mesh compared to the  $\Psi_r$  real mesh:

$$\varepsilon_p^{\Psi_s/\Psi_r} = \frac{1}{m} \sum_{i=0}^{m-1} (d(S_i, N^{S/R}(S_i)))$$

With,

$N^{S/R}(i)$ , an application which provides the geometrical point from  $\Psi_r$ , of which the Euclidian distance to the point belonging to  $\Psi_s$  is the shortest:

$d(A,B)$ , the Euclidian distance measurement between the two geometrical points  $A$  and  $B$  :

$$d(A,B) = \|\vec{AB}\|$$

The point-to-point error  $\varepsilon_p$ , depends on the sequence in which the meshes are considered, thus the point to point error of a first mesh compared to a second one, would not provide the same result as the error computed from the second mesh compared to the first one (Cf. Figure 4.41).

Thus, on a general fashion:

$$\varepsilon_p^{\Psi_r/\Psi_s} \neq \varepsilon_p^{\Psi_s/\Psi_r}$$

Subsequently, it could be interesting to process a symmetrical computation in order to make it independent from the direction used to compare the two meshes. In practice, this consists in processing the same computation inverting the role of the real mesh with the simulated one. In such case, the value of the  $\varepsilon_p$  point-to-point error is the mean value of the two previous computations.

In the end, we defined the  $\varepsilon_p$  point-to-point error as follows:  $\varepsilon_p = \frac{1}{2} \left( \varepsilon_p^{\Psi_s \rightarrow \Psi_r} + \varepsilon_p^{\Psi_r \rightarrow \Psi_s} \right)$

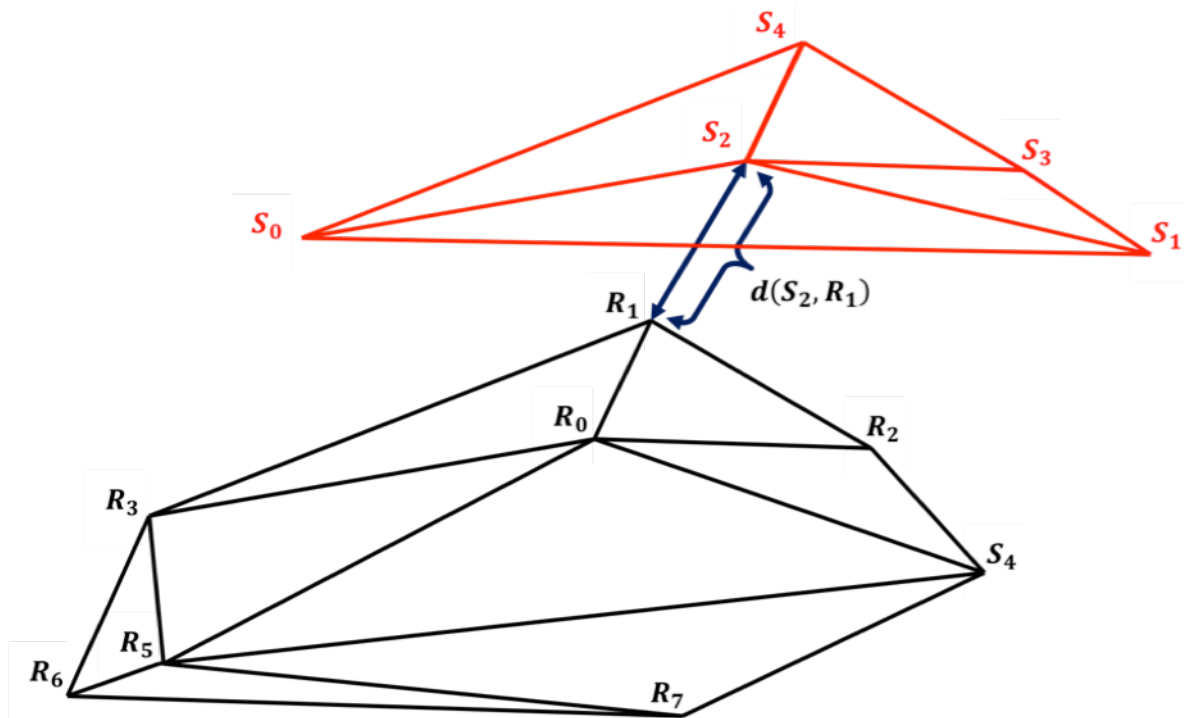


**Figure 4.41: Point-to-point error measurement method.**

The figure depicts two portions of meshes consisting of triangles. The set of all vertices  $\{S_0, S_1, S_2, S_3\}$  belongs to the  $\Psi_s$  simulated mesh, whereas the set of all vertices  $\{R_0, R_1, R_2, R_7\}$  belongs to the  $\Psi_r$  real mesh. The contribution of point  $S_2$  is the Euclidian distance value  $d(S_2, R_1)$  since the closest point to  $S_2$  belonging to  $\Psi_r$  is the point  $R_1$ .

This comparison method between two meshes obviously depends on the mean distance existing between two vertices of a same mesh.

### 4.5.2.2 Point-to-surface error

We saw in the previous section that the value of point-to-point error  $\epsilon_p$ , which is processed from the minimal mean distance existing between two points of a same mesh can carry an undesired bias.

One solution to this problem consists in no longer computing the distance between the vertex points of the two meshes, but rather processing the mean distance between a point of the first mesh and the orthogonal projection of this same point onto the surface of the closest mesh.

The point-to-surface error measurement  $\epsilon_{ps}$  is also depending on the sequence in which the meshes are considered.

Let  $\epsilon_s^{\Psi_s/\Psi_r}$ , the point-to-surface error of the  $\Psi_s$  simulated mesh compared to the  $\Psi_r$  real mesh,

$$\epsilon_{ps}^{\Psi_s/\Psi_r} = \frac{1}{m} \sum_{i=0}^{m-1} (d(S_i, \xi(S_i)))$$

And  $\epsilon_p^{\Psi_r/\Psi_s}$ , the point-to-surface error of the  $\Psi_r$  real mesh, compared to the  $\Psi_s$  simulated mesh.

$$\epsilon_{ps}^{\Psi_r/\Psi_s} = \frac{1}{n} \sum_{i=0}^{n-1} (d(R_i, \xi(R_i)))$$

With,  $\xi(R_i)$ , the application which provides the orthogonal projection of point  $R_i$  onto the side from  $\Psi_r$ , of which the Euclidian distance to the  $R_i$  point is the shortest (Cf. Figure 4.42).

Therefore, on a general fashion:

$$\epsilon_{ps}^{\Psi_r/\Psi_s} \neq \epsilon_{ps}^{\Psi_s/\Psi_r}$$

We will define the  $\epsilon_s$  point-to-surface error as follows:

$$\epsilon_{ps} = \frac{1}{2} (\epsilon_{ps}^{\Psi_s \rightarrow \Psi_r} + \epsilon_{ps}^{\Psi_r \rightarrow \Psi_s})$$

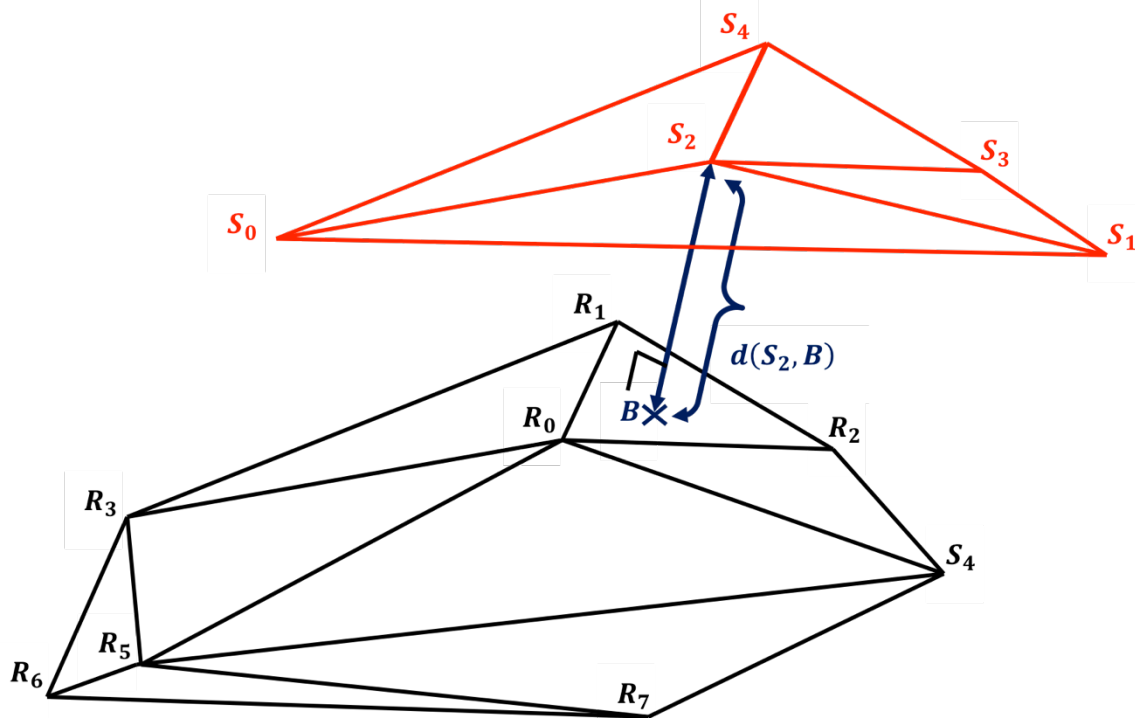


**Figure 4.42: Point-to-surface error measurement method.**

The figure depicts two portions of meshes consisting of triangles. The set of all vertices  $\{S_0, S_1, S_2, S_3\}$  belongs to the  $\Psi_s$  simulated mesh, whereas the set of all vertices  $\{R_0, R_1, R_2, R_3, R_5, R_6, R_7\}$  belongs to the  $\Psi_r$  real mesh. The contribution of point  $S_2$  is the Euclidian distance value  $d(S_2, B)$  since the orthogonal projection of  $S_2$  onto the triangle closest to point  $S_2$  and belonging to  $\Psi_r$  real mesh is the point  $B$ .

If this measurement provides independence from the mesh resolution, the problem due to the adaptive size of triangles remains. Indeed, if the local radius of curvature of a mesh surface is great, the density of triangles per surface unit, therefore the areal density of vertices will be small. On the contrary, if the radius of curvature is locally small, which if any, can result from a local small segmentation error, the number of vertices greatly increases. Thus, a small asperity on the mesh surface can influence the measurement between two meshes.

#### 4.5.2.3 Point-to-weighted-surface error

We saw in the previous section that the value of point-to-surface error  $\varepsilon_{ps}$ , which is processed from the minimal mean distance existing between one point of a first mesh and the closest surface of a second mesh can cause an undesired bias due to the automated meshing methods which may generate triangles of significantly various sizes.

One solution to this problem consists in weighting the distance value between a mesh vertex and its orthogonal projection using the value of the triangle surface to which the point belongs, in order to confer more influence to a point coming from a large triangle than to a point coming from a small triangle. However, a triangle vertex often belongs to other adjacent triangles. As a result, it becomes difficult to confer to

every mesh vertex a weight correlated to a surface, which we have trouble defining. Therefore, in order to solve this issue, we will simply compute no longer considering the mesh vertices, but rather using the points located at every triangle center of gravity. Hence, to every new point of a mesh can be easily conferred a weight, which is simply equivalent to the triangle surface of which the computation point is the center of gravity (Cf. Figure 4.43).

Using the same conventions as in the two previous sections, we define the measurement of weighted-surface error, noted as  $\epsilon_{pws}$ .

Let,  $\{R_0, R_1, R_2, \dots, R_{n-1}\}$ , the set of  $n$  geometrical points belonging to a real organ mesh, noted  $\Psi_r$ .

Let,  $\{R_0^g, R_1^g, R_2^g, \dots, R_{n-1}^g\}$ , the set of  $n'$  geometrical points belonging to every triangle center of gravity from a real organ mesh, noted  $\Psi_r^{24}$ .

Let,  $\{S_0, S_1, S_2, \dots, S_{m-1}\}$ , the set of  $m$  geometrical points belonging to a simulated organ mesh, noted  $\Psi_s$ .

Let,  $\{S_0^g, S_1^g, S_2^g, \dots, S_{m-1}^g\}$ , the set of  $m'$  geometrical points belonging to every triangle center of gravity from a simulated organ mesh, noted  $\Psi_s$ .

The point-to-weighted-surface error measurement  $\epsilon_{pws}$  is also depending on the sequence in which the meshes are considered.

Let  $\epsilon_{pws}^{\Psi_s / \Psi_r}$ , the point-to-weighted-surface error of the  $\Psi_s$  simulated mesh compared to the  $\Psi_r$  real mesh,

$$\epsilon_{pws}^{\Psi_s / \Psi_r} = \frac{1}{m' * \mathfrak{R}} \sum_{i=0}^{m'-1} (d(S_i^g, \varnothing(S_i^g)) * \mathfrak{S}(S_i^g))$$

$$\mathfrak{R} = \sum_{i=0}^{m'-1} (\mathfrak{S}(S_i^g))$$

And  $\epsilon_{pws}^{\Psi_r / \Psi_s}$ , the point-to-weighted-surface error of the  $\Psi_r$  real mesh, compared to the  $\Psi_s$  simulated mesh.

---

<sup>24</sup> In a mesh, where elementary units are triangles, the number of triangles, and the subsequent number of these triangles centers of gravity, is generally not equivalent to the number of this mesh vertices, and therefore,  $n' \neq n$ .

$\varphi(R_i^g)$ , an application which provides the orthogonal projection of geometrical point  $R_i^g$  onto the side from  $\Psi_r$ , of which the Euclidian distance to the point belonging to  $\Psi_s$  is the shortest.

With,

$\mathfrak{S}(R_i^g)$ , an application which provides the surface value of the triangle of which point  $R_i^g$  is the center of gravity.

And finally,  $d(A,B)$ , the Euclidian distance measurement between the two geometrical points  $A$  and  $B$ :

$$d(A,B) = \|\overline{AB}\|$$

Therefore, on a general fashion:

$$\varepsilon_{pws}^{\Psi_r/\Psi_s} \neq \varepsilon_{pws}^{\Psi_s/\Psi_r}$$

We will define the  $\varepsilon_{pws}$  point-to-weighted-surface error as follows:

$$\varepsilon_{pws} = \frac{1}{2} * (\varepsilon_{pws}^{\Psi_s \rightarrow \Psi_r} + \varepsilon_{pws}^{\Psi_r \rightarrow \Psi_s})$$

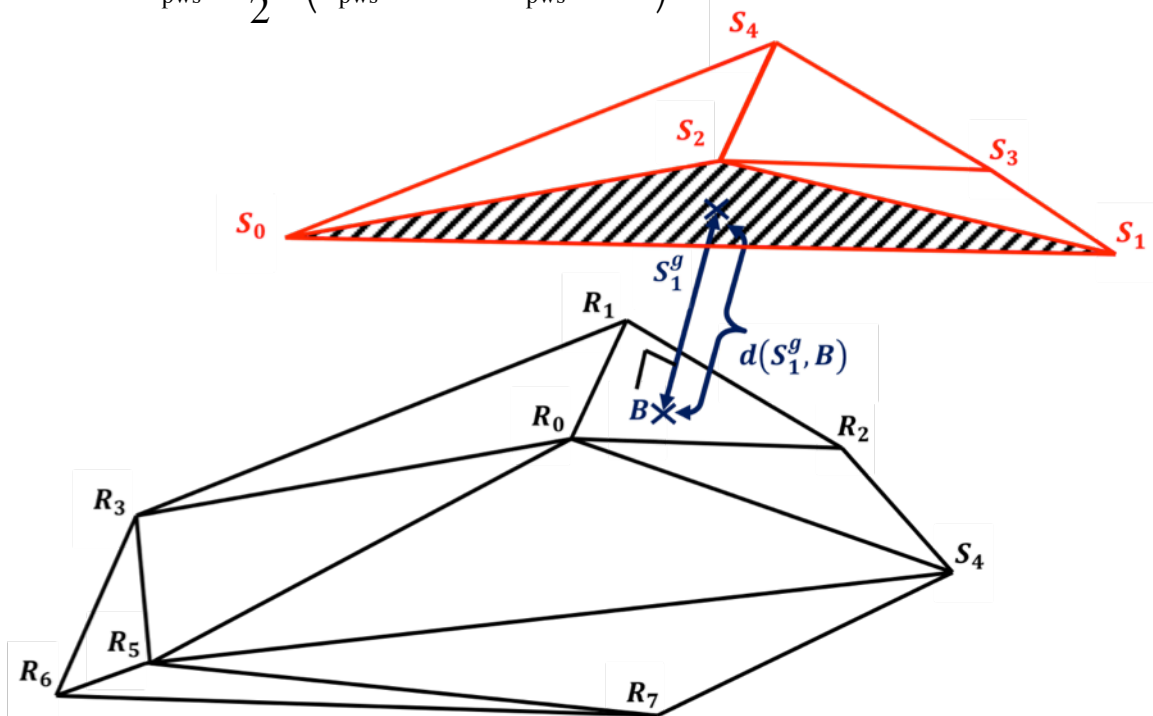


**Figure 4.43: Point-to-weighted-surface error measurement method.**

The figure depicts two portions of meshes consisting of triangles. The set of all vertices  $\{S_0, S_1, S_2, S_3\}$  belongs to the  $\Psi_s$  simulated mesh, whereas the set of all vertices  $\{R_0, R_1, R_2, R_7\}$  belongs to the  $\Psi_r$  real mesh. Subsequently, since the orthogonal projection of  $S_1^g$  point onto the closest triangle belonging to  $\Psi_r$  is the point  $B$  and, since the  $S_1^g$  point is the center of gravity of  $(S_0 S_1 S_2)$  triangle, the contribution of point  $S_1^g$  is the Euclidian distance value  $d(S_1^g, B)$  weighted by the surface of triangle  $(S_0 S_1 S_2)$ .



This method allows us to provide every mesh triangle with a value, which consists of the distance between this triangle center of gravity and its orthogonal projection onto the closest triangle belonging to the second mesh. If two surface meshes are in contact, then, our measurement value of the weighted-surface error is zero. However, since our method does not rely on physical points identified in both meshes, in the case where a point of the first mesh is not well positioned but located close to the second mesh surface, its contribution to the weighted-surface error computation would be the one of a perfectly positioned point.

### **4.5.2.4 Preliminary conclusion**

We saw in the previous sections that the point-to-point error measurement greatly depends on the mean minimal distance existing between two vertices of a same mesh. The point-to-surface error measurement is very similar to the measure obtained through the computation of the point-to-weighted-surface error. However, the value obtained from the point-to-surface error computation is a source of more errors than the point-to-weighted-surface computation, since small asperities resulting from a local approximate segmentation have a stronger impact on the overall computation than a large triangle in adequate position.

We applied these three methods to compare the postoperative simulated patient skin mesh to the postoperative one.

### 4.5.3 Software integration and evaluation display

An evaluation service was created to assess the approach accuracy.

The computation of average distances according to the three above described methods (point-to-point error, point-to-surface error, point-to-weighted-surface error) is processed and the corresponding three values are displayed on the interface and respectively named “cumuled error”, “cumuled error projection” and “cumuled error projection surface”. In order to facilitate interpretation of such an evaluation, we have chosen to gather error values using ranges. A dedicated color has been assigned to every given range. The default range size was set at 0.5 mm. Indeed, since the surgical displacement of bones is in the order of 5 mm, such setting provided about 10 ranges. Of course, this value could be interactively adjusted using a dedicated slider in the interface (Cf. Figure 4.44).

We also specified for every range the option of being excluded for purposes described in the next two sections, as well as for additional reasons.

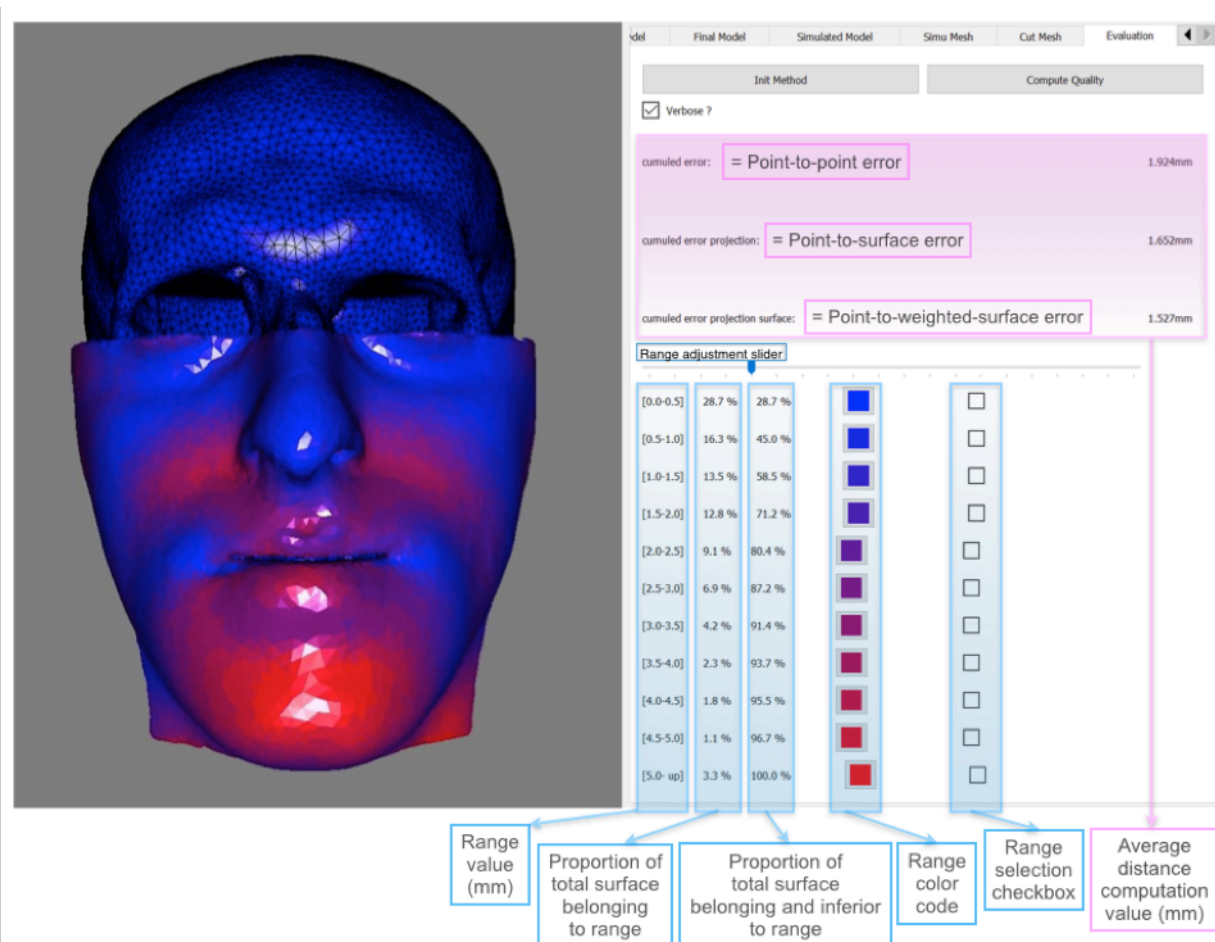


**Figure 4.44: Distance evaluation display.** The color map (left) illustrates the distance between the preoperative and the postoperative position of the skin. A dedicated color has been assigned to every given range. In the window (right), the top part displays the 3 average distance computation values respectively according to the 3 computation methods. The bottom part displays the skin surface evaluation in relation to ranges. The first column consists of the range value in mm. The second one consists of the proportion of the total evaluated surface belonging to the range. The third column consists of the proportion of the total evaluated surface belonging and inferior to the range. The fourth column illustrates the colored assigned to every range. The fifth column consists of checkboxes allowing excluding the corresponding range from the computation.

### 4.5.4 Reference values

Evaluating the average distance between the pre-operative and the post-operative position using the 3 methods previously described, resulted in respectively 1.9, 1.7 and 1.5 mm (Cf. Figure 4.45). These values were low, since a large part of the evaluated patient skin surface was not impacted by the displacement of underlying bone structures. Indeed, bone displacement, actually in the order of 5 mm, primarily impacts the perioral and chin areas.

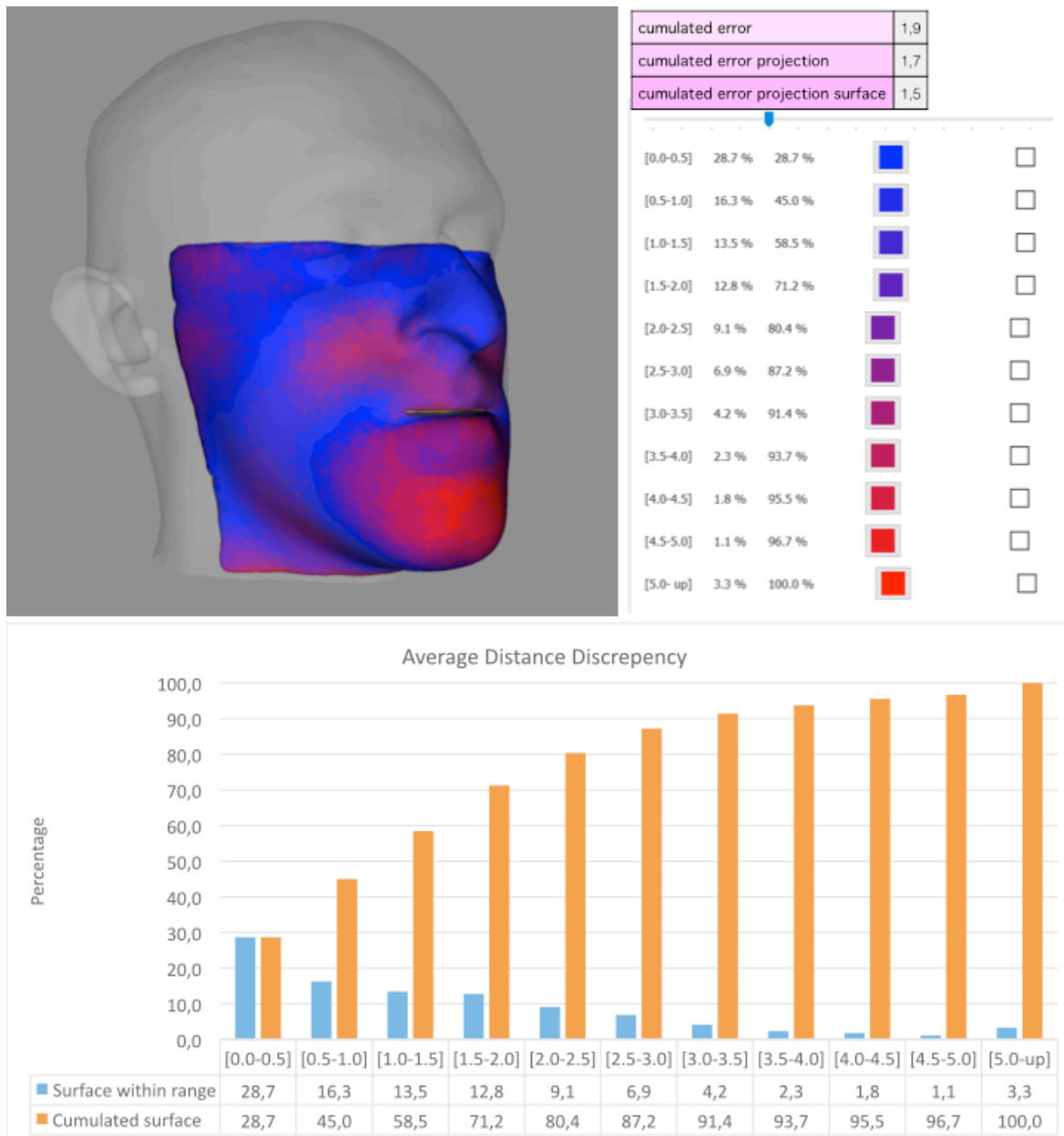


**Figure 4.45: Magnitude of displacements between postoperative and preoperative.** The 3 average distance computation values respectively according to the 3 computation methods automatically displayed in the top right part of the interface (Cf. Figure 4.44) have been transferred to a table (top right, pink) for readability purposes. The proportion of the surface belonging to every range is depicted in the associated graph (blue histogram). The proportion of the surface corresponding to the cumulated error is also depicted (orange histogram). For example, 13.5 % of the evaluated surface ranges between 1 and 1.5 mm. Also, 58.5 % of the evaluated surface ranges between 0 and 1.5 mm.

In order to obtain a reference value to which we could reasonably compare the results of our simulation, we excluded from this computation part of the patient skin surface. Therefore, we excluded from computation the points belonging to every range, one after the other, until isolating the skin surface actually affected by surgery. Thus, we were able to discriminate the areas of skin surface featuring the most significant postoperative alterations. Through successive exclusion of the different ranges, we were able to objectively decide to consider for **reference value computation**, the only part of the facial skin affected by a displacement greater than 1.0 mm. This value is consistent with segmentation accuracy (Cf. Chapter 3, section 3.5.3) but also with surgical accuracy considering the surgical instruments yet used.

In the end, through the exclusion of points affected by a displacement smaller than 1.0 mm, using our three evaluation methods, we measured an average distance of respectively 2.7, 2.5 and 2.4 mm, with values locally outlying 5 mm in the perioral and chin areas (Cf. Figures 4.46 – 4.48).

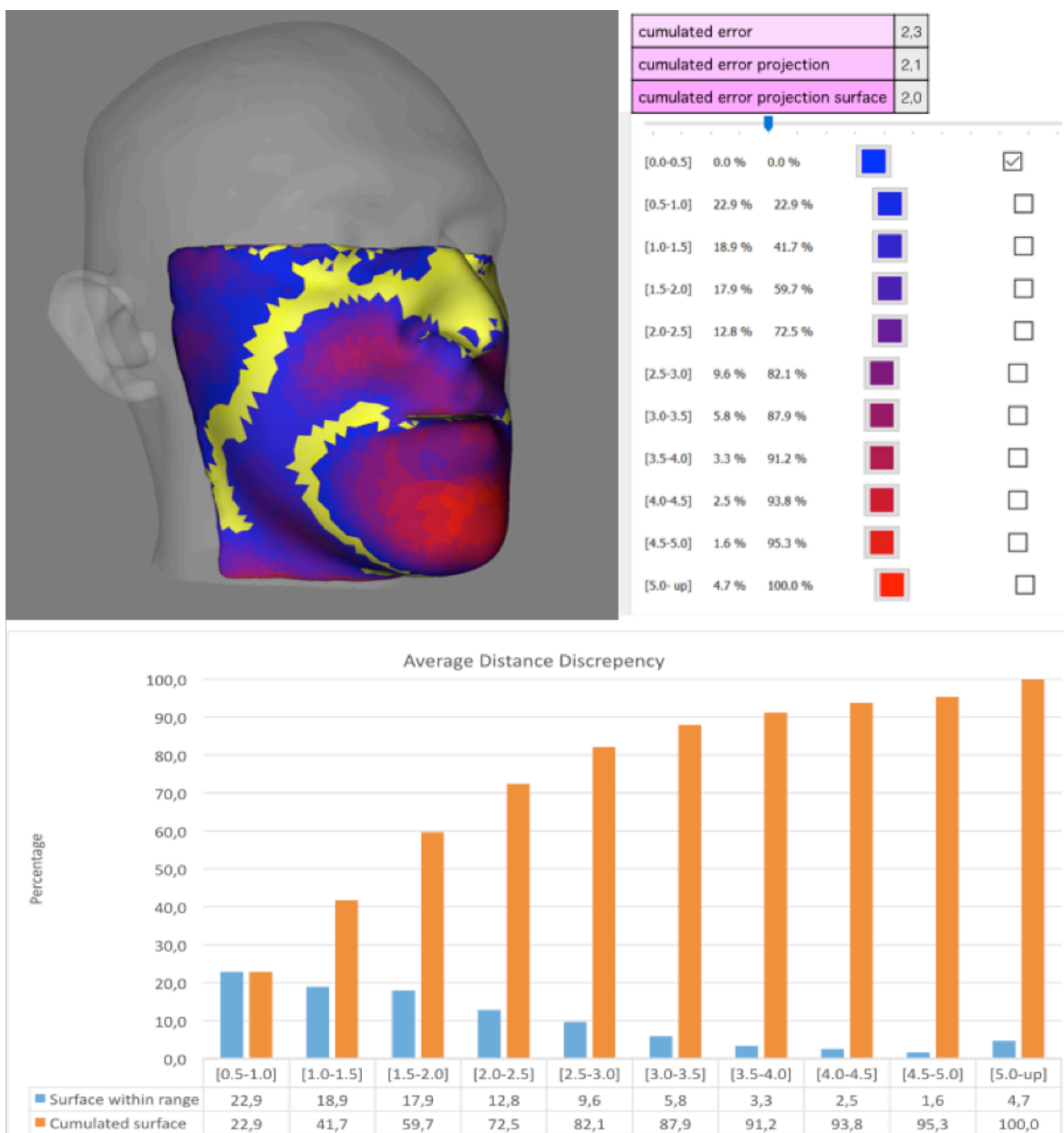


Figure 4.46: Magnitude of displacements between postoperative and preoperative excluding error up to 0.5 mm.

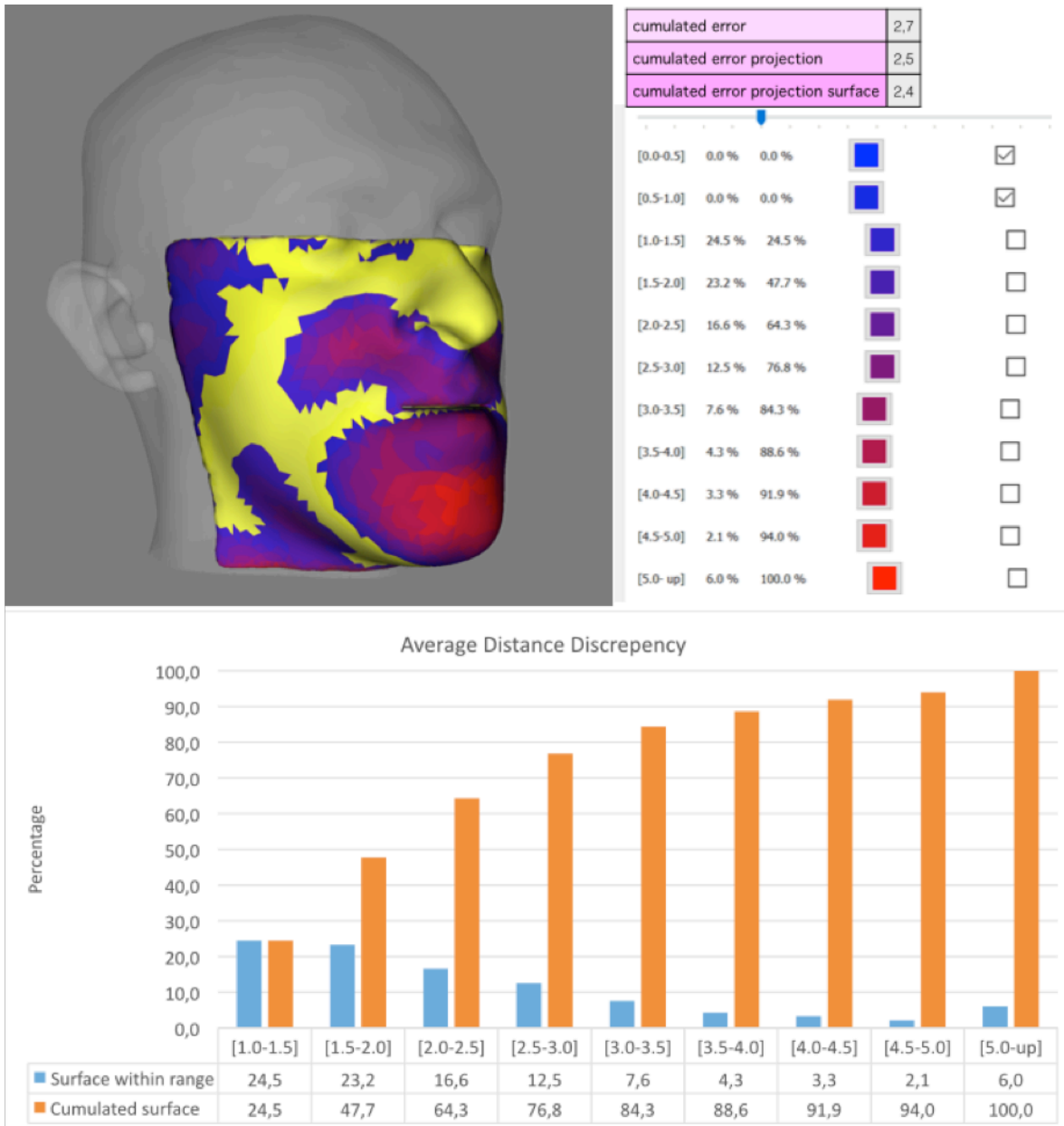


Figure 4.47: Magnitude of displacements between postoperative and preoperative excluding error up to 1 mm.

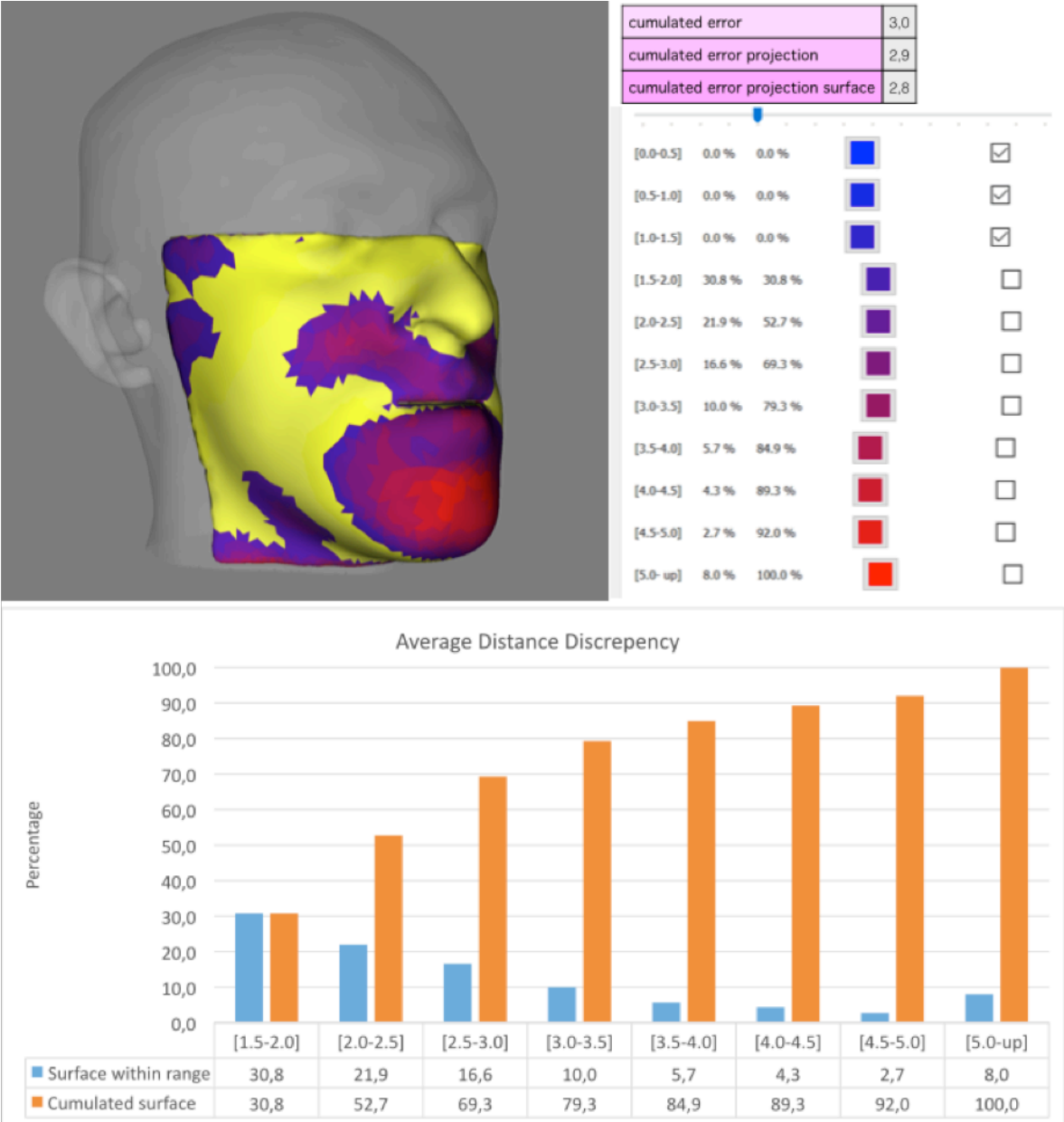


Figure 4.48: Magnitude of displacements between postoperative and preoperative excluding error up to 1.5 mm.

#### 4.5.5 Accuracy of simulation software outcome

We were then able to evaluate the quality of our simulation, yet comparing the postoperative position of patient skin to the skin position resulting from our simulation step. Namely, such process actually consisted in evaluating the result of segmentation<sup>25</sup>, planning (bone cuts and displacement) and simulation.

As previously, the computation of average distances according to the three above described methods (point-to-point error, point-to-surface error, point-to-weighted-surface error) is processed and the corresponding three values are, once again, displayed on the interface and respectively named “cumuled error”, “cumuled error projection” and “cumuled error projection surface”.

We exclude from this evaluation the surfaces, which were not intended to be evaluated. Namely, these surfaces consisted of the neck and the interlabial space<sup>26</sup> (NOTE: space between the upper and the lower lips).

The neck surface differed, since head angulation varies between the preoperative and the postoperative CT acquisition.

The interlabial space is also excluded, since it does not exist in the postoperative image due to patient acquisition with his mouth closed. Let us remind that this space was artificially generated in the preoperative model in order to allow independent sliding between the soft tissue displaced together with the maxilla and the one displaced together with the mandible.

In order to identify the value ranges meant to be excluded, we proceeded as previously and addressed the ranges one after the other (Cf. Figures 4.49 to 4.52). We observed that it was advisable to exclude the ranges greater than 2.5 mm (Cf. Figure 4.50).

Subsequently, using our three evaluation methods, we measured an average distance of respectively 1.4, 1.0 and 0.9 mm.

These values were smaller than the 1 mm margin of error and therefore consistent with segmentation accuracy (Cf. Chapter 3, section 3.5.3) but also with surgical accuracy considering the surgical instruments yet used.

As a result, it did not seem useful to seek a finer result and an evaluation below 1 mm did not seem relevant.

---

<sup>25</sup> Segmentation of, on the one hand, the preoperative CT image to generate a mechanical model subject to simulation, and on the other hand, the actual postoperative CT image.

<sup>26</sup> Interlabial space: the space between the upper and the lower lips.

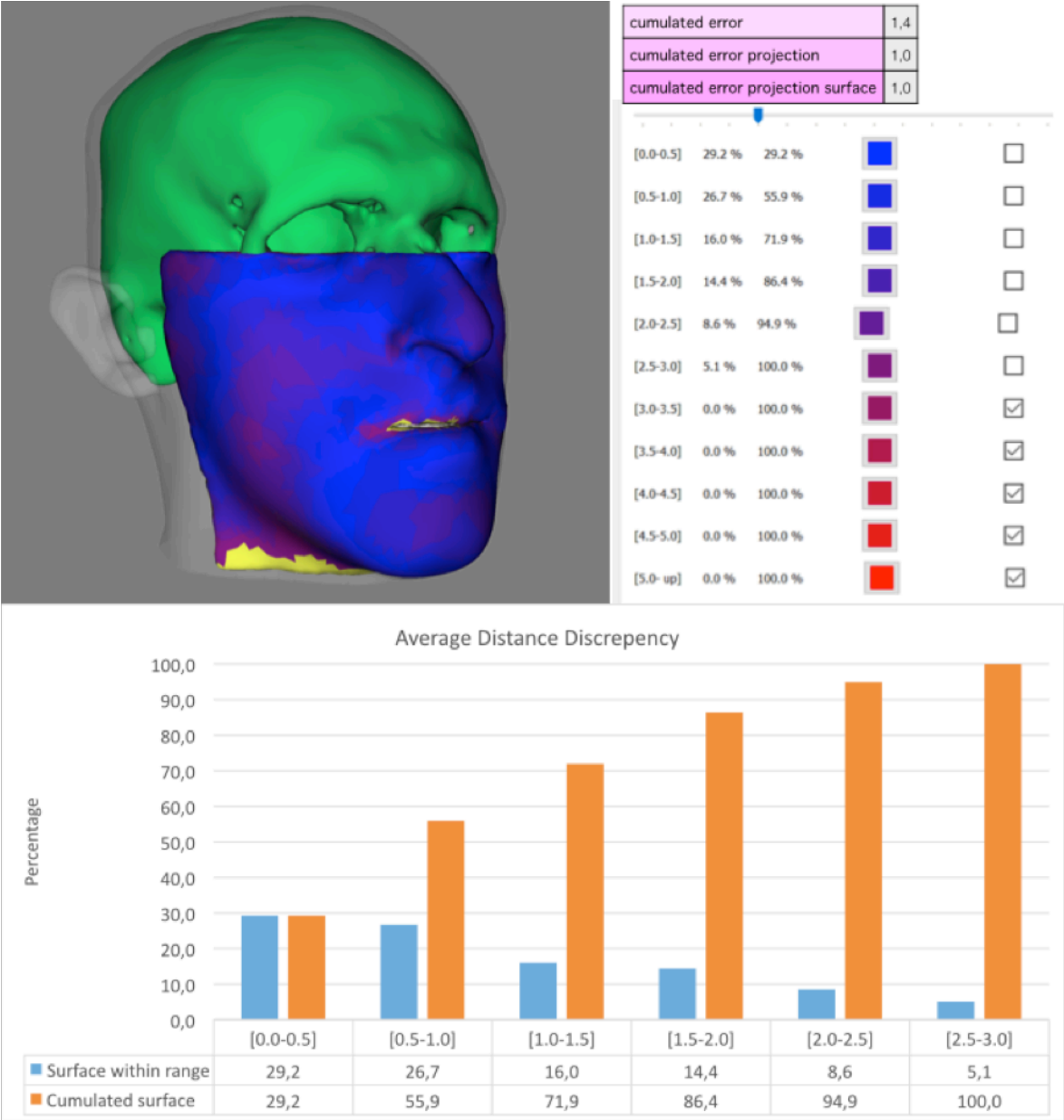


Figure 4.49: Magnitude of displacements between simulated and actual postoperative excluding error over to 3 mm.



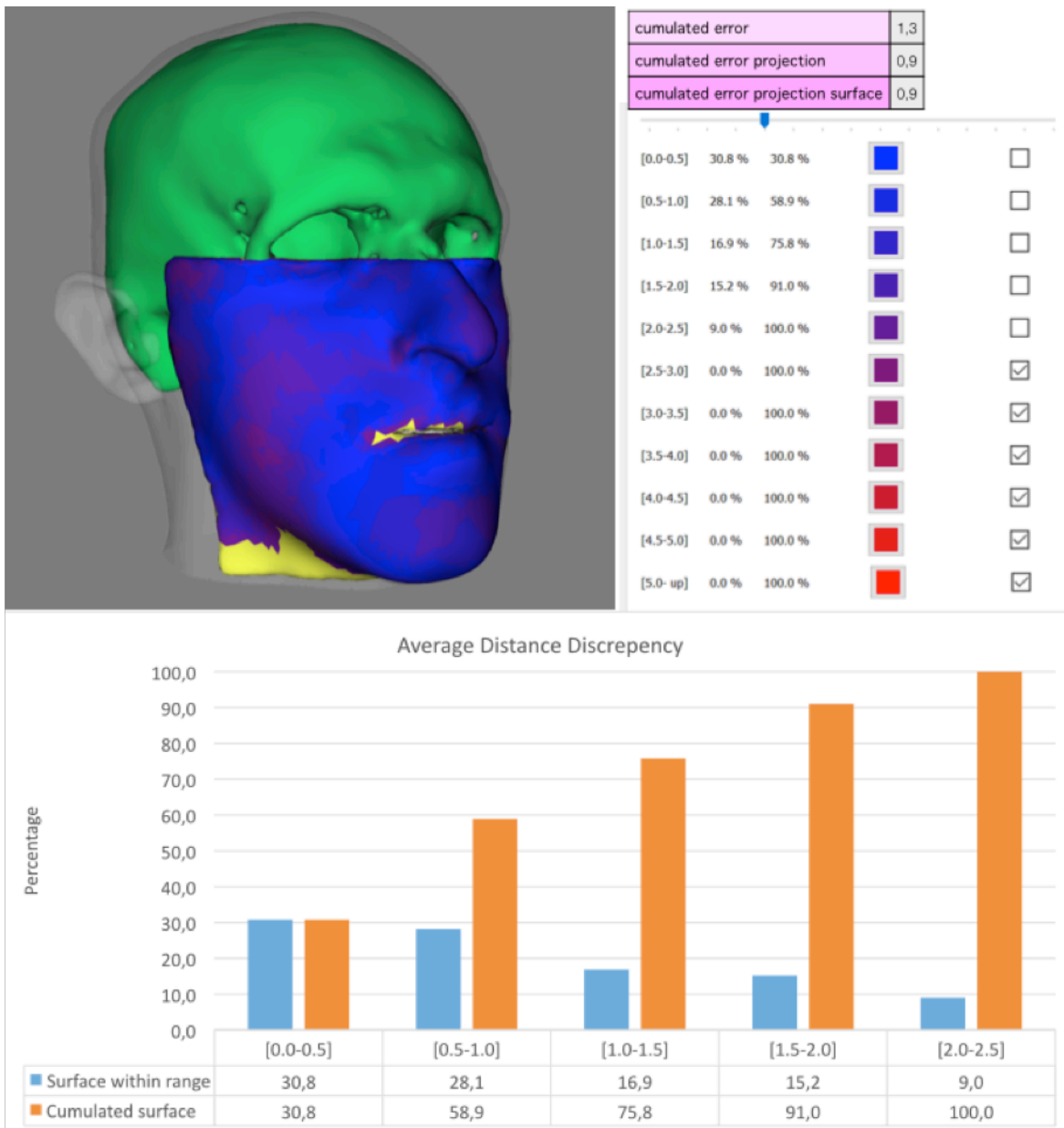


Figure 4.50: Magnitude of displacements between simulated and actual postoperative excluding error over to 2.5 mm.

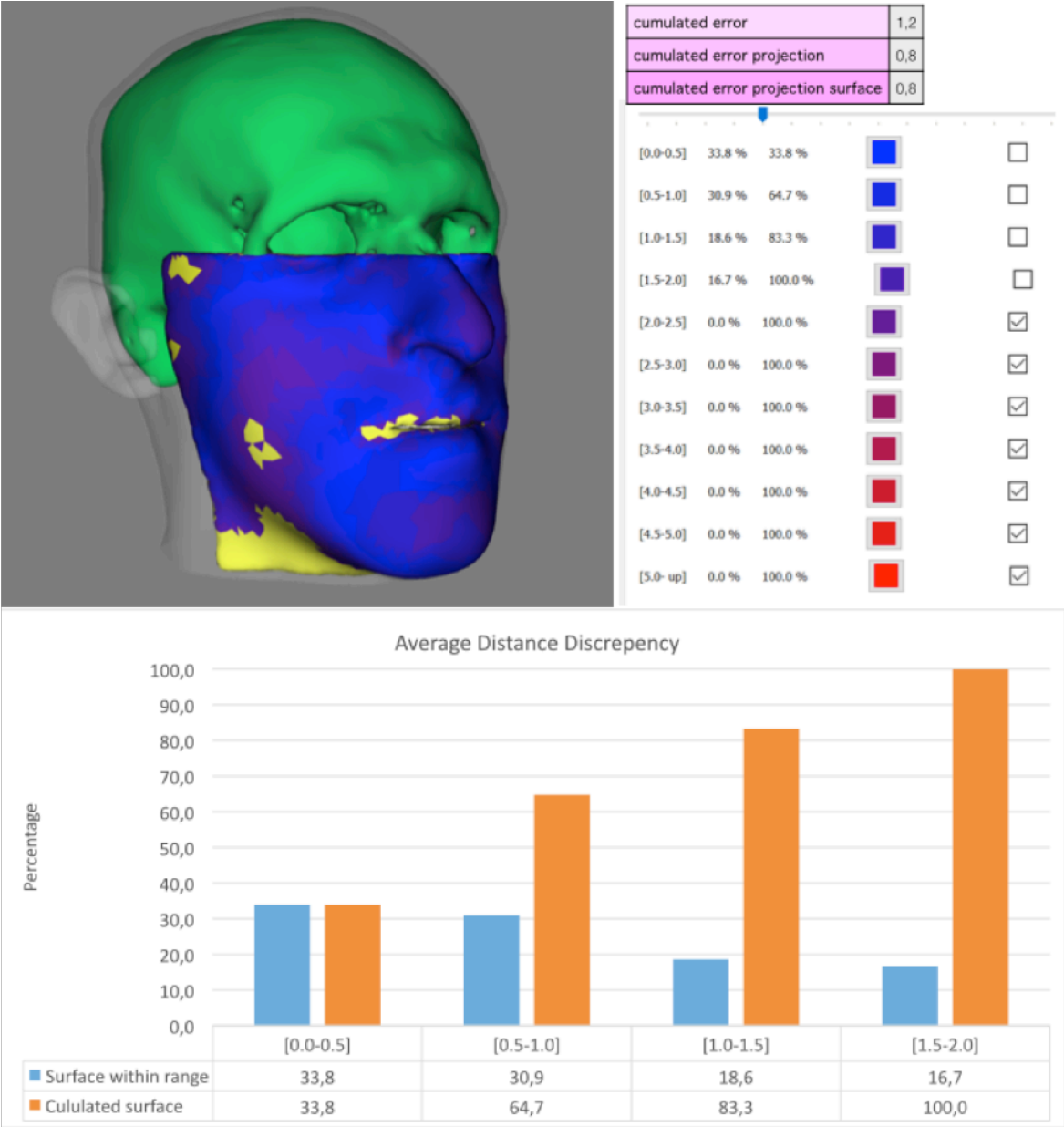


Figure 4.51: Magnitude of displacements between simulated and actual postoperative excluding error over to 2 mm.

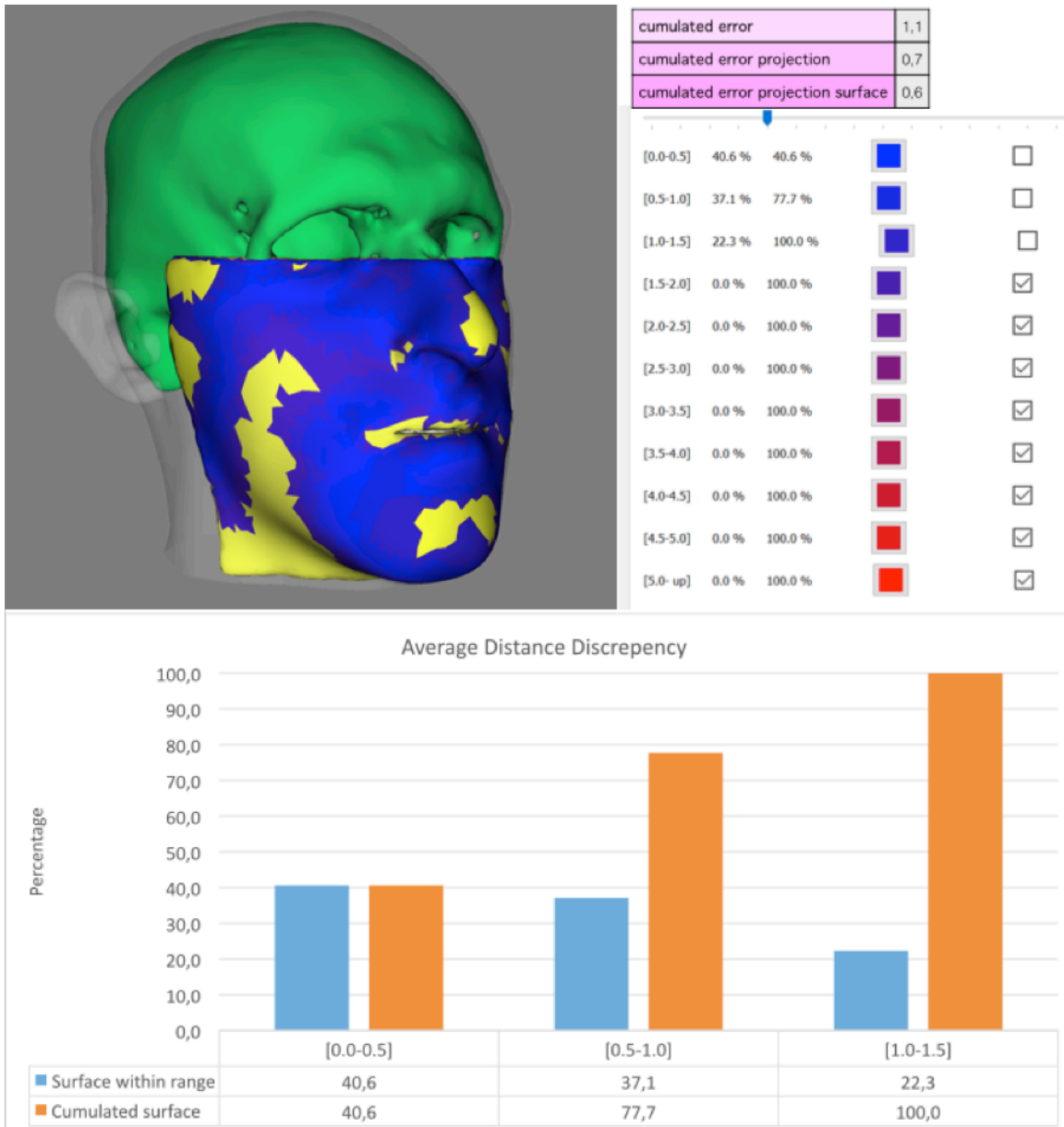


Figure 4.52: Magnitude of displacements between simulated and actual postoperative excluding error over to 1.5 mm.

## 4.6. Conclusion

In this chapter, we have presented how we have mathematically converted the surgical steps of cutting the maxilla and moving the facial bone segments. We have explained how we used software to generate a soft tissue geometric volume mesh. Then, we showed how we processed alteration of this volume mesh according to the surgical movements of the underlying skeleton, in order to simulate the facial soft tissue postoperative outcome.

In the last part, we explained how we conducted the evaluation of the soft tissue simulated mesh based on the comparison between the simulated and the actual position of the skin extracted from the postoperative CT scan. Therefore, we had to define three methods to measure the average distance between two meshes.

We have shown that our facial soft tissue simulation provides promising results, since accuracy is below 1 mm, when excluding the area located around the neck. Indeed, neck morphology is modified by varying patient head position between the preoperative and the postoperative CT acquisition.

Finally, the accuracy achieved using such a model and its refreshing speed can allow our simulation to be used in real-time applications requiring to being realistic.

Therefore, such software could be used in clinical routine for patient communication, and surgeon validation of the planned operative procedure (Cf. Figure 4.53).

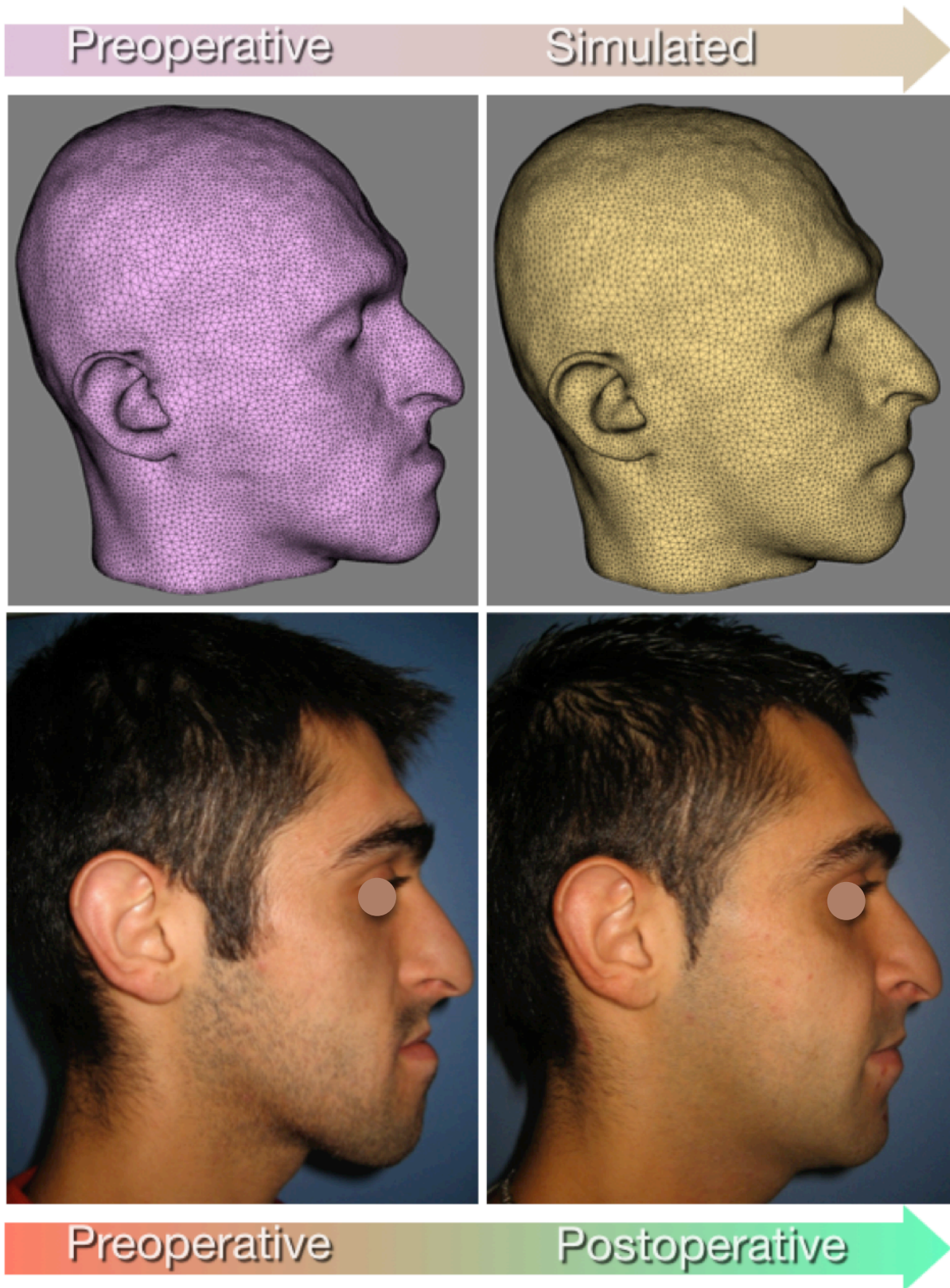


Figure 4.53: Comparison between the preoperative and simulated models and respectively the preoperative and postoperative clinical morphology.

---

## REFERENCES

1. Aulignac, D. d', R. Balaniuk, and C. Laugier. 2000. "A Haptic Interface for a Virtual Exam of the Human Thigh." In *Proceedings 2000 ICRA. Millennium Conference. IEEE International Conference on Robotics and Automation. Symposia Proceedings (Cat. No.00CH37065)*, 3:2452–2457 vol.3. doi:10.1109/ROBOT.2000.846395.
2. Avril, Stéphane, and Sam Evans. 2016. *Material Parameter Identification and Inverse Problems in Soft Tissue Biomechanics*. Springer.
3. Balaniuk, Remis, and Kenneth Salisbury. 2003. "Soft-Tissue Simulation Using the Radial Elements Method." In *Surgery Simulation and Soft Tissue Modeling*, 48–58. Springer, Berlin, Heidelberg. [https://link.springer.com/chapter/10.1007/3-540-45015-7\\_5](https://link.springer.com/chapter/10.1007/3-540-45015-7_5).
4. Baraff, David, and Andrew Witkin. 1998. "Large Steps in Cloth Simulation."
5. Casson, F. B. De, and C. Laugier. 2000. "Simulating 2D Tearing Phenomena for Interactive Medical Surgery Simulators." In *Proceedings Computer Animation 2000*, 9–14. doi:10.1109/CA.2000.889020.
6. Casson, François Boux de. 2000. "Simulation dynamique de corps biologiques et changements de topologie interactifs". Phdthesis, Université de Savoie. <https://tel.archives-ouvertes.fr/tel-00010170/document>.
7. Cevidanes, Lucia H. C., Scott Tucker, Martin Styner, Hyungmin Kim, Jonas Chapuis, Mauricio Reyes, William Proffit, Timothy Turvey, and Michael Jaskolka. 2010. "Three-Dimensional Surgical Simulation." *American Journal of Orthodontics and Dentofacial Orthopedics* 138 (3): 361–71. doi:10.1016/j.ajodo.2009.08.026.
8. Chabanas, Matthieu, Vincent Luboz, and Yohan Payan. 2003. "Patient Specific Finite Element Model of the Face Soft Tissues for Computer-Assisted Maxillofacial Surgery." *Medical Image Analysis* 7 (2): 131–51. doi:10.1016/S1361-8415(02)00108-1.
9. Chen, Y., Qing-Hong Zhu, A. Kaufman, and S. Muraki. 1998. "Physically-Based Animation of Volumetric Objects." In *Computer Animation 98. Proceedings*, 154–60. doi:10.1109/CA.1998.681920.
10. Cotin, S., H. Delingette, and N. Ayache. 1999. "Real-Time Elastic Deformations of Soft Tissues for Surgery Simulation." *IEEE Transactions on Visualization and Computer Graphics* 5 (1): 62–73. doi:10.1109/2945.764872.
11. Dakpé, Stéphanie, Tien Tuan Dao, B Devauchelle, and MC Ho Ba Tho. 2016. "Deformation Pattern of Skeletal Muscle Derived from MRI: Application to the Facial Mimics." In Lyon, France.

12. Dao, Tien Tuan, Stéphanie Dakpé, Philippe Pouletaut, Bernard Devauchelle, and Marie Christine Ho Ba Tho. 2013. “Facial Mimics Simulation Using MRI and Finite Element Analysis.” *Conference Proceedings: ... Annual International Conference of the IEEE Engineering in Medicine and Biology Society. IEEE Engineering in Medicine and Biology Society. Annual Conference 2013*: 4585–88. doi:10.1109/EMBC.2013.6610568.
13. Debunne, Gilles. 2000. “Animation Multirésolution D’objets Déformables En Temps-Réel, Application À La Simulation Chirurgicale”. Institut National Polytechnique de Grenoble.
14. Delingette, H., S. Cotin, and N. Ayache. 1999a. “A Hybrid Elastic Model Allowing Real-Time Cutting, Deformations and Force-Feedback for Surgery Training and Simulation.” In *Proceedings Computer Animation 1999*, 70–81. doi:10.1109/CA.1999.781200.
15. Delingette, H., S. Cotin, and N. Ayache. 1999b. “Efficient Linear Elastic Models of Soft Tissues for Real-Time Surgery Simulation.” *Studies in Health Technology and Informatics* 62: 100–101.
16. Delingette, Herve, and Nicholas Ayache. n.d. *Soft Tissue Modeling for Surgery Simulation*.
17. E. Promayon, P. Baconnier, C. Puech. 1996. “Physically Based Deformations Constrained in Displacements and Volume”. presented at the Proc. Computer Graphic Forum, Eurographics’96. <http://maverick.inria.fr/Publications/1996/PBP96/index.php>.
18. Frisken-Gibson, S. F. 1999. “Using Linked Volumes to Model Object Collisions, Deformation, Cutting, Carving, and Joining.” *IEEE Transactions on Visualization and Computer Graphics* 5 (4): 333–48. doi:10.1109/2945.817350.
19. Fung, Y.C. 1993. *Biomechanics - Mechanical Properties of Living Tissues* | Y. C. Fung | Springer. Springer Verlag, 2nd edition. <http://www.springer.com/us/book/9780387979472>.
20. Gibson, Sarah, Joe Samosky, Andrew Mor, Christina Fyock, Eric Grimson, Takeo Kanade, Ron Kikinis, et al. 1997. “Simulating Arthroscopic Knee Surgery Using Volumetric Object Representations, Real-Time Volume Rendering and Haptic Feedback.” In *CVRMed-MRCAS’97*, 367–78. Springer, Berlin, Heidelberg. <https://link.springer.com/chapter/10.1007/BFb0029258>.
21. Granados, Alejandro. 2008. “Haptic Deformable Shapes Using Open Source Libraries”. MSc Thesis, Imperial College London.

22. James, Doug L., and Dinesh K. Pai. 1999. "ArtDefo: Accurate Real Time Deformable Objects." In *Proceedings of the 26th Annual Conference on Computer Graphics and Interactive Techniques*, 65–72. SIGGRAPH '99. New York, NY, USA: ACM Press/Addison-Wesley Publishing Co. doi:10.1145/311535.311542.
23. James, Doug L., and Dinesh K. Pai. 2003. "Multiresolution Green's Function Methods for Interactive Simulation of Large-Scale Elastostatic Objects." *ACM Trans. Graph.* 22 (1): 47–82. doi:10.1145/588272.588278.
24. Keeve, E., S. Girod, R. Kikinis, and B. Girod. 1998. "Deformable Modeling of Facial Tissue for Craniofacial Surgery Simulation." *Computer Aided Surgery: Official Journal of the International Society for Computer Aided Surgery* 3 (5): 228–38. doi:10.1002/(SICI)1097-0150(1998)3:5<228::AID-IGS2>3.0.CO;2-I.
25. Koch, Rolf M., Markus H. Gross, Friedrich R. Carls, Daniel F. von Büren, George Fankhauser, and Yoav I. H. Parish. 1996. "Simulating Facial Surgery Using Finite Element Models." In *Proceedings of the 23rd Annual Conference on Computer Graphics and Interactive Techniques*, 421–28. SIGGRAPH '96. New York, NY, USA: ACM. doi:10.1145/237170.237281.
26. Koehl, C., L. Soler, and J. Marescaux. 2002. "A Distributed System for 3D Anatomical Structures Visualization and Surgical Planning." In *CARS 2002 Computer Assisted Radiology and Surgery*, edited by Professor Heinz U. Lemke, Professor Kiyonari Inamura, Professor Kunio Doi, Professor Michael W. Vannier MD, Professor Allan G. Farman DSc, and Professor Johan H. C. Reiber, 1082–1082. Springer Berlin Heidelberg. [http://link.springer.com/chapter/10.1007/978-3-642-56168-9\\_238](http://link.springer.com/chapter/10.1007/978-3-642-56168-9_238).
27. Lee, Yuencheng, Demetri Terzopoulos, and Keith Waters. 1995. "Realistic Modeling for Facial Animation." In *Proceedings of the 22Nd Annual Conference on Computer Graphics and Interactive Techniques*, 55–62. SIGGRAPH '95. New York, NY, USA: ACM. doi:10.1145/218380.218407.
28. Li, Ying, and Ken Brodlie. 2003. "Soft Object Modelling with Generalised ChainMail — Extending the Boundaries of Web-Based Graphics." *Computer Graphics Forum* 22 (4): 717–27. doi:10.1111/j.1467-8659.2003.00719.x.
29. Mollemans, W., F. Schutyser, N. Nadjmi, F. Maes, and P. Suetens. 2007. "Predicting Soft Tissue Deformations for a Maxillofacial Surgery Planning System: From Computational Strategies to a Complete Clinical Validation." *Medical Image Analysis* 11 (3): 282–301. doi:10.1016/j.media.2007.02.003.
30. Mollemans, Wouter, Filip Schutyser, Johan Van Cleynenbreugel, and Paul Suetens. 2003. "Tetrahedral Mass Spring Model for Fast Soft Tissue Deformation." *Lecture Notes in Computer Science* 2673 (January): 145–54.
31. Mollemans, Wouter, Filip Schutyser, Nasser Nadjmi, Frederik Maes, and Paul Suetens. 2006. "Parameter Optimisation of a Linear Tetrahedral Mass Tensor Model for a Maxillofacial Soft Tissue Simulator." In *Biomedical Simulation*, 159–68. Springer, Berlin, Heidelberg. doi:10.1007/11790273\_18.



32. Monserrat, C., U. Meier, M. Alcañiz, F. Chinesta, and M. C. Juan. 2001. "A New Approach for the Real-Time Simulation of Tissue Deformations in Surgery Simulation." *Computer Methods and Programs in Biomedicine* 64 (2): 77–85. doi:10.1016/S0169-2607(00)00093-6.
33. Nava, A., E. Mazza, M. Furrer, P. Villiger, and W. H. Reinhart. 2008. "In Vivo Mechanical Characterization of Human Liver." *Medical Image Analysis* 12 (2): 203–16. doi:10.1016/j.media.2007.10.001.
34. Nedel, L. P., and D. Thalmann. 1998. "Real Time Muscle Deformations Using Mass-Spring Systems." In *Proceedings. Computer Graphics International (Cat. No.98EX149)*, 156–65. doi:10.1109/CGI.1998.694263.
35. Bro-Nielsen, M. 1998. "Finite Element Modeling in Surgery Simulation." *Proceedings of the IEEE* 86 (3): 490–503. doi:10.1109/5.662874.
36. Bro-Nielsen, Morten, and Stephane Cotin. 1996. "Real-Time Volumetric Deformable Models for Surgery Simulation Using Finite Elements and Condensation." doi:10.1111/1467-8659.1530057.
37. Nisansala, Aruni, Maheshya Weerasinghe, G. K. A. Dias, Damitha Sandaruwan, and Nihal Kodikara. 2015. "Soft Tissue Modeling Techniques in Surgery Simulation." *International Journal of Computer and Information Technology* 04 (05): 826–31.
38. Parke, F. I. 1982. "Parameterized Models for Facial Animation." *IEEE Comput. Graph. Appl.* 2 (9): 61–68. doi:10.1109/MCG.1982.1674492.
39. Picinbono, Guillaume, Hervé Delingette, and Nicholas Ayache. 2003. "Non-Linear Anisotropic Elasticity for Real-Time Surgery Simulation." *Graphical Models* 65 (5): 305–21. doi:10.1016/S1524-0703(03)00045-6.
40. Platt, Stephen M., and Norman I. Badler. 1981. "Animating Facial Expressions." *SIGGRAPH Comput. Graph.* 15 (3): 245–52. doi:10.1145/965161.806812.
41. Samur, Evren, Mert Sedef, Cagatay Basdogan, Levent Avtan, and Oktay Duzgun. 2007. "A Robotic Indenter for Minimally Invasive Measurement and Characterization of Soft Tissue Response." *Medical Image Analysis* 11 (4): 361–73. doi:10.1016/j.media.2007.04.001.
42. Schendel, Stephen A., and Kevin Montgomery. 2009. "A Web-Based, Integrated Simulation System for Craniofacial Surgical Planning." *Plastic and Reconstructive Surgery* 123 (3): 1099–1106. doi:10.1097/PRS.0b013e318199f653.
43. Schill, Markus A., Sarah F. F. Gibson, H.-J. Bender, and R. Männer. 1998. "Biomechanical Simulation of the Vitreous Humor in the Eye Using an Enhanced ChainMail Algorithm." In *Medical Image Computing and Computer-Assisted Intervention — MICCAI'98*, 679–87. Springer, Berlin, Heidelberg. doi:10.1007/BFb0056254.

44. Schutyser, Filip, Johan Van Cleynenbreugel, Matthieu Ferrant, Joseph Schoenaers, and Paul Suetens. 2000. "Image-Based 3D Planning of Maxillofacial Distraction Procedures Including Soft Tissue Implications." In *Medical Image Computing and Computer-Assisted Intervention – MICCAI 2000*, 999–1007. Springer, Berlin, Heidelberg. doi:10.1007/978-3-540-40899-4\_104.
45. Soler, Luc, Didier Mutter, and Jacques Marescaux. 2011. "Computer-Assisted Liver Surgery: from preoperative 3D patient modelling to peroperative guidance." <http://hdl.handle.net/2042/45133>.
46. Sundaraj, K., C. Mendoza, and C. Laugier. 2002. "A Fast Method to Simulate Virtual Deformable Objects with Force Feedback." In *7th International Conference on Control, Automation, Robotics and Vision, 2002. ICARCV 2002.*, 1:413–418 vol.1. doi:10.1109/ICARCV.2002.1234857.
47. Sundaraj, Kenneth. 2004. "Simulation Dynamique En Temps-Réel et Interaction 3D de Tissu Biologique: Application Aux Simulateurs Médicaux". PhD Thesis, Institut National Polytechnique de Grenoble (INPG), France. <http://scholar.google.com/scholar?cluster=9876823816456411172&hl=en&oi=scholar>.
48. Taylor, Russell H. 1996. *Applications of Simulation, Morphometrics, and Robotics in Craniofacial Surgery*. Vol. Computer-integrated Surgery: Technology and Clinical Applications. MIT Press.
49. Teran, J., S. Blemker, V. Ng Thow Hing, and R. Fedkiw. 2003. "Finite Volume Methods for the Simulation of Skeletal Muscle." In *Proceedings of the 2003 ACM SIGGRAPH/Eurographics Symposium on Computer Animation*, 68–74. SCA '03. Aire-la-Ville, Switzerland, Switzerland: Eurographics Association. <http://dl.acm.org/citation.cfm?id=846276.846285>.
50. Terzopoulos, D., and K. Waters. 1990. "Analysis of Facial Images Using Physical and Anatomical Models." In *[1990] Proceedings Third International Conference on Computer Vision*, 727–32. doi:10.1109/ICCV.1990.139628.
51. Terzopoulos, Demetri, John Platt, Alan Barr, and Kurt Fleischer. 1987. "Elastically Deformable Models." *SIGGRAPH Comput. Graph.* 21 (4): 205–14. doi:10.1145/37402.37427.
52. Teschner, M., S. Girod, and B. Girod. 2001. "3-D Simulation of Craniofacial Surgical Procedures." *Studies in Health Technology and Informatics* 81: 502–8.
53. Teschner, M., B. Heidelberger, M. Muller, and M. Gross. 2004. "A Versatile and Robust Model for Geometrically Complex Deformable Solids." In *Computer Graphics International, 2004. Proceedings*, 312–19. doi:10.1109/CGI.2004.1309227.
54. Waters, Keith. 1987. "A Muscle Model for Animation Three-Dimensional Facial Expression." *SIGGRAPH Comput. Graph.* 21 (4): 17–24. doi:10.1145/37402.37405.

55. Westermark, Anders, Stefan Zachow, and Barry L. Eppley. 2005. "Three-Dimensional Osteotomy Planning in Maxillofacial Surgery Including Soft Tissue Prediction." *The Journal of Craniofacial Surgery* 16 (1): 100–104.
56. Wu, Wen, and Pheng Ann Heng. 2004. "A Hybrid Condensed Finite Element Model with GPU Acceleration for Interactive 3D Soft Tissue Cutting." *Computer Animation and Virtual Worlds* 15 (3-4): 219–27. doi:10.1002/cav.24.
57. Xia, J., N. Samman, R. W. Yeung, S. G. Shen, D. Wang, H. H. Ip, and H. Tideman. 2000. "Three-Dimensional Virtual Reality Surgical Planning and Simulation Workbench for Orthognathic Surgery." *The International Journal of Adult Orthodontics and Orthognathic Surgery* 15 (4): 265–82.

## Chapter 5

### Navigation software

#### Development and evaluation

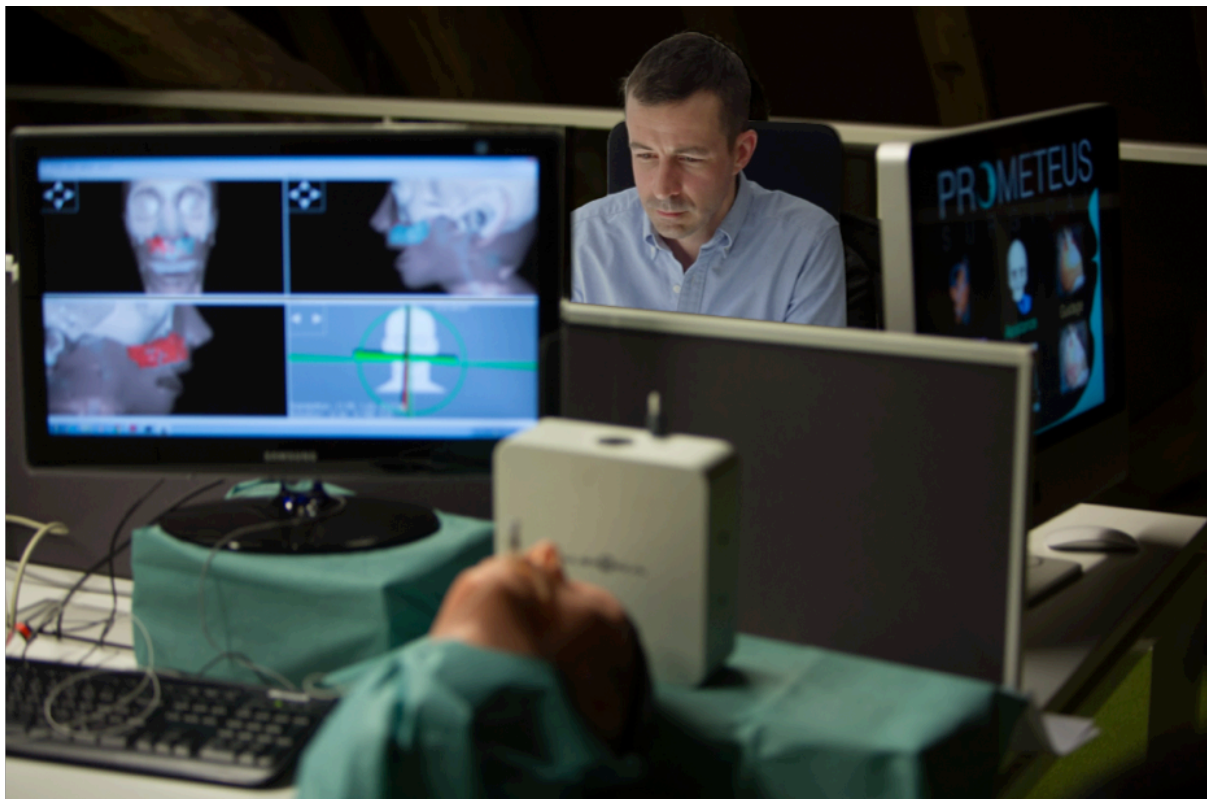
---

*Appropriate positioning of the maxilla is critical in orthognathic surgery, since it is usually the first step of the procedure and will greatly influence the quality of the outcome, especially in terms of facial aesthetics and smile harmony (Kretschmer et al. 2009). Maxilla position is traditionally achieved thanks to an intermediate splint manufactured in the prosthodontics laboratory. Such a process requires specific training and time-consuming careful preparation.*

*Computer assistance has contributed to substantial improvement in maxillary positioning. Numerous software packages, relying on similar data processes from computed tomography (CT) scans, allow intuitive preoperative planning and are today widely spread (Neumann et al. 1999). We have explained in **Chapter 4** the principles of the planning procedure we have used.*

*One of the main challenges remains in the transfer of computer planning to the operating theatre. Indeed, it should ensure conformity between the planned position and the actual surgical procedure achieved by the operator.*

---



Source: DNA Dernières Nouvelles d'Alsace.

In Chapter 2, we have explained why CAD physical guiding methods (e.g. CAD cutting guides, splints and plating systems) did not appear to us as the most relevant ones. Indeed, they restrain the surgeon to a single intraoperative workflow, allow limited versatility regarding unexpected surgical occurrences and generate repeated additional costs. They are not perfectly suited to help correcting the vertical dimension intraoperatively. As a result, in surgical routine, many experienced surgeons choose to achieve free-hand maxillary positioning under sole visual control. External positioning tools (Borumandi et al. 2013) have been proposed but they are bulky and their use is often not intuitive.

Navigation systems therefore appear as an alternative to improve accuracy and favorably let the surgeon decide whether virtual positioning information is to be followed. Chapter 2 also emphasized that navigation systems used in orthognathic surgery mostly rely on optical-based tracking systems (Zinser et al. 2013)(Bettega et al. 1996; Bettega and Leitner 2013) based on bulky fiducials and an easily-disrupted line of sight where intraoral surgical exposure is so critical (Benassarou et al., 2013). Optical-based navigation either uses steady head support with a Mayfield clamp or fixation of bulky fiducial markers on the patient when head tracking is intended (Robert A Mischkowski et al. 2006; R. A. Mischkowski et al. 2007) (Zinser et al. 2013).

Recent studies have proved electromagnetic (EM) tracking systems can provide sufficient accuracy (< 1mm) considering the thickness of cutting devices (1 mm) (Seeberger et al. 2012)(Cartellieri, Kremser, and Vorbeck 2001). Most notably, since electromagnetic sensors are tiny and allow free surgical movements between the sensors and the generator, EM systems seem relevant for orthognathic surgery.

Considering the above elements, our aim was to develop and assess a novel navigation system which specifications were adapted to the surgical constraints especially of asepsis, restricted operative sight and bulk of fiducials, as described in Chapter 2.

Therefore, we decided to base our navigation system on electromagnetic tracking of the maxilla using inconspicuous fiducials. This system had to include real-time registration of head movements, therefore making steady head support unnecessary. A user-friendly 3D registration procedure between the actual patient and its virtual model was also required. Since researchers have underlined the influence of the navigation system interface on the accuracy of the procedure (Traub, Stefan, Heining, Riquarts, et al. 2006), we purposely designed and evaluated an original, user-friendly interface.

## 5.1. Material and method

### 5.1.1. Head phantom

We used a real-size medical plastic head model (Airway management Simulator “Bill I”<sup>®</sup>, VBM Medizintechnik GmbH, Germany) consisting of a realistic maxillofacial skeleton coated with a skin-mimicking layer of soft material (Cf. Figure 5.1).

A standard LeFort one osteotomy was performed and the maxilla was fixed in an unchanged position using a standard titanium plating system (Modus<sup>®</sup> 1.5 Medartis<sup>®</sup>, Switzerland).

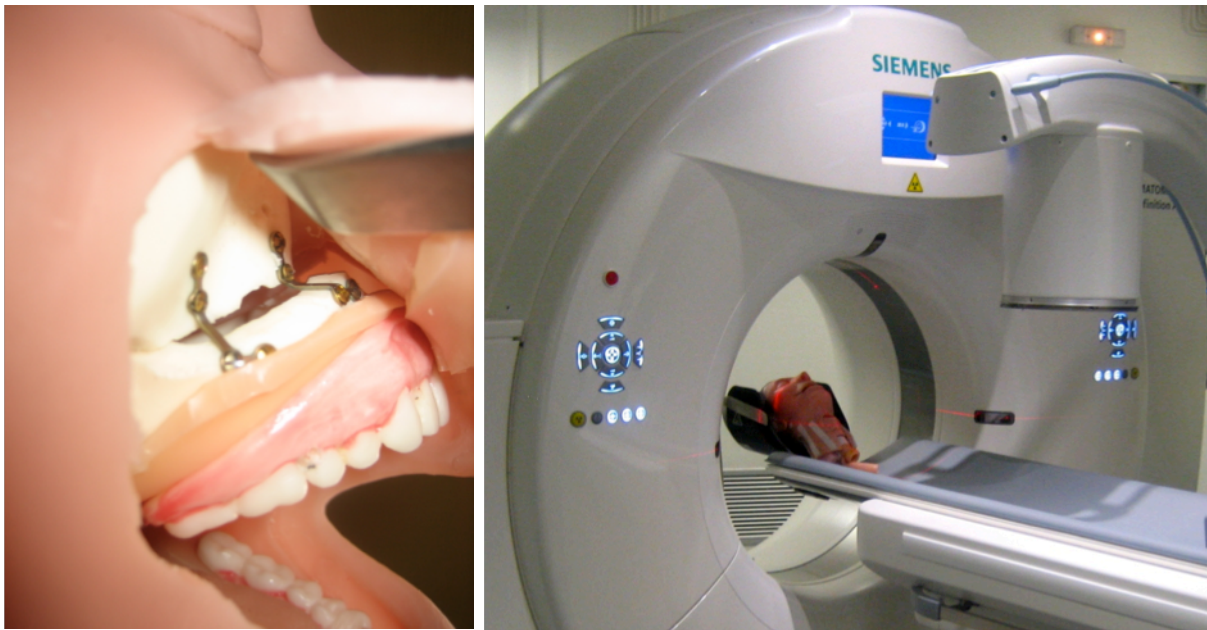


**Figure 5.1: Plastic head model:** mimicking surgery (left) and scanning (right).

Afterwards, a CT scan (SOMATOM<sup>®</sup> Definition AS+, Siemens<sup>®</sup>, Germany) of the model was acquired (Cf. Figure 5.1). The field of view was  $256 \times 256 \times 304 \text{ mm}^3$  and voxel size was  $0.5 \times 0.5 \times 1 \text{ mm}^3$ .

Segmentation of the CT data was performed using VR-Med Software (D’Agostino et al. 2012) resulting in three different virtual models, the maxilla, the remaining superior facial skeleton, and the mandible which was not considered in our study.

Rigid fixation was then removed from the maxilla in order to allow free 3D movements.

### 5.1.2. Electromagnetic tracking system

An electromagnetic (EM) tracking system (Aurora<sup>®</sup>, NDI<sup>®</sup>, Canada) (Cf. Figure 5.2) was used to achieve registration from the real environment (plastic model) to the virtual one (segmented CT scans) of both the head model and the maxilla and their real-time tracked position.

The NDI<sup>®</sup> Company is known worldwide for its expertise in metrology applied to different areas such as research, industry or medical practice. It particularly develops

electromagnetic or optical tracking systems, but also motion capture systems and laser scanners.

The Aurora<sup>®</sup> electromagnetic tracking system is a technology developed by NDI<sup>®</sup> that was specifically designed for medical application. The system featured miniaturized sensors, designed to be attached to surgical instruments without restricting their movement, since sensors were quite flexible.

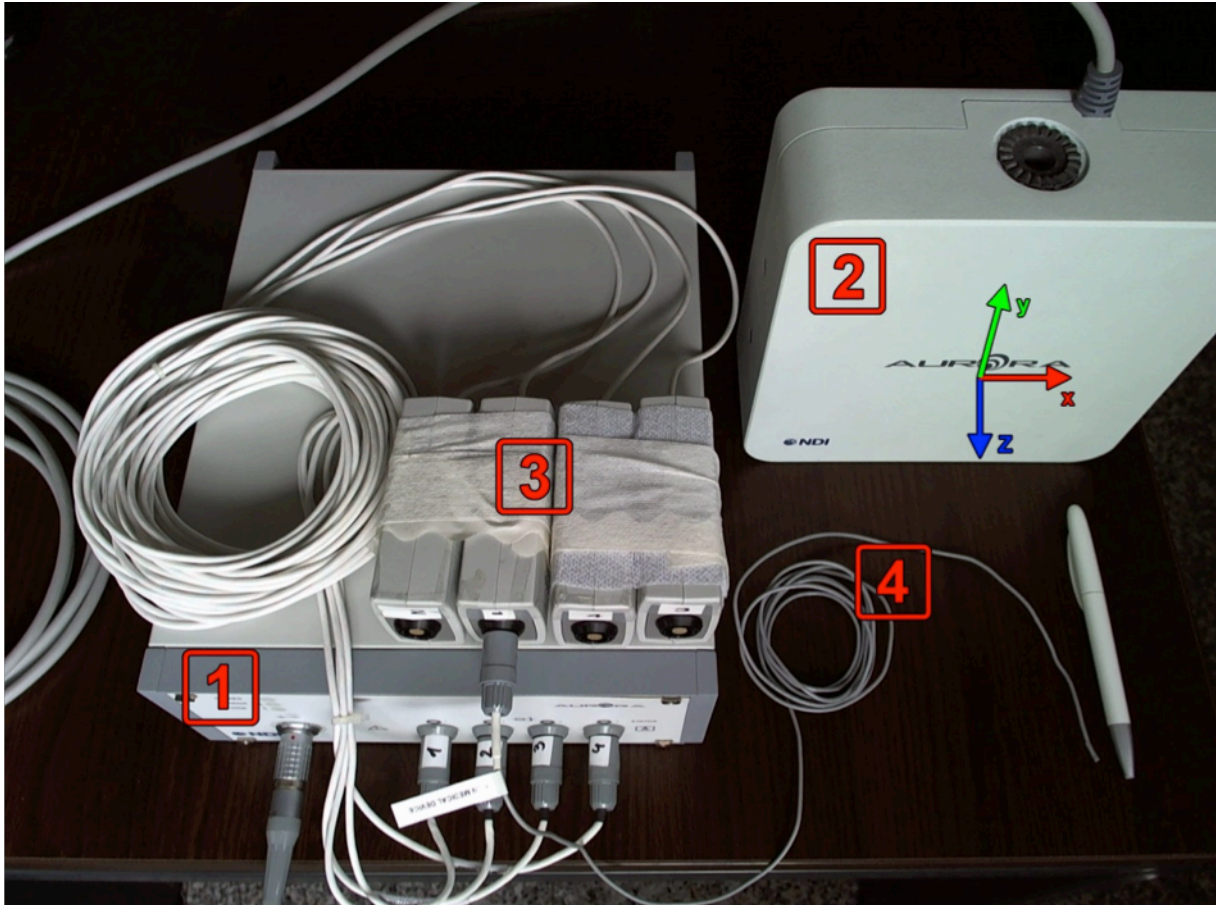


**Figure 5.2: The Aurora<sup>®</sup> electromagnetic tracking system.**

1. System control unit. 2. Field generator. 3. Sensor interface units. 4. Sensor

The whole system is depicted in Figure 5.2. It consisted of several sub-systems which functions are intimately bound:

1. **The system control unit** collected information transmitted by the sensor interface units and processed position and orientation of every 6-DOF sensor. It also interfaced with the computer to which it was connected and transmitted these data through an USB port. Data acquisition frequency was of 40 Hz.
2. **The field generator** emitted a low intensity dynamic electromagnetic field in a cubic volume of approximately  $50 \times 50 \times 50 \text{ cm}^3$ . It also defined the origin of the coordinate system of tracked objects. This **landmark** was located at the center of the anterior side of the generator (Cf. Figure 5.2).
3. **The sensor interface units** amplified and digitalized the analogical signals transmitted by the sensors to which they were connected. The sensor interface units transmitted these signals to the system control unit.
4. **The sensors** were embedded in 1.3 mm diameter catheters. Each sensor contained small coils into which electrical current was induced by the electromagnetic field generated. The specifications of these electrical signals directly depended on the position and the orientation of the sensor relative to the electromagnetic field source. Each sensor had 6 degrees of freedom (Aurora 6DOF catheter, Type 2). Sensor accuracy allowed 95% of position errors to be smaller than 0.9 mm and 95% of orientation errors to be smaller than  $0.5^\circ$ .

The purpose of using this system was to develop a navigation application (that we named "**3D Guidance**") dedicated to accurately register the position and orientation of the elements involved in the surgical procedure.

In the considered protocol, the goal was to **track the maxilla position** in relation to the patient's head position. Indeed, bone movements were planned relative to the head but patient's head could move during the procedure. Therefore, tracking of the maxilla was not sufficient, since head movements needed to be registered. As a result, we used one sensor for maxilla tracking and one for **head tracking**. We designed an experimental set-up that mimicked the surgical environment in order to facilitate transfer of the procedure to the OR. Our set-up used three flexible catheters. **Tracking of the maxilla** was achieved by means of a **surgical splint**, since such a device is commonly used in the standard surgical workflow. Therefore, one sensor was embedded into a custom-made acrylic splint attached to the maxillary dental arch using stainless steel wires (Cf. Figures 5.3 and 5.4). Tracking of the maxilla actually consisted in the tracking of the maxilla-splint unit.

**Tracking of the head** was performed using another sensor attached to the middle of the forehead using a Velcro band, since such a set-up is compatible with accessibility and asepsis constraints in the OR (Cf. Figure 5.3, n°3).

**A third sensor** was used for registration and accuracy control.



### 5.1.3. Experimental set-up

It was designed as depicted in Figure 5.3:

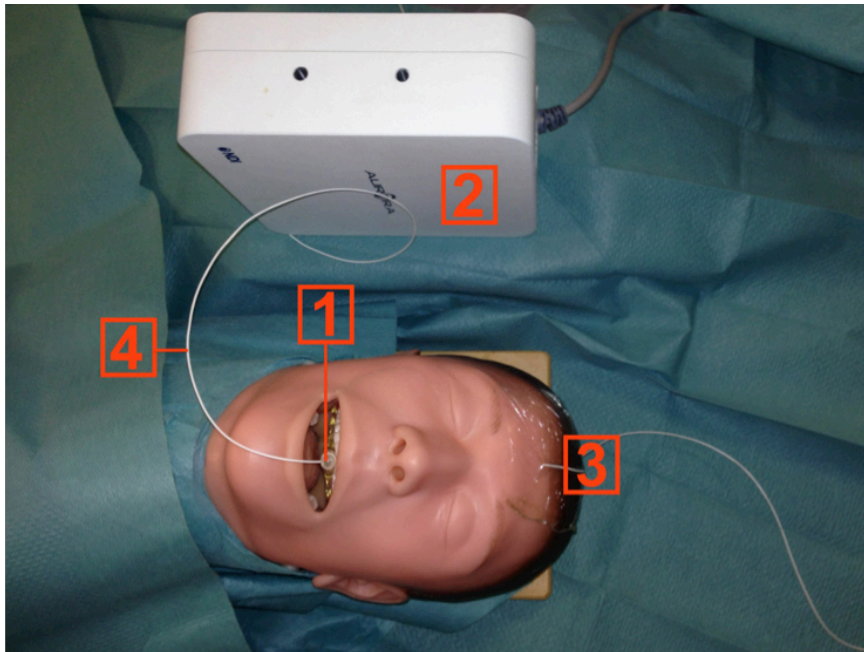


**Figure 5.3: Experimental set-up for EM-based navigation system.**

1. Sensor embedded in a custom-made surgical splint attached to the maxillary dental arch.  
2. EM generator. 3. Sensor attached to the middle of the forehead to track head movements.  
Note: the third sensor, used for registration and accuracy control was not included in the picture.

1. **The maxilla-splint unit** was meant to be surgically repositioned by the operator.
2. **The EM field generator** was positioned close to the head model, in order for the EM sensors to be tracked as accurately as possible. A set distance of 100 mm laterally from the head model was chosen. Aside from restriction of the tracking volume, accuracy of electromagnetic registration decreased when distance between the sensors and the generator increased.
3. **A first sensor was attached to the middle of the forehead** using a Velcro band (removed in Figure 5.3 to reveal the sensor) in order to consider possible head movements during surgery.
4. **A second sensor was embedded into the splint** attached integrally with the maxilla. The maxilla-splint unit was further subject to navigation. The maxilla-splint-sensor unit is detailed in Figure 5.4.

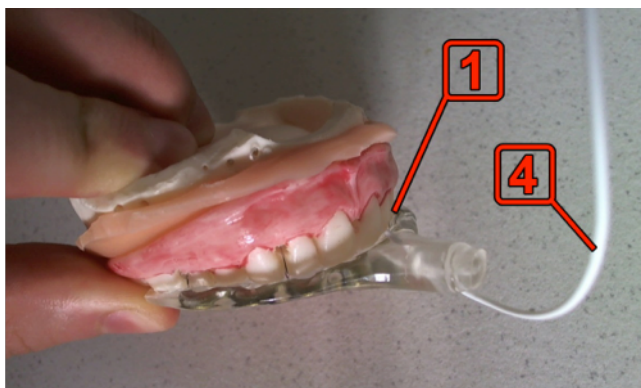


**Figure 5.4: Maxilla-splint unit with embedded EM sensor.**

## 5.2. Navigation software development

We developed navigation software using the open source fw4spl<sup>27</sup> framework and the Virtual Toolkit library.

The whole EM-system communicated position data to the 3D Guidance Software, which displayed the real-time position of both the 3D model of the maxilla and the upper facial skeleton onto the screen.

These 3D models were not automatically generated but previously reconstructed using CT scan images (collection of 2D sections) from the patient acquired preoperatively for the surgeon to plan the procedure. As described in Chapter 3, CT scan images were first segmented (segmentation of skin, maxilla and mandible) then meshed in order to produce 3D surface models (Cf. Figure 5.5). This initial step was achieved thanks to VRMed<sup>®</sup> IRCAD software, specially designed for such protocols.

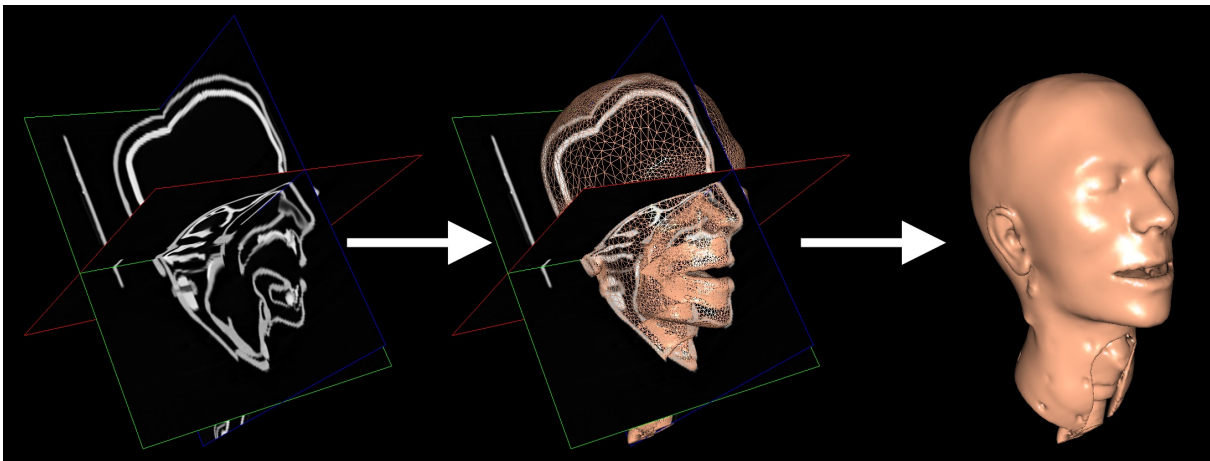


Figure 5.5: Three-dimensional reconstruction of plastic head model.

### 5.2.1. Prerequisite calibration and registration issue

The origin of the coordinate system was the one of CT scan images used for reconstruction. This point was rather different from the origin of the coordinate system related to the sensors. Subsequently, one could not directly express the position of a point in one coordinate system in relation to the other coordinate system. Therefore, it was prerequisite is to determine the relative position of, respectively, the 3D head model and the maxilla model, in relation to, respectively, the sensor attached to the forehead and the one embedded into the splint.

Practically speaking, this involved calculating a rotation and a translation allowing switching from the 3D model coordinate system to the EM sensor coordinate system. This preliminary **calibration** was only achieved once before the procedure. Without this step, display of the models could not be consistent. The following paragraph details the **calibration** step.

<sup>27</sup> fw4spl framework: <https://code.google.com/p/fw4spl/wiki/poc1>

The system previously described featured several coordinate systems as depicted in Figure 5.6.

- **<Head>** was the origin of the coordinate system regarding 3D reconstructions from the uncut upper facial skeleton in relation to the head (skin, skull,...)
- **<Splint>** was the origin of the coordinate system regarding 3D reconstructions from the movable maxilla
- **<Em>** was the origin of the coordinate system regarding the Aurora<sup>®</sup> system: the position of all the tracked sensors were expressed within this system.
- **<Head sensor>** was the coordinate system of the sensor attached to the forehead.
- **<Placement sensor>** was the coordinate system of the sensor embedded into the splint.

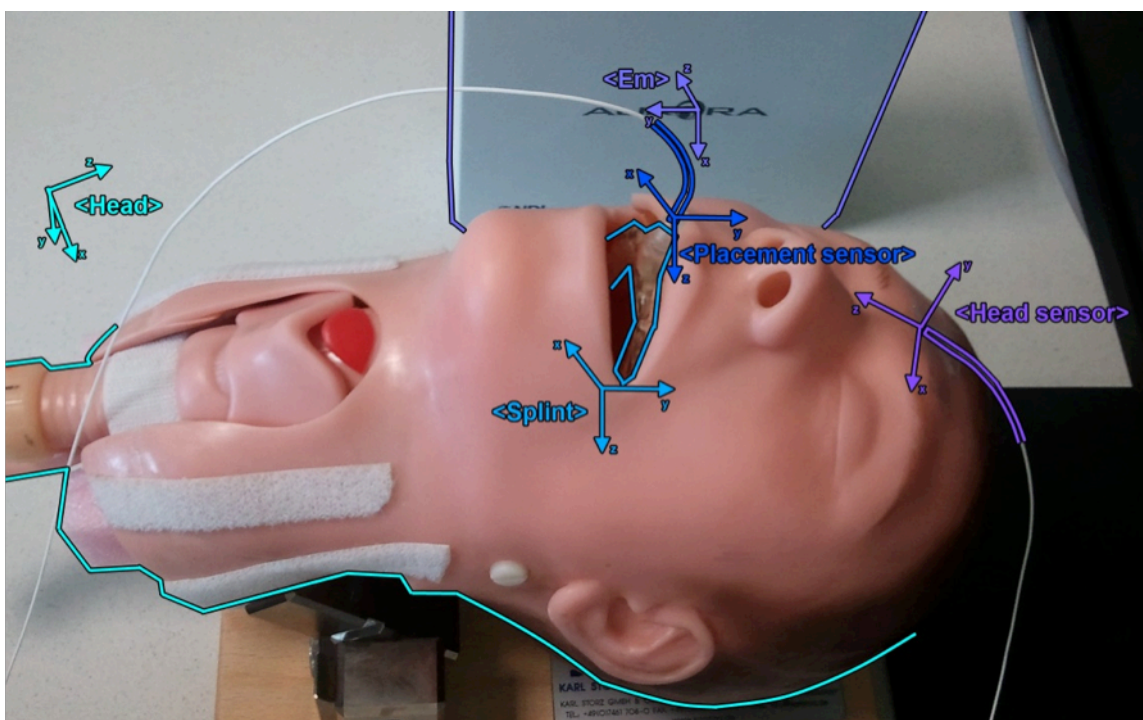


Figure 5.6: Illustration of the coordinate systems used in the navigation system.

Considering all these coordinate systems, it was necessary to adopt some conventions. We particularly decided to express all the coordinate systems within a common basis. Therefore, we chose the origin of the coordinate system of the Aurora<sup>®</sup> system, abbreviated **<Em>**, as the common basis. This choice appeared quite obvious, since the position of all the sensors was expressed within that **<Em>** coordinate system. Hence, we did not need to conduct any changes in the coordinate systems of **<Head sensor>** and **<Placement sensor>**, which were related to **<Em>**. Nevertheless, we had to establish a relation between the **<Splint>** and **<Em>** coordinate systems on one hand, and the **<Head>** and **<Em>** coordinate systems, on the other hand.

Therefore, the calibration step needed to be conducted both for the head and the splint. We will explain these steps in the next paragraph.

### 5.2.1.1. Calibration of the head in relation to the sensor attached to the forehead

This procedure is depicted in Figure 5.7. Its workflow proceeded as follows:

- The operator clicked several anatomical landmarks on the **3D virtual head model**: at least 3, unaligned points. These landmarks were expressed in the **<Head>** coordinate system. Practically speaking, according to literature (Seeberger et al. 2012), we achieved a 6-point registration procedure, since it has been proven to provide more accuracy in measurements.
- Then, the operator pinpointed the same landmarks on the **actual plastic head model** using the third electromagnetic sensor in order to register these new positions, which were further expressed in the **<Em>** coordinate system.

Correlation between these two sets of points was established by computing the transformation matrix from **<Head>** to **<Em>**. This involved finding the best couple

(Rotation R, Translation T) that minimized the sum  $\sum_{i=1}^n \|(R \times p_i) + \vec{T} - q_i\|^2$ ,

$p_i$  and  $q_i$  being the positions of, respectively, the  $n$  points in the 3D model and the  $n$  points recorded through tracking. Finding R and T was achieved through a known algorithm (Arun, Huang, and Blostein 1987) available in a C++ IRCAD routine.

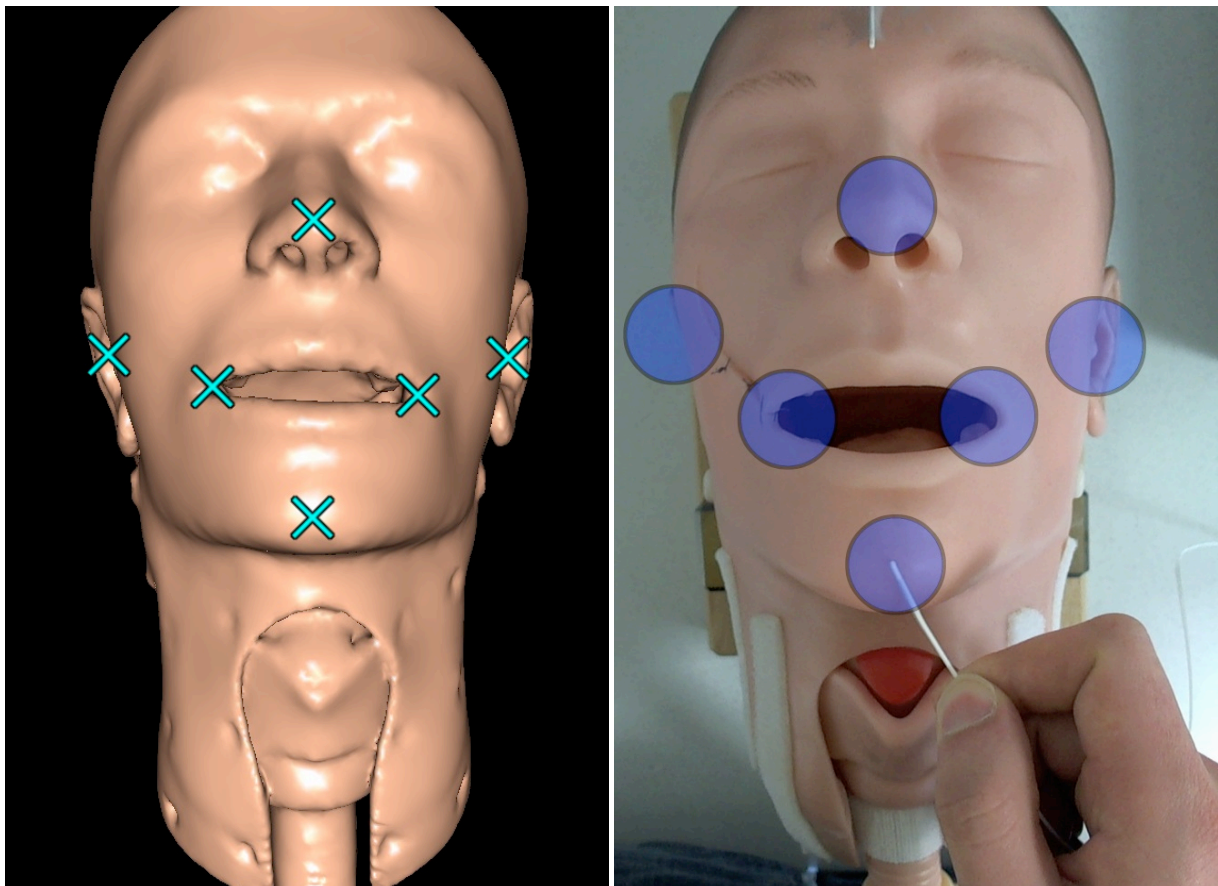


Figure 5.7: Correlation between landmarks in the virtual head model and landmarks on the actual plastic head model.

### 5.2.1.2. Calibration of the splint in relation to its embedded sensor

Regarding the movable maxilla, the same calibration procedure could not be applied, since the splint did not feature specific enough landmarks for registration to be accurate. However, by construction, the splint was calibrated together with its embedded sensor (Cf. Figure 5.4). **Therefore, the position of the splint embedded sensor relative to the teeth (and therefore the maxilla) was known.** On such a basis, our solution consisted in interactive (manual) registration that relied on hard-coding the transformation matrix from the <Splint> coordinate system to the <Em> coordinate system. Practically speaking, the system was initially calibrated, once and for the whole duration of the procedure, using an initialization button. Subsequently, the position of the splint sensor relative to the reference forehead sensor was known. The position of reference used regarding the maxilla-splint-sensor unit was the one where the maxilla was held in an unchanged position (i.e.: neutral position without any surgical displacement), as it was before the maxilla would further be cut off. This workflow did not induce any restriction, since the sensor was always embedded in the same fashion within the splint. Additionally, one can think that, if this device were to be industrialized, splint and sensor would be rigidly fixed, therefore ensuring an invariable registration matrix.

### 5.2.2. Navigation interface

Traub J et al (Traub, Stefan, Heining, Riquarts, et al. 2006; Traub, Stefan, Heining, Sielhorst, et al. 2006) have worked on the development of a hybrid navigation interface and compared slice based navigation system with in-situ visualization. In their paper describing a navigated drilling experiment, they report that both, operative time and accuracy are improved when using an intuitive interface.

On this basis, we decided to purposely design and develop a novel **user-friendly interface dedicated to the specifications of orthognathic surgery** (Lutz et al. 2015).

The user interface featured a four-area split screen display as depicted in Figure 5.8:

- Each of the first three areas (top left, top right and bottom left) displayed a different view of the virtual 3D head model.
- The fourth area of the screen (bottom right) displayed an original colored crosshair.

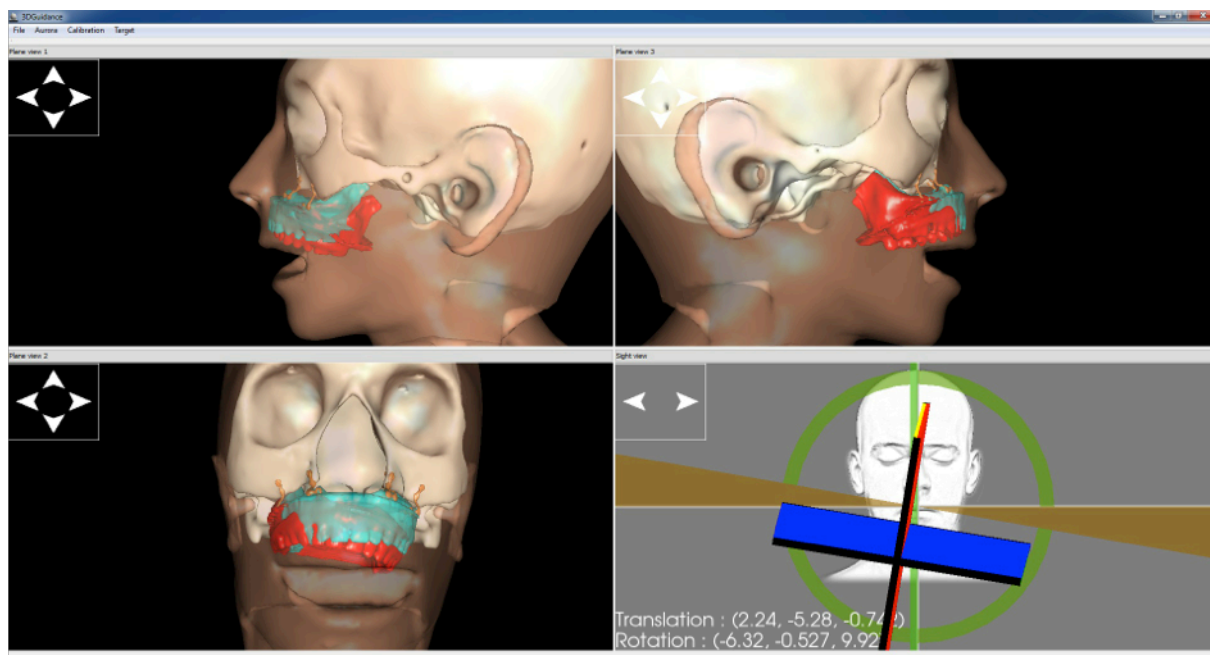


Figure 5.8: User Interface of the navigation software.

### 5.2.2.1. The three views of the virtual 3D head model and its color-code

These views (top left, top right and bottom left) displayed reconstructed 3D models of patient's head from various customizable angles of view. Each view displayed two categories of objects:

- the 3D models related to patient's head including skin surface mesh, and bone surface meshes of the upper facial skull and the planned (target) postoperative position of the maxilla. For readability purposes, the mesh of the postoperative position of the maxilla was colored in cyan.
- the movable maxilla that consisted of the actual position of the tracked maxilla. Its mesh was colored in red.

The 3D models could be turned to any position chosen by the operator. The default setting used frontal view (bottom left area), right lateral view (top right area), and left lateral view (top left area), since this is a standard way to examine patients and to assess them intraoperatively in orthognathic surgery.

In this framework, navigation consisted in achieving superimposition of the red maxilla onto the cyan maxilla. This navigation actually represented a control guidance tool that provided limited accuracy. However, it helped visualizing actual position of the navigated maxilla in relation to the planned position.

### 5.2.2.2. Colored crosshair and its color code

This original feature was displayed in the bottom right area of the interface. The purpose of developing this crosshair was to provide a tool to refine the navigated position, once it has been roughly initiated using the three views of the virtual 3D head model. The crosshair illustrated the difference between the actual position of the maxilla and its planned position. In addition, this area of the interface also displayed the accurate rotation and translation metrics to be applied in order to match the planned position.

We will now detail the crosshair and its features.

**The 3D colored crosshair consisted of a cross, surrounded by a circle.** This crosshair was the main navigation tool and the most accurate one. Several development steps were required before its assessment on the plastic head model was to be considered.

A first prototype was developed as depicted in Figure 5.9. The idea was then to display on screen a 3D cross allowing visualization of translational and rotational differences between the actual and the target position of an object.

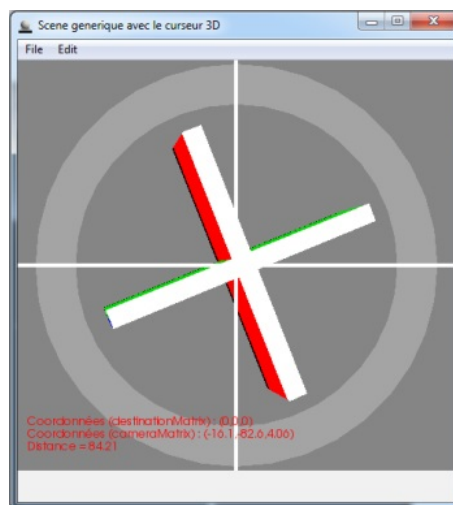


**Figure 5.9: Prototype of 3D colored crosshair**

The 3D colored cross consisted of the intersection of two orthogonal planes passing through the maxilla, the median sagittal and the horizontal occlusal (transversal) plane. The right side of the vertical plane was red, the left side yellow. The upper side of the horizontal plane was blue, whereas the lower side was green. In the background, an orthogonal white steady cross was displayed as the reference for the achieved target position. This virtual cross moved in real-time together with the actual detached maxilla. A circle, surrounding the cross, illustrated the maxillary posteroanterior position.

Differences in **translation** were displayed in two ways:

- regarding movements along the transversal and the frontal planes (Cf. Chapter 2 for definition of planes): by the shift of the cross in relation to the origin in the center
- regarding movements along the sagittal plane: by the size of the cross in relation to its surrounding circle. In case of a perfect translation of the maxilla, i.e.: completely matching the planned position, all the branches of the cross would be integrally contained within the inner edge of the circle.

Differences in **rotation** were represented by the position of the cross itself. In cases where the cross was not facing the camera, its colored sides became visible and indicated a rotation.

**Therefore, a perfect match, translation-wise and rotation-wise, between the planned and the actual maxilla position would result in the alignment of the crosshair with the background white steady cross and the disappearance of its colored sides.**

The differences in position (translation, rotation) depicted by the crosshair and the steady background cross involved a transformation matrix. In the navigation software, this matrix was directly computed by the tracking system.

Along with the development of the crosshair prototype, we had to assemble and develop the basis bricks of navigation software, particularly the remaining part of the interface, as well as the tracking system. Once the crosshair prototype was achieved, we conducted its integration to the software. This step went swiftly thanks to the fw4spl modular architecture.



### 5.2.2.3. Additional features

Once software integration of the crosshair was achieved, we conducted some early tests. Subsequently, we implemented several improvements in order to make it more intuitive. In its final version, the navigation crosshair therefore featured a more complete and user-friendly interface (Cf. Figure 5.9).

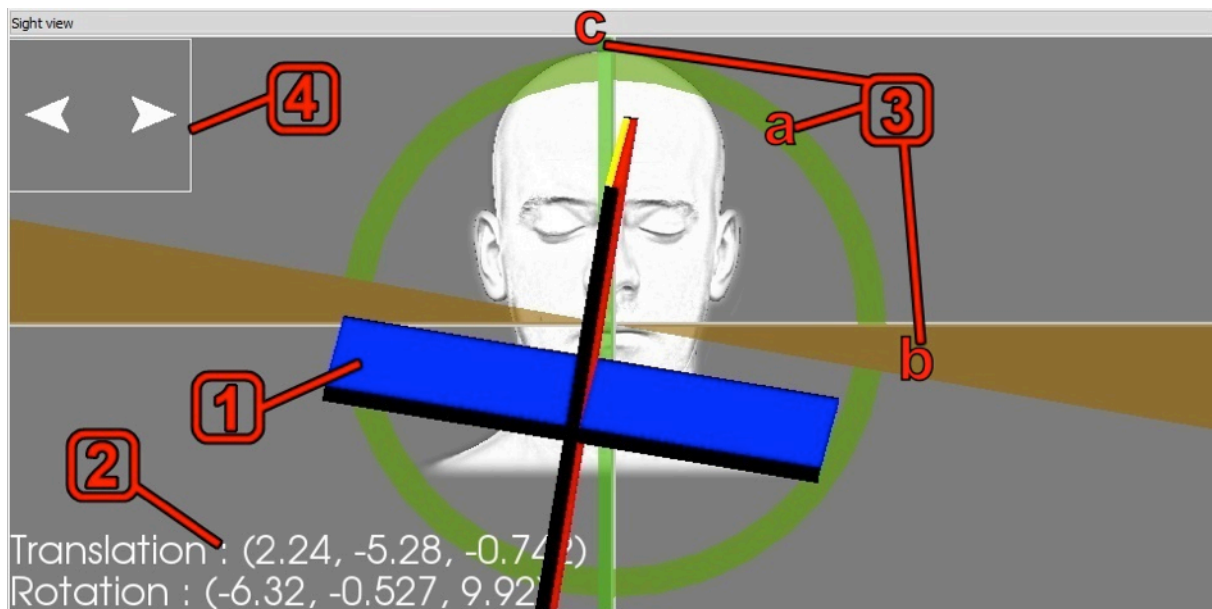


**Figure 5.10: Final version of the navigation crosshair.** Cross (1); raw values of actual matrix (2); additional indicators (3): versatile ring (a), “butterfly-shaped” horizontal line (b), versatile vertical line (c); widget for interface rotation (4).

1. **The cross** behaved as it did in the prototype, i.e.: when placement was perfect:
  - it was centered and facing the camera
  - its colored sides were not to be seen.
2. **Raw values of actual matrix** (matrix related to the actual position of the maxilla) **and target matrix** (matrix related to the planned position) were replaced by values of translation and rotation of one matrix in relation to the other. This allowed even more position refinement, once the cross was almost perfectly centered.
3. **Three additional indicators:** a **versatile ring (a)** replacing the surrounding circle, a new **“butterfly-shaped” horizontal line (b)** and a new **versatile vertical line (c)**. Each indicator displayed the differences between the planned and the actual position regarding respectively, postero-anterior movements (depth), roll and yaw (Cf. Chapter 2). When these differences tended to decrease, the indicators tended to get narrower and to turn from red to green.

- a. The versatile surrounding ring displayed the translation along the sagittal axis (depth), which consisted of postero-anterior movements. When the actual position of the maxilla was far from the planned target position, the circle would appear wide and red. As this position came closer to the target one, the ring would progressively narrow down and turn to green until disappearing.
- b. The “butterfly-shaped” horizontal line displayed rotation around the sagittal axis (roll). It purposely exaggerated the information provided by the horizontal plane of the cross, using thickness and color.
- c. The versatile vertical line displayed rotation around the longitudinal axis (yaw). Its behavior could be compared to the one of a rudder, or to the vertical flap of an airplane. Therefore, the vertical line became wider and redder on the side where the yaw was inaccurate.

It is obvious that such indicators provided redundant information compared to the rest of the crosshair. However, conveniently, such additional information made easier the interpretation of the ideal position, thanks to the color code.

4. A **widget**<sup>28</sup> was created in order to achieve a 90°clockwise or counterclockwise rotation of the whole interface. This function was required for the surgeon to have a matching position between the interface on screen and the actual operative position of the patient (Cf. Figure 5.11). Indeed, if the surgeon is used to conduct clinical examination on a patient facing him and sitting in an upright position, at the time of surgery the patient is lying down on his back (dorsal decubitus) in the OR. This is one of the reasons why intraoperative assessment of horizontality and symmetry is difficult (Cf. Chapter 2). It is also the reason why the benefit from navigation is obvious. It was therefore confusing for the operator to see the actual face of his patient from the side, since in dorsal decubitus and, at the same time, to look at the software interface onscreen displaying patient’s head in an upright position. Such a set-up was a source of fatigue, since it forced the surgeon to perform a mental registration between the patient, which he operated on and the display he watched. The purpose of navigation is to prevent such inconveniences. Hopefully, adjunction of this widget solved this issue.

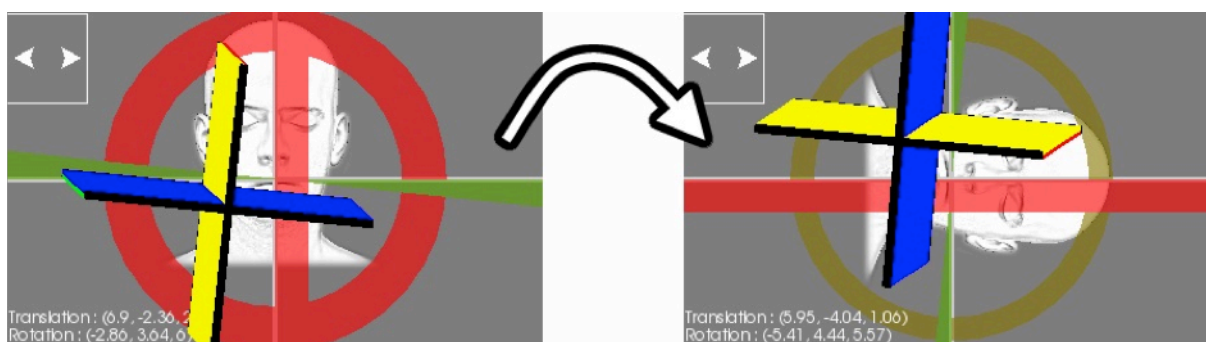


**Figure 5.11:** Rotation of the interface using a dedicated widget<sup>26</sup>.

<sup>28</sup> Interactive component of a graphic interface

### **5.3. Conclusion regarding navigation software development**

In the previous sections, we provided the specifications of the electromagnetic system onto which we decided to build navigation software.

We then described the experimental set-up we designed and explained how it could be relevantly transferred to an actual surgical environment.

Further, we detailed the mathematical procedure we have conducted in order to achieve registration between the actual patient's head and its virtual reconstructed CT scan head model. Indeed, since the coordinate systems were different between the real world and the virtual one, we applied a 6-point registration procedure. This step involved computing translation and rotation matrices.

Our procedure was designed to be relevant even in cases of head movements during surgery. Such initial 6-point registration procedure used specific facial anatomical landmarks. For the sake of simplicity, 3 out of the 6 points we chose, were located at respectively, the tip of the nose, the right and the left corner of the mouth. It should be emphasized that, if these 3 points were quite rigid on a plastic head model, it would not be the case in a real patient. Indeed, these cutaneous structures would not directly rely onto the facial skeleton. Depending on how much pressure would be exerted for pinpoint calibration, the recorded landmark could vary. As a result, this could be a source of inaccuracy in the registration between the actual patient's head and its 3D virtual model. However, at this stage, this did not seem to represent an obstacle. Furthermore, changing the location of the calibration landmarks to skeletal-sustained skin landmarks would not alter in any way the operating principles of our software.

In the last sections, we detailed how we have designed and developed an original user-interface, since literature demonstrates that the quality of the interface greatly impacts the surgical outcome.

Therefore, since our interface seemed to provide intuitive information through a user-friendly display, we believed that it could facilitate the surgical procedure and make it more efficient.

Of course, in order to demonstrate this hypothesis together with the ambition to bring our navigation system to the operative theater, the next logical step was to conduct its preclinical evaluation by a representative sample of operators. We will describe this qualitative and quantitative evaluation in the next sections.

#### 5.4. Evaluation of navigation software

In the previous sections, we described the technical specifications and interface developments of our navigation system. We have detailed how initial landmark calibration and further real-time fiducial registration was conducted in order to provide the surgeon with **augmented virtuality** (Cf. Chapter 2). After a few initial bench tests, we implemented some additional features.

Our ultimate goal being to navigate an actual surgical procedure, we will, in this section, have our system evaluated by a sample of representative operators in a surgical-mimicking environment. In section 5.4.1, we will describe the experimental procedure we have conceived. Indeed, our concern was to accurately reproduce routine surgical movements at the same time as preventing any alteration to our experimental model, since some destructive steps can be necessary in real surgery. We will describe the experimental tasks we have designed, ranging from simple movements within a unique plane to complex movements involving three axes.

In sections 5.4.2 and 5.4.3, we will explain the methods used to evaluate the accuracy of our system and the relevance of its interface. We will then present our findings and their statistics using tables and figures. In section 5.4.4, we will detail our results and will discuss our findings in 5.5, regarding the operator's level of expertise and regarding the nature of the experimental task. We will then analyze the advantages and drawbacks demonstrated by the evaluation of our system. Subsequently, we will consider the context our software could be used in, as well as necessary improvements to the navigation system.

**5.4.1. Description of the experimental procedure**

A set of eight surgical-like positions of the maxilla was defined (Cf. Table 5.1 and Figure 5.12). Table 5.1 details the equivalence between the surgical interpretation of a dedicated position (maxillary target position), the required displacement (maxillary displacement), its mathematical conversion (transformation matrix) and its clinical combination of elementary displacements (vertical dimension, translation and rotation).

Task Ref	Maxillary target position	Maxillary displacement	Transformation Matrix	Vertical dimension (mm)				Translation (mm)	Rotation (mm)	
				Anterior		Posterior			Postero anterior	towards Right side of patient
			<b>R(Axis, Angle)</b> <b>T</b>	Right	Left	Right	Left			
0	Neutral position		Matrix 4x4 identity	0	0	0	0	0	0	0
1	3 mm right downward movement	Roll 3 mm Right	$R(P_1P_0, \text{roll\_angle}(3\text{mm}))$	3	0	3	0	0	0	0
2	5 mm left downward movement	Roll 5 mm Left	$R(P_2P_3, \text{roll\_angle}(5\text{mm}))$	0	5	0	5	0	0	0
3	5 mm advancement	Translation postero anterior 5 mm	$T(N, 5\text{mm})$	0	0	0	0	5	0	0
4	3 mm right rotation	Yaw 3 mm Right	R (normal to the point $P_6$ , 3mm)	0	0	0	0	0	3	0
5	2 mm left rotation	Yaw 5 mm Left	R (normal to the point $P_6$ , -5mm)	0	0	0	0	0	0	2
6	3 mm global downward movement		$T([0.0,-1], 3\text{mm})$	3	3	3	3	0	0	0
7	3 mm left downward movement + 2 mm right rotation	Roll 3 mm Left + Yaw 2 mm Right	R (normal to the point $P_6$ , 3mm) X $R(P_2P_3, \text{roll\_angle}(3\text{mm}))$	0	3	0	3	0	2	0
8	2 mm right downward movement + 3 mm left rotation + 5 mm advancement	Roll 2 mm Right + Yaw 3 mm Left + Translation postero anterior 5 mm	$R(P_1P_0, \text{roll\_angle}(3\text{mm}))$ X R(normal to the point $P_6$ , -3mm) X $T(N, 5\text{mm})$	2	0	2	0	5	0	3

**Table 5.1:** Clinical and mathematical equivalences of the 8 surgical-like target positions.

The neutral position was the one considering the maxilla already cut but held steady against the upper facial skeleton with no displacement. Every operator was asked to perform eight tasks consisting in sequentially setting the maxilla by hand to each of the eight predefined target positions starting from the neutral position.



**Figure 5.12: Graphic illustration of the eight surgical target positions of the maxilla.** VAR : vertical anterior right movement ; VAL : vertical anterior left movement ; VPR : vertical posterior right movement ; VPL : vertical posterior left movement ; Rot R : rotation towards right side of patient ; Rot L : rotation towards left side of patient ; Transl : translation (posteroanterior).

Two consecutive sessions of eight tasks each were organized. The tracking system was activated during both sessions in order for time and accuracy to be automatically recorded by the software in every task. During the first session, the surgeon could only rely on clinical landmarks, just as he would do in a conventional surgical procedure (CONV). Surgeons were provided with a ruler and a caliper, but had no access to the computer interface. During the second session, the surgeons could use the navigation software (NAV). Every operator was granted a five-minute practice in order to familiarize himself with the system.

Twelve operators were recruited from among our surgical staff to undertake the tasks: four experts, four intermediate and four trainees in maxillofacial surgery.

### 5.4.2. Qualitative evaluation

Qualitative evaluation focused on the influence of the software and its interface over the procedure. All twelve operators answered a 17-item questionnaire using a 4-entry Likert scale after they had performed the experiment (Cf. Table 5.2).

### 5.4.3. Quantitative evaluation

Quantitative evaluation consisted in the measurement of two parameters for every task and each operator:

1. Time (seconds) needed to achieve an ideal match with the target position and accuracy of the actual splint position compared with the target one (Cf. Figure 5.12)
2. Accuracy was obtained by measuring the translational (mm) and the angular distance (degrees) between the planned and the actual position of the splint, considering dedicated teeth landmarks (Cf. Figure 5.13).

These two parameters were compared between the two sessions CONV and NAV. Measurements were recorded by software, always controlled by the same engineer.

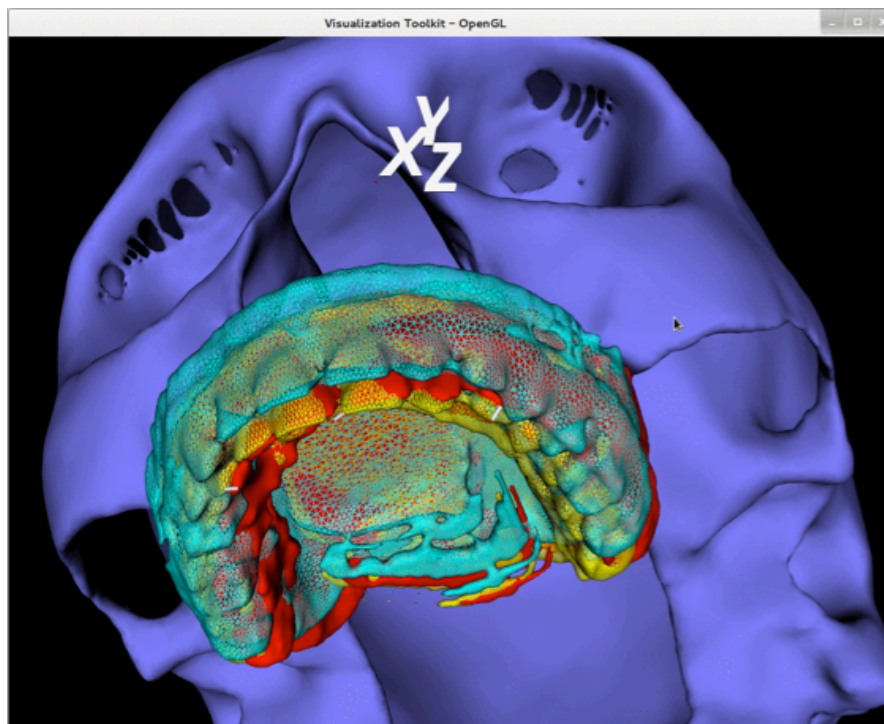


**Figure 5.13:** Three-dimensional illustration of maxillary position errors regarding translation and rotation.

## 5.4.4. Results

### 5.4.4.1. Qualitative evaluation (Cf. Table 5.2)

<b>A. EXPERIMENTAL DESIGN</b>		
1. The experimental set-up is similar to real surgical environment.	Strongly agree (4/4)	3
	Agree (3/4)	7
	Disagree (2/4)	2
	Strongly disagree (1/4)	0
2. The sensors do not bother the achievement of the experimental surgical procedure.	Strongly agree (4/4)	8
	Agree (3/4)	3
	Disagree (2/4)	1
	Strongly disagree (1/4)	0
<b>B. NAVIGATION SYSTEM</b>		
During the session when the display was available, in order to assist surgical movements, I would:		
1. Mainly watch the colored crosshair.	Strongly agree (4/4)	9
	Agree (3/4)	2
	Disagree (2/4)	0
	Strongly disagree (1/4)	1
2. Mainly watch the 3D models in front and side views.	Strongly agree (4/4)	1
	Agree (3/4)	0
	Disagree (2/4)	10
	Strongly disagree (1/4)	1
3. Mainly watch the "patient" (mannequin).	Strongly agree (4/4)	1
	Agree (3/4)	3
	Disagree (2/4)	6
	Strongly disagree (1/4)	2
Regarding the user's interface:		
1. It is rather intuitive.	Strongly agree (4/4)	8
	Agree (3/4)	3
	Disagree (2/4)	1
	Strongly disagree (1/4)	0
2. It is adequate to achieve the surgical goals.	Strongly agree (4/4)	4
	Agree (3/4)	7
	Disagree (2/4)	1
	Strongly disagree (1/4)	0
3. It allows good comprehension of movements in 3D.	Strongly agree (4/4)	8
	Agree (3/4)	4
	Disagree (2/4)	0
	Strongly disagree (1/4)	0
4. It allows increased accuracy in maxillary positioning.	Strongly agree (4/4)	5
	Agree (3/4)	5
	Disagree (2/4)	2
	Strongly disagree (1/4)	0
5. It seems to allow decreased operative time.	Strongly agree (4/4)	1
	Agree (3/4)	7
	Disagree (2/4)	4
	Strongly disagree (1/4)	0
6. The part of the interface displaying the colored crosshair provides explicit information.	Strongly agree (4/4)	7
	Agree (3/4)	4
	Disagree (2/4)	1
	Strongly disagree (1/4)	0
7. The surrounding circle of the crosshair provides explicit information.	Strongly agree (4/4)	5
	Agree (3/4)	4
	Disagree (2/4)	3
	Strongly disagree (1/4)	0
8. Crosshair sensitivity is high	Strongly agree (4/4)	9
	Agree (3/4)	2
	Disagree (2/4)	1
	Strongly disagree (1/4)	0
9. Crosshair sensitivity is useful for better achievement of the surgical task	Strongly agree (4/4)	2
	Agree (3/4)	7
	Disagree (2/4)	2
	Strongly disagree (1/4)	1
<b>C. GENERAL REMARKS</b>		
During the navigated part of the experiment (when the display was available):		
1. Such system would be favorably combined with a mechanical system in order to hold steadily the position achieved through navigation.	Strongly agree (4/4)	10
	Agree (3/4)	2
	Disagree (2/4)	0
	Strongly disagree (1/4)	0
2. Such navigation system would prove very useful in everyday practice of orthognathic surgery.	Strongly agree (4/4)	2
	Agree (3/4)	9
	Disagree (2/4)	1
	Strongly disagree (1/4)	0
3. Such navigation system would prove particularly helpful in complex orthognathic surgery cases.	Strongly agree (4/4)	9
	Agree (3/4)	3
	Disagree (2/4)	0
	Strongly disagree (1/4)	1

**Table 5.2:** Qualitative evaluation form collecting answers of the 12 surgeons enrolled based on a 17-item questionnaire using a 4-entry Likert scale.



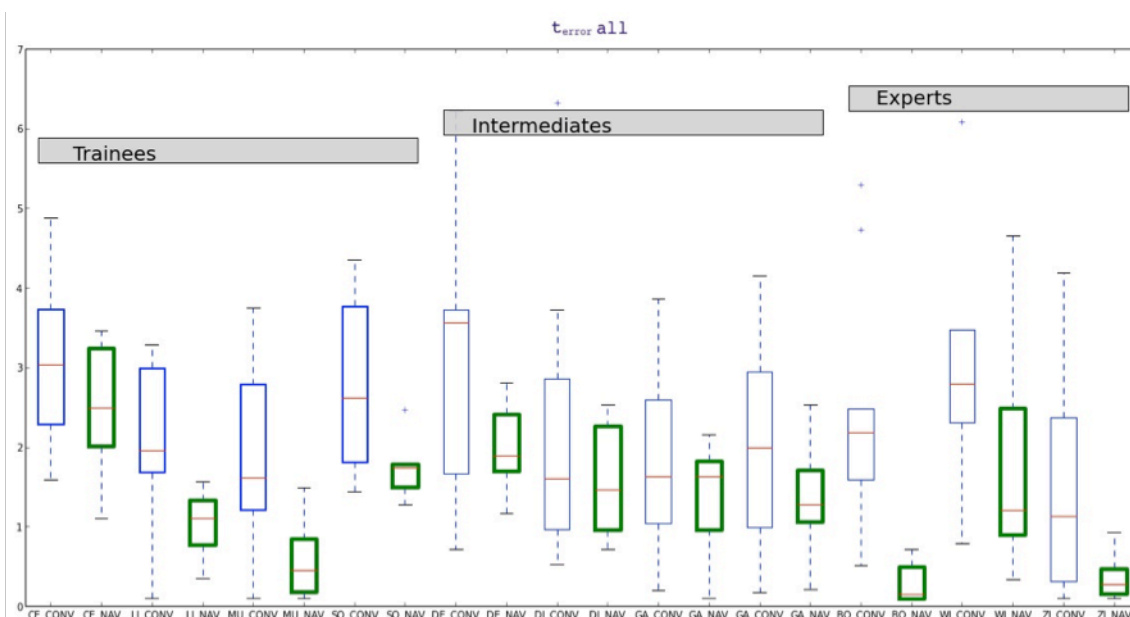
Table 5.2 summarizes the answers to the questionnaire. Most of the surgeons were convinced that the system allowed increased accuracy in maxillary positioning (10/12 strongly agree or agree). As to whether operative time was decreased, surgeons were not as strongly convinced.

### 5.4.4.2. Quantitative evaluation

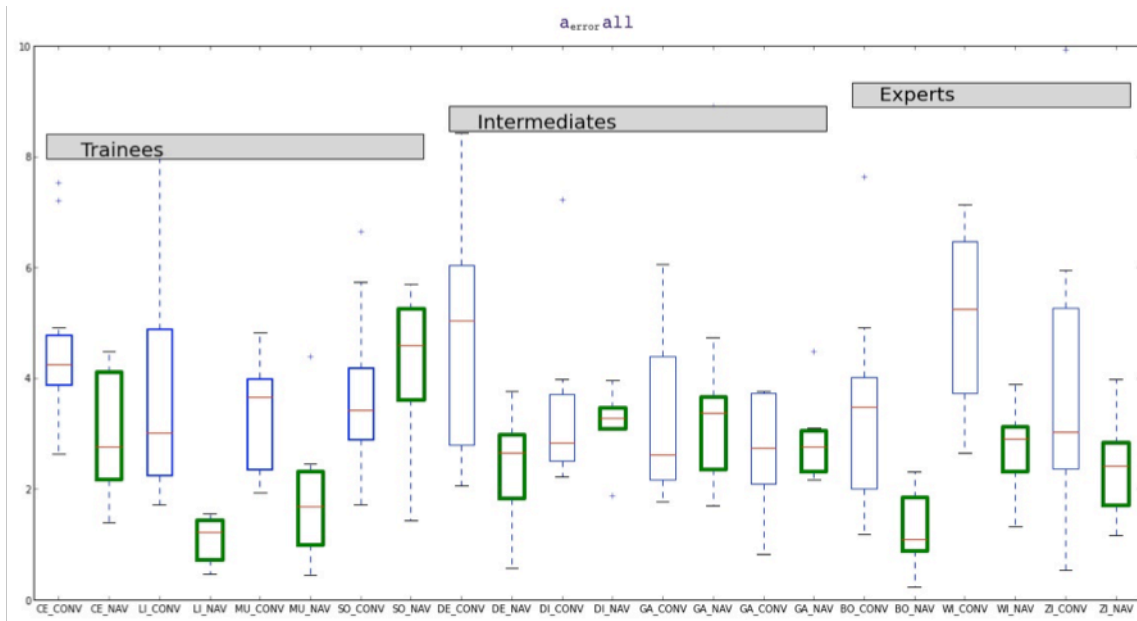
Results are displayed both in Table 5.3 and Graphs 5.1 - 5.3, which are box plot graphs illustrating translational error (Cf. Graph 5.1), angular error (Cf. Graph 5.2) and duration (Cf. Graph 5.3), for every surgeon (designated using their initials) within their group of expertise (trainees, intermediate, experts). The boxes display the range of measurements and the horizontal bar stands for the mean value. For every group, measurements are shown for the two experimental sessions, the box outline being fine (blue) for the conventional method (CONV) and wide (green) for the navigated method (NAV). The results of one operator out of twelve could not be used due to technical problems and have therefore been removed from our dataset.

	Group	Global		Trainees		Intermediates		Experts	
		mode	CONV	NAV	CONV	NAV	CONV	NAV	CONV
<b>Metric</b>	<b>stat</b>								
<b>Duration</b>	<b>mean</b>	26.70	34.81	41.69	30.88	20.09	31.26	13.02	41.87
	<b>sd</b>	32.92	32.94	42.53	15.64	19.95	36.64	19.81	39.22
<b>a<sub>error</sub></b>	<b>mean</b>	3.94	2.62	3.89	2.48	3.78	3.06	4.22	2.29
	<b>sd</b>	2.04	1.39	1.61	1.66	2.31	1.42	2.26	0.97
<b>t<sub>error</sub></b>	<b>mean</b>	2.38	1.29	2.50	1.45	2.26	1.59	2.35	0.84
	<b>sd</b>	1.43	0.97	1.17	0.92	1.59	0.70	1.60	1.10

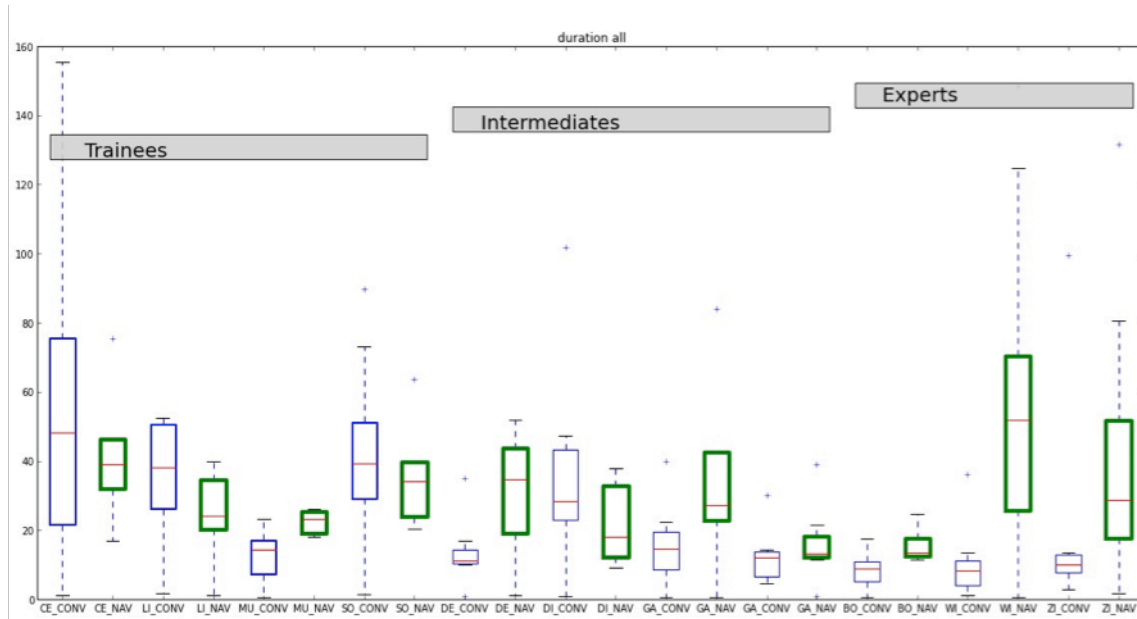
**Table 5.3:** Statistics for duration (seconds, s), angular error (a<sub>error</sub> in degrees, °) and translational error (t<sub>error</sub> in millimetres, mm) for the different groups i.e.: the whole sample of surgeons (global) and by user category (Trainees, Intermediates, Experts) and session modality (either conventional (CONV) or navigated (NAV)).



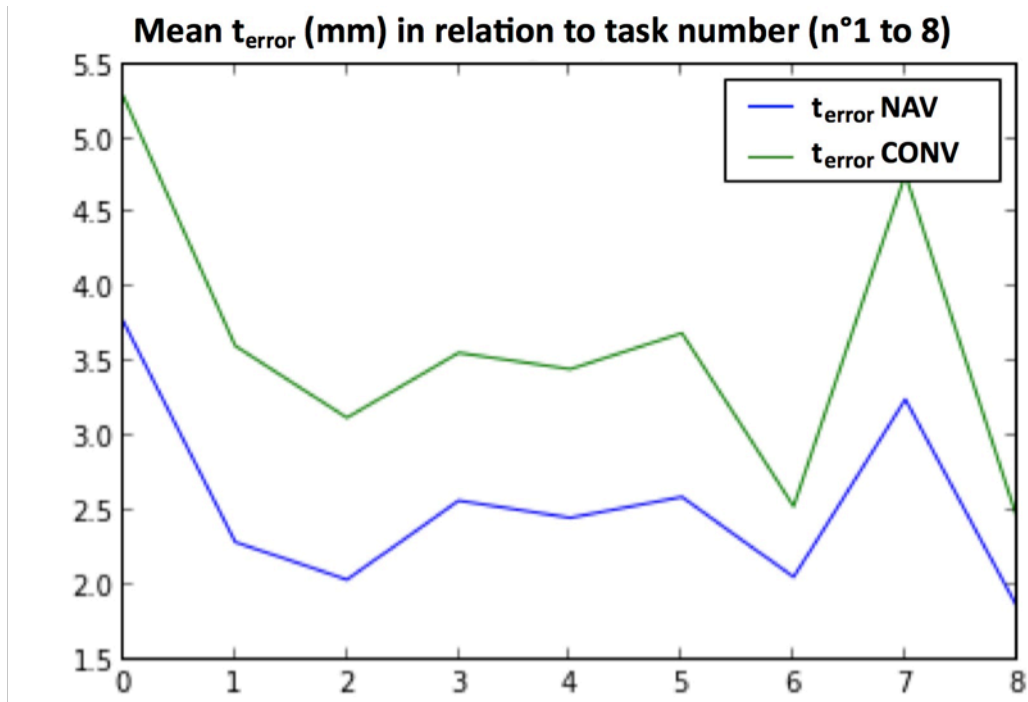
**Graph 5.1:** Comparative task translational error (t<sub>error</sub> in mm) sorted by surgeon (XX\_) using conventional (CONV)(blue boxes) and navigated (NAV)(green boxes) method



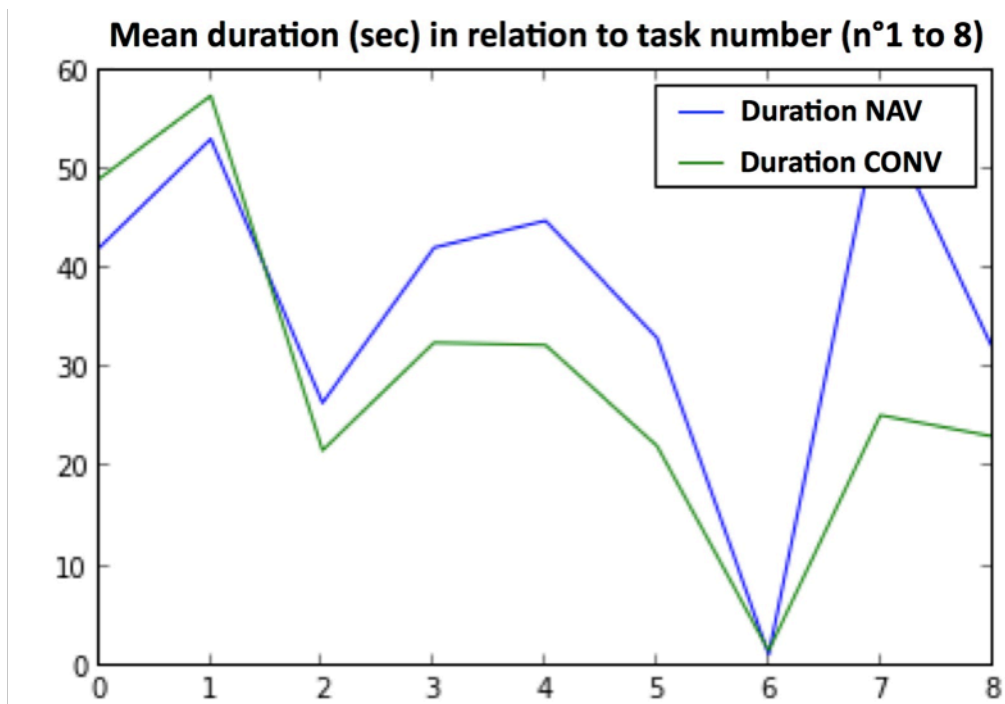
**Graph 5.2:** Comparative task angular error ( $a_{error}$  in degrees) sorted by surgeon (XX\_) using conventional (CONV)(blue boxes) and navigated (NAV)(green boxes) method



**Graph 5.3:** Comparative task duration (seconds) sorted by surgeon (XX\_), using conventional (CONV)(blue boxes) and navigated (NAV)(green boxes) method.



**Graph 5.4:** Mean translational error (mm) in relation to experimental task number (n°1 to 8)



**Graph 5.5:** Mean duration (sec) in relation to experimental task number (n°1 to 8)

## 5.5. Discussion

A first finding was that a majority of surgeons agreed that our experimental design was similar to an actual surgical framework.

We will now analyze the other findings through two different criteria, then discuss the advantages of electromagnetic system, and, in the end, assess software and user interface.

### 5.5.1. Considering the operator's level of expertise: increased accuracy, variability reduction, time reduction in trainees

Using conventional positioning, all surgeons performed in a close range of translational (mean  $t_{\text{error}} = 2.38 \pm 1.43$  mm) and angular **accuracy** (mean  $a_{\text{error}} = 3.94 \pm 2.04$  °) (Table 5.3) (Graphs 5.1 - 5.3). The **time** needed to achieve every task decreased when the level of expertise increased (Graph 5.3).

When **navigation** was available, every single surgeon performed with **higher accuracy** (Graphs 5.1 - 5.2). Indeed, global translational error was improved (mean  $t_{\text{error}}$  difference = 1.11 mm) as well as global angular accuracy (mean  $a_{\text{error}}$  difference =  $1.32^\circ$ ) compared with the conventional session (Table 5.3). Such improvement increased when the operator level of expertise decreased (Table 5.3).

There was **great discrepancy** in the accuracy between operators when navigation was not used. Indeed, global  $t_{\text{error}}$  SD = 1.43 and global  $a_{\text{error}}$  SD = 2.04 (Table 5.3) report great variability which was quite reduced during the NAV session ( $t_{\text{error}}$  SD = 0.97,  $a_{\text{error}}$  SD = 1.39 (Table 5.3).

The level of expertise could be clearly identified looking at the measurements for every task. Indeed, the results were centered on three clusters matching the three categories (expert, intermediate, trainee). Notably, **experts** achieved every task in a short time during the CONV session (mean = 13.02 sec, SD = 19.81). This duration was increased when navigation was used (mean = 41.87 sec, SD = 39.22). However, **trainees** needed more time for every task during the CONV session (mean = 41.69 sec, SD = 42.53) whereas the result was quicker in the NAV session (mean = 30.88 sec, SD = 15.64) (Table 5.3, Graph 5.3). The **improvement of both accuracy and operative time in younger, less experienced surgeons** due to the use of navigation could result from their acquaintance with computer systems experienced as video games.

### 5.5.2. Considering the nature of the experimental task

It is interesting to consider the mean performance of all operators in relation to the type of surgical test task (Graphs 5.4 - 5.5). Indeed, as detailed through Table 5.1 and Figure 5.12, tasks n°1 through n°6 only involved movements in one surgical plane. Task n°6 was singular, since it allowed no contact point between the maxilla and the upper skull, therefore making a steady position quite uneasy. Task n°7 and n°8 could be considered as the most complex ones, since they involved movements along respectively 2 and 3 axes.

**Our results showed that all surgeons performed with more accuracy in every task thanks to navigation.** However, in 7 tasks out of 8, mean duration was increased when navigation was used compared to the conventional method. As we will further discuss, this result could be explained by surgeons' stubbornness to achieve a perfect navigational result using the interface that had been set to an exaggerated sensitivity.

If complex tasks (e.g. n°7) required increased duration, it is also where the benefits in terms of accuracy were the greatest.

### 5.5.3. Advantages of the electromagnetic system

#### 5.5.3.1. Low bulk

The electromagnetic sensors were perceived as inconspicuous (Table 5.2, question A2: eight surgeons strongly agree, three surgeons agree). Indeed, their position allowed free movements of the surgeon's hands and head with no problems with disruption of line of sight. The low bulk of EM sensors compared with optical fiducials is of utmost importance in orthognathic surgery where the intraoral approach greatly restricts operative sight (Robert A Mischkowski et al. 2006).

#### 5.5.3.2. Relevance of system design and accuracy for surgery

Our results confirmed that the **EM system accuracy was about 1 mm**, thus being consistent with manufacturer data and literature (Cartellieri, Kremser, and Vorbeck 2001; Cartellieri, Vorbeck, and Kremser 2001; Seeberger et al. 2012; R. A. Mischkowski et al. 2007). This also means that **6-point registration provided relevant accuracy** (Seeberger et al. 2012; Sun et al. 2012).

Cartellieri et al. also noted that "the calculated system precision (distance) seems to depend on the angle between the tracking system and the pointing device at the moment the point of interest is touched". Our system was designed to set a steady angle of the 2 main sensors, the one fixed on the forehead using a Velcro strap and the one embedded into the dental splint. Therefore, source of error due to angulation was decreased.

Our splint-embedded EM sensor allowed real-time tracking, whereas some procedures based on optical systems assess the structure of interest position by using a pointing instrument (Benassarou, Benassarou, and Meyer 2013a; Sadiq et al. 2012) in a bothersome additional step. Some teams described an optical sensor

attached to a splint (Benassarou, Benassarou, and Meyer 2013b) using a metallic rod. This bulky design compels the surgeon to hold the rod rather than the maxilla, making the procedure less intuitive (Cf. Chapter 2, Figure 2.20).

We formerly stated our reluctance towards intermediate splints, yet we used a splint. However, our splint served a double purpose: embedding an EM sensor for navigated positioning of the maxilla and, once completed, actually setting the final occlusion, as it is conducted through the conventional workflow.

### 5.5.3.3. Unnecessary invasive head fixation

In our system, head tracking proved quite useful since it allowed navigation even in case of head displacement, which is likely to occur during the procedure (Neumann et al. 1999). Tracking of the head prevents the use of a Mayfield clamp (Zinser et al. 2013) for steady holding. EM-based tracking is much more convenient than optical tracking (bulk, line of sight) (Robert A Mischkowski et al. 2006).

### 5.5.4. Software and user interface

It has been demonstrated (Traub, Stefan, Heining, Riquarts, et al. 2006) that the interface quality improves surgical performance in needle placement or drilling procedures. Subsequently, we designed a specific interface displaying a colored crosshair in addition to frontal and lateral 3D views.

**Augmented reality** has been used by a few researches (Robert A Mischkowski et al. 2006; Zinser et al. 2013) in order to superimpose additional information in the surgeon's field of view (Cf. Chapter 2, Figure 2.21). In such a technique, video acquisition of the actual surgical scene was mandatory. Camera point of view and position of the visualization display therefore became primary concerns. **Depth perception** is a critical issue, even when using head mounted displays (Birkfellner et al. 2002)(Sielhorst et al. 2006). In order to address depth perception in our display, we designed a versatile (in color and thickness) ring surrounding a central positioning crosshair. We therefore, used **Augmented Virtuality**, since it had the great advantage of restraining the number of registration steps whilst providing optimal accuracy in maxillary repositioning and satisfactory visualization.

Indeed, through qualitative evaluation, a large majority of operators agreed that the system was intuitive, adequate to achieve surgical goals and to provide good comprehension of 3D movements. In the course of the navigated part of the experiment, surgeons would initially watch the mannequin to initiate movement of the maxilla, and then mainly focus on the navigation display to refine the position. Notably, the more experience they gained, the more the surgeons would mainly rely on the user interface, feeling it was unnecessary to look at the patient anymore.

**Most of the surgeons explained that the crosshair was the most helpful information on the interface** (11/12 surgeons 'strongly agree' or 'agree' on explicit information provided by the crosshair). Indeed, they scarcely watched the frontal and lateral 3D views of the model, except when they were confused by the position of the crosshair, especially in terms of posteroanterior position of the maxilla.

Three surgeons even suggested that the interface would favorably display full-screen of the sole colored crosshair.

In our experimental design, we purposely set a high sensitivity of the crosshair in order to provide great accuracy.

As a result, it was quite difficult for the surgeons to keep holding the maxilla steady once they had achieved perfect crosshair alignment. This was generally perceived as bothersome and explains why, despite the high accuracy provided by our system, it was unable to significantly decrease operative time. Experts especially needed a longer time to achieve the tasks through navigation, probably due to their urge of achieving a perfect match with the highly sensitive crosshair (Graph 5.3). Indeed, their experience would allow experts to perform very quickly using the conventional method, namely sole visual control of the patient's bone segments. They did not turn to the computer assistance to confirm they had achieved the right position. However, trainees would rather rely on the 3D interface to control their position, therefore achieving a faster task when using navigation.

These findings appeared quite satisfactory regarding our technological choice of **Augmented Virtuality**. Qualitative analysis could make us believe that standard **Augmented Reality** using an external view might not represent a significant improvement in terms of navigational assistance.

## 5.6. Conclusion

Our software definitely allowed a **reduction in variability both, of time and accuracy** among different operators and could therefore **help standardize maxillary positioning**. Along with educational purposes, such a system would be of **benefit especially to trainees**, as operative time was mainly decreased in their category.

Of the surgeons who strongly agreed that such a navigation system would prove very helpful in complex deformities, the majority of them stated that it would also be **helpful in everyday orthognathic procedures**.

Notably, even though navigation can achieve an ideal maxillary position, misplacement is likely to occur during rigid fixation. Therefore, 9/12 surgeons strongly agreed that such system would be favorably combined with a mechanical system in order to hold steady the position achieved through navigation.

Our next step is to evaluate our system in the operating theatre with real patients and to address the issue of maintaining a steady maxillary position for fixation.

---

**REFERENCES**

1. Arun, K. S., T. S. Huang, and S. D. Blostein. 1987. "Least-Squares Fitting of Two 3-D Point Sets." *IEEE Transactions on Pattern Analysis and Machine Intelligence* 9 (5): 698–700.
2. Benassarou, M., A. Benassarou, and C. Meyer. 2013b. "[Computer-assisted navigation in orthognathic surgery. Application to Le Fort I osteotomy]." *Revue de Stomatologie, de Chirurgie Maxillo-Faciale et de Chirurgie Orale*, no. 114 (August): 219–27. doi:10.1016/j.revsto.2013.06.004.
3. Bettega, G, and F Leitner. 2013. "[Computer assisted orthognathic surgery: Condyle repositioning.]" *Revue de stomatologie, de chirurgie maxillo-faciale et de chirurgie orale*, July. doi:10.1016/j.revsto.2013.06.001.
4. Bettega, G., V. Dessenne, B. Raphaël, and P. Cinquin. 1996. "Computer-Assisted Mandibular Condyle Positioning in Orthognathic Surgery." *Journal of Oral and Maxillofacial Surgery: Official Journal of the American Association of Oral and Maxillofacial Surgeons* 54 (5): 553–58.
5. Birkfellner, Wolfgang, Michael Figl, Klaus Huber, Franz Watzinger, Felix Wanschitz, Johann Hummel, Rudolf Hanel, et al. 2002. "A Head-Mounted Operating Binocular for Augmented Reality Visualization in Medicine--Design and Initial Evaluation." *IEEE Transactions on Medical Imaging* 21 (8): 991–97. doi:10.1109/TMI.2002.803099.
6. Borumandi, Farzad, Christian Brandtner, Christian Krenkel, and Alexander Gaggl. 2013. "Navigated Repositioning of the Maxilla: Technical Note." *The British Journal of Oral & Maxillofacial Surgery* 51 (6): 568–69. doi:10.1016/j.bjoms.2013.02.003.
7. Cartellieri, M, J Kremser, and F Vorbeck. 2001. "Comparison of Different 3D Navigation Systems by a Clinical 'User.'" *European Archives of Oto-Rhino-Laryngology: Official Journal of the European Federation of Oto-Rhino-Laryngological Societies (EUFOS): Affiliated with the German Society for Oto-Rhino-Laryngology - Head and Neck Surgery* 258 (1): 38–41.
8. Cartellieri, M, F Vorbeck, and J Kremser. 2001. "Comparison of Six Three-Dimensional Navigation Systems during Sinus Surgery." *Acta Oto-Laryngologica* 121 (4): 500–504.
9. D'Agostino, Jacopo, Michele Diana, Michel Vix, Luc Soler, and Jacques Marescaux. 2012. "Three-Dimensional Virtual Neck Exploration before Parathyroidectomy." *The New England Journal of Medicine* 367 (11): 1072–73. doi:10.1056/NEJMc1201488.



10. Kretschmer, W. B., W. Zoder, G. Baciut, Mihaela Bacuit, and K. Wangerin. 2009. "Accuracy of Maxillary Positioning in Bimaxillary Surgery." *British Journal of Oral and Maxillofacial Surgery* 47 (6): 446–49. doi:10.1016/j.bjoms.2009.06.004.
11. Lutz, Jean-Christophe, Stéphane Nicolau, Vincent Agnus, Frédéric Bodin, Astrid Wilk, Catherine Bruant-Rodier, Yves Rémond, and Luc Soler. 2015. "A Novel Navigation System for Maxillary Positioning in Orthognathic Surgery: Preclinical Evaluation." *Journal of Cranio-Maxillofacial Surgery* 43 (9): 1723–30. doi:10.1016/j.jcms.2015.08.001.
12. Mischkowski, R. A., M. J. Zinser, L. Ritter, J. Neugebauer, E. Keeve, and J. E. Zöllner. 2007. "Intraoperative Navigation in the Maxillofacial Area Based on 3D Imaging Obtained by a Cone-Beam Device." *International Journal of Oral and Maxillofacial Surgery* 36 (8): 687–94. doi:10.1016/j.ijom.2007.04.001.
13. Mischkowski, Robert A, Max J Zinser, Alexander C Kübler, Barbara Krug, Ulrich Seifert, and Joachim E Zöllner. 2006. "Application of an Augmented Reality Tool for Maxillary Positioning in Orthognathic Surgery - a Feasibility Study." *Journal of Cranio-Maxillo-Facial Surgery: Official Publication of the European Association for Cranio-Maxillo-Facial Surgery* 34 (8): 478–83. doi:10.1016/j.jcms.2006.07.862.
14. Neumann, P., D. Siebert, A. Schulz, G. Faulkner, M. Krauss, and T. Tolxdorff. 1999. "Using Virtual Reality Techniques in Maxillofacial Surgery Planning." *Virtual Reality* 4 (3): 213–22. doi:10.1007/BF01418157.
15. Sadiq, Zaid, Jeremy Collyer, Ken Sneddon, and Stephen Walsh. 2012. "Orthognathic Treatment of Asymmetry: Two Cases of 'Waferless' Stereotactic Maxillary Positioning." *The British Journal of Oral & Maxillofacial Surgery* 50 (2): e27–29. doi:10.1016/j.bjoms.2011.07.016.
16. Seeberger, Robin, Gavin Kane, Juergen Hoffmann, and Georg Eggers. 2012. "Accuracy Assessment for Navigated Maxillo-Facial Surgery Using an Electromagnetic Tracking Device." *Journal of Cranio-Maxillo-Facial Surgery: Official Publication of the European Association for Cranio-Maxillo-Facial Surgery* 40 (2): 156–61. doi:10.1016/j.jcms.2011.03.003.
17. Sielhorst, Tobias, Christoph Bichlmeier, Sandro Michael Heining, and Nassir Navab. 2006. "Depth Perception – A Major Issue in Medical AR: Evaluation Study by Twenty Surgeons." In *Medical Image Computing and Computer-Assisted Intervention – MICCAI 2006*, edited by Rasmus Larsen, Mads Nielsen, and Jon Sporring, 364–72. Lecture Notes in Computer Science 4190. Springer Berlin Heidelberg. [http://link.springer.com/chapter/10.1007/11866565\\_45](http://link.springer.com/chapter/10.1007/11866565_45).
18. Sun, Yi, Heinz-Theo Luebbbers, Jimoh Olubanwo Agbaje, Serge Schepers, Luc Vrielinck, Ivo Lambrichts, and Constantinus Politis. 2012. "Validation of Anatomical Landmarks-Based Registration for Image-Guided Surgery: An in-Vitro Study." *Journal of Cranio-Maxillo-Facial Surgery: Official Publication of the European Association for Cranio-Maxillo-Facial Surgery*, December.

---

doi:10.1016/j.jcms.2012.11.017.

19. Traub, Joerg, Philipp Stefan, Sandro M. Heining, Christian Riquarts, Tobias Sielhorst, Ekkehard Euler, and Nassir Navab. 2006. "Towards a Hybrid Navigation Interface: Comparison of a Slice Based Navigation System with In-Situ Visualization." In *Medical Imaging and Augmented Reality*, edited by Guang-Zhong Yang, TianZi Jiang, Dinggang Shen, Lixu Gu, and Jie Yang, 179–86. Lecture Notes in Computer Science 4091. Springer Berlin Heidelberg. [http://link.springer.com/chapter/10.1007/11812715\\_23](http://link.springer.com/chapter/10.1007/11812715_23).
20. Traub, Joerg, Philipp Stefan, Sandro Michael Heining, Tobias Sielhorst, Christian Riquarts, Ekkehard Euler, and Nassir Navab. 2006. "Hybrid Navigation Interface for Orthopedic and Trauma Surgery." *Medical Image Computing and Computer-Assisted Intervention: MICCAI ... International Conference on Medical Image Computing and Computer-Assisted Intervention* 9 (Pt 1): 373–80.
21. Zinser, Max J, Robert A Mischkowski, Timo Dreiseidler, Oliver C Thamm, Daniel Rothamel, and Joachim E Zöller. 2013. "Computer-Assisted Orthognathic Surgery: Waferless Maxillary Positioning, Versatility, and Accuracy of an Image-Guided Visualisation Display." *The British Journal of Oral & Maxillofacial Surgery* 51 (8): 827–33. doi:10.1016/j.bjoms.2013.06.014.



## Chapter 6

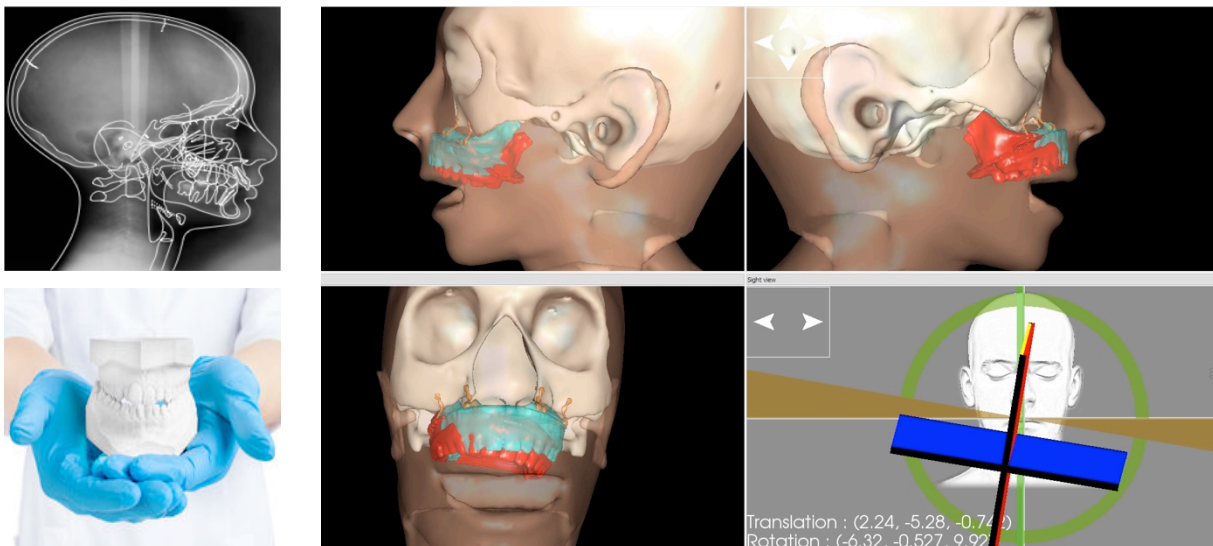
### CONCLUSION

---

*Our ultimate purpose was to develop a navigation system to facilitate intraoperative achievement of orthognathic surgical procedures.*

We have identified the prerequisite steps mandatory to achieve this purpose, namely achieving a segmentation-based model from patient's CT scan, developing planning tools and we have provided a simulation method of the postoperative outcome along the way. We believe we have developed the embryo of a software suite enabling the maxillofacial surgeon to overcome several obstacles throughout his management of orthognathic surgery patients. Yet, our research identified several points subject to improvement and further development perspectives.

---



## 6.1. Achievements

We have first addressed **modeling** (Chapter 3). After considering the issues compelling swift segmentation (continuum between upper and lower jaws, dental metal artifacts) we determined the ground truth using an interactive segmentation method. Therefore, we could compute automation accordingly.

### **A semi-automated segmentation pipeline overcoming dental metal artifacts**

We were able to achieve distinct segmentations of the facial bones (maxilla, on the one hand, and mandible, on the other hand), and soft tissue, using a unique semi-automated algorithm with few interactive entries. This resulted in a complete surface mesh model of patient's head used as input data for further planning and simulation purposes.

This segmentation pipeline, using raw CT scan input data was based on successive mathematical morphology operators in order to independently process image masks. We first were able to achieve distinct segmentation of the facial bones, namely the maxilla and the mandible. Using an original approach based on **segmentation of the dental pulp**, based on the combination especially of "threshold", "labeling" and "dilate" operators, allowed us to meet or goals even in the presence of dental metal artifacts and despite the continuum between maxilla and mandible (Cf. Chapter 3, 3.4.2.2.1).

Skin and soft tissue layer segmentation were achieved despite the skin contour defects secondary to metal artifacts. We solved this issue thanks to the extraction of a smooth contour gradient using a "watershed" operator and appropriate seeds, combined with soft tissue layer smoothing and subtraction of the bone surface from the soft tissue layer using a distance transform ("Maurer" distance) (Cf. Chapter 3, 3.4.2.2.2). The resulting soft tissue layer model was purposely designed to fit or even interpenetrate the bone surface in order to allow further simulation.

Evaluation was based on the comparison of the semi-automated segmentation pipeline to the interactive (manual) one, using a database of 8 patients CT scans. Metrics consisted of processing time in seconds, and accuracy using border-to-border distance error in millimeters.

Regarding processing time, we found an improvement by a factor of 6 thanks to automation. We can note that during the automated process, interaction of the operator is extremely short, since he only needs to set a few parameters.

In terms of accuracy, we found mean distance errors ranging from 0.72 to 1.68 mm, the median from 0.71 to 1.16 mm, and the standard deviation from 0.22 to 2.24.

We could note that the number of outliers (distance error > 1.5 mm) do not exceed 25%. Many outliers (distances outside the 25%-75% range) occurred in the posterior part of the dental arches, where artifacts are usually numerous. This is not a problem, since the clinical focus lies on the external facial morphology and since such errors do not impact soft tissue segmentation.

Since voxel sizes are nearly 0.5 X 0.5 X 0.5 mm, 75% of distance errors are less than 3 pixels.

Moreover, such accuracy is quite satisfactory considering that the interpretation of the bone limit can vary depending on the windowing chosen by the operator. Indeed, the partial volume effect induces a smooth transition (typically 2 to 3 pixels) between bones and soft tissues.

Of course, optimal evaluation would have involved iterative segmentations by the same operator as well as segmentation of the same image by different operators. Due to time and staff constraints, we seek conducting such study in further developments.

Unfortunately, this pipeline was not fully automated, since it required manual operations, especially to determine the values of the thresholds through interactive measurements.

Since existing alternative methods to process simultaneously mask images are not yet implemented in the software version we have used, we are looking forward to try and process a fully automated pipeline in further research.

Considering partial volume effect and surgical accuracy of 1 mm, we can consider the 1.5 mm distance error we obtained between semi-automated and interactive segmentation is acceptable.

We have demonstrated that the proposed semi-automated segmentation pipeline could replace the interactive segmentation conducted by an expert in terms of accuracy.

The semi-automated pipeline also prevents from inter-operator discrepancy, therefore providing reproducibility. Thanks to the mainly automated pipeline, the great benefit is that it makes the surgeon available for more critical tasks.

### **Conversion of surgical displacements into mathematical computation allowing virtual planning**

In order to achieve **planning**, we had to mathematically convert actual surgical displacements in order to display them on the patient's virtual model. We focused on the maxillary surgical step, since it is the most crucial one in the whole procedure. We analyzed the geometrical basis of surgical movements in order to define the points and axes along which standard displacements occurred. We then computed the dedicated transformation matrices to move the virtual model accordingly. Actually, we proposed a unique 4 x 4 matrix suited to define translation and rotation around any axis. Along this study, were able to categorize all movements of the maxilla using a standard grid, which, in our understanding had never been achieved previously.

The computed positions were relevant to be used as target for navigation software evaluation.

### **Proposal of a facial soft tissue simulation method**

As far as simulation was concerned, we analyzed and transferred the surgical boundary conditions to our software engine.

We used a physical method based on a mechanical **mass-spring model**, which is suitable enough for the real-time simulation of elastic deformation of the facial soft tissue, since the soft tissue deformation induced by facial surgery is small compared to the associated translation. In order to provide realistic simulation, we used volume rather than surface meshes. The framework-integrated library called **TetGen**<sup>®</sup> was used to compute high-quality volume meshes from surface meshes. Indeed, mechanical engines, such as **Bullet**<sup>®</sup>, require high-quality tetrahedron-based **volume meshes**. We used two mechanical approaches through **Bullet**<sup>®</sup>. First, forces were applied to designated vertices of the volume mesh so that the mechanical engine computed the displacement onto the neighboring vertices until reaching a state of equilibrium. The second approach had a similar purpose, except that it was a new position, which was applied to designated vertices of the volume mesh. The designated vertices were chosen as the ones belonging to both, the **volume** mesh of the facial soft tissue and the volume corresponding to the facial bones **surface** mesh. Indeed, it is the position of facial bones, which is affected by surgery, whereas the alteration of soft tissues is only the consequence.

This method allowed us to generate simulation of the facial postoperative outcome.

We then conducted an evaluation of our simulation software on actual patients. To do so, we used a database of preoperative and postoperative CT-scans of the same patient.

In an initial step, we analyzed the range of distance discrepancy between the preoperative and the postoperative soft tissue layer surface.

Then, through a retro-planning step, we compared the soft tissue layer surface mesh in contact with patient's skin surface (simulated mesh) to the surface mesh of the skin surface extracted from the postoperative CT scan (representing the ground truth).

This evaluation relied on 3 different measurement methods of the distance errors between the simulated and the actual postoperative meshes. These quantitative measurements were associated to a color distance-map for convenient interpretation.

We have shown that our facial soft tissue simulation provides promising results, since accuracy is below 1 mm.

Finally, the accuracy achieved using such a model and its refreshing speed can allow our simulation to be used in real-time applications requiring to being realistic.

### **A navigation system set-up based on electromagnetic tracking featuring a novel user interface**

We designed a **navigation system set-up** on a mannequin considering spatial, time and asepsis restrictions that applied to a real operating environment.

According to qualitative evaluation conducted on twelve surgeons, this set-up could be directly transferred to the operating theatre.

Specific developments were conducted in order to achieve calibration and registration from the 3D model (CT scan) coordinate system to the EM sensor coordinate system.

We designed and developed an original **user interface** for navigation in orthognathic surgery allowing displaying 6 degrees of freedom on a unique screen and providing real-time head tracking. Part of this interface consisted of a colored 3D-crosshair that provided intuitive information about positions of the maxilla in the surgical field. The GUI<sup>29</sup> was enhanced with views of the 3D model in order to match the real operative set-up. The GUI displayed additional features to ease intraoperative assessment (versatile ring, “butterfly-shaped” horizontal line, versatile vertical line and widget for interface rotation to match patient’s surgical position). Translation and rotation could therefore be simultaneously visualized on frontal and lateral views.

**Qualitative evaluation** showed that most of the surgeons were convinced that the system allowed increased accuracy in maxillary positioning. It also showed that the system featured low bulk, since electromagnetic sensors were perceived as inconspicuous especially thanks to the novel design of splint-embedded sensor. Inconspicuous EM real-time head tracking also prevented from any invasive head fixation.

Regarding GUI, a large majority of operators agreed that the system was intuitive, adequate to achieve surgical goals and to provide good comprehension of 3D movements. Most of the surgeons explained that the crosshair was the most helpful information on the interface. Indeed, they scarcely watched the frontal and lateral 3D views of the model and three surgeons even suggested that the interface would favorably display full-screen of the sole colored crosshair.

Our use of **Augmented Virtuality**, had the great advantage of restraining the number of registration steps whilst providing optimal accuracy in maxillary repositioning and satisfactory visualization, particularly regarding depth perception. Qualitative analysis could make us believe that standard Augmented Reality using an external view might not represent a significant improvement in terms of navigational assistance.

**Quantitative evaluation** confirmed that the EM system **accuracy** was approximately **1 mm**, therefore being consistent with manufacturer data and literature.

---

<sup>29</sup> GUI: Graphical User Interface



Quantitative evaluation of accuracy and operative duration showed that Navigation allowed every single surgeon to perform with higher accuracy, since both, global and angular error were improved. Such improvement increased when the operator level of expertise decreased. Indeed, navigation provided the greatest benefits in both accuracy and operative time in younger, less experienced surgeons. Navigation also proved the most relevant in complex bone movements (along 2 and 3 axes).

Our software definitely allowed a **reduction in variability both, of time and accuracy** among different operators and could therefore **help standardize maxillary positioning**. Along with educational purposes, such a system would be of **benefit especially to trainees**, since operative time was mainly decreased in their category.

Of the surgeons who strongly agreed that such a navigation system would prove very helpful in complex deformities, the majority of them stated that it would also be **helpful in everyday orthognathic procedures**.

On the downside, even though navigation can achieve an ideal maxillary position, misplacement is likely to occur during rigid fixation. Therefore, 9/12 surgeons strongly agreed that such system would be favorably combined with a mechanical system in order to hold steady the position achieved through navigation.

Of course, we shall emphasize that we only conducted a phantom experiment and that the system and interface shall be evaluated on several actual patients during real surgical procedures. Our aim is to achieve this step through further research.

## 6.2. Perspectives

### Planning

Our semi-automated segmentation pipeline is an asset that has been **integrated into the service provided by Prometheus Surgical<sup>®</sup>**, a start-up our team founded in 2015, further merged with the Visible Patient<sup>®</sup> company.

Of course, improvements could yet be considered, particularly in providing full automation of the current interactive segmentation steps mainly conducted to determine the values of several thresholds.

Using or developing relevant filters to provide alternate solutions to address dental artifacts is also a path for further research.

Another area of improvement relies in **segmentation of arteries and nerves**. Indeed, orthognathic surgery entails significant risks of damage to concealed facial arteries and nerves. Particularly, the posterior palatal artery can be wounded during maxillary section, therefore potentially inducing life-threatening hemorrhage and necrosis of the maxilla. Iatrogenic<sup>30</sup> damage can also occur during mandibular spilt regarding the inferior alveolar nerved coursing within the bone.

Yet extracting such delicate structures from patient medical image in order to display them during planning would provide increased procedure safety. MRI-specific segmentation pipelines shall probably be considered, since such imaging modality seems the most appropriate in this purpose.

Additionally, the planning software could integrate **a library of different brands of existing fixation plates and screws**. Therefore, the surgeon could choose the most appropriate material in terms of shape, thickness and size and anticipate intraoperative plate modeling to fit the bone. Custom design according to planning could subsequently be easily considered.

### Simulation

Other research teams, such as the Compiègne Technology University, have conducted MRI-based facial muscle segmentation for integration to **a realistic model of facial soft tissue**. This research was pursued in collaboration with the “Facing Faces Institute” in Amiens, a spin-off from the Maxillo-facial surgery department of Pr. Devauchelle. Our research could favorably be considered in synergy with this team purposes.

In the same perspective of achieving a realistic mechanical model of facial soft tissue, we could consider patient-specific assessment of tissue properties thanks to the use of a measurement device yet commercially available. Rather than using average values of soft-tissue elasticity collected through literature, actual clinical measurements would ensure optimal implementation of the mechanical model.

---

<sup>30</sup> Iatrogenic: relating to impairment caused by medical examination or treatment.

**Layering skin texture** onto the 3D surface model is also a path for improvement. Many open-source systems allow swift 3D registration of digital pictures for surface mapping. Technological obstacles are no longer standing and reasonable development seems to be required to provide a realistic model of skin texture. We have actually already achieved such an outcome using basic computer tools. However, we would need to integrate such function in the simulation workflow.

### Navigation

As we explained in Chapter 2, our technological choice was to develop an **Augmented Virtuality (AV)**-based interface, since our main concern was to provide the surgeon with optimal accuracy in maxillary repositioning and ergonomics for visualization, particularly regarding depth perception. This choice was also conditioned by the restrained number of registration steps.

We had conducted initial tests using on-screen display of an Augmented Reality view of the patient thanks to video acquisition of a camera embedded in the operative light handle. Discrepancy between the surgeon's and the camera point of view, together with qualitative analysis of our **Augmented Virtuality**-based navigation system initially lead us to think that standard **Augmented Reality (AR)** using an external view might not represent a significant improvement in terms of navigational assistance.

**However, AV lacks any possibility of control in case of error, whereas AR dramatically increases real-time feedback, since information is directly superimposed to the actual patient.**

The recent emergence of head-mounted displays could trigger a paradigm shift.

If Google glasses<sup>®</sup> and other brands of AR glasses (Optinvent<sup>®</sup>, Laster<sup>®</sup>) seemed promising at first, it appears that novel devices such as HoloLens<sup>®</sup> provide quite impressive results in terms of rendering and GUI ergonomics. In a close future, such devices could probably be used on a routine basis in medical applications such as the one we addressed.

In the end, we have identified in the quantitative evaluation of our navigation system that, even though navigation can achieve an ideal maxillary position, misplacement is likely to occur during rigid fixation. Indeed, 9/12 surgeons strongly agreed that such system would be favorably combined with a system holding steady the position achieved through navigation. Giving strong credit to this outcome, we have already addressed this issue and **have started developing a system consisting of a mechanical arm connected to a novel interface allowing patient-specific fixation with the maxilla.** We will definitely pursue in this direction, seeking to provide an integrated system, which would solve this issue thanks to the combination of accurate navigation and steady support for bone fixation.

## Software development process

Our research has unfortunately been disturbed by software instability, particularly regarding simulation software, secondary to framework updates. Indeed, our research software is yet research prototype. Therefore, in order for a clinical use to be considered, it would appear necessary to conduct a development process subject to a quality management system (QMS), according to the 93/42/CEE directive regulating medical devices (ISO 13485). In order to take a leap forward and therefore to achieve validation on actual patients, such regulatory processes become mandatory in order for CE or FDA certification to be granted.

We thus conducted a regulatory study in order to identify the legal framework our tools should fit into.

This study concluded that all software components were to be considered as **active medical devices intended for diagnosis purposes**. As opposed to modeling software, it appeared that planning and simulation software featured a measurement function.

Section 8.4 of the Manual on Borderline and Classification For Medical Devices Version 1.6 (02-2010) provides different definitions for Picture Archiving and Communication System (PACS):

- a. PACS used for viewing, archiving and transmitting images.
- b. Where the post-processing of the image for diagnostic purposes is such as:
  - image processing functions which alter the image data (e.g. filtering, multiplanar reconstruction, 3D reconstruction)
  - complex quantitative functions (e.g. arterial stenosis evaluation, ventricular volume calculation, calcium scoring, automatic indication (detection) of potential lesions).
- c. With image enhancing by controlling image acquisition.

Modeling and planning software meet definition (b), whereas navigation software meets definition (c).

The rule that applied to modeling and planning software is rule 10, subparagraph 3, since it modifies source image and allows direct diagnosis. Therefore, they had to be considered as **Class IIa** medical device.

The rule that applied to navigation software is rule 10, subparagraph 3, second part, since it allowed a direct control of physiological processes with immediate danger for patient's life. Therefore, it had to be considered in to **Class IIb** medical device.

The study mentioned above also described the architecture and modalities of the QMS required.

In the end, these elements would greatly facilitate the evolution of our research prototypes into commercial releases.

### **Clinical validation**

If modeling software has been evaluated on a series of 8 real patient-cases, simulation has only been evaluated on 1 actual patient. Yet, navigation was only assessed by 12 operators on a phantom experiment mimicking an actual surgical environment. Of course, validation of the whole software suite would require a large number of patients and various surgical teams.

### **Implementation to other surgical fields**

In our introduction, we stated that the genesis of our research arose after looking at other surgical fields, namely Neurosurgery, ENT, orthopedics and dental implantology, in which planning, simulation and navigation were already present. After having initiated our own software suite dedicated to orthognathic surgery, we yet can consider further implementation to fields still vacant from routine computer assistance.

Indeed, our technology could easily be applied to **facial trauma surgery** since its purpose is to reposition a displaced facial bone, just like in orthognathic surgery. If trauma procedures usually occur under short notice due to emergency constraints, they are always based on initial CT scan. Therefore, thanks to swift automated segmentation and planning, intraoperative navigation based on our protocol could provide improved accuracy. With the further development of a mechanical holding system, ergonomics of such procedures could also be increased.

**Small joint surgery, such as hand and wrist surgery** have historically been close to maxillo-facial surgery, since it also focuses on delicate bone structures. Some plating and fixation systems used in maxillofacial surgery (mandibular condyle osteosynthesis) are actually derived from the ones used in hand surgery. Quite logically, our software suite could easily be implemented to this field.

At last, some deformities affecting the thorax, such as pectus excavatum<sup>31</sup>, feature common concerns with orthognathic surgery, namely, functional and cosmetic issues. Treatment relies on the reconstruction of the thoracic wall thanks to metallic implants. Therefore, in **thoracic surgery**, planning but also simulation of the cosmetic outcome together with intraoperative assistance are of primary importance and would benefit of a software solution like the one we developed.

Of course, the spreading of this technology will apply to many other fields and we hope to have contributed to such future development on our level.

---

<sup>31</sup> Pectus excavatum (PE) is an abnormal development of the rib cage where the breastbone (sternum) caves in, resulting in a sunken chest wall deformity. Sometimes referred to as "funnel chest," pectus excavatum is a deformity often present at birth (congenital) that can be mild or severe in adults and children.

### **6.3. General conclusion**

Through our research, we have developed the embryo of a software suite dedicated to assist the maxillofacial surgeon throughout his whole management of orthognathic surgery patients. If we overcame several technological obstacles, we have also identified several points subject to improvement and further development perspectives.

Regarding the preoperative phase, our planning software allows both, the surgeon to visually apprehend his procedure and the patient to understand what surgery will consist in.

The simulation software allows the surgeon to validate the surgical outcome he seeks and to present it to the patient in order to obtain his agreement.

During the intraoperative phase, our navigation software seems to bring an unprecedented answer to positioning issues thanks to an innovative interface, which lead to patent registration.

Since the accuracy provided through navigation might be affected by subsequent unexpected human motion, we have already initiated the development of a mechanical holding system that would solve this issue and therefore complete the integrated suite.

Under the condition of clinical tests conducted on a wider scale and of certification, we believe our research could, in the long term, provide significant improvements for patient optimal care.



## Chapitre 6 bis

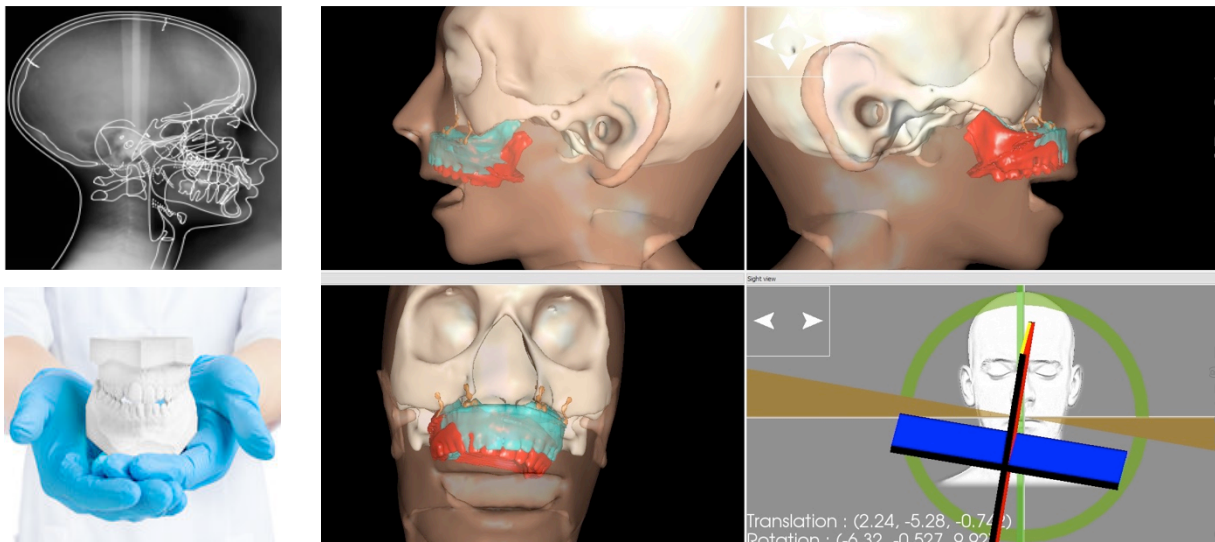
### CONCLUSION (version française du chapitre 6)

---

*Notre but ultime était de développer un système de navigation destiné à faciliter l'accomplissement des interventions de chirurgie orthognathique.*

*Nous avons identifié les étapes pré-requises à la réalisation de cet objectif, c'est à dire l'obtention d'un model numérique du patient à partir de la segmentation de son scanner, le développement d'outils de planification et nous avons par la même occasion proposé une méthode de simulation du résultat postopératoire. Nous pensons avoir développé un embryon de suite logicielle permettant au chirurgien maxillo-facial de surmonter plusieurs obstacles qu'il est susceptible de rencontrer au cours de la prise ne charge de patients relevant d'une intervention orthognathique. Ceci étant, notre travail a identifié plusieurs points susceptibles d'être améliorés ainsi que des perspectives de développement futurs.*

---





## 6.1.bis Réalisations

Nous avons tout d'abord abordé la modélisation (Chapitre 3). Après avoir considéré les obstacles empêchant une segmentation aisée (continuité entre les mâchoires supérieure et inférieure, artéfacts métalliques d'origine dentaire), nous avons établi la « réalité terrain » à l'aide d'une méthode de segmentation interactive. À la lumière de celle-ci, nous avons pu programmer une méthode automatisée.

### Un pipeline de segmentation semi-automatique surmontant les artéfacts métalliques d'origine dentaire

Nous avons été en mesure d'accomplir une segmentation distincte des os de la face (maxillaire, d'une part, et mandibule, d'autre part) et des tissus mous grâce à l'utilisation d'un algorithme unique de segmentation semi-automatique ne faisant appel qu'à de rares entrées interactives. Celui-ci a permis d'obtenir un modèle complet de maillages surfaciques de la tête du patient qui a pu être utilisé comme donnée d'entrée dans le cadre des étapes de planification et de simulation.

Ce pipeline de segmentation, utilisant des données scanner brutes en entrée, était fondée sur la succession d'opérateurs de morphologie mathématique visant à traiter indépendamment les masques des images.

Nous nous sommes tout d'abord employés à effectuer une segmentation distincte du maxillaire et de la mandibule. Nous avons utilisé une approche originale fondée sur la **segmentation de la pulpe dentaire**, associant notamment des opérateurs de seuillage, d'extraction de la composante connexe principale et de dilatation. Ainsi avons-nous pu atteindre nos objectifs malgré la continuité entre le maxillaire et la mandibule et la présence d'artéfacts métalliques d'origine dentaire (Cf. Chapitre 3, 3.4.2.2.1).

La segmentation de la peau et des tissus mous faciaux a pu être réalisée en dépit des déficiences du contour cutané consécutives aux artéfacts métalliques. Nous avons résolu ce problème grâce à l'extraction d'un gradient de contour lissé en utilisant un opérateur de ligne de partage des eaux et des graines appropriées associé à un lissage de la couche de tissus mous et à la soustraction de la surface osseuse de la couche de tissus mous grâce à une transformée de distance (Maurer) (Cf. Chapitre 3, 3.4.2.2.2). Le modèle de tissus mous résultant a été conçu de façon à ce qu'il soit en contact intime avec la surface osseuse - voire l'interpénètre – afin de permettre la simulation ultérieure.

L'évaluation a été fondée sur la comparaison entre les pipelines de segmentation semi-automatique et interactive (manuelle), en utilisant une base de données de scanner de 8 patients. Les mesures étaient représentées par le temps de calcul en secondes et la précision en utilisant la distance bord à bord en millimètres.

Pour ce qui concerne le temps de calcul, nous avons constaté une amélioration d'un facteur 6 grâce à l'automatisation.

Nous notons également que, lors de la procédure semi-automatique, les interactions de l'opérateur sont extrêmement courtes puisqu'il n'a besoin de régler que quelques paramètres.

En termes de précision, la moyenne des erreurs de distance s'étendait entre 0,72 et 1,68 mm, la médiane entre 0,71 et 1,16 mm et l'écart-type entre 0,22 et 2,24.

Nous avons également relevé que le nombre des valeurs extrêmes (erreur de distance > 1,5 mm) ne dépassait pas les 25%. De nombreuses valeurs extrêmes (distance en dehors de l'intervalle 25% - 75%) étaient retrouvées dans la partie postérieure des arcades dentaires où les artefacts sont généralement nombreux. Ceci ne représentait donc pas un problème, puisque d'une part, l'intérêt clinique se porte sur la morphologie faciale externe et que, d'autre part, ces erreurs n'avaient aucun impact sur la segmentation des tissus mous.

Puisque la taille des voxels était proche de 0,5 X 0,5 X 0,5 mm, 75% des erreurs de distance représentaient moins de 3 voxels.

Plus avant, une telle précision est tout à fait satisfaisante si l'on considère que l'interprétation de la position des contours osseux peut varier selon le type de fenêtrage choisi par l'opérateur. Il est vrai que l'effet de volume partiel génère une transition douce (habituellement de 2 à 3 voxels) entre les os et les tissus mous.

Bien sûr, une évaluation optimale aurait nécessité des segmentations de différentes images conduites par le même opérateur aussi bien que des segmentations itératives d'une même image par différents opérateurs. En raison de contraintes de temps et de personnel, nous avons pour objectif de mener une telle étude lors de développements ultérieurs.

Malheureusement, ce pipeline n'était pas complètement automatisé puisqu'il nécessitait des interventions manuelles, en particulier pour déterminer la valeur de seuils d'après des mesures interactives.

Puisque des méthodes alternatives permettant de traiter simultanément les masques d'images ne sont pas encore implémentées dans la version du logiciel que nous avons utilisée, nous étudierons la possibilité de développer un pipeline complètement automatisé lors des étapes ultérieures de nos recherches.

En tenant compte de l'effet de volume partiel et de la précision chirurgicale d'1 mm, nous pouvons considérer que l'erreur de distance d'1,5 mm que nous avons constatée entre la segmentation semi-automatique et l'interactive est acceptable.

Nous avons démontré que le pipeline de segmentation semi-automatique que nous avons proposée pourrait remplacer la segmentation interactive menée par un expert en termes de précision.

Le pipeline semi-automatique limite également la variabilité inter-opérateurs, favorisant ainsi une meilleure reproductibilité. Grâce à ce pipeline quasi-automatisé, le bénéfice significatif est qu'il rend le chirurgien disponible pour des tâches plus critiques.

## **Conversion des déplacements chirurgicaux en opérations mathématiques à des fins de planification virtuelle.**

Afin de pouvoir effectuer une planification, nous avons dû traduire mathématiquement les déplacements chirurgicaux pour pouvoir reproduire ceux-ci sur le modèle virtuel du patient. Nous nous sommes focalisés sur le temps chirurgical maxillaire puisqu'il s'agit du plus crucial de toute l'intervention. Nous avons analysé les bases géométriques des mouvements chirurgicaux afin de définir les points et axes selon lesquels les déplacements standards s'effectuent. Nous avons ensuite établi les matrices de transformation dédiées permettant de déplacer le modèle virtuel de façon concordante. En réalité, nous avons proposé une matrice 4 X 4 unique permettant de définir la translation et la rotation autour d'un axe. Au cours de cette étude, nous avons été en mesure de catégoriser tous les mouvements du maxillaire en utilisant une grille standardisée, ce qui, selon nous, n'avait pas encore été réalisé précédemment.

Les positions ainsi définies pouvaient être utilisées comme positions-cibles dans l'évaluation ultérieure du système de navigation.

## **Proposition d'une méthode de simulation des tissus mous faciaux**

Pour ce qui concerne la simulation, nous avons analysé et transféré les conditions aux limites à notre moteur logiciel.

Nous avons utilisé une méthode physique fondée sur un modèle mécanique masse-ressort, qui était suffisamment adapté à la simulation temps réel des déformations élastiques des tissus mous faciaux, puisque l'ampleur de celle-ci est faible en comparaison de la translation associée. Afin de fournir une simulation réaliste, nous avons utilisé des maillages volumiques plutôt que surfaciques. La bibliothèque **TetGen**<sup>®</sup> intégrée à la plateforme a été utilisée pour générer des maillages volumiques de haute qualité à partir de maillages surfaciques. En effet, les moteurs mécaniques, tels que **Bullet**<sup>®</sup>, requièrent des maillages volumiques de haute qualité constitués de tétraèdres. Nous avons employé deux approches mécaniques avec **Bullet**<sup>®</sup>. Tout d'abord, des forces étaient appliquées à certains sommets du maillage volumique de façon à ce que le moteur mécanique calcule le déplacement engendré sur les sommets voisins jusqu'à atteindre un état d'équilibre. La seconde approche avait un objectif similaire si ce n'est qu'une nouvelle position était imposée à certains sommets du maillage, et non une force. Les sommets considérés ont été choisis comme appartenant à la fois au maillage **volumique** des tissus mous faciaux et au volume correspondant au maillage **surfacique** des tissus mous faciaux. En effet, c'est la position des os de la face qui est affectée par la chirurgie, tandis que la déformation des tissus mous n'en est que la conséquence.

Cette méthode nous a permis de générer une simulation du résultat postopératoire.

Nous avons ensuite réalisé une évaluation de notre logiciel sur des patients réels. Pour ce faire, nous avons utilisé une base de données constituée des scanners postopératoire et préopératoire du même patient.

Dans un premier temps, nous avons analysé l'ampleur de l'intervalle de distance entre la surface des tissus mous postopératoire et préopératoire. Ensuite, nous avons comparé le maillage surfacique des tissus mous en contact avec la surface cutanée du patient (maillage simulé) au maillage surfacique de la surface cutanée extrait du scanner postopératoire (représentant la vérité terrain).

Cette évaluation reposait sur 3 méthodes différentes de calcul des erreurs de distance entre les maillages simulé et postopératoire réel. Ces mesures quantitatives ont été associées à une carte de distance colorée à des fins de commodité d'interprétation.

Nous avons montré que notre simulation des tissus mous faciaux fournit des résultats prometteurs puisque sa précision est supérieure à 1 mm.

Enfin, la précision obtenue en utilisant un tel modèle et sa vitesse de rafraîchissement peuvent permettre à notre simulation d'être utilisée dans des applications temps réel nécessitant un rendu réaliste.

### **Un système de navigation fondé sur le tracking électromagnétique Disposant d'une interface utilisateur innovante**

Nous avons conçu l'installation d'un **système de navigation** sur un mannequin en tenant compte des contraintes temporelles, spatiales et d'asepsie qui s'appliquent à un environnement chirurgical réel.

Selon notre évaluation qualitative menée auprès de 12 chirurgiens, cette installation pourrait être directement transférée au bloc opératoire.

Des développements spécifiques ont été menés afin d'effectuer la calibration et le recalage entre le repère du modèle 3D (scanner) et le repère du système électromagnétique.

Nous avons conçu et développé une interface utilisateur originale dédiée à la navigation en chirurgie orthognathique permettant d'afficher 6 degrés de liberté sur un écran unique et permettant un tracking en temps réel. Une partie de cette interface consistait en une mire tridimensionnelle colorée fournissant des informations intuitives concernant la position spatiale du maxillaire dans le champ opératoire. L'IHM<sup>32</sup> était agrémenté de vue 3D du modèle virtuel afin de correspondre à l'installation opératoire réelle. L'IHM affichait des éléments supplémentaires destinés à faciliter l'appréhension de la position opératoire (anneau périphérique de largeur variable, ligne d'horizon en papillon, ligne verticale en gouvernail, et bouton d'orientation de la tête du modèle pour mise en correspondance avec la déclivité du patient). Ainsi, la translation et la rotation pouvaient être simultanément visualisées sur des vues frontales et latérales.

---

<sup>32</sup> IHM: Interface Homme Machine

L'**évaluation qualitative** montrait que la plupart des chirurgiens étaient convaincus que le système permettait une précision de positionnement du maxillaire accrue. Elle a aussi conclu que le système était peu encombrant puisque les sondes électromagnétiques étaient perçues comme très discrètes, en particulier grâce au design de la sonde intégrée à la gouttière. La discrétion de la sonde de tracking de la position de la tête évitait également tout système de fixation invasif de la tête.

Concernant l'IHM, une grande majorité des opérateurs s'accordait sur le caractère intuitif du système, adapté à l'accomplissement des objectifs chirurgicaux et permettant une bonne compréhension des mouvements tridimensionnels. La plupart des chirurgiens a expliqué que la mire fournissait l'information la plus utile de l'interface. En effet, ils ne regardaient que peu les vues 3D frontale et latérales du modèle et 3 chirurgiens ont même suggéré que l'interface gagnerait à n'afficher que la seule mire 3D en plein écran.

Notre utilisation de la **Virtualité Augmentée** présentait le grand avantage de limiter le nombre d'étapes de recalage tout en permettant une précision optimale de positionnement du maxillaire et une visualisation satisfaisante, notamment en termes de perception de profondeur. L'analyse qualitative nous a conduit à penser que la Réalité Augmentée standard, utilisant une vue externe, ne représenterait pas une amélioration significative en termes d'assistance à la navigation.

L'**évaluation quantitative** a confirmé que la précision du système électromagnétique était d'approximativement 1 mm, ce qui était conforme aux données du fabricant et à la littérature.

L'évaluation quantitative de la précision et de la durée opératoire a montré que la navigation permettait à chacun des chirurgiens de travailler avec une précision accrue puisqu'à la fois l'erreur globale et angulaire étaient améliorées. Une telle amélioration augmentait quand le niveau d'expérience du chirurgien diminuait. En effet, la navigation apportait les bénéfices les plus importants en termes de précision et de temps opératoire chez les chirurgiens novices, peu expérimentés. La navigation est également apparue comme la plus pertinente dans les cas de mouvements osseux complexes (selon 2, voire 3 axes).

Notre logiciel permettait indéniablement une réduction de variabilité autant en termes de temps opératoire qu'en termes de précision, ceci se vérifiant dans les différentes catégories d'opérateurs. Ainsi, ce système serait à même de favoriser la standardisation du positionnement maxillaire. En plus de son bénéfice en termes de pédagogie chirurgicale, un tel système pourrait également être profitable en particulier pour les internes, puisque le temps opératoire s'avérait particulièrement amélioré dans leur catégorie.

Toutefois, il est à noter que, même si la navigation contribue à positionner le maxillaire de façon optimale, un déplacement inopiné peut se produire lors de sa fixation. Ainsi, 9 chirurgiens sur 12 ont été tout à fait d'accord avec le fait qu'un tel système de navigation pourrait être avantageusement combiné à un système mécanique de maintien de la position du maxillaire.

Bien sûr, nous pouvons également souligner le fait que nous n'avons mené qu'une expérience sur mannequin et que le système et son interface nécessiteraient une évaluation sur plusieurs patients au cours d'interventions chirurgicales réelles. Notre objectif est d'envisager une telle étape dans la poursuite de nos recherches.

## 6.2.bis Perspectives

### Planification

Notre pipeline de segmentation semi-automatique est un atout qui a été intégré au service proposé par la société **Prometeus Surgical**<sup>®</sup>, une start-up fondée par notre équipe en 2015 qui a ultérieurement fusionné avec la société Visible Patient<sup>®</sup>.

Des améliorations peuvent, bien sûr, être d'ores et déjà envisagées, en particulier par l'automatisation complète des étapes actuelles de segmentation interactive principalement dédiées à la détermination de la valeur de quelques seuils.

L'utilisation ou le développement de filtres pertinents pour apporter des solutions alternatives au traitement des artéfacts dentaires est également une voie de recherche.

Une autre cible de perfectionnement consiste en la **segmentation des artères et nerfs**. En effet, la chirurgie orthognathique comporte des risques significatifs de lésion d'éléments vasculo-nerveux occultes. En particulier, l'artère palatine postérieure peut être blessée lors de la section chirurgicale (ostéotomie) du maxillaire, exposant ainsi à la nécrose du maxillaire et à une hémorragie pouvant engager le pronostic vital. Une lésion iatrogénique<sup>33</sup> peut également survenir lors du clivage de la mandibule à l'encontre du nerf alvéolaire inférieur qui la traverse.

Ainsi, l'extraction de telles structures à partir de l'image médicale du patient serait susceptible d'accroître la sécurité de l'intervention. Des algorithmes de segmentation spécifiques à l'IRM seraient alors à considérer puisque cette modalité d'imagerie semble la plus adaptée à l'analyse de ces structures vasculo-nerveuses molles.

Par ailleurs, le logiciel de planification pourrait avantageusement intégrer une bibliothèque des différents modèles existants de plaques et vis de fixation osseuse (ostéosynthèse). Ainsi, le chirurgien pourrait choisir en préopératoire, le dispositif le plus approprié en termes de forme, d'épaisseur et de taille et anticiper le modelage opératoire indispensable à une bonne congruence osseuse. La fabrication de plaques sur mesure serait alors facilement envisagée.

### Simulation

D'autres équipes de recherche, telle que celle de l'Université de Technologie de Compiègne ont effectué une segmentation des muscles faciaux à partir d'IRM à des fins d'intégration à un modèle réaliste des tissus mous faciaux. Ce projet est mené en partenariat avec l'«Institut Faire Faces» à Amiens émanant du service de Chirurgie Maxillo-Faciale du Pr. Devauchelle. Notre spectre de recherche pourrait être synergique avec les objectifs de telles équipes.

Dans la même perspective de réaliser un modèle mécanique réaliste des tissus mous faciaux, on pourrait envisager l'enregistrement patient-spécifique des

---

<sup>33</sup> Iatrogénique: se réfère à une lésion causée par un examen ou un traitement médical.

propriétés tissulaires grâce à l'utilisation d'instruments de mesure d'ores et déjà disponibles sur le marché. Plutôt que d'utiliser des valeurs moyennes d'élasticité des tissus mous relevées par l'analyse de la littérature scientifique, des mesures cliniques réelles permettraient l'implémentation optimale du modèle mécanique.

L'application de la texture cutanée sur le modèle surfacique 3D est également une voie de perfectionnement. Plusieurs systèmes *open source* permettent le recalage aisé de photographies numérisées à des fins de texturage surfacique. Les obstacles technologiques étant tombés, un effort de développement raisonnable devrait être en mesure d'aboutir à un modèle texturé réaliste de la peau faciale. Nous avons en réalité déjà pu obtenir un tel modèle en utilisant des outils informatiques de base.

Toutefois, nous devrions implémenter une telle fonctionnalité dans le flux de travail de la simulation.

## Navigation

Comme nous l'avons expliqué dans le Chapitre 2, notre choix technologique était de développer une interface fondée sur la **Virtualité Augmentée (VA)**, puisque notre objet principal était de fournir au chirurgien un outil de positionnement précis du maxillaire avec une ergonomie visuelle optimale, notamment en termes de perception de la profondeur. Ce choix a également été dicté par le nombre limité d'étapes nécessaires au recalage.

Nous avons mené des tests initiaux affichant sur un écran une vue du patient en Réalité Augmentée grâce à l'acquisition vidéo d'une caméra intégrée à la poignée de l'éclairage chirurgical (scialytique). L'écart entre les points de vue respectifs du chirurgien et de la caméra, associé aux bons résultats de l'analyse qualitative du système par Virtualité Augmentée, nous ont conduit à penser que la Réalité Augmentée standard s'appuyant sur une vue externe, ne représenterait pas une amélioration significative en termes d'assistance par navigation.

**Toutefois, la VA ne permet pas de contrôle en cas d'erreur, au contraire de la RA qui améliore considérablement le rétrocontrôle en temps réel du fait de la superposition directe de l'information sur le patient réel.**

L'apparition récente des interfaces visuelles à support céphalique pourrait conduire à un changement de paradigme. Si les Google glasses<sup>®</sup>, au même titre que d'autres marques de lunettes de RA (Optinvent<sup>®</sup>, Laster<sup>®</sup>), apparaissaient comme prometteuses initialement, il semble que les nouveaux dispositifs tels que Hololens<sup>®</sup> procurent des résultats impressionnants en termes de rendu et d'ergonomie de l'IHM. Dans un futur proche, de tels dispositifs seront probablement d'utilisation routinière dans les applications médicales telles que celle que nous avons étudiée.

Enfin, l'évaluation quantitative de notre système de navigation nous a permis d'identifier que malgré l'obtention d'un positionnement optimal par la navigation, un



déplacement secondaire est susceptible d'intervenir lors de la fixation du maxillaire. En effet, 9 chirurgiens sur 12 ont été tout à fait d'accord avec le fait qu'un tel système de navigation pourrait être avantageusement combiné à un système mécanique de maintien du maxillaire en position stable. Accordant un fort crédit à cette observation, nous avons d'ores et déjà considéré cet enjeu et avons commencé à développer un système comprenant un bras mécanique connecté à une interface innovante permettant une fixation patient spécifique au maxillaire. Nous poursuivrons indubitablement dans cette voie en vue de proposer un système intégré répondant à cet enjeu, grâce à la combinaison d'une navigation précise et d'un système de maintien stable du maxillaire facilitant la fixation osseuse.

### **Procédure de développement et de maintien du logiciel**

Nos recherches ont malheureusement été perturbées par une instabilité logicielle notamment pour ce qui concerne le système de navigation, ce en raison des mises à jour itératives de la plate-forme. En effet, notre logiciel de recherche n'est pour l'instant qu'un prototype. Ainsi, pour qu'une utilisation clinique puisse être envisagée, il semble nécessaire que le processus de développement soit mené dans le cadre d'un système de management de la qualité conformément à la directive 93/42/CEE qui régit les dispositifs médicaux (ISO 13485). Afin de passer à l'étape suivante et ainsi d'effectuer une validation sur des patients réels, une telle démarche réglementaire apparaît comme indispensable en vue de l'obtention d'un marquage CE ou FDA.

C'est la raison pour laquelle nous avons mené une étude réglementaire afin d'identifier le cadre légal dans lequel nos dispositifs sont susceptibles de s'intégrer.

Au contraire d'un logiciel de modélisation, il apparaît que les logiciels de planification et de simulation comportent une fonction de mesurage.

La section 8.4 du *Manual On Borderline And Classification For Medical Devices* version 1.6 (02-2010) fournit différentes définitions pour les systèmes d'archivage et de communication d'images (PACS) :

- a. PACS utilisé pour visualisation, archivage et transmission d'images
- b. Où le post-traitement de l'image à des fins diagnostiques est tel que :
  - les fonctions de traitement d'image altèrent les données de l'image (i.e. : filtrage, reconstruction multiplanaire ou 3D)
  - des fonctions quantitatives complexes sont utilisées (i.e. : évaluation d'une sténose artérielle, calcul du volume ventriculaire, classification des calcifications, indication automatiques (détection) de lésions potentielles).
- c. Avec une amélioration de l'image en contrôlant l'acquisition de l'image.

Les logiciels de modélisation et de planification correspondent à la définition (b), tandis que le logiciel de navigation correspond à la définition (c). La règle qui

s'applique aux logiciels de modélisation et de planification est la règle 10, article 3, puisque ces logiciels modifient l'image source et permettent un diagnostic direct. Ainsi ils doivent être considérés comme des dispositifs médicaux de **classe IIa**.

La règle qui s'applique au logiciel de navigation est la règle 10, article 3, seconde partie, puisque ce logiciel permet un contrôle direct des processus physiologiques comportant un danger immédiat pour la vie du patient. Ainsi, il doit être considéré comme un dispositif médical de classe 2B.

L'étude de mentionnée plus haut décrivait également l'architecture et les modalités du système de management de la qualité (SMQ) requis.

Ainsi, la prise en compte de ces éléments permettrait de grandement faciliter l'évolution de nos prototypes de recherche vers des produits commercialisables.

### **Validation clinique**

Si le logiciel de modélisation a été évalué sur une série de 8 patients réels, le logiciel de simulation, lui, a seulement été évalué sur un seul patient réel. De la même façon, le système de navigation allaiter par 12 opérateurs au cours d'une expérience sur un mannequin imitant un environnement chirurgical réel. Bien sûr, la validation de l'ensemble de la suite logicielle nécessiterait un échantillon large de patients ainsi que diverses équipes chirurgicales.

### **Application à d'autres domaines chirurgicaux**

Dans notre introduction, nous avons énoncé que notre sujet de recherche a trouvé son origine suite à notre observation d'autres domaines chirurgicaux, en particulier la Neurochirurgie, l'ORL, l'orthopédie et l'implantologie dentaire, dans lesquels la planification, la simulation et la navigation étaient déjà largement utilisées. Maintenant que nous avons initié le développement de notre suite logicielle dédiée à la chirurgie orthognathique, nous pouvons désormais envisager son application ultérieure à des domaines chirurgicaux dépourvus d'assistance informatique de routine.

En effet, notre technologie pourrait facilement être appliquée à la **chirurgie traumatologique faciale** puisque son objectif est de repositionner toute ou partie d'un os facial déplacé, tout comme c'est le cas en chirurgie orthognathique. Si les interventions de traumatologie faciale sont généralement menées après un court préavis en raison du caractère d'urgence, elles sont toutefois toujours précédées d'un scanner. Ainsi, grâce à une segmentation automatique et une planification aisée, une navigation peropératoire fondé sur notre protocole permettrait une précision accrue. Avec le développement ultérieur d'un système de maintien mécanique, l'ergonomie de telles procédures pourrait aussi être amélioré.

**La chirurgie des petites articulations, telle que la chirurgie de la main et du poignet** a été historiquement proche de la chirurgie maxillo-faciale puisqu'elle s'adresse également à des structures osseuses délicates. En effet, certaines plaques et certains systèmes de fixation utilisés en chirurgie maxillo-faciale (ostéosynthèse du condyle mandibulaire) sont en réalité dérivés de ceux utilisés en chirurgie de la main. Assez logiquement, notre suite logicielle pourrait être facilement appliquée à ce domaine.

Enfin, certaines déformations touchant le thorax, tel que le pectus excavatum<sup>34</sup>, présentent des enjeux communs avec la chirurgie orthognathique, c'est-à-dire une problématique à la fois fonctionnelle et cosmétique. Leur traitement repose sur la reconstruction de la paroi thoracique à l'aide d'implants métalliques. Ainsi, **en chirurgie thoracique**, la planification mais également la simulation du résultat cosmétique associé à l'assistance peropératoire sont d'une importance cruciale et pourraient grandement bénéficier d'une solution logicielle telle celle que nous avons développée.

Bien sûr, la diffusion de cette technologie concernera de nombreux autres domaines chirurgicaux et nous espérons avoir contribué, à notre niveau, à de tels développements futurs.

---

<sup>34</sup> Le pectus excavatum correspond à un développement anormal de la cage thoracique où le sternum s'excave vers l'intérieur, ce qui aboutit à une déformation plongeante de la paroi thoracique. Parfois désignée par le terme de « thorax en entonnoir », le pectus excavatum est une difformité souvent présente à la naissance (congénitale), qui peut être légère ou sévère chez les adultes et les enfants.

### **6.3.bis Conclusion générale**

À travers nos recherches, nous avons développé l'embryon d'une suite logicielle destinée à assister le chirurgien maxillo-facial tout au long de sa prise en charge des patients candidats à une intervention de chirurgie orthognathique.

Si nous avons surmonté plusieurs obstacles technologiques, nous avons également identifié plusieurs pistes d'amélioration ainsi que de nombreuses perspectives de développement ultérieur.

Pour ce qui concerne la phase préopératoire, notre logiciel de planification permet d'une part, au chirurgien d'appréhender visuellement son intervention et, d'autre part, au patient de comprendre en quoi la chirurgie va consister.

Le logiciel de simulation permet non seulement au chirurgien de valider l'objectif chirurgical qu'il envisage, mais aussi de le présenter au patient afin d'obtenir son consentement éclairé.

Durant la phase peropératoire, notre logiciel de navigation semble apporter une réponse sans précédent aux enjeux de positionnement grâce à une interface innovante qui a fait l'objet d'un dépôt de brevet.

Puisque la précision apportée par la navigation risque d'être compromise par un mouvement inopiné d'origine humaine, nous avons d'ores et déjà envisagé le développement d'un système de maintien mécanique qui permettrait de résoudre cette problématique et d'ainsi compléter cette suite intégrée.

À la condition de tests cliniques menés à large échelle et d'une certification réglementaire de nos logiciels, nous pensons que nos recherches pourraient, sur le long terme, permettre des améliorations significatives pour une prise en charge optimale des patients.



## APPENDIX I:

### VR-MED<sup>®</sup> user's manual and image processing operators

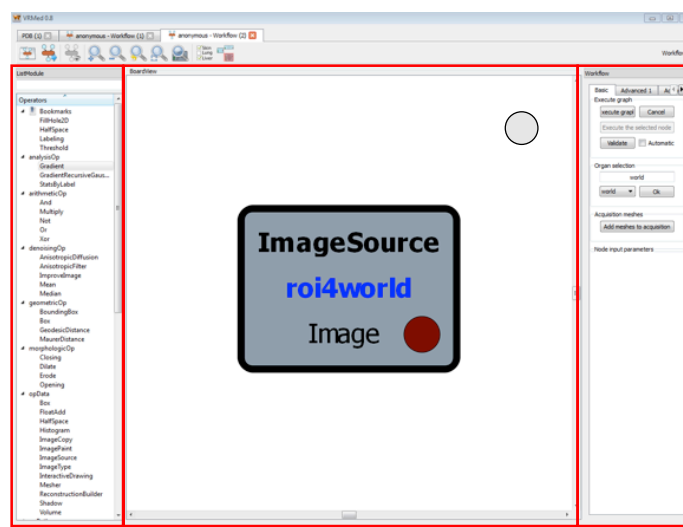
We used the VR-Med software v.1.3.2 running on FW4spl. FW4SPL<sup>35</sup> is a framework for fast and easy creation of applications, mainly in the medical imaging field. It includes various features such as 2D and 3D digital image processing, visualization, augmented reality and medical interaction simulation. We describe here the specifications and features of this software (courtesy of Luc SOLER, PhD).

#### Workflow view

The Workflow allows for a visualization of patient images in order to delineate his/her visible anatomical and pathological structures.

For open the workflow window, you need to charge a patient, click on the button “new processing” on the “processing selector” area. After that, you can launch a new workflow tab by clicking on the “workflow view” button on the tool bar.

The Workflow tab are composed by three areas, the “ListModule” (1) area, the “BoardView” (2) area and the “Workflow” area (3).



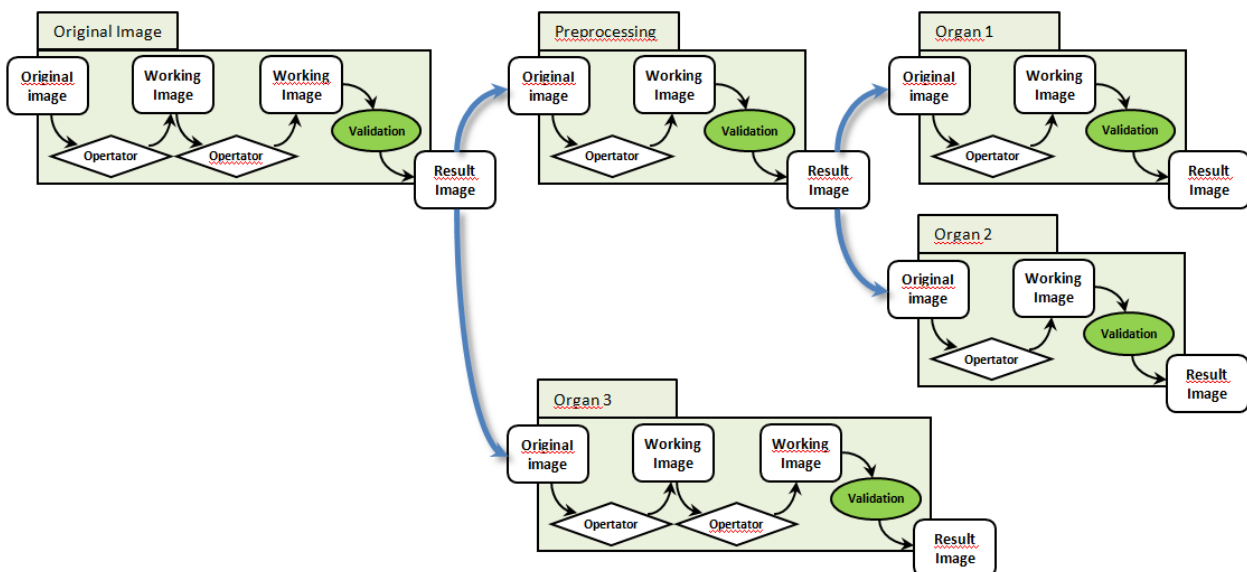
<sup>35</sup>FW4spl: <https://github.com/fw4spl-org/fw4spl>

The tool bar contains respectively the following buttons:



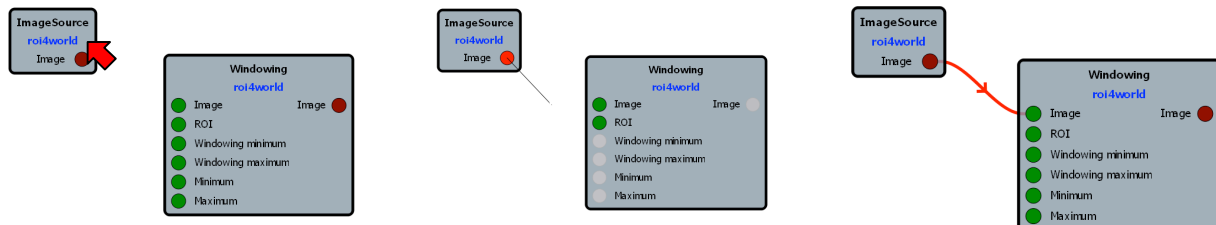
- 1 : *Merge Graph* for launch a procession previously saving.
- 2 : *Export script* for save a script.
- 3 : *View selected node* for change the setting/see the result of operators.
- 4 : *Zoom in* : for zoom in the “BoardView”.
- 5 : *Zoom out* : for zoom out the “BoardView”.
- 6 : *Reset zoom*.
- 7 : *Fit zoom*.
- 8 : *Fit selection*.
- 9 : *Show tag manager* : for show/hide several operators on the “BoardView”.
- 10 : *Show overview*.

VRMed allows visualizing two main images, the original image and the working image. The working image is the image obtained by processing operators. The original image is initially the loaded DICOM image. After processing, this original image will change according to the pre-processing or delineation of each organ as shown on the diagram below.

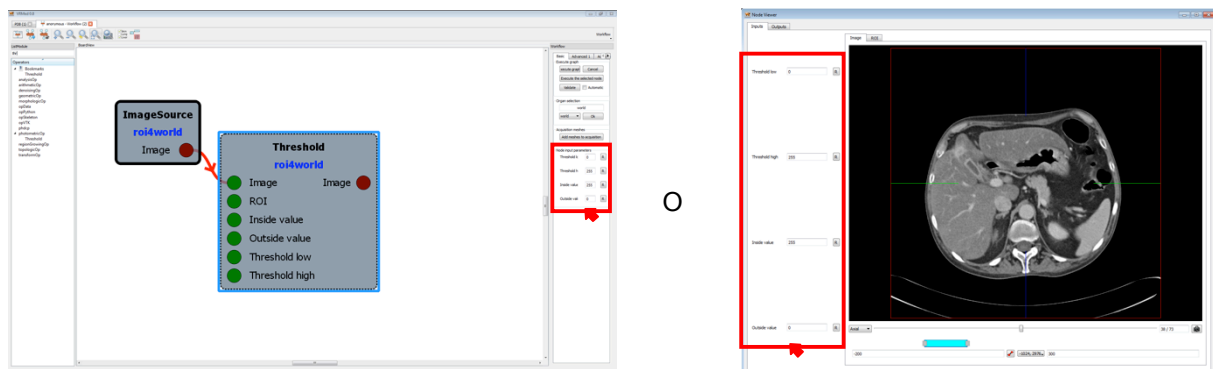


The Workflow is dedicated to organ modeling. Such modeling is seen as a hierarchical segmentation realized through a processing where organs are segmented one by one. Each organ segmentation can be done by applying a set of Geometrical, Morphological, Smoothing, Topological, Manual, Logical and Photometrical operators. The resulting set of operators can then be seen as a script that VRMed can record and apply on any new image. The global list of organs and associated set of operators is called the processing line. This processing line appears in the “BoardView” located at the center of your screen.

Before any organ modeling, users can decide to modify the original image by applying one or several filtering. To do it, users have to select by a simple left press on the “ListeModule” area and drag on the “BoardView”. By default the first operator in the BoardView are the ImageSource, that is to say the original image of the patient. The operators must be linked together, in order to connect respectively the outputs of one operator to the inputs of the following one.



To apply any operator, users have to enter the operator parameter (if it exists). The operator parameter can be seen on the “inputs” tag or on the “Node Viewer”. For open the “Node Viewer” you need to select the operator and click on the “View selected node” button.



Finally, click on the “execute graph” or “execute the selected node” on the Basic tag of the Workflow area for apply operator.

To look at the result of your processing you need to select an operator and clicking on the “Node Viewer” button. In the Node Viewer windows you can see the initial image in the tab “input”, see the ROI (if she exist) in the tab “ROI” and see the result of the operator in the tab “outputs”.

All operators can be associated with an organ. This method allows to organize the processing into a hierarchy and to define organ mask and ROI.

ROI allows limiting the operator application to a reduced area of the medical image according to already delineated anatomical or pathological structures. Thus, the “Liver\_Tumour” type in the dictionary will automatically limit the image analysis to the Liver area if already delineated.



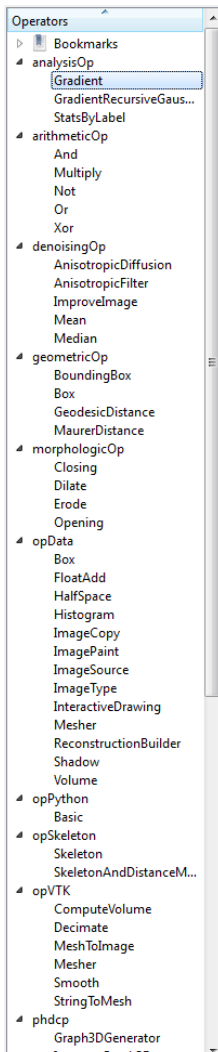
To create a new organ and use this like a mask, users have then to select an operator and select an organ in the drop down menu of the “organ selection” in the Workflow, then click “ok”.

All the next operators connect automatically to this process line will be define like the same organ. At the and of the process, when the resulting image gives the desired organ, you can validate our results by a simple right click on the last operator and select “Validate Organ Mask”.

To create a new define of organ, users have then to click on the “Advanced 1” tag of the workflow. In this tag, you have access to the dictionary of organ. Click on the “new” button of the “organ editor” for specify the name and the setting of the new organ. For define the setting you need to use the next command: inter, union, not, shadow and halfSpace.

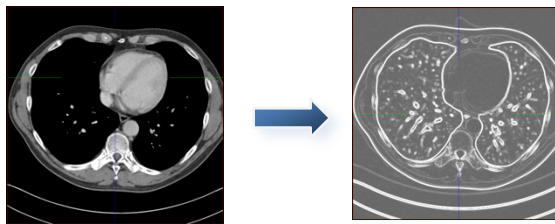
**Operators**

The workflow of VRmed includes a list of basic operators allowing to delineate organs and then create an automated processing line. In the next chapter, we will explain some of the main operators.



**The “analysis” operators:**

Gradient: this operator returns the gradient of the working Image. This operator has no option or parameterization.



**The “arithmetic” operators:**

And: it makes the logical operation “and” behind two working images. It return the grey level 1 when the images are the same and the grey level 0 elsewhere. This operator has no option or parameterization.

b	a	X
0	0	0
0	1	0
1	0	0
1	1	1

**Multiply**: it multiplies the grey level of working image by another working image. This operator has no option or parameterization.

**Not**: it changes the grey level 0 into 1 and changes all other grey levels into 0. It is usually used on binary images to obtain the negative of the image. This operator has no option or parameterization.

**Or**: it makes the logical operation “or” behind two working image. This operator has no option or parameterization.

b	a	X
0	0	0
0	1	1
1	0	1
1	1	1

**Xor**: it makes the logical operation “Xor” behind two working image. This operator has no option or parameterization.

b	a	X
0	0	0
0	1	1
1	0	1
1	1	0

## The “denoising” operators

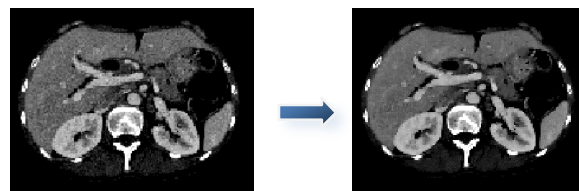
**Anisotropic diffusion** : This operator allows to smooth grey-levels of an image without removing high gradient grey level. It thus keeps the border of visible anatomical and pathological structures. VRmed developed functions using the Karl Krissian iterative algorithm based on three main parameters: the conductance value K, the iteration number I and the time step T. An ideal K value corresponds to the standard deviation of the grey level distribution of the organ that users want to delineate (between 10 and 20 according to the organs)

Node input parameters

Conductance

Number of iterations

Time step



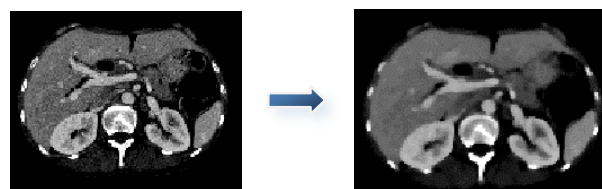
**Mean**: This operator allows to smooth grey-levels of an image by computing the average grey level value around each voxel of the image. It will blur the image. Three parameters can be modified: the area size around each voxel where the mean is computed in X, Y and Z axis.

Node input parameters

Size X

Size Y

Size Z

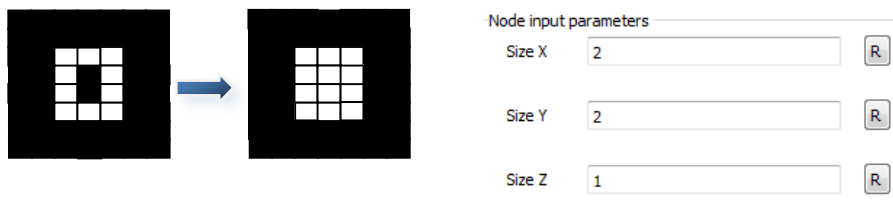


**Median:** This operator allows to smooth grey-levels of an image by computing the median grey level value around each voxel of the image. It will less blur the image than a mean operator. 3 parameters can be modified: the area size around each voxel where the median is computed in X, Y and Z axis.

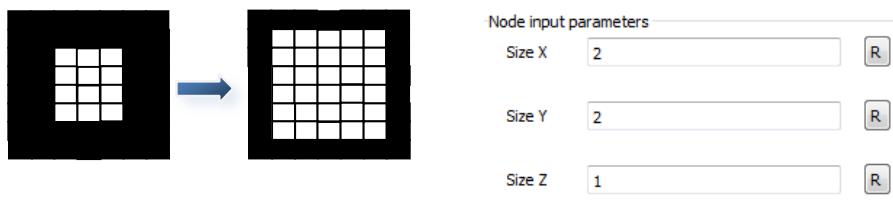


**The “morphologic” operators**

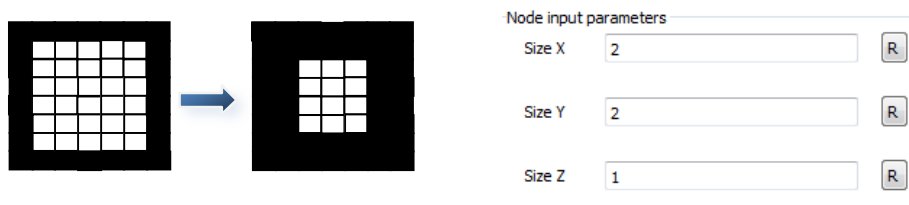
**Closing:** This operator allows to morphologically close the image. 3 parameters can be modified: the closing radius size in X, Y and Z axis.



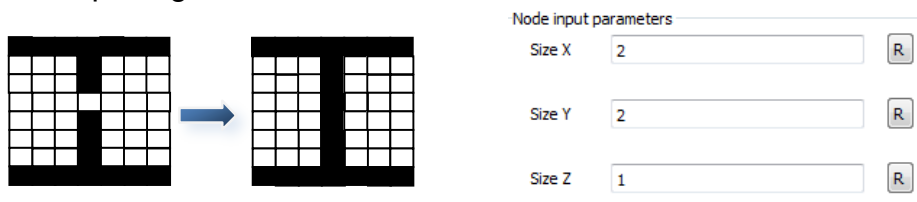
**Dilate:** This operator allows to morphologically dilate the image. 3 parameters can be modified: the dilation size in X, Y and Z axis.



**Erode:** This operator allows to morphologically erode the image. 3 parameters can be modified: the erosion size in X, Y and Z axis.



**Opening:** this operator allows to morphologically open the image. 3 parameters can be modified: the opening radius size in X, Y and Z axis.





## The “OpData” operator

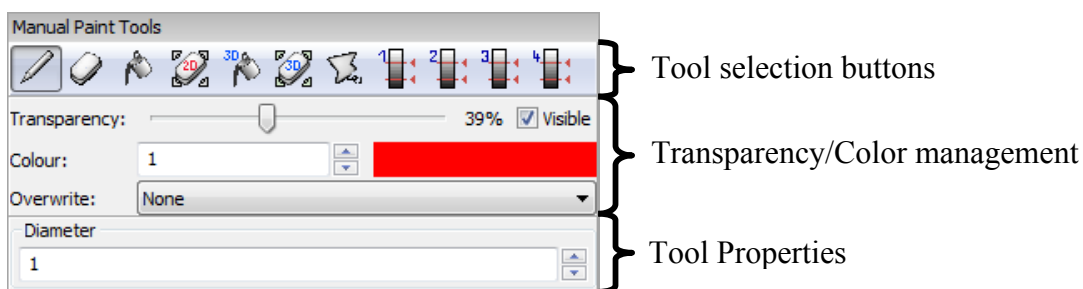
**Shadow:** this operator makes the propagation of the object on the working image according to X, Y or Z axis. You can include or exclude the mask with the button “Include mask”.



## The “Manual” operators:

Manual operators represent the most interactive part of the 3D VPM 2.0 software. It allows to simply draw on the image or to use more automated propagation algorithm. The two operators “Draw from nothing”  and “Draw from mask”  give the same set of tools. The only difference is that the “Draw from Nothing” operator allows to draw in an empty image where all voxels have the same value 0, whereas the “Draw from mask” operator draws in the selected image (original or working image) by keeping its initial grey levels.


When one of these two operators is selected, the “Operator Properties” window is replaced by the “Manual Paint Tools” window that is divided into three parts. The first part is the “Tool list” buttons. The second is the color and transparency management. The last one is the “Tool properties” parameterization. The two first parts will always be the same. The last one will change from one tool to another.

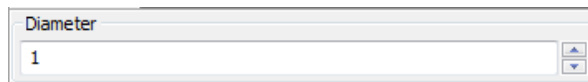



When the drawing is achieved, the resulting image replaces the working image. Like the working image, it is possible to fuse visually these two images by using the Transparency cursor. In the same way, unselecting the “Visible” Box will make the drawing image invisible. The “Color” area allows to choose among a table of colors automatically defined from the grey level value that varies from 0 to 255. Indeed, this color is only used to make the visualization of the drawing easier, the real recorded value being the grey level.

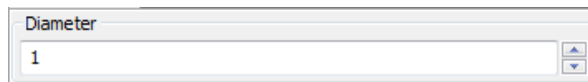







Finally the “overwrite” option offers three options: **None**, **Always**, **Color**. **None** indicates that the tools will never overwrite any already colored voxel. **Always** indicates that the tools will always overwrite any already colored voxel. **Color** indicates that the tools will only overwrite voxels already colored with the same color. This last option is sometimes not available according to the tool.

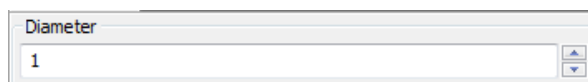
- Pencil Paint Tool : This tool works like any pencil of drawing software. It has only one option: the diameter of the pencil indicated in voxel.




- Eraser Paint Tool : This tool works like any Eraser of drawing software. It has only one option: the diameter of the Eraser indicated in voxel.



- Fill2D Paint Tool : This tool works like any Fill tool of drawing software in 2D, which means on the selected slice.
- Erase2D Paint Tool : This tool works like the Fill2D paint tool but with the color 0, which erases drawn voxels. It has no option.
- Paint3D Paint Tool : This tool works like any Fill tool of drawing software in 3D, which means on all slices. It has no option.
- Erase3D Paint Tool : This tool works like the Fill3D paint tool but with the color 0, which erases drawn voxels. It has no option.
- Polygone Paint Tool : This tool works like any Polygone drawing software. It has only one option: the diameter of the drawn lines in voxel.

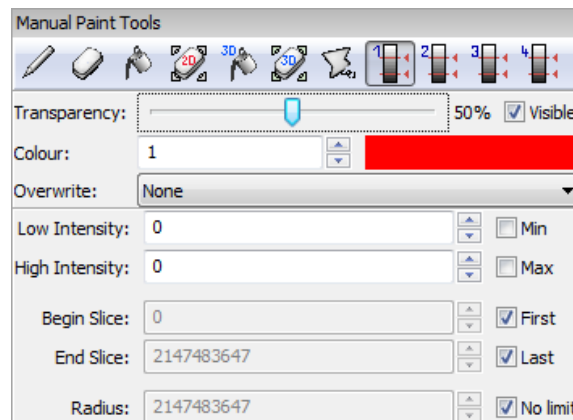



- Min-Max propagation Tool : This automated tool allows to realize a propagation from selected voxels in the image. This iterative process includes any neighbor Voxel of the seed wave that verifies the five conditions that can be parameterized in the Tool Properties area: Density  $\geq$  **Min Intensity**, Density  $\leq$  **Max Intensity**, Z value of its coordinate  $\geq$  **Begin Slice**, Z value of its coordinate  $\leq$  **End Slice** and Distance from the initial Seed  $\leq$  **Radius**. The Min and Max densities are computed from the user interactive selection of the initial seed wave:

**Min Intensity** = Minimal Grey Level of the initial seed wave - **Low intensity**

**Max Intensity** = Maximal Grey Level of the initial seed wave + **High intensity**

Users can modify the parameters **Low intensity**, **High intensity**, **Begin Slice**, **End Slice** and **Radius** in the Tool Properties area.

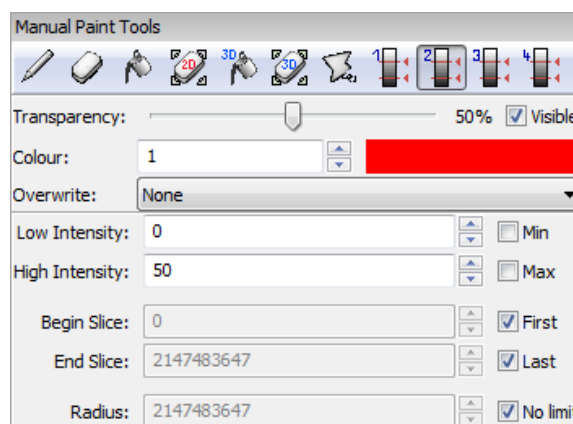



- Mean propagation Tool : This automated tool allows to realize a propagation from selected voxels in the image. This iterative process includes any neighbor Voxel of the seed wave that verifies the five conditions that can be parameterized in the Tool Properties area: Density  $\geq$  **Min Intensity**, Density  $\leq$  **Max Intensity**, Z value of its coordinate  $\geq$  **Begin Slice**, Z value of its coordinate  $\leq$  **End Slice** and Distance from the initial Seed  $\leq$  **Radius**. The Min and Max densities are computed from the user interactive selection of the initial seed wave:

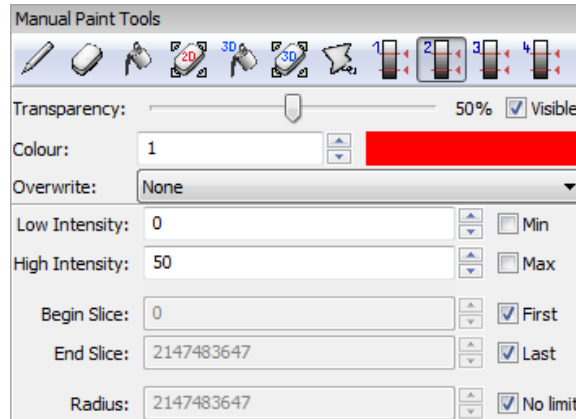
**Min Intensity** = Mean Grey Level of the initial seed wave - **Low intensity**

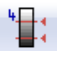
**Max Intensity** = Mean Grey Level of the initial seed wave + **High intensity**

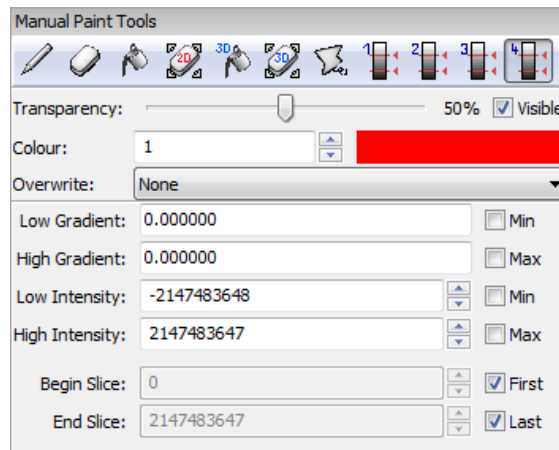
Users can modify the parameters **Low intensity**, **High intensity**, **Begin Slice**, **End Slice** and **Radius** in the Tool Properties area.



- Basic Gradient propagation Tool : This automated tool allows to realize a propagation from selected voxels in the image. This iterative process includes any neighbor Voxel of the seed wave that verifies the five conditions that can be parameterized in the Tool Properties area: Gradient  $\geq$  **Low intensity**, Gradient  $\leq$  **High intensity**, Z value of its coordinate  $\geq$  **Begin Slice**, Z value of its coordinate  $\leq$  **End Slice** and Distance from the initial Seed  $\leq$  **Radius**.

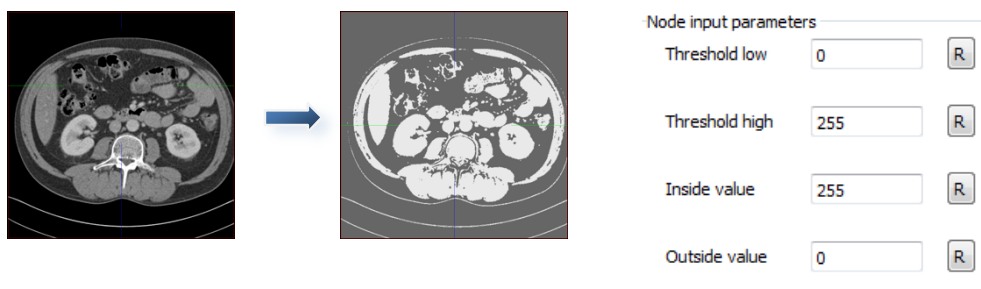


- Gradient propagation Tool : This automated tool allows to realize a propagation from selected voxels in the image. This iterative process includes any neighbor Voxel of the seed wave that verifies the six conditions that can be parameterized in the Tool Properties area: Gradient  $\geq$  **Low Gradient**, Gradient  $\leq$  **High Gradient**, Density  $\geq$  **Low Intensity**, Density  $\leq$  **High Intensity**, Z value of its coordinate  $\geq$  **Begin Slice** and Z value of its coordinate  $\leq$  **End Slice**.

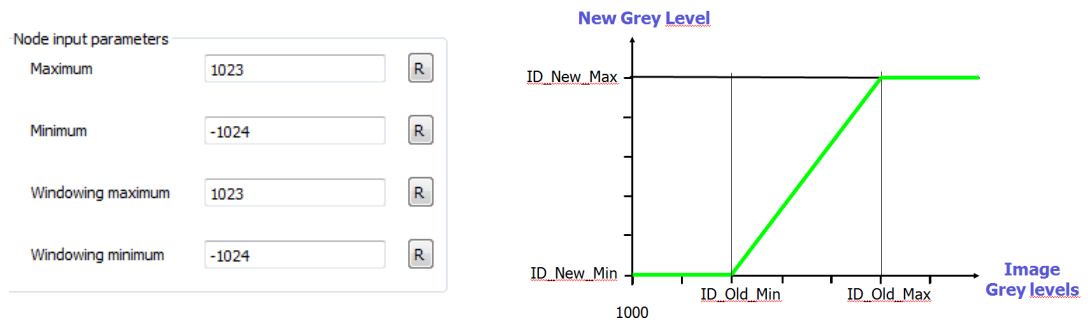


**The “photometric” operators**

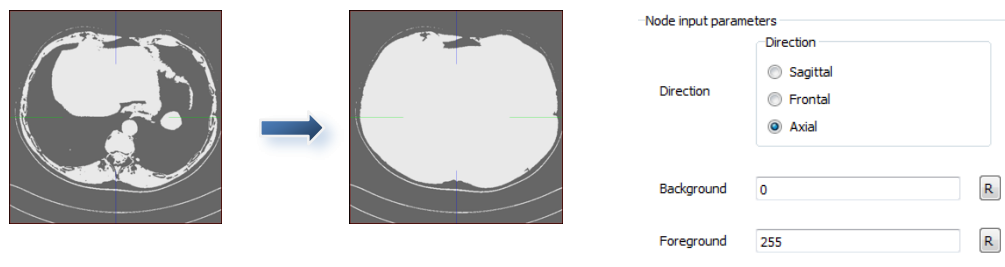
Threshold: this operator allows to binarize a grey level image. It will thus replace the grey levels between “Threshold low” and “Threshold high” by the value “Inside value”, the other grey levels being replaced by the value “Outside value”.



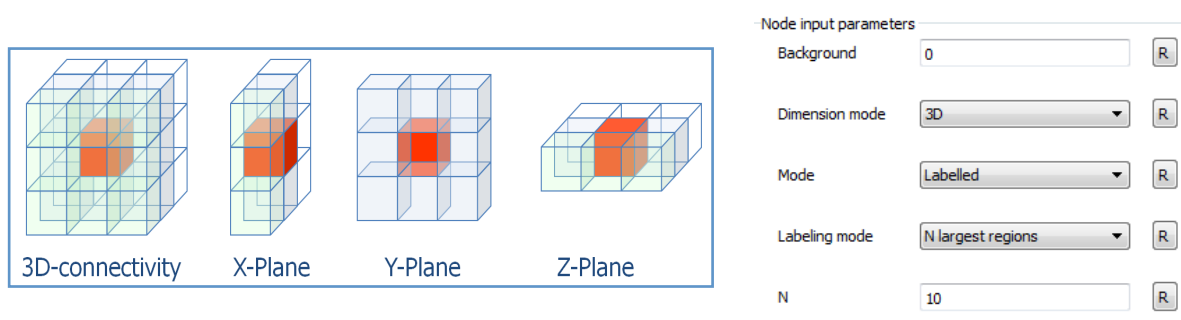
**Windowing:** This operator modifies grey levels of an image by doing a windowing. As a normal windowing, it transforms grey levels of the image between the “Windowing minimum” value and the “Windowing maximum” value by replacing it by new grey levels linearly distributed between “Minimum” value and the “Maximum”.



**FillHole2D:** this operator allows to fill 2D holes in each slice of a binary image. You can choose the slice axis between X (sagittal), Y (frontal) and Z (axial).



**Labeling:** this operator allows to compute the connected components of an image. The resulting image is a grey level image, each grey level corresponding to a connected component classified from the biggest one (grey level value = 1) to the smallest one (grey level value = n), this is the labeling. Some parameters can be changed. The first one is the “Dimension mode” that defines the neighborhood used. Then, the “Mode”: labeled or Binary. In Binary, all different connected components take the value 255, the other part of the working image turn into 0. The two following ones are defining the components that will be kept between four choices: the N largest, the N smallest, the components with a size  $\leq N$  and the components with a size  $\geq N$ .







## **APPENDIX II**

### **French Patent for colored-crosshair-based navigation Interface**

Equipement d'aide au positionnement d'un fragment osseux, d'une prothèse ou d'un implant osseux lors d'une intervention chirurgicale.

5 Domaine de l'invention

La présente invention concerne le domaine des équipements chirurgicaux et plus précisément des équipements d'aide visuelle du chirurgien. De tels équipements mettent en œuvre des systèmes magnétiques de localisation spatiale  
10 associés au patient et à l'instrumentation pour fournir des signaux de localisation spatiale qui sont traités par un système informatique pour fournir au chirurgien des informations graphiques destinées à l'assister dans une intervention par une visualisation de ces informations sur un  
15 écran placé à proximité du champ opératoire. Le terme écran est utilisé de manière générique pour désigner une interface visuelle (écran, tablette informatique, projecteur, lunettes).

Ce domaine comprend notamment les équipements destinés à l'aide au positionnement adéquat d'un os ou d'un  
20 fragment osseux, par exemple du maxillaire lors d'une ostéotomie maxillo-mandibulaire ou dans le cadre de la chirurgie orthopédique, notamment du rachis. Ce domaine comprend également les équipements destinés à l'aide au positionnement de prothèses ou d'implants osseux en chirurgie  
25 maxillo-faciale, dentaire ou orthopédique, notamment du rachis. Dans ces applications, le risque d'erreur de position entre ce qui a été planifié et ce qui est effectivement réalisé lors de l'intervention est non négligeable et fondamental pour la sécurité du patient et le succès de  
30 l'intervention.

Etat de la technique

On connaît dans l'état de la technique différentes solutions mettant en œuvre deux familles de solutions.

La première famille de solutions vise à afficher sur un écran d'ordinateur ou une console à proximité visuelle du praticien.

La demande de brevet US2011275957 décrit par exemple un système de navigation chirurgicale pour la chirurgie de remplacement du genou. Il met en œuvre des capteurs inertiels composés de puces d'inertie à six degrés de liberté, dont les mesures sont traitées par une série d'algorithmes intégration, quaternions, et filtre de Kalman, pour suivre la position et l'orientation des os et des instruments chirurgicaux.

Le système enregistre la géométrie anatomique, calcule les centres communs et l'axe mécanique du genou, et détermine en temps réel une visualisation de l'extrémité inférieure pour permettre la projection sur un écran disposé dans le champ opératoire une image agrandie de la zone opératoire.

Le brevet européen EP469966 décrit un dispositif chirurgical assisté par ordinateur possédant un système de coordonnées tridimensionnelles de référence qui lui est associé pour assister un chirurgien dans le positionnement d'un instrument chirurgical ou d'un implant lors d'une intervention chirurgicale, ou d'un examen, sur des parties d'un patient, lesdites parties occupant des positions et des orientations dans ou sur ledit patient définies soit par une mesure physique des positions et orientations soit par la communication audit dispositif à partir d'une source d'information d'image extérieure.

Ce dispositif comprend :

- un moyen de référence possédant un point de référence dans le système de coordonnées de référence disposés à l'extérieur et à côté dudit patient ;
- des moyens pour déterminer la position et l'orientation de ladite partie dudit patient dans ledit

système de coordonnées de référence par rapport audit point de référence et pour former des données d'affichage du patient en deux ou trois dimensions, proportionnelles auxdites positions et orientations de ladite partie ;

5                   - des moyens de détermination de la position de l'instrument comprenant des moyens de détection pour détecter la position et l'orientation dudit instrument ou implant dans ledit système de coordonnées de référence par rapport audit point de référence et pour former des données d'instrument en  
10 deux ou trois dimensions proportionnelles auxdites positions et orientations dudit instrument. Un électrogoniomètre dont une extrémité est lié mécaniquement au patient et est couplé mécaniquement avec le support par un cylindre avec une vis à auto-indexation.

15                   Ce dispositif comprend un moyen pour convertir lesdites données d'affichage du patient en signaux objectifs pour présenter un affichage objectif sur lesdits moyens d'affichage et pour convertir lesdites données d'instrument en  
20 signaux d'instrument pour présenter la position et l'orientation dudit instrument ou implant sur lesdits moyens d'affichage.

25                   La demande de brevet européen EP1523950 décrit un système d'aide à l'implantation d'un implant, comprenant :

                  - un premier élément de localisation fixé à l'implant, avec six degrés de liberté, apte à agir comme un cadre de référence dynamique,

30                   - un second élément de localisation pour la détermination de la position d'un second élément de l'implant, avec six degrés de liberté,

                  - un détecteur pour détecter ces éléments de localisation

35                   - ledit processeur traitant les informations de position pour déterminer une position relative des deux

éléments et afficher des icônes représentant le premier et le second élément et de permettre ainsi la navigation d'au moins un dudit premier élément et dudit second élément sans nécessiter des images du patient.

5 Une deuxième famille de solutions de l'art antérieur concerne la visualisation d'une représentation symbolique calculée à partir des signaux de localisation.

La demande de brevet internationale W0200280824 décrit par exemple un procédé pour assurer une bonne insertion  
10 de la tête sphérique d'une prothèse fémorale dans sa cuvette.

Le système comprend un outil pour la commande de l'angle mutuel entre la tige de la prothèse et la coupelle en plus d'un système de positionnement pour la définition d'un système de référence et pour la détermination et le réglage du  
15 décalage et de la longueur de la jambe.

#### Inconvénients de l'art antérieur

Les solutions de l'art antérieur présentent différents inconvénients.

En premier lieu, certaines solutions prévoient une  
20 liaison mécanique entre le référentiel patient et le référentiel mobile, lié par exemple à un ancillaire, pour enregistrer les positions et déplacements relatifs. Une telle liaison limite les gestes chirurgicaux et impose des contraintes sur le déroulement d'une intervention.

En second lieu, l'information fournie par les  
25 solutions de l'art antérieur produisent une représentation homothétique, c'est-à-dire conservant les angles, les parallèles et les rapports de longueurs de la zone d'intervention chirurgicale, n'apportant de ce fait pas  
30 beaucoup d'informations supplémentaires au chirurgien.

Solutions apportées par l'invention

Afin de répondre à ces inconvénients, l'invention propose une solution destinée à la visualisation sur un écran bidimensionnel d'un objet-mire tridimensionnel symbolique et la superposition d'une image symbolique de la partie mobile avec des moyens techniques n'introduisant aucune gêne pour le chirurgien et lui permettant d'améliorer son geste chirurgical grâce à l'affichage d'informations intuitives et efficaces.

A cet effet, l'invention concerne selon son acception la plus générale un équipement d'aide au positionnement d'un fragment osseux lors d'une intervention chirurgicale caractérisé en ce qu'il comporte une série de sondes électromagnétiques interagissant avec un générateur de champ électromagnétique et un calculateur traitant les informations pour fournir des signaux à 6 dimensions sur la position et l'orientation de chacune des sondes ainsi qu'un processeur calcule la position et l'orientation de chaque capteur et assure la communication avec l'ordinateur hôte. Cet ordinateur hôte assure un traitement des signaux provenant du processeur pour générer une représentation graphique symbolique sur un écran disposé dans le champ visuel du chirurgien, ledit processeur calculant une représentation graphique symbolique sous forme d'une mire du patient en fonction des coordonnées  $C_{\text{patient}}$ , en superposition avec la représentation graphique symbolique de la première mire et de la représentation graphique de la seconde mire.

De préférence, l'équipement selon l'invention comporte une base comprenant un calculateur relié à des circuits d'interface capteur amplifiant et échantillonnant les signaux électriques provenant des capteurs, et assurant un prétraitement des signaux pour réduire le bruit et les anomalies des données.

L'invention concerne aussi un procédé d'aide au positionnement d'un fragment osseux lors d'une intervention chirurgicale caractérisé en ce qu'il comporte les étapes suivantes :

- 5           ○ fixation d'un marqueur à six degrés de liberté sur ledit fragment osseux
- calibrage de la position relative dudit marqueur par rapport audit fragment osseux
- acquisition périodique des coordonnées  $C_{\text{marqueur}}$  dans  
10           les six degrés de liberté dudit marqueur dans un référentiel  $R_1$
- acquisition périodique des coordonnées  $C_{\text{patient}}$  de la position du patient dans ledit référentiel  $R_1$
- calcul de la position et de la géométrie d'une  
15           représentation graphique bidimensionnelle d'une mire en fonction desdites coordonnées  $C_{\text{marqueur}}$  du marqueur [croix]
- calcul de la position et de la géométrie d'une  
          représentation graphique bidimensionnelle d'une  
20           seconde mire en fonction des coordonnées  $C_z$  du marqueur selon la position selon une desdits degrés de liberté [cercle]
- représentation sur un écran d'affichage d'une  
          représentation graphique du patient en fonction des  
25           coordonnées  $C_{\text{patient}}$ , en superposition de ladite représentation graphique de la première mire et de la représentation graphique de la seconde mire [cible à atteindre].

Avantageusement le procédé selon l'invention  
30 comporte une étape initiale de recalcul du référentiel des représentations graphiques sur l'écran d'affichage par rotation globale.



---

Description détaillée d'un exemple non limitatif de l'invention

La présente invention sera mieux décrite à la lecture de la description qui suit, se référant aux dessins annexés où :

- la figure 1 représente une vue schématique d'un équipement selon l'invention.

Contexte de l'exemple de réalisation

Un exemple de contexte est celui de la chirurgie maxillo-faciale (CMF) visant à réparer des malformations des os du visage, en particulier la mauvaise position des mâchoires (rétrognathisme, prognathisme) et l'asymétrie faciale, sont à l'origine de troubles de la mastication, de l'élocution, voire de la perte des dents et de difficultés psycho-sociales venant accompagner une disgrâce faciale.

La chirurgie orthognathique consiste à sectionner et repositionner les segments osseux concernés.

L'une des étapes les plus cruciales de ce type d'interventions est le positionnement du maxillaire. En effet, ce temps chirurgical, généralement initial, repose sur des mouvements complexes dans les 3 dimensions. Il va servir de référence pour le restant de l'intervention et déterminer son succès et l'apparence finale du patient et son sourire.

Cette étape-clef, est délicate, car elle impose au chirurgien de rétablir une anatomie aussi parfaite que possible en termes de symétrie et d'orthogonalité: alignement du milieu entre les incisives supérieures avec l'axe médian de du visage, positionnement horizontal du plan occlusal passant par les dents. Si des repères visuels existent lorsque le chirurgien examine son patient en consultation (ligne horizontale passant par les pupilles, ligne verticale passant par le milieu du visage), ces repères disparaissent chez un

patient installé pour l'intervention chirurgicale dont le visage est recouvert par des draps stériles et déformé par de multiples sondes. Ainsi, en l'absence de repères, le positionnement adéquat du maxillaire repose bien souvent sur  
5 l'unique évaluation visuelle et sur l'expérience du chirurgien.

#### Equipement d'acquisition des informations de localisation

L'équipement comprend une série de sondes  
10 électromagnétiques (1, 2) interagissant avec un générateur de champs et un calculateur traitant les informations pour fournir des signaux à 6 dimensions sur la position et l'orientation de chacune des sondes.

Un tel équipement comprend :

15 - une base (4) munie d'un générateur de champ émettant un champ électromagnétique de faible intensité qui définit un espace de détection. Ce générateur de champ comprend une antenne (3) généralement planaire fixée dans le référentiel du bloc opératoire.

20 - optionnellement un générateur de champ de table destiné à minimiser les distorsions de suivi causés par des matériaux conducteurs ou ferromagnétiques

- des capteurs électromagnétiques (1, 2) échangeant avec la base des signaux électriques sont fonction  
25 de la distance et l'angle entre un capteur et le générateur de champ (3).

La base (4) comprend un calculateur relié à des circuits d'interface capteur amplifiant et échantillonnant les signaux électriques provenant des capteurs, et assurant un  
30 prétraitement des signaux pour réduire le bruit et les anomalies des données.

Le processeur calcule la position et l'orientation de chaque capteur (1, 2) et assure la communication avec l'ordinateur hôte (5). Cet ordinateur hôte (5) assure un

traitement des signaux provenant du processeur pour générer une représentation graphique symbolique sur un écran (6) disposé dans le champ visuel du chirurgien.

5                   A titre d'exemple, cet ensemble d'acquisition électromagnétique est un ensemble Aurora® de la société Northern Digital Inc., Waterloo, Ontario, Canada.

#### Positionnement des sondes

10                   Au moins une sonde (1) est fixée sur le patient (7), par exemple sur son front.

                  Une autre sonde (2), mécaniquement indépendante de la première sonde (1), est fixée sur le maxillaire (8). Une troisième sonde (2') est laissée libre.

15                   Les sondes (1, 2, 2') fournissent des informations sur six degrés de liberté. Il s'agit par exemple de capteurs Aurora 6DOF cathéter, de type 2 de la société Northern Digital Inc., Waterloo, Ontario, Canada). Elles présentent un diamètre de 1,3 mm et fournissent une information d'orientation avec une précision de (0,5 °) en orientation et  
20 de moins d'un millimètre en position.

                  Le générateur de champ est positionné à une distance de consigne de 100 mm latéralement à partir de la zone de positionnement des sondes (1, 2, 2').

25                   L'espace de suivi présente un volume d'environ 50x50x50 cm. La fréquence d'acquisition est de 20 Hz.

                  La sonde (1) est fixée à la partie médiane du front à l'aide d'une bande adhésive pour suivre les mouvements de la tête au cours de la procédure.

30                   Le capteur (2) est noyé dans une gouttière chirurgicale sur mesure fixée à l'arcade dentaire maxillaire.

Traitement des données fournies par le système de localisation

L'ordinateur (5) reçoit les signaux de position et d'orientation des sondes (1, 2, 2') calculés par le processeur de la base (4) pour commander l'affichage d'une représentation symbolique sur l'écran (6).

Les données de localisation sont :

- Les coordonnées  $C_{\text{marqueur}}$  dans les six degrés de liberté du marqueur (2, 2') dans un référentiel  $R_1$  calculées à partir des signaux échangés avec la sonde (2, 2') fixée sur le maxillaire,
- Les coordonnées  $C_{\text{patient}}$  de la position dans les six degrés de liberté du patient (7) dans ledit référentiel  $R_1$  calculées à partir des signaux échangés avec la sonde (1) fixée sur le patient (7).

A partir de ces données, l'ordinateur (5) procède aux traitements suivants :

- calcul de la position et de la géométrie d'une représentation graphique bidimensionnelle d'une mire (10) en fonction desdites coordonnées  $C_{\text{marqueur}}$  du marqueur. Cette mire (10) se traduit par une représentation graphique en forme de croix, dont le centre et l'inclinaison sont déterminés par le résultat du calcul.
- calcul de la position et de la géométrie d'une représentation graphique bidimensionnelle d'une seconde mire (11) en fonction des coordonnées  $C_z$  du marqueur selon la position selon une desdits degrés de liberté. Cette seconde mire (11) se traduit par une représentation graphique en forme d'anneau, dont le centre et le rayon sont déterminés par le résultat du calcul.
- représentation sur un écran d'affichage d'une représentation graphique du patient en fonction des coordonnées  $C_{\text{patient}}$ , en superposition de ladite

représentation graphique de la première mire (10) et de la représentation graphique de la seconde mire (11) correspondant à la cible à atteindre.

## 5 Systeme de navigation

Le calcul de navigation commande l'affichage de la position en temps réel des deux modèles symboliques 3D du maxillaire segmenté (8) et squelette facial supérieur (7), sans aucun lien avec la forme réelle de ces deux parties.

10 Pour initialiser la position réelle du modèle facial (7) par rapport au cadre électromagnétique (3) et la position de sa représentation virtuelle, une procédure d'inscription initiale six points est effectuée. Elle consiste à acquitter les données sur six repères anatomiques faciaux,  
15 sur le modèle virtuel et sur le patient (7), en utilisant un capteur dédié. La corrélation entre ces deux ensembles de points est établie en calculant la matrice de transformation  $T_{CT \rightarrow EM}$  (rotation  $R$ , translation  $t$ ) qui minimise la somme  $\sum_{ni} ||R \cdot p_i + t - q_i||^2$  où  $p_i$  et  $q_i$  désignent les coordonnées des  $n$   
20 points d'acquiescement respectivement identifiés et mesurés. Une fois  $T_{CT \rightarrow EM}$  calculée, on calcule la position du modèle virtuel  $m$  dans le repère lié à (1) qui est égal à  $T_{EM \rightarrow sonde1} \times T_{CT \rightarrow EM} \times m$ . Cela nous permet de connaître la position du modèle virtuel dans le repère EM quel que soit le mouvement de la  
25 tête du patient pendant l'intervention..

On fixe ensuite une gouttière sur l'arcade maxillaire dentaire et on enregistre la position du capteur (2) lorsque le maxillaire est maintenu en position d'étalonnage. Cette étape permet de déterminer la position du  
30 maxillaire avant découpe par rapport au capteur (2). Soit  $M$  le modèle virtuel du maxillaire, sa position par rapport au repère lié à (2) est calculée de la manière suivante :  $T_{sonde1 \rightarrow sonde2} \times T_{EM \rightarrow sonde1} \times T_{CT \rightarrow EM} \times M$ .

Supposons que la position souhaitée du maxillaire ait été calculée dans le repère lié au CT. Il s'agit d'une rotation et translation définies dans CT  $T_{\_target}^{CT}$  à appliquer au modèle virtuel du maxillaire. Il est aisé de calculer ce mouvement souhaité dans le repère mobile (1)  $T_{\_target}^{sonde1}$  en se servant de  $T_{EM \rightarrow sonde1} \times T_{CT \rightarrow EM}$  préalablement calculé.

La représentation graphique comprend un réticule de couleur permettant de visualiser l'intersection de deux plans orthogonaux passant par le maxillaire, la sagittal médian et le plan horizontal d'occlusion.

Les côtés respectivement droit et gauche du plan vertical sont affichés avec des couleurs différenciées, par exemple rouge et jaune. Les cotés respectivement inférieur et supérieur du plan horizontal nt affichés avec des couleurs différenciées, par exemple bleu et vert). Dans le fond, une croix blanche fixe orthogonale constitue la référence pour la position de l'objectif atteint. Ce réticule virtuel est déplacé en temps réel avec le maxillaire détaché réelle grâce aux données périodiquement acquises par le système d'acquisition. Une correspondance parfaite se traduit par la disparition des côtés de la croix de couleur et son alignement sur la constante croix blanche. Ce réticule de couleur permet de positionner avec une grande précision le maxillaire détaché

La position du maxillaire est illustrée par un cercle, autour de la croix. Un petit mouvement dans le sens de la profondeur sera moins visible (orthogonal au plan du réticule) et donc moins précis.

La profondeur du maxillaire est donc illustrée par un cercle supplémentaire, autour de la croix. Lorsque la profondeur du maxillaire réel est éloignée de la position de la cible prévue, le cercle apparaît large et rouge. Lorsque cette position se rapproche de l'objectif, le cercle se rétrécit et vire au vert jusqu'à atteindre 1 pixel de largeur.

Revendications

1 - Equipement d'aide au positionnement d'un fragment osseux, d'une prothèse ou d'un implant osseux lors d'une intervention chirurgicale caractérisé en ce qu'il comporte une série de sondes électromagnétiques (1, 2) interagissant avec un générateur de champs et un calculateur traitant les informations pour fournir des signaux à 6 dimensions sur la position et l'orientation de chacune des sondes ainsi qu'un processeur qui calcule la position et l'orientation de chaque capteur (1, 2) et assure la communication avec l'ordinateur hôte (5). Cet ordinateur hôte (5) assure un traitement des signaux provenant du processeur pour générer une représentation graphique symbolique sur un écran (6) disposé dans le champ visuel du chirurgien, ledit processeur calculant une représentation graphique symbolique sous forme d'une mire (10) du patient en fonction des coordonnées  $C_{\text{patient}}$ , en superposition avec la représentation graphique symbolique de la première mire et de la représentation graphique de la seconde mire (11).

20

2 - Equipement d'aide au positionnement d'un fragment osseux, d'une prothèse ou d'un implant osseux lors d'une intervention chirurgicale selon la revendication 1 caractérisé en ce qu'il comporte une base (4) comprenant un calculateur relié à des circuits d'interface capteur amplifiant et échantillonnant les signaux électriques provenant des capteurs, et assurant un prétraitement des signaux pour réduire le bruit et les anomalies des données.

30 3 - Procédé d'aide au positionnement d'un fragment osseux, d'une prothèse ou d'un implant osseux lors d'une intervention chirurgicale caractérisé en ce qu'il comporte les étapes suivantes :

- fixation d'un marqueur à six degrés de liberté sur ledit fragment osseux
- enregistrement de la position relative dudit marqueur par rapport audit fragment osseux
- 5 ○ acquisition périodique des coordonnées  $C_{\text{marqueur}}$  dans les six degrés de liberté dudit marqueur dans un référentiel  $R_1$
- acquisition périodique des coordonnées  $C_{\text{patient}}$  de la position du patient dans ledit référentiel  $R_1$
- 10 ○ calcul de la position et de la géométrie d'une représentation graphique bidimensionnelle d'une mire en fonction desdites coordonnées  $C_{\text{marqueur}}$  du marqueur [croix]
- calcul de la position et de la géométrie d'une
- 15 représentation graphique bidimensionnelle d'une seconde mire en fonction des coordonnées  $C_z$  du marqueur selon la position selon un desdits degrés de liberté [cercle]
- représentation sur un écran d'affichage d'une
- 20 représentation graphique du patient en fonction des coordonnées  $C_{\text{patient}}$ , en superposition de ladite représentation graphique de la première mire et de la représentation graphique de la seconde mire [cible à atteindre].

25

4 - Procédé d'aide au positionnement d'un fragment osseux, d'une prothèse ou d'un implant osseux lors d'une intervention chirurgicale selon la revendication principale caractérisé en ce qu'il comporte

30 une étape initiale de recalcul du référentiel des représentations graphiques sur l'écran d'affichage par rotation globale.

35



ABREGE

5 L'invention concerne un équipement d'aide au  
positionnement d'un fragment osseux, d'une prothèse ou d'un  
implant osseux lors d'une intervention chirurgicale qui  
comporte une série de sondes électromagnétiques (1, 2)  
interagissant avec un générateur de champs et un calculateur  
10 traitant les informations pour fournir des signaux à 6  
dimensions sur la position et l'orientation de chacune des  
sondes ainsi qu'un processeur qui calcule la position et  
l'orientation de chaque capteur (1, 2) et assure la  
communication avec l'ordinateur hôte (5).

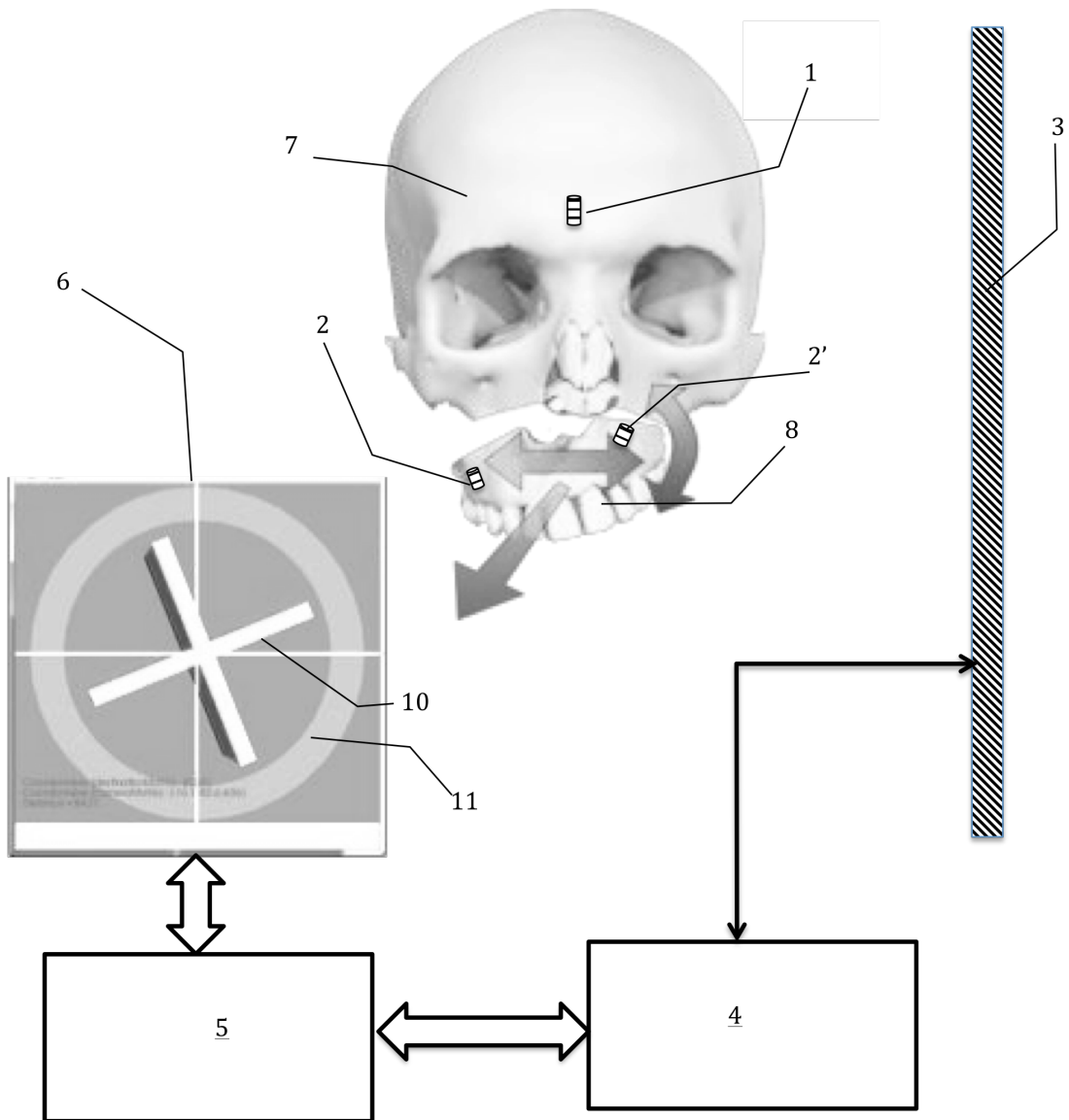
15

Cet ordinateur hôte (5) assure un traitement des  
signaux provenant du processeur pour générer une  
représentation graphique symbolique sur un écran (6) disposé  
dans le champ visuel du chirurgien, ledit processeur calculant  
20 une représentation graphique symbolique sous forme d'une mire  
(10) du patient en fonction des coordonnées  $C_{\text{patient}}$ , en  
superposition avec la représentation graphique symbolique de  
la première mire et de la représentation graphique de la  
seconde mire (11).

25

Figure de l'abrégé : 1

Fig. 1





## **APPENDIX III**

### **Object Service Registry (OSR) diagram for navigation software**

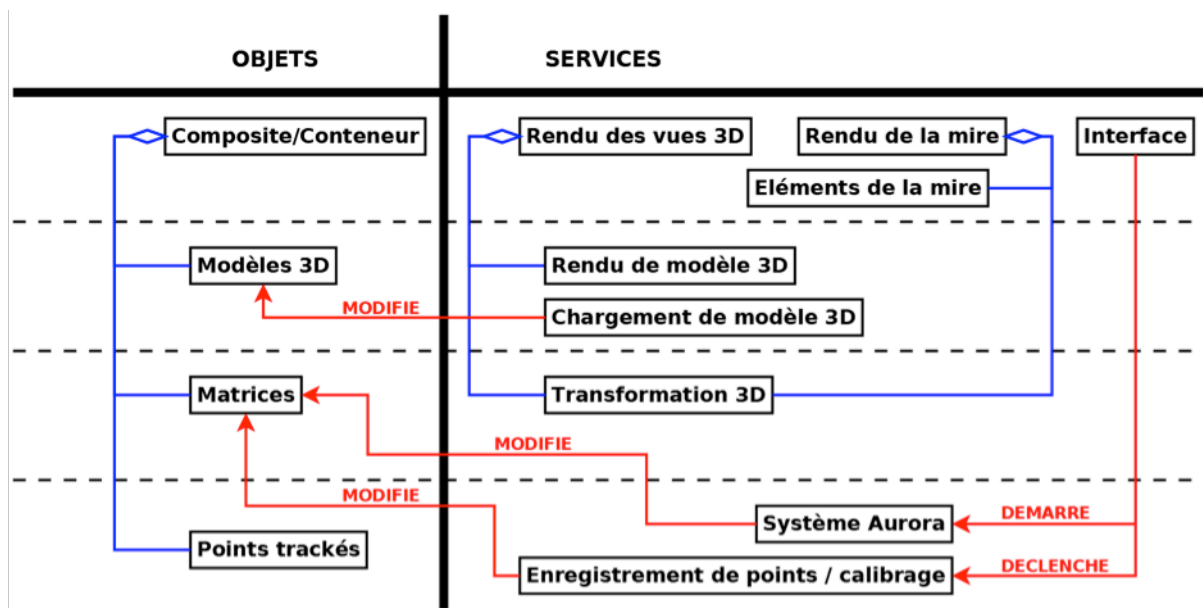


Figure III.1: Simplified Object Service Registry (OSR) diagram.

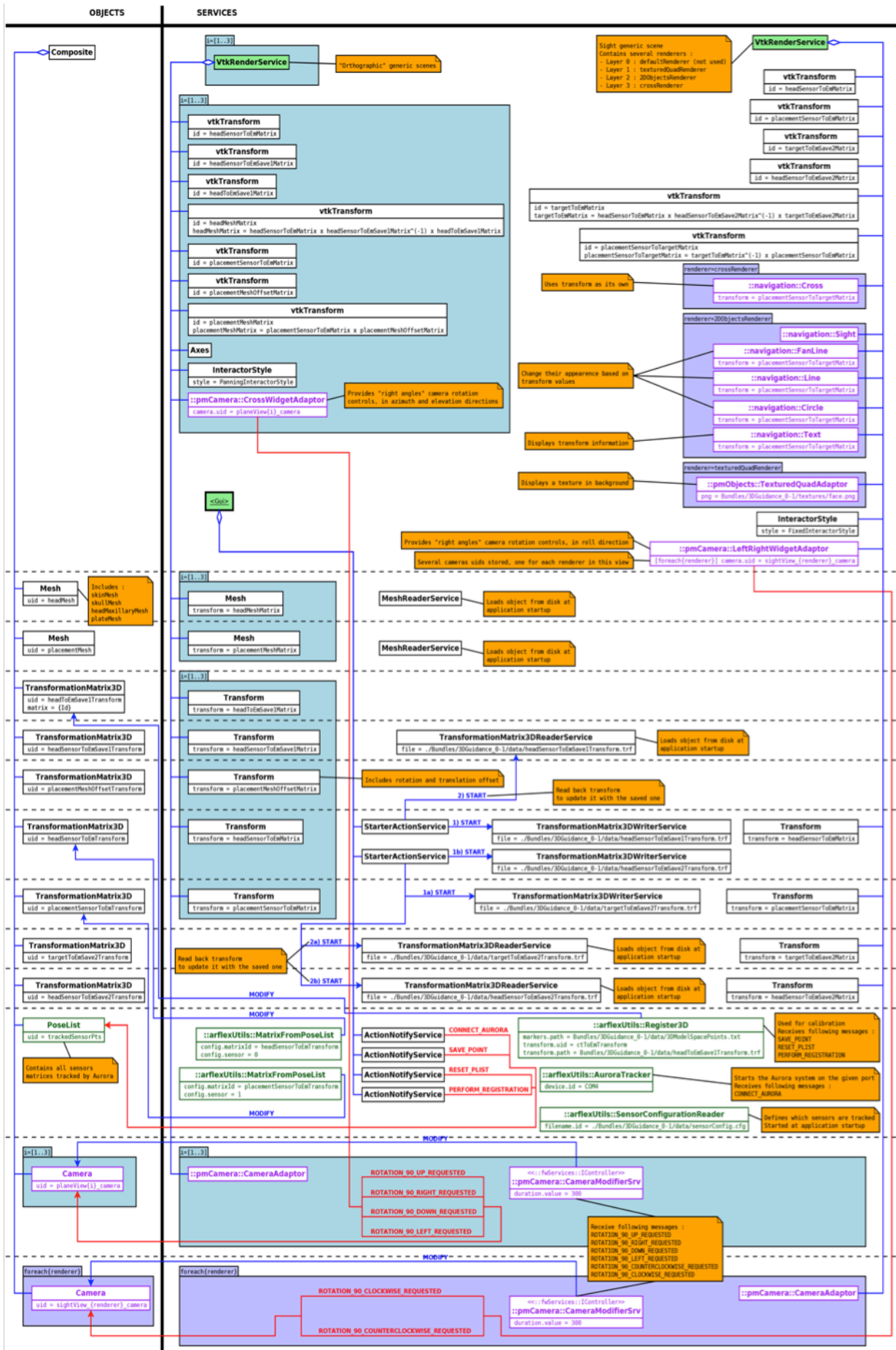


Figure III.2: Complete Object Service Registry (OSR) diagram.

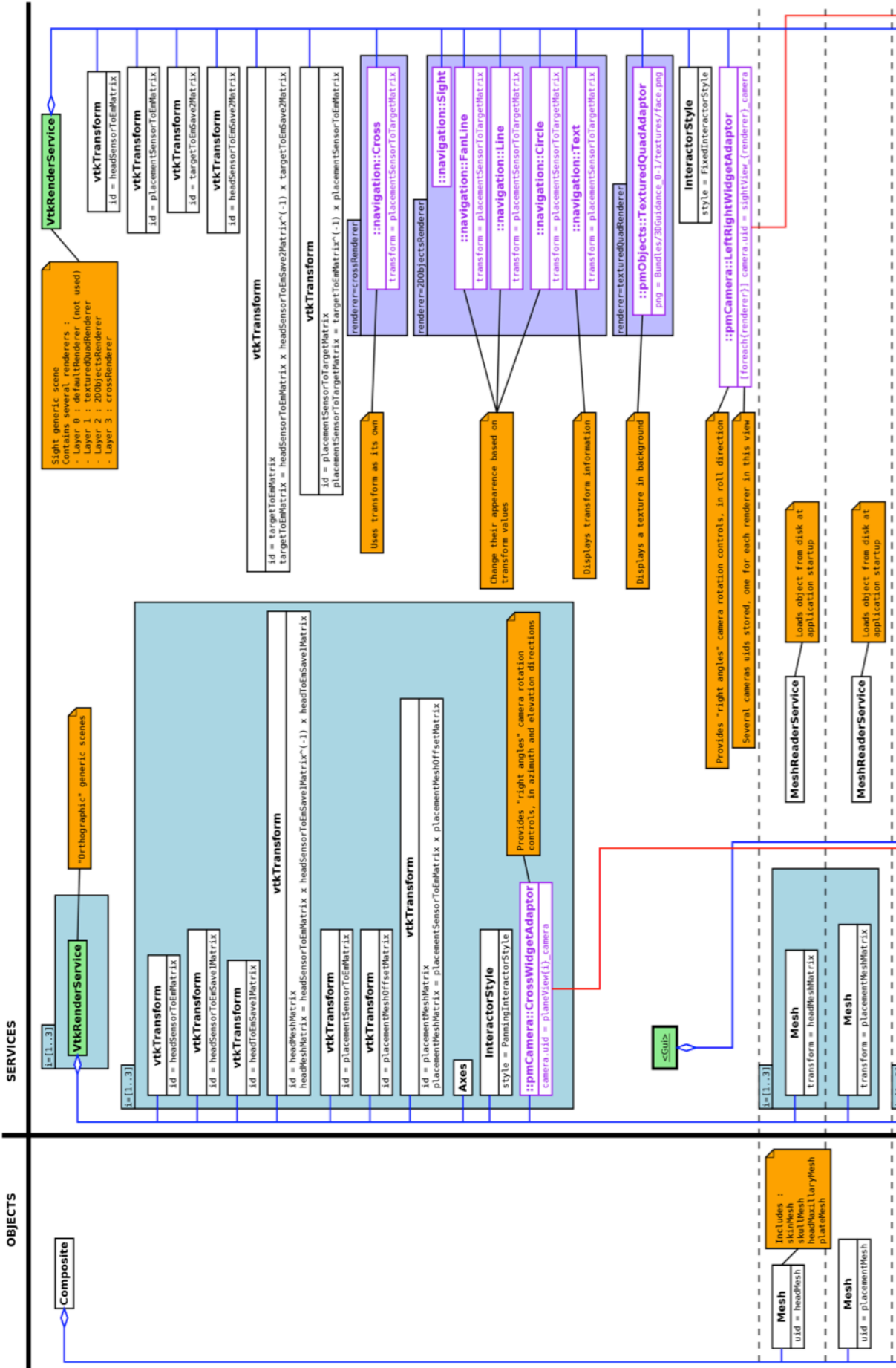


Figure III.3: Object Service Registry (OSR) diagram – detail (top part).

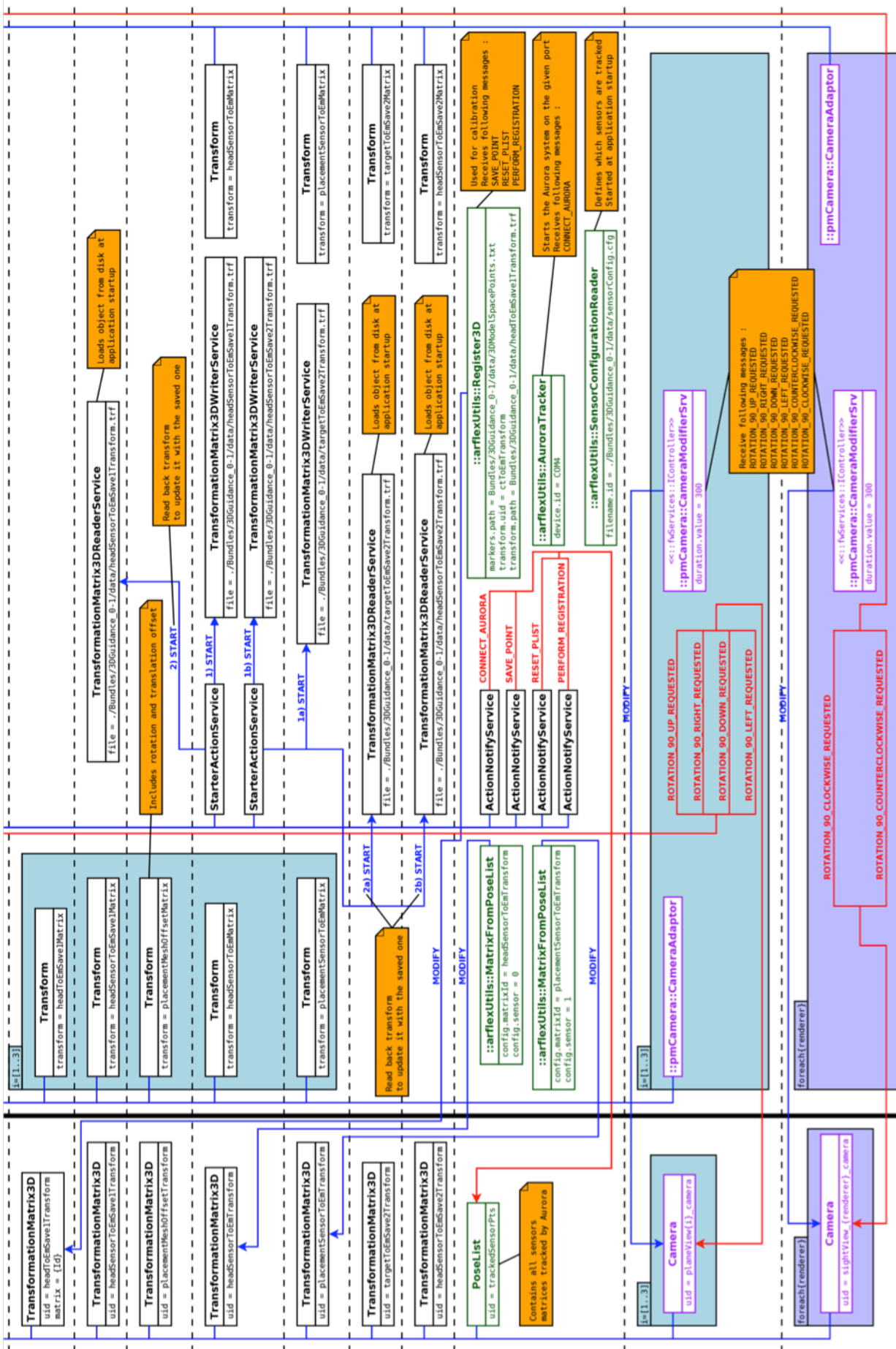


Figure III.4: Object Service Registry (OSR) diagram – detail (bottom part).





## Figure caption

### 1. Introduction.

1.1	From the first medical X-ray by Wilhelm Röntgen of his wife's hand (1895) to the futuristic use of Computed Tomography 3D models .....	3
1.2	Scopis® Planning station and surgical navigation system for Neurosurgery .....	6
1.3	Four area split-screen displaying a neurosurgical tumor and its vicinity .....	6
1.4	Navigation in orthopedic surgery (prosthetic knee replacement) .....	6
1.5	Brainlab® Spinal navigation system .....	6
1.6	Simplant® planning software for oral implantology. ....	7
1.7	Robodent® navigation software for oral implantology. ....	7
1.8	Computer-assisted workflow in orthognathic surgery from preoperative diagnosis, planning and simulation to transfer to the operating theatre.....	8

### 2. Orthognathic Surgery: Issues and development purposes.

2.1	Basic maxillofacial anatomy for orthognathic surgery .....	20
2.2	Sagittal cross-section of a tooth into the alveolar bone illustrating its segments and different mineral layers.....	20
2.3	Anatomical definition of reference axes and planes. Definition of movements along these axes .....	20
2.4	Clinical aspects of retrognathism, prognathism and asymmetry. ....	21
2.5	Number of maxillofacial surgeons and orthognathic surgical procedure per year worldwide .....	21
2.6	Intraoral orthodontic appliances used to treat prognathism during growth.....	22
2.7	Extraoral device used to treat prognathism during growth .....	22
2.8	Schematic illustration of a maxillary osteotomy also called « Le Fort I » osteotomy (left) and mandibular osteotomy, also called bilateral sagittal split ramus osteotomy.....	23
2.9	Orthognathic osteotomy and fixation .....	23
2.10	Correction of bone discrepancy and restoration of dentofacial harmony. ....	24
2.11	Preoperative and postoperative clinical aspects in terms of facial morphology	25
2.12	Preoperative and postoperative clinical aspects in terms of dental occlusion ...	25
2.13	Conventional 2D analysis through cephalometry and cephalometric tracings ..	26
2.14	Screen captures of 3D simulation software .....	28
2.15	Illustration of clinical landmarks loss .....	30
2.16	Schematic and photographic illustration of intermediate dental splint process .	31
2.17	Schematic illustration of surgical planning transfer using an intermediate and final dental splint for intraoperative positioning of the maxilla .....	31
2.18	CAD/CAM intramaxillary positioning guides. ....	33
2.19	Principle in optical-based tracking and required line of sight integrity .....	37

2.20 Bulk of optical fiducials in orthognathic surgical navigation.....	37
2.21 Augmented-reality-based surgical navigation.....	41
2.22 Interactive Augmented Reality System we developed and tested in the OR. ...	42
2.23 Illustration of the principle of our Augmented Virtuality navigation software .....	44

### **3. Modeling. Segmentation: from DICOM data to the virtual model**

3.1 Average densities in Hounsfield Unit in a Head CT-Scan .....	63
3.2 Sagittal section of a tooth .....	63
3.3 CT-scan acquired in dental occlusion (volume rendering) .....	64
3.4 Native postoperative CT-Scan slice featuring streak metal artifacts .....	65
3.5 Interactive bone segmentation pipeline designed on VR-Med. ....	71
3.6 Propagation affecting the whole facial skeleton .....	71
3.7 Detail of the contact between the upper and lower teeth due to one voxel causing propagation from the skull to the mandible.....	72
3.8 Detail of the separation between the upper and lower teeth .....	72
3.9 Result of two different thresholds applied to respectively the upper facial skeleton and the mandible .....	73
3.10 The two distinct virtual models of respectively the upper facial skeleton and the mandible.....	73
3.11 Scheme illustrating our global semi-automated segmentation pipeline and its partition .....	75
3.12 Footer scheme illustrating the part of the global pipeline addressing bone and teeth segmentation through 4 steps.....	76
3.13 Scheme summarizing the bone and teeth part of the segmentation pipeline....	77
3.14 Footer scheme illustrating the part of the bone + teeth segmentation pipeline addressing bone segmentation .....	78
3.15 Radiological anatomy and density (Hounsfield Units) of the pulp-dentin junction in a Head CT-Scan.....	79
3.16 Detail of bone segmentation pipeline .....	79
3.17 Footer scheme illustrating the part of the bone + teeth segmentation pipeline addressing pulp segmentation .....	80
3.18 Detail of Pulp segmentation pipeline .....	81
3.19 Output resulting from a threshold operator applied to the image source.....	81
3.20 Output resulting from a NOT operator .....	81
3.21 Output resulting from Labeling and NOT operators.....	82
3.22 Output resulting from Threshold, Labelling and XOR operators.....	81
3.23 Output resulting from Box, Labeling, Dilate and Labeling operators .....	83
3.24 Footer scheme illustrating the part of the bone + teeth segmentation pipeline addressing intersection pulp-bone .....	84
3.25 Detail of Intersection Bone-pulp segmentation pipeline .....	84
3.26 Footer scheme illustrating the part of the bone + teeth segmentation pipeline addressing bone image refinement.....	85

3.27. Detail of Bone image refinement segmentation pipeline .....	86
3.28 Surface meshes of respectively the maxilla + skull and the mandible resulting from the bone + teeth segmentation pipeline .....	86
3.29 Native postoperative CT-Scan slice featuring streak metal artifacts due to metallic dental restorations .....	87
3.30 Footer scheme illustrating the part of the global pipeline addressing skin segmentation through 3 steps.....	88
3.31 Scheme summarizing the skin and soft tissue layer part of the segmentation pipeline through output images of key steps.....	89
3.32 Footer scheme illustrating the part of the skin segmentation pipeline addressing skin rough segmentation .....	90
3.33 Detail of Skin rough segmentation pipeline .....	90
3.34 Output resulting from a Threshold operator applied to the image source .....	91
3.35. Output resulting from a sequence of Not-Labeling-Not-Threshold operators applied to the output image in Figure 3.34.....	91
3.36 Output resulting from a sequence of 3 Median operators in order to remove the remaining spikes .....	92
3.37. Output resulting from a Fillhole 2D operator applied providing the expected rough segmentation of the skin outline .....	92
3.38 Footer scheme focusing on the bottom line of the skin rough segmentation step, meant to extract a smooth contour gradient.....	93
3.39 Detail of the Bottom line of the Skin rough segmentation step, meant to extract a smooth contour gradient .....	93
3.40 Footer scheme illustrating the part of the skin segmentation pipeline addressing skin and soft tissue layer segmentation .....	94
3.41 Detail of Skin + Soft tissue layer segmentation pipeline.....	94
3.42 Abstract from Skin + Soft tissue layer segmentation pipeline illustrating the two input images required for the watershed.....	95
3.43 Illustration of contour alteration secondary to rough skin segmentation.....	96
3.44 Footer scheme illustrating the part of the skin segmentation pipeline addressing skin outer surface extraction and soft tissue layer smoothing.....	97
3.45 Detail of soft tissue layer smoothing pipeline .....	97
3.46 Detail of the alternate skin + soft tissue layer pipeline.....	99
3.47 Surface meshes resulting from the 4 distinct segmentations of respectively, the maxilla attached to the skull, the mandible, the outside skin surface and the soft tissue layer .....	100
3.48 Principles used to implement the evaluation pipeline between the automated segmentation and the interactive one .....	103
3.49 Evaluation pipeline between the automated segmentation and the interactive one. ....	104
3.50 Image detail from the evaluation pipeline displaying the distance error between interactive (manual) and automated segmentation. ....	107
3.51 Illustration of the partial volume effect.....	107

#### 4. Planning and Simulation

4.1	Definition of the maxilla surgical cutting plane modeled as two symmetrical planes.....	118
4.2	Computing a new mesh subset of the maxilla .....	118
4.3	Planning software interface. ....	119
4.4	Postero-anterior translation axis.....	120
4.5	The set of 7 points interactively chosen to define 4 rotation axes allowing to plan for surgical movements in 3 dimensions. ....	120
4.6	Definition of rotational displacements of the maxilla.....	121
4.7	Schematic representation of the 3 axes and definition of the elementary rotational displacements .....	122
4.8	Examples of common surgical movements .....	124
4.9	Illustration of the 2D Chain mail deformation model. ....	127
4.10	A rigid sphere resting on a deformable solid .....	129
4.11	Two faces animated by a mass-spring model .....	131
4.12	Thigh model defined through a mass-spring method .....	133
4.13	Deformation grid .....	133
4.14	Multi-resolution model .....	135
4.15	Deformation of arm muscles through the finite volume method .....	137
4.16	Service communication diagram .....	141
4.17	Application organization diagram .....	141
4.18	Surface meshes of the patient's upper skull including the maxilla, the mandible, the skin surface and the soft tissue layer surface .....	142
4.19	Superimposition of all surface meshes .....	143
4.20	Result of surface mesh conversion into a volume mesh .....	143
4.21	VRTools main view .....	144
4.22	Mesher 3D main view .....	144
4.23	Vertices of the mandible linked to the closest ones belonging to the soft tissue layer .....	146
4.24	Simulation software interface .....	148
4.25	Surface bone meshes and reference planes (frontal view) .....	149
4.26	Surface bone meshes and reference planes (right lateral view) .....	149
4.27	Surface bone meshes and maxillary section plane (right lateral view).....	149
4.28	Surface bone meshes of the upper facial skeleton and the maxillary segment after section.....	149
4.29	Surface bone meshes of the upper facial skeleton, the maxillary segment after section and the attachment of soft tissue layer volume mesh.....	149
4.30	Surface bone meshes of the upper facial skeleton, the maxillary segment after osteotomy and the simulated soft tissue layer volume mesh.....	150
4.31	Surface bone meshes of the upper facial skeleton, the maxillary segment after osteotomy and the simulated soft tissue layer volume mesh. The postoperative skin surface mesh is added.....	150

---

4.32	Surface bone meshes of the upper facial skeleton, the maxillary segment after section and the attachment of the simulated soft tissue layer volume mesh. A posterior movement of the mandible has been performed.....	150
4.33	Surface bone meshes of the upper facial skeleton, the maxillary segment after section and the attachment of the soft tissue layer volume mesh. A posterior movement of the mandible has been performed. The postoperative skin surface mesh is added.....	150
4.34	Superimposition of the simulated skin mesh and the real postoperative skin surface mesh.....	150
4.35	The two surfaces used to evaluate our method accuracy .....	151
4.36	Surface bone meshes of the upper facial skeleton, the maxillary segment after section and the phantom of the postoperative maxillary position.....	152
4.37	Surface bone meshes of the upper facial skeleton, the maxillary segment after section and the maxilla interactively moved to the postoperative position.....	152
4.38	Surface bone meshes of the upper facial skeleton, the maxillary segment after section and the maxilla moved to the postoperative position. The mandible has been moved from its original position to its postoperative position .....	152
4.39	Surface bone meshes of the upper facial skeleton, the maxillary segment after section and the maxilla interactively moved to the postoperative position. The mandible has been moved from its original position to its postoperative position. The attachment of the simulated soft tissue layer volume mesh is displayed as well as the postoperative skin surface mesh.....	152
4.40	Image and mesh intersection view .....	153
4.41	Point-to-point error measurement method.....	155
4.42	Point-to-surface error measurement method.....	157
4.43	Point-to-weighted-surface error measurement method.....	159
4.44	Distance evaluation display .....	161
4.45	Magnitude of displacements between postoperative and preoperative .....	162
4.46	Magnitude of displacements between postoperative and preoperative excluding error up to 0.5 mm.....	163
4.47	Magnitude of displacements between postoperative and preoperative excluding error up to 1 mm.....	164
4.48	Magnitude of displacements between postoperative and preoperative excluding error up to 1.5 mm.....	165
4.49	Magnitude of displacements between simulated and actual postoperative excluding error over to 3 mm. ....	167
4.50	Magnitude of displacements between simulated and actual postoperative excluding error over to 2.5 mm. ....	168
4.51	Magnitude of displacements between simulated and actual postoperative excluding error over to 2 mm .....	169
4.52	Magnitude of displacements between simulated and actual postoperative excluding error over to 1.5 mm .....	170
4.53	Comparison between the preoperative and simulated models and respectively the preoperative and postoperative clinical morphology .....	172

**5. Navigation software: development and evaluation**

5.1 Plastic head model: mimicking surgery and scanning ..... 181

5.2 The Aurora® electromagnetic tracking system..... 182

5.3 Experimental set-up for EM-based navigation system ..... 184

5.4 Maxilla-splint unit with embedded EM sensor ..... 184

5.5 Three-dimensional reconstruction of plastic head model ..... 185

5.6 Illustration of the coordinate systems used in the navigation system ..... 186

5.7 Correlation between landmarks in the virtual head model and landmarks on the actual plastic head model..... 187

5.8 User Interface of the navigation software ..... 189

5.9 Prototype of 3D colored crosshair ..... 190

5.10 Final version of the navigation crosshair ..... 192

5.11 Rotation of the interface using a dedicated widget..... 193

5.12 Graphic illustration of the eight surgical target positions of the maxilla. .... 197

5.13 Three-dimensional illustration of maxillary position errors regarding translation and rotation ..... 198

**Appendix III. Object Service Registry (OSR) diagram for navigation software**

III.1 Simplified Object Service Registry (OSR) diagram ..... 268

III.2 Complete Object Service Registry (OSR) diagram ..... 269

III.3 Object Service Registry (OSR) diagram – detail (top part)..... 270

III.4 Object Service Registry (OSR) diagram – detail (bottom part)..... 271

## Table caption

2.1	Specifications of the main tridimensional planning and simulation software .....	35
3.1	Interactive segmentation duration of anonymized patients .....	74
3.2	Parameters chosen for the definition of the 3 seeds intended to extract the soft tissue layer .....	95
3.3	Duration of automated and interactive segmentation of 8 patient CT-Scans ..	102
3.4	Numerical results of border-to-border distance error between the automated segmentation and the interactive one .....	106
4.1	Numerical example of the conversion of 8 surgical target positions into mathematical language using transformation matrices.....	125
5.1	Clinical and mathematical equivalences of the 8 surgical-like target positions	196
5.2	Qualitative evaluation form collecting answers of the 12 surgeons enrolled ...	199
5.3	Statistics for duration, angular and translational error for the different groups	200

## Graph caption

3.1	Boxplot graph illustrating the statistical distribution of border-to-border distance error between the automated segmentation and the interactive one .....	105
3.2	Detail of Boxplot graph illustrating the statistical distribution of border to border distance error between the automated segmentation and the interactive one	106
5.1	Comparative task translational error sorted by surgeon using conventional and navigated method.....	200
5.2	Comparative task angular error sorted by surgeon using conventional and navigated method.....	201
5.3	Comparative task duration sorted by surgeon using conventional and navigated method .....	201
5.4	Mean translational error in relation to experimental task number (n°1 to 8) ....	202
5.5	Mean duration in relation to experimental task number (n°1 to 8).....	202



Jean-Christophe LUTZ

**DEVELOPMENT OF NOVEL TOOLS  
BASED ON PATIENT-SPECIFIC MODELS  
FOR GUIDANCE AND EDUCATION  
IN ORTHOGNATHIC SURGERY**

**Résumé :**

Notre pratique courante de la chirurgie orthognathique se heurte aux limites des outils standard de planification et de simulation ainsi qu'à l'absence d'assistance peropératoire.

L'objectif de notre travail était de développer de nouveaux outils répondant à cette problématique. Ainsi, dans un premier temps, un algorithme de segmentation semi-automatique a permis une modélisation 3D patient-spécifique rapide et précise. Nous avons ensuite élaboré un logiciel de simulation des parties molles fondé sur un modèle mécanique de type masse-ressort permettant une précision millimétrique.

Enfin, nous avons conçu un système de navigation temps-réel fondé sur un guidage électromagnétique mini-invasif doté d'une interface utilisateur intuitive. Son évaluation a montré une réduction de la variabilité inter-opérateurs. En plus de son caractère pédagogique, ce système bénéficiait particulièrement aux débutants. Les chirurgiens ont souligné l'intérêt de ce système, tant pour les dysmorphoses complexes que pour les cas de routine.

Ces développements constituent ainsi une suite logicielle susceptible d'améliorer la qualité de prise en charge des patients.

**Mots-clefs :** chirurgie orthognathique, chirurgie assistée par ordinateur, simulation, navigation, guidage électromagnétique.

**Abstract:**

In our routine practice of orthognathic surgery, we face the limitations of conventional planning and simulation tools, and the lack of convenient intraoperative assistance.

If computer science has provided satisfactory solutions for planning, yet simulation and navigation appear improvable.

The aim of our research was to provide novel tools to improve these issues.

Therefore, we first developed a semi-automated segmentation pipeline allowing accurate and time-efficient patient-specific 3D modeling.

We then conceived 1mm-accurate facial soft tissue simulation software based on a mechanical mass-spring model.

Finally, we developed a real-time navigation system based on minimally-invasive electromagnetic tracking, featuring a novel user-friendly interface. Evaluation showed that our software reduced time and accuracy discrepancy between operators. Along with educational purposes, such a system benefited especially trainees. Surgeons emphasized system relevance in the treatment of both, complex and common deformities.

Such developments establish a software suite that could provide significant improvement for patient optimal care.

**Keywords:** orthognathic surgery, computer-assisted surgery, simulation, navigation, electromagnetic tracking.